Measurements of the Tau g-2 in Pb-Pb Collisions at the CMS Experiment and Future Improvements of the CMS Tracker

Dissertation

zur

Erlangung der naturwissenschaftlichen Doktorwürde
(Dr. sc. nat.)

vorgelegt der

Mathematisch-naturwissenschaftlichen Fakultät

der

Universität Zürich

von

Arash Jofrehei

aus

dem Iran

Promotionskommission

Prof. Dr. Ben Kilminster (Vorsitz)

Prof. Dr. Peter Stoffer

Dr. Anna Macchiolo

Dr. David d'Enterria

Zürich, 2024

Acknowledgment

I would like to thank all my colleagues at UZH and CERN who helped me throughout my PhD studies, especially our two senior scientists, Dr. Stefanos Leontsinis and Dr. Anna Macchiolo, for their guidance and supervision from the beginning. Thanks to Dr. Izaak Neutelings, my fellow doctoral student, whose documentation and guidance facilitated the life of many students in our group. Above all, I express my deepest gratitude for the support I received throughout my doctoral studies from my supervisor Prof. Ben Kilminster. I greatly benefited from his deep understanding of physics, his wisdom in navigating academic and collaborative challenges, and his unique talent in people management of his group.

Finally, I would like to thank my family and friends in Zurich and all over the world who provided me with immeasurable moral support. Specifically, thanks to Amin, Zeinab, and Maryam for their irreplaceable role in my life in the past years.

Contents

1 Introduction

In the quest to understand the world around us, scientists have proposed many models throughout history to describe nature. The predictions of each model are studied thoroughly until it fails to predict some observations, which often leads to improved models to describe the observed universe. Currently, the Standard Model (SM) of particle physics is the best model in hand to describe the fundamental building blocks of the universe and their interactions.

In numerous, stringent measurements of observables of nature, the SM has been remarkably successful in its predictions. For example, the anomalous magnetic moment of the electron (a_e) is a fundamental quantity that determines the strength of the interaction between a photon and an electron. An experimental measurement of a_e has a precision of 10 significant figures, in agreement with the SM prediction, making it the most accurate prediction verified in the history of physics.

Although the SM has been remarkably successful, there are both theoretical and experimental reasons that it cannot be the ultimate fundamental theory of nature. This includes the failure of the SM to predict the nonzero mass of neutrinos, and its failure to provide a candidate for the dark matter in the universe. Recently, precise measurements of the anomalous magnetic moment of the electron and the muon, a heavier copy of an electron, have shown evidence of deviations from the SM prediction by up to $5.1\,\sigma$ standard deviations, depending on the chosen theoretical calculation of the SM prediction. Should a deviation in the anomalous magnetic moment be observed, it would mean that unknown interactions beyond the SM are modifying the expected value. The tau lepton, the second and heaviest copy of the electron, is more sensitive to modifications from the SM to its anomalous magnetic moment (a_τ) due to its mass. Given the short lifetime of tau particles, a_τ cannot be measured directly, and the best current measurement of a_τ by the DELPHI collaboration is many orders of magnitude less precise than that of the electron and muon. However, since most theories expect orders of magnitude larger deviations of the anomalous magnetic moment for tau leptons than for electrons and muons, this can compensate for the lower precision in the measurement of a_τ. This motivates innovative methods to measure a_τ, as presented here.

In this dissertation, a summary of the SM theory is given in chapter 2. In chapter 3, the theoretical contributions to the anomalous magnetic moment and the current best measurements of this quantity for electrons, muons, and taus are discussed. In chapter 4, the Large Hadron Collider (LHC) and the Compact Muon Solenoid (CMS) detector as experimental tools for measuring a_τ are presented. In chapter 5, I present my first measurement of a_τ, the first measurement at the LHC. Chapter 6 presents my ongoing studies towards a future measurement of a_τ at the LHC with improved precision. The prospects of these measurements in the future are discussed in chapter 7, which motivates the need for an improved tracking detector for the CMS experiment. This tracking detector and the upgrade plans are discussed in chapter 8. Chapters 9, 10, and 11 summarize my contributions to the upgrade studies of this tracking detector.

2 Standard Model of particle physics

2.1 Timeline of modern particle physics

The search for the smallest elements constituting our world led to the discovery of atoms in the early 1800s when John Dalton discovered that chemicals always contain ratios of elements according to fixed ratios of whole numbers. In 1897, after years of research on cathode rays to understand the source of electricity, J.J. Thomson found out that cathode rays consist of small negatively charged subatomic particles which he named *electrons*. Therefore, it was realized that atoms are not the most *elementary* particles, and instead have a structure consisting of negatively charged electrons and a positive part to ensure the neutrality of the atoms. This discovery was arguably the start of the modern search for the *elementary particles* constituting our world and their interactions, under the name of *particle physics*. Figure 2.1 shows a timeline of some of the major findings of modern particle physics.

The journey continued with the discovery of photons as the constituent particles of light in 1905 by Albert Einstein. Between 1908 and 1913, Hans Geiger and Ernest Marsden, under the direction of Ernest Rutherford, performed a set of experiments in which they impinged a thin metal foil with alpha particles, which are helium atoms after their two electrons have been stripped. They observed that the alpha particles do not scatter most of the time, and when they do, they scatter with large angles. From this observation, it was inferred that the atoms have a small, heavy, and positively charged nucleus. This was a conceptually important experiment, as it marked the first time that particle physicists used a scattered beam of particles to understand sub-atomic structure. Given the insight from Louis de Broglie on the wave nature of particles and their corresponding wavelength, which decreases with momentum, the use of energetic scattering particles is needed to achieve a high resolving power in the observation of small targets.

Following an experiment by Ernest Rutherford in 1899, it was observed that an atom could gain a positive charge by emitting an electron. This phenomenon was known as β decay, and following the discovery of the atomic nucleus and protons as the positively charged constituents of the nucleus, it was thought that the nucleus contained A protons and $(A - Z)$ electrons, with A being the atomic mass and Z the atomic number, such that the nucleus had a mass of A and charge of Z. However, this hypothesis could not explain one of the characteristics of the nitrogen atom, called *spin*. In quantum mechanics, spin is the intrinsic angular momentum of a particle. In contrast to angular momentum, which is an integer, spin can take both integer and half-integer values. The spin of protons and electrons was measured to be $\frac{1}{2}$. For the nitrogen nucleus with $A = 14$ and $Z = 7$, a half-integer total spin was expected from the above hypothesis, while the spin was measured to be 1. This was resolved by the discovery of *neutrons* by James Chadwick in 1932. He observed the emission of electrically neutral radiation from a Beryllium layer hit by the alpha particles from a radioactive Polonium source. The neutral particles were capable of traversing several centimeters of Pb and hit a paraffin layer. Although the electrically neutral neutron was not directly visible, the protons from the recoil of the target

nucleus in paraffin was observed in an ionization chamber.
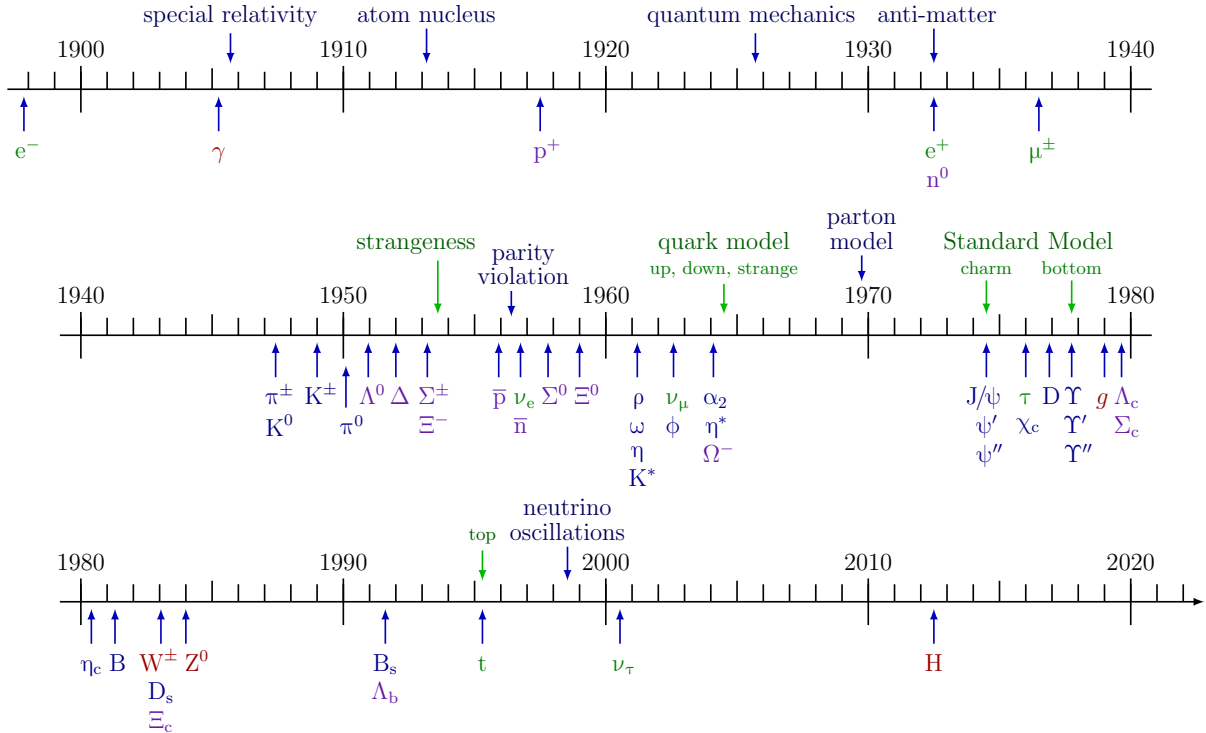
Figure 2.1: A timeline of particle physics in the last 130 years. Adapted from reference [1].

The discovery of electrons, protons, neutrons, and photons provided a model for the constituents of our everyday world. The electromagnetic force and gravitation were already known to be the dominant forces involved in everyday life. The *weak force* was thought to be responsible for the β decays and some strong nuclear force was responsible for holding the positively charged protons and the neurons together in the nucleus. Following the postulation of the uncertainty principle in quantum mechanics by Werner Heisenberg, Yukawa predicted in 1935 that a new particle with mass around $200\,\mathrm{MeV}$ should be responsible for carrying the strong nuclear force. Carl Anderson and Seth Neddermeyer observed a new particle from cosmic rays with a mass much larger than the mass of the electron and much smaller than the mass of the proton. It decayed into an electron, and some other missing invisible particle inferred from momentum conservation, and it was initially thought to be Yukawa's proposed particle. However, the muon could either decay into an electron, or when passing through a heavy material, be captured by a nucleus as in a reversed β decay, with a capturing rate consistent with the weak force. Therefore, the newly found particle, named *muon* was not Yukawa's predicted particle. The discovery of the muon was unanticipated and could not be explained by the models in hand.

It was in 1947 when Cesar Lattes, Giuseppe Occhialini, and Cecil Powell found a new particle from cosmic rays at high altitudes which decayed to a muon and then an electron. As opposed to the muon, which had a long decay time consistent with weak interactions, the newly found particle, called the *pion* ($\pi^{\pm}$), had a fast decay consistent with the strong force and Yukawa's postulated particle.

In the same year, a *strange* particle was found originating from cosmic rays that decayed to two pions. It was strange because of its anomalously long lifetime compared to pions, and was later called the kaon ($K^{\pm}$). A similar strange particle (Λ^0) was found in 1950 that decayed to a proton and a pion after a similarly long time.

The 1950s marked a revolution in particle physics when powerful accelerators were built to accelerate particles before colliding them with fixed targets. Compared to radioactive sources and cosmic rays, accelerators could be tuned to specific high energies with a controlled and relatively large number of interacting particles. A large number of K$^{\pm}$ and Λ^0 particles were produced using accelerators that hinted at their production through strong interactions and their decay through weak interactions. Following the development of many accelerators, many other particles were discovered in the 1950s and 1960s, as shown in figure 2.1. This included *neutrinos* (ν) produced in accelerator collisions, which are the missing invisible particles observed in β decays. For each charged particle, its oppositely charged *antiparticle* was also found. Antiparticles were predicted by Paul Dirac in 1928 in his model for spin-half particles and were first observed by the discovery of the positron (anti-electron) in 1932 by Carl Anderson.

The discovered particles that interacted through the strong interaction were referred to as *hadrons*. The abundance and properties of the hadrons found until the 1960s hinted at the presence of some underlying order. The situation was comparable to the time when abundant number of atoms were being found, and the ordering offered by Dmitri Mendeleev based on the characteristics of these elements led to the prediction for new elements, and eventually the discovery of subatomic elements as new, more *elementary* particles.

The quest for order was started by defining a conserved variable called the *baryonic number* (B) which was 1 for protons and neutrons, -1 for their antiparticles, and 0 for the rest of the particles. Conservation of the baryonic number could justify why decay modes such as p$^+ \rightarrow \pi^+ + \nu$ could not be observed and the proton, as the lightest particle with a baryonic number, was stable.

The next order concerned strange particles. They were abundantly produced in collisions of accelerated protons and neutrons, hinting at production through strong interactions, but were always produced in pairs. They also had a relatively long decay time, hinting at their decay through the weak interaction. Murray Gell-Mann and Kazuhiko Nishijima proposed a conserved quantity called *strangeness* (S) which was conventionally 1 for the K^0 and -1 for the Λ^0. The protons and neutrons had 0 strangeness. Therefore, the strange particles had to be produced in pairs, as strangeness is conserved in strong interactions. However, the strange particles could decay to non-strange particles through weak interactions, which do not conserve strangeness. Gell-Mann and Nishijima came up with the following formula, which related the charge Q, baryonic number, strangeness, and isospin (I). The latter is a quantity that was conceptually introduced in 1932 by Werner Heisenberg, assuming that protons and neutrons are different isospin states of the same particle and hence can be grouped together similar to spin up and down electrons, with $I_3 = +\frac{1}{2}$ for protons and $I_3 = -\frac{1}{2}$ for neutrons.

$$Q = I_3 + \frac{1}{2}(B + S) \tag{2.1}$$

Having the charge, strangeness, and isospin, Gell-Mann and Yuval Neeman proposed an ordering for the hadrons. The spin-$\frac{1}{2}$ ones were grouped into an octet based on charge, strangeness, and isospin, while the spin-$\frac{3}{2}$ ones were grouped similarly into a decuplet. The same categorization was applied to spin-0 hadrons. This categorization facilitated the discovery of the Ω^- missing from the spin-$\frac{3}{2}$ decuplet, similar to the discovery of new atoms using the Mendeleev table. Moreover, this categorization allowed Gell-Mann and Zweig to independently come up with the *quark model*, proposing three spin-$\frac{1}{2}$ *quarks* of *up* (u), *down* (d), and *strange* (s) as the constituents of all discovered hadrons. The up, down, and strange were referred to as different

flavors of quarks.

Following the observation of the suppressed decay of $K^0 \rightarrow \mu^+\mu^-$, Glashow, Iliopoulos, and Maiani proposed a mechanism in 1970 [2] that could reduce the production probability of this decay, given the presence of a fourth flavor of quarks, named *charm* (c). In 1974, Brookhaven, SLAC, and Frascati laboratories discovered a new particle, later called J/ψ with a mass of 3.1 GeV and a lifetime of 7×10^{-21} s, three orders of magnitude longer than the expected lifetime in decays with strong interaction. The J/ψ hadron was consistent with a bound state of a charm and anti-charm quark. It made the quark model more compelling and predicted a few hadrons containing the charm quark, which were discovered later.

In 1977, another particle decaying to two muons was observed at Fermilab and later confirmed by DESY. It was consistent with a bound state of some new additional quark, perhaps of a third generation, and was called the *bottom* or *beauty* quark. As a result of the observed symmetry in quark flavors in which they could be grouped into generations of up-down and charm-strange, the presence of another flavor from this new third generation was postulated. The predicted quark flavor was referred to as *top* (t) and was discovered in 1995 by the CDF and D0 experiments. With the full list of flavors, the equation relating particle types becomes

$$Q = I_3 + \frac{1}{2}(B + S + C + B' + T) \tag{2.2}$$

with charm (C), bottomness (B'), and topness (T) defined in a similar way to strangeness.

2.2 The Standard Model

The Standard Model (SM) of particle physics is the only model that describes all currently observed elementary particles in the universe and the known electromagnetic, weak, and strong interactions between them. The elementary particles of the SM are shown in figure 2.2. Fermions have a spin of $\frac{1}{2}$ and are divided into quarks and leptons. The quarks and leptons are each divided into three *generations* which are assumed to be copies of each other except for their mass differences. The *gauge* bosons are responsible for the interactions. In particular, the photon *carries* the electromagnetic force between charged particles, the W and Z bosons carry the weak force, and the gluon carries the strong force. The interaction with the Higgs boson is responsible for giving mass to all massive elementary particles, which will be discussed in section 2.2.4.

The SM is a quantum field theory (QFT), which describes matter and the forces as quantum fields and particles as excited states of these fields. It describes the kinetics of each of these fields, the interactions between them through the gauge bosons, and a mechanism that gives mass to the massive particle states. The QFT describing the electromagnetic interactions of charged particles is known as *quantum electrodynamics* (QED), which will be discussed in section 2.2.1. The weak interaction can be unified with QED to form the electroweak (EW) theory discussed in section 2.2.2. The strong interactions between quarks and mediated by gluons is described by *quantum chromodynamics* (QCD), which will be discussed in section 2.2.3.

According to a theorem by Emmy Noether [4], each conservation law is associated with a symmetry of the underlying *physics*. For instance, if the physics of a system, as determined by its Lagrangian, is symmetric with regards to transformations of time, then the system will conserve energy. If the space is isotropic in classical physics, the Lagrangian of the system does not depend on the rotation in space, and hence angular momentum is conserved. In quantum mechanics, a

Figure 2.2: A table of the particles in Standard Model of particle physics and their properties. Figure is taken from Ref. [3].

spin $\frac{1}{2}$ and a spin $-\frac{1}{2}$ electron are similar as far as the physics of the system is concerned, so the Lagrangian is invariant under the SU(2) spin rotations. As mentioned earlier, similar attempts were made before the SM was established to categorize the elementary particles by symmetries such as spin, isospin, and charge. In the SM, all three sectors of QED, weak theory, and QCD follow specific symmetries which arise from local gauge invariance, meaning that the Lagrangian does not change as a result of applying the transformation operators with free and local gauge parameters.

2.2.1 Quantum electrodynamics

The theory of quantum electrodynamics was developed [5] as a relativistic quantum description of electrodynamic interactions between charged particles, previously modeled by Maxwell's equations in classical electromagnetism. QED is a gauge theory with the symmetry group U(1). Fermions are represented by spin-$\frac{1}{2}$ fields. Their electromagnetic interaction is mediated by the photon field as the single gauge field of U(1). The Lagrangian of QED [6, p78] is

$$\mathcal{L} = -\frac{1}{4}F^{\mu\nu}F_{\mu\nu} + \bar{\psi}(i\gamma^\mu D_\mu - m)\psi, \tag{2.3}$$

where γ^μ are the Dirac matrices, ψ is a bispinor field of the spin-$\frac{1}{2}$ particle with $\bar{\psi}$ its Dirac adjoint, and m is the mass of the spin-$\frac{1}{2}$ particle. D_μ is the gauge covariant derivative defined by $\partial_\mu + ieA_\mu + ieB_\mu$, where e is the coupling constant, equal to the electric charge of the bispinor field, and A_μ is the covariant four-potential of the electromagnetic field generated by the spin-$\frac{1}{2}$ particle itself. It is also known as a gauge field or a U(1) connection. B_μ is the external field imposed by an external source. Finally, $F_{\mu\nu} = \partial_\mu A_\nu - \partial_\nu A_\mu$ is the tensor of the electromagnetic field or the curvature of the gauge field.

Using the Euler-Lagrange equation for $\bar{\psi}$ and setting $B_\mu = 0$, or equivalently absorbing it into a new A_μ, it is found that the equation of motion for the spin-$\frac{1}{2}$ particle is

$$(i\gamma^\mu\partial_\mu - m)\psi = e\gamma^\mu A_\mu\psi. \tag{2.4}$$

The equation of motion for A_μ is similarly derived to be

$$\partial_\mu F^{\mu\nu} = e\bar{\psi}\gamma^\nu\psi. \tag{2.5}$$

Taking

$$j^\nu = \bar{\psi}\gamma^\nu\psi \tag{2.6}$$

as the conserved U(1) current arising from Noether's theorem, one find the equation of motion for the A_μ mediator to be

$$\partial_\mu F^{\mu\nu} = ej^\nu. \tag{2.7}$$

After imposing the arbitrary *Lorenz gauge condition* of $\partial_\mu A^\mu = 0$, equation 2.7 reduces to

$$\Box A^\mu = ej^\mu, \tag{2.8}$$

which is a wave equation for the four-potential, the QED version of the classical Maxwell equations in the Lorenz gauge.

Richard Feynman proposed an intuitive method to calculate the interaction probabilities in QED. His method is based on what became known as *Feynman diagrams* as graphical representations of specific interactions, as well as a mathematical method to calculate the probability of interactions. Feynman diagrams in QED are built by combining three elements:

- A fermion propagating in space, shown by a straight line
- A photon propagating in space, shown by a wavy line
- A junction of two fermions and a photon representing the interaction.

These elements are shown in figure 2.3. By connecting copies of this basic vertex element, one can visualize any arbitrary QED interaction like the one in figure 2.4.
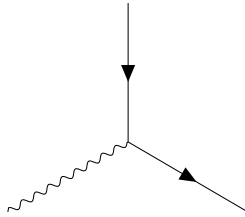
Figure 2.3: The three constructing elements of a Feynman diagram in QED. Propagating fermions are shown with solid lines, with an arrow for their propagating direction. A photon propagating in space is shown with a wavy line. The interaction point is shown by the junction of these three lines, representing the interaction of ψ, $\bar{\psi}$, and A^μ according to the Lagrangian in equation 2.3.

Mathematically, Feynman proposed a set of probability amplitudes for each propagation or interaction. The probability amplitude of an interaction with multiple vertices as in figure 2.4 is a multiplication of the probability amplitudes of individual vertices. Any chosen kinematics for the photon in this figure does not affect the initial and final physical observables, making it a *virtual* photon. Therefore, the probability amplitudes of all possible kinematics for the propagator of the virtual photon have to be integrated to find the probability amplitude of the interaction. The interaction rate or decay rate of the particles and the *cross section* of the interaction can be calculated using the probability amplitude, integrating over possible initial and final kinematics.
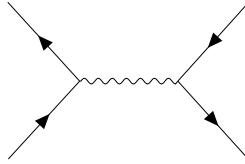
Figure 2.4: A Feynman diagram representing the electromagnetic interaction of two fermions in the so-called *s-channel*. The chronological order of Feynman diagrams is conventionally from left to right. Fermions propagating towards the left represent antiparticles. This diagram could represent the electromagnetic interaction of an electron and a positron through a *virtual* photon.

The cross section is an intrinsic measure of the probability of interaction independent of the environmental conditions, like beam intensity in scattering collisions. Experimentally, it is defined by the number of interactions per unit of time per unit of flux of incoming particles.

2.2.2 The electroweak theory

As mentioned in section 2.1, weak interactions were first discovered in the β decay of a neutron to a proton, an electron, and the antineutrino of an electron, and later on in the decay of hadrons. The weak force was found to be short-ranged, similar to the strong force but orders of magnitude weaker, so that the decay times of weakly decaying hadrons were longer than the decays mediated by the strong or electromagnetic forces. This weak and short-range nature can be explained if the mediator of the weak force was massive.

In 1959, Sheldon Glashow [7], Abdus Salam [8], and Steven Weinberg [9] proposed the *electroweak* (EW) theory which unified the interactions mediated by the weak and electromagnetic forces. In this theory, the weak interactions were mediated by three spin-1 massive W bosons, W^1, W^2, and W^3, with their respective 3rd component of isospin (I_3) to be +1, −1, and 0. They are responsible for transformations in the SU(2) isospin phase space. Fermions have an isospin of $\frac{1}{2}$. The up, charm, and top quarks as well as the neutrinos have an isospin of $+\frac{1}{2}$ while their partners in each generation have an isospin of $-\frac{1}{2}$. In all cases, the antiparticles have isospin of opposite sign. W^1 and W^2 only interact with *left-handed* particles and *right-handed* antiparticles, where left- and right-handedness is based on chirality, an intrinsic quantum mechanical property like spin. They are responsible for the conversion of isospin states within each generation. For instance, a W^2 with $I_3 = -1$ is emitted through the transition of a left-handed down quark with $I_3 = -\frac{1}{2}$ to a left-handed up quark with $I_3 = +\frac{1}{2}$. It can then similarly decay to an electron and antineutrino of the electron. This is in fact the underlying interaction of the β decay of a neutron, described by n(udd)→p(udu)+W⁻ →p(udu)+e⁻+$\bar{\nu}_e$ and depicted in the Feynman diagram in figure 2.5
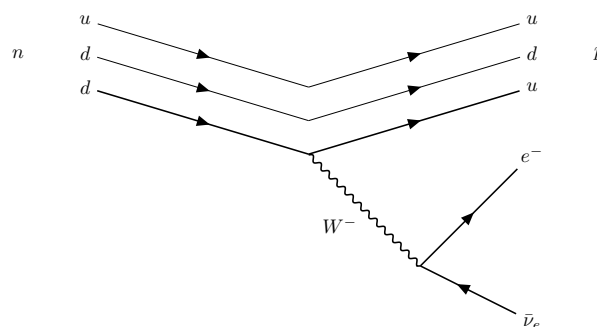
Figure 2.5: A Feynman diagram representing the weak interaction known as the beta decay of the neutron.

The SU(2) weak and U(1) QED interactions are unified in the EW Lagrangian:

$$\mathcal{L}_{\text{EW}} = \sum_{\text{f}} \sum_{\psi_{\text{f}}} \overline{\psi_{\text{f}}} i\gamma^\mu D_\mu \psi_{\text{f}} - \tfrac{1}{4} W_a^{\mu\nu} W_{\mu\nu}^a - \tfrac{1}{4} B^{\mu\nu} B_{\mu\nu}, \qquad (2.9)$$

where ψ_{f} is a doublet for left-handed fermions with flavor f, and a singlet for right-handed ones.

$$D_\mu \equiv \partial_\mu - ig' \tfrac{1}{2} Y_{\text{W}} B_\mu - ig \tfrac{1}{2} \vec{\tau}_{\text{L}} \vec{W}_\mu, \qquad (2.10)$$

with B_μ being the U(1) gauge field, Y_{W} the weak hypercharge and the generator of the U(1) group, W_μ the 3-component SU(2) gauge field explained above, and τ_{L} the the Pauli matrices as infinitesimal generators of the SU(2) group acting only on the left-handed chiral fermions. The variable g' is the U(1) coupling constant and g is the SU(2) coupling constant. $W^{a\mu\nu}$ $(a = 1, 2, 3)$ and $B^{\mu\nu}$ are the field strength tensors for the weak isospin and weak hypercharge fields.

The electromagnetic charge arises from a combination of EW isospin and EW hypercharge as $Q = T_3 + \tfrac{1}{2} Y_3$. The EW Lagrangian in equation 2.9 does not have any $\bar\psi m \psi$ mass term similar to equation 2.3 as such a mass term will not respect the SU(2) symmetry. Section 2.2.4 will present how the SU(2) symmetry will be spontaneously broken by the addition of the Higgs boson and mechanism to give mass to the fermions and weak gauge bosons. The mass eigenstates of the SU(2) weak gauge field after spontaneous symmetry breaking are two charged W bosons and a neutral Z boson. The photon and Z boson after spontaneous symmetry breaking can be derived as a linear combination of W^3 and the U(1) gauge field before spontaneous symmetry breaking by

$$\begin{pmatrix} \gamma \\ Z^0 \end{pmatrix} = \begin{pmatrix} \cos\theta_{\text{W}} & \sin\theta_{\text{W}} \\ -\sin\theta_{\text{W}} & \cos\theta_{\text{W}} \end{pmatrix} \begin{pmatrix} B \\ W_3 \end{pmatrix}, \qquad (2.11)$$

where θ_{W} is the weak mixing angle or the Weinberg angle [10]. The charged W bosons after the symmetry breaking are found by

$$W^\pm = \frac{1}{\sqrt{2}} \left(W^1 \mp i W^2 \right). \qquad (2.12)$$

Following this transformation, a mismatch arises between the masses of the Z and $W^\pm$ bosons, which is found to be

$$m_{\text{Z}} = \frac{m_{\text{W}}}{\cos\theta_{\text{W}}}. \qquad (2.13)$$

Unlike strange interactions, weak interactions do not respect strangeness, as, for instance, in the decay of $K^\pm \to \pi^\pm \pi^0$. Nicola Cabibbo proposed that the quark eigenstates in the weak interactions are not identical to the mass eigenstates of the quarks, and instead can be a mixed combination [11] as

$$\begin{bmatrix} d' \\ s' \end{bmatrix} = \begin{bmatrix} \cos\theta_{\text{c}} & \sin\theta_{\text{c}} \\ -\sin\theta_{\text{c}} & \cos\theta_{\text{c}} \end{bmatrix} \begin{bmatrix} d \\ s \end{bmatrix}, \qquad (2.14)$$

with d' and s' as the weak eigenstates, d and s as the mass eigenstates, and θ_{c} as the Cabibbo angle. A generalized form of the mixing matrix with the addition of bottom and top quarks was

given by Makoto Kobayashi and Toshihide Maskawa [12] in the form of

$$
\begin{bmatrix} d' \\ s' \\ b' \end{bmatrix} = \begin{bmatrix} V_{\text{ud}} & V_{\text{us}} & V_{\text{ub}} \\ V_{\text{cd}} & V_{\text{cs}} & V_{\text{cb}} \\ V_{\text{td}} & V_{\text{ts}} & V_{\text{tb}} \end{bmatrix} \begin{bmatrix} d \\ s \\ b \end{bmatrix},
\tag{2.15}
$$

with the best measured values [13] of

$$
\begin{bmatrix} |V_{ud}| & |V_{us}| & |V_{ub}| \\ |V_{cd}| & |V_{cs}| & |V_{cb}| \\ |V_{td}| & |V_{ts}| & |V_{tb}| \end{bmatrix} = \begin{bmatrix} 0.97401 \pm 0.00011 & 0.22650 \pm 0.000488 & 0.00361 \pm 0.00010 \\ 0.22636 \pm 0.00048 & 0.97320 \pm 0.00011 & 0.04053 \pm 0.00072 \\ 0.00854 \pm 0.00020 & 0.03978 \pm 0.00071 & 0.999172 \pm 0.000030 \end{bmatrix}.
\tag{2.16}
$$

2.2.3 Quantum chromodynamics

Quantum chromodynamics (QCD) is the theory that describes the strong interaction between the quarks and gluons. The strong force in QCD is mediated by massless and charge-neutral *gluons*. Since the observation of the Δ^{++} hadron with three up quarks was in tension with Pauli's exclusion principle in quantum mechanics, given the up states had the same quantum numbers, a new quantum number of *color* was defined for quarks which could take one of three values named after the colors red, green, and blue. The number of colors was later confirmed in electron-positron collisions by taking the ratio

$$
R(s) = \frac{\sigma(e^+e^- \to \text{hadrons})}{\sigma(e^+e^- \to \mu^+\mu^-)}
\tag{2.17}
$$

where s is the square of the center-of-mass energy and σ denotes the cross section of the hadronic and leptonic collisions shown in figure 2.6 at each collision energy. This ratio is dependent on the number of independent states the muon and the quark can have, as well as the relative charges of quarks over the charge of muon, as the charges determine the electromagnetic coupling constant. This ratio can be written as

$$
R = N_{\text{C}} \sum_q e_q^2,
\tag{2.18}
$$

with N_{C} being the number of color states each quark can take, and e_q being the charge of each quark flavor. It has been measured to be $R = 2$ for collision energies enough to create up, down, and strange quarks, $R = \frac{10}{3}$ when charm quarks can also be created, and $R = \frac{11}{3}$ when bottom quarks can also be created. These measurements confirm that the number of color states is 3.
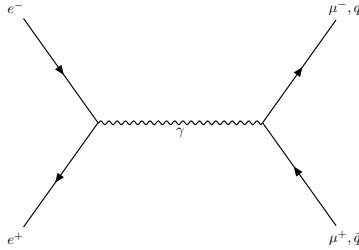
Figure 2.6: Feynman diagram of the annihilation of an electron and a positron to a photon, decaying to a pair of muon-antimuon or quark-antiquark of the same flavor.

QCD respects an SU(3) symmetry of color, with eight multi-colored gluon mediators connecting to a quark and its antiparticle. As the gluons also have color, they can interact with

themselves in vertices connecting three or four gluons. These self-interactions lead to the short-range nature of the strong force. Hadrons in QCD are colorless, a phenomenon known as the *color confinement* of QCD, which ensures that hadrons with one quark and one antiquark with an integer total charge, *mesons*, and hadrons with either three quarks or three antiquarks, *baryons*, have no aggregate color.

The Lagrangian of QCD is given by

$$\mathcal{L}_{\mathrm{QCD}} = \sum_f \overline{\psi_f} i \gamma^\mu D_\mu \psi_f - \frac{1}{4} G^a_{\mu\nu} G^{\mu\nu}_a, \tag{2.19}$$

where ψ_f is a 3-component vector of Dirac spinors for the three colors of quark with flavor f, $D_\mu \equiv \partial_\mu - i g_s \frac{1}{2} \lambda^a G^a_\mu$ is the gauge covariant derivative of QCD with G^a_μ as the 8-component SU(3) gauge field, λ^a are the generators of the SU(3) color group, and g_{s} is the coupling constant of the strong interactions. Finally, $G^a_{\mu\nu}$ is the gluon field strength tensor.

2.2.4 The Higgs mechanism and the Yukawa interactions

The EW and QCD terms mentioned in equations 2.9 and 2.19 describe the kinetics and interaction of fermions and gauge bosons in the SM. However, the short range of the weak interactions implies that their mediators are massive. This is ensured in the SM by the *Higgs mechanism* [14][15][16]. The Higgs Lagrangian is

$$\mathcal{L}_{\mathrm{H}} = \frac{1}{2} \left(D_\mu \varphi \right)^\dagger \left(D^\mu \varphi \right) - V(\varphi), \tag{2.20}$$

with D_μ from equation 2.10, and φ is a doublet of complex scalar fields respecting the EW SU(2) symmetry and written as

$$\varphi = \begin{pmatrix} \varphi^+ \\ \varphi^0 \end{pmatrix} = \frac{1}{\sqrt{2}} \begin{pmatrix} \varphi_1 + i\varphi_2 \\ \varphi_3 + i\varphi_4 \end{pmatrix}. \tag{2.21}$$

The Higgs potential, $V(\varphi)$, is

$$V(\varphi) = -\mu^2 \varphi^\dagger \varphi + \lambda \left(\varphi^\dagger \varphi \right)^2, \tag{2.22}$$

with positive λ and μ^2. While it is common in QM for the ground state of the potential to be zero, the Higgs potential has a nonzero vacuum expectation value at $\varphi^\dagger \varphi = \frac{\mu^2}{2\lambda}$ which leads to infinite solutions for φ. By a gauge transformation to a basis where the other three components are zero, one finds the third component to be $\varphi_3 = \frac{\mu}{\sqrt{\lambda}} \equiv v$, which is an input parameter of SM and is measured to be 246 GeV. When the physical system goes to this minimum, the potential is no longer symmetric in SU(2), a phenomena referred to as *spontaneous symmetry breaking*, causing the weak mediators to gain mass values of $m_W = \frac{1}{2} g v$ and $m_Z = \frac{1}{2} \sqrt{g^2 + g'^2} v$. These are predictions of the theory and match well with the observed masses. The spin-0 Higgs boson is the excited state of the Higgs field and is predicted to have a mass of $m_H = \sqrt{2\mu^2} = \sqrt{2\lambda} v$. This was measured in 2012 to be around 125 GeV, after the discovery of a boson with the expected characteristics of the SM Higgs boson by CMS and ATLAS in 2012 [17][18][19][20]. This may be the last piece of the SM, since a single Higgs boson is the simplest solution to spontaneous symmetry breaking. However, it can also be achieved with more than one Higgs boson, although this has so far not been observed.

As mentioned in section 2.2.2, the fermion mass term of $m\bar{\psi}\psi$ does not respect the EW SU(2)

symmetry. Instead, the fermions gain mass from their *Yukawa coupling* to the Higgs boson. The Yukawa term of the SM Lagrangian before spontaneous symmetry breaking respects the EW SU(2) symmetry and has a form of

$$\mathcal{L}_{\text{Yukawa}} = \frac{g_{\text{Y}}}{\sqrt{2}} \sum \bar{\psi}_{\text{L}} \varphi \psi_{\text{R}}, \tag{2.23}$$

with ψ_{R} and $\bar{\psi}_{\text{L}}$ as the right-handed singlet and left-handed doublet of the EW theory, respectively. The summation is over all flavors in addition to the Hermitian conjugates. φ is the Higgs scalar field defined above, which after symmetry breaking, can be written as a perturbation of H around its vacuum expectation value by $\varphi = v + H$. So the Yukawa term after the spontaneous symmetry breaking will be

$$\mathcal{L}_{\text{Yukawa}} = \frac{g_{\text{Y}} v}{\sqrt{2}} \sum \bar{\psi}_{\text{L}} \psi_{\text{R}} + \frac{g_{\text{Y}} H}{\sqrt{2}} \sum \bar{\psi}_{\text{L}} \psi_{\text{R}}. \tag{2.24}$$

The first term is the required $m\bar{\psi}\psi$ mass term of the fermions with $m = \frac{g_{\text{Y}} v}{\sqrt{2}}$, and the second term describes the coupling of fermions to the Higgs field. Therefore, the Yukawa coupling of the fermions with the Higgs boson should be proportional to their mass, which has been confirmed experimentally [21][22].

3 The anomalous magnetic moment

This dissertation presents a measurement of the anomalous magnetic moment of tau leptons, and steps towards an improved subsequent measurement. After a brief definition of this particle property, and motivation for pursuing its measurement, its prediction arising from SM QED, EW, and QCD contributions will be discussed in section 3.1. Section 3.2 discusses potential contributions from beyond the standard model (BSM). Sections 3.3 and 3.4 discuss the current best measurement of this property for electrons and muons and their respective agreement with the SM predictions. Finally, section 3.5 discusses the best current measurement of this variable for tau leptons, and the potential for measurements using the data collected at the Large Hadron Collider (LHC), which will be introduced in chapter 4.

In classical electrodynamics, the magnetic strength of an object producing a magnetic field is represented by its *magnetic moment* vector. These magnetic objects range from macroscopic magnetic material and electrical currents to microscopic molecules and atoms, and even elementary particles like electrons. Charged particles with an angular momentum arising from their orbital angular momentum or *spin*, a quantum mechanical property, can also show a magnetic moment, which can be written as

$$\boldsymbol{\mu}_{\mathrm{m}} = g \frac{e}{2m} \mathbf{S},\tag{3.1}$$

where e is the electric charge and m is the mass of the particle. $\mathbf{S}$ and $\boldsymbol{\mu}_{\mathrm{m}}$ are the spin and magnetic moment vectors, respectively. The value g is referred to as the *g-factor* and for a Dirac spin-$\frac{1}{2}$ particle, $g = 2$. However, small deviations from the Dirac prediction have been observed in the magnetic moment of electrons and later explained by QED corrections. In QED, the magnetic moment of a fermion is given by its coupling to a photon. At the first order, this leads to the Dirac prediction. However, higher order loops in the coupling of an initial-state and final-state fermion to a photon contribute to the magnetic moment of the fermion. The deviation in the g-factor from Dirac's prediction of $g = 2$ is represented by the *anomalous magnetic moment* (a) which is defined as

$$a = \frac{g - 2}{2}.\tag{3.2}$$

3.1 Anomalous magnetic moment in Standard Model

In the SM, the anomalous magnetic moment gets contributions from all three sectors of QED, EW, and QCD, providing infinite complexity for the generic interaction of a photon with an initial-state and an final-state charged fermion. Each contributing process can be represented by its corresponding Feynman diagram, while all diagrams have the same physical observables, namely they represent the vertex of two charged fermions and a photon. Starting from the most dominant contributions and going towards the least contributing processes, they are summed to get a precise determination of the coupling of a photon with two charged fermions.

The QED contributions can be ordered in powers of the fine-structure constant (α), which
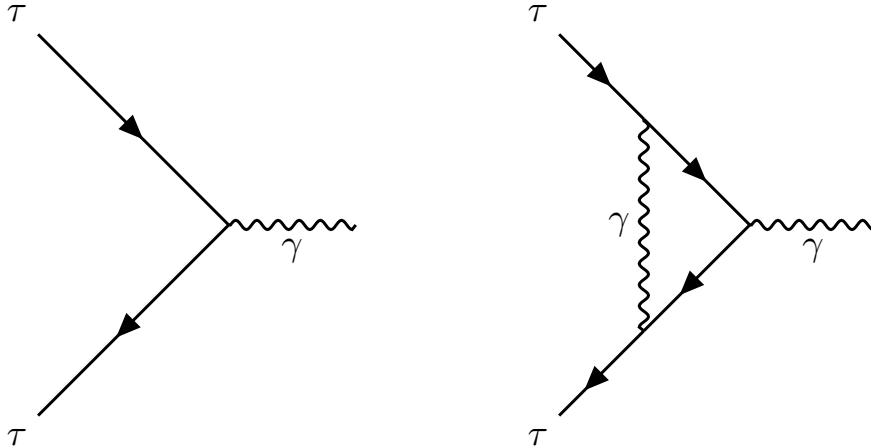
Figure 3.1: Tree-level (left) and one-loop (right) QED contributions to the coupling of the tau lepton with photon. The tree-level diagram gives $a_\tau = 0$ and the one-loop diagram adds $a_\tau = \frac{\alpha}{2\pi}$.

quantifies the QED coupling and is approximately equal to $\frac{1}{137}$. Figure 3.1 shows the tree-level and one-loop Feynman diagrams of the $\tau\gamma\tau$ vertex. At tree level, the coupling of the tau lepton to the photon matches the predictions by Dirac for spin-$\frac{1}{2}$ charged particles and gives $g = 2$. The dominant correction to the g-factor comes from the one-loop diagram and is equal to $\frac{\alpha}{2\pi} \approx 0.00116$.

Figure 3.2 shows the two-loop contributions from QED, which are on the order of α^2. The relative mass of the lepton (ℓ) in the top-left plot to the mass of the τ lepton varies the predicted two-loop effect. Therefore, contributions of second order and above to the anomalous magnetic moment are different for the three charged leptons and have to be calculated separately. While the QED contribution has been calculated up to the tenth order for the anomalous magnetic moment of the muon (a_μ) [23], it has been calculated for the anomalous magnetic moment of the tau lepton (a_τ) up to the third order of α, which is $a_\tau^{\mathrm{QED}} = (117324 \pm 2) \times 10^{-8}$ [24].

Contributions from EW interactions can be estimated in the same manner. Due to the relatively high mass of the EW gauge bosons compared to that of the leptons, the EW contributions are suppressed. For instance, the EW contribution to a_τ is of the same order as the three-loop QED contribution. It is calculated for one- and two-loop EW effects and is found to be $a_\tau^{\mathrm{EW}} = (47.4 \pm 5) \times 10^{-8}$ [24].

While the QED and EW contributions can be calculated from first principles of perturbation theory to any arbitrary order, the QCD contributions cannot be estimated by perturbation, as the QCD coupling constant runs to infinity at low energies. Therefore, the contribution of QCD is mainly estimated using experimental measurements of the ratio defined in equation 2.17, as well as theoretical evaluations based on specific models of low-energy hadronic interactions with electromagnetic currents. The current best estimation of the QCD contributions to a_τ is $a_\tau^{\mathrm{QCD}} = (350.1 \pm 4.8) \times 10^{-8}$ [24] which leads to an overall SM estimation of

$$a_\tau = (117\,721 \pm 5) \times 10^{-8}. \tag{3.3}$$

Table 3.1 shows a summary of the SM contributions to the anomalous magnetic moment of the electron, muon, and tau lepton based on a few recent calculations. A tension between the theoretical calculations of the QCD contributions to a_μ is shown. Here, we quote the calculations in references [25–40] for the QCD contributions to a_μ. The QED contributions to
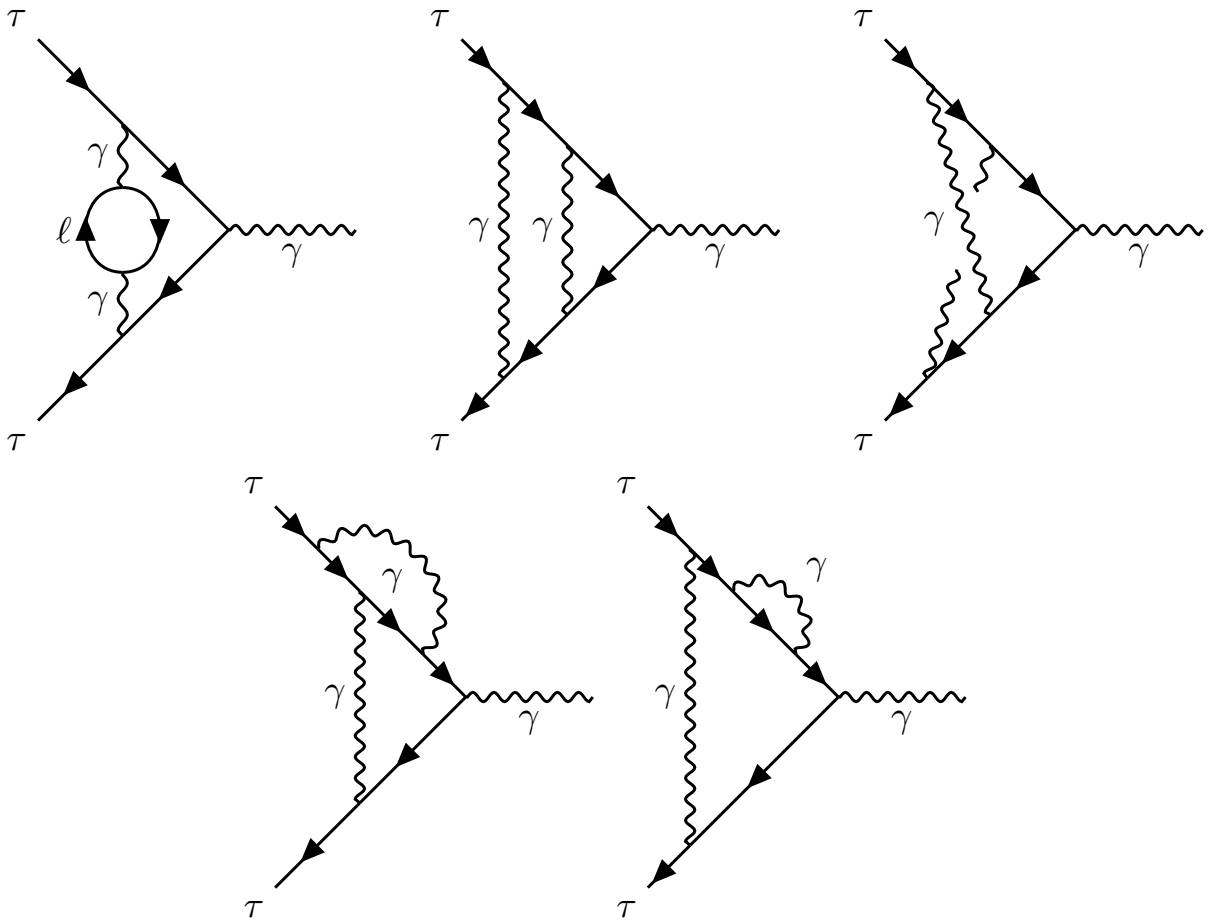
Figure 3.2: Two-loop QED contributions to the coupling of the tau lepton with photon. ℓ can be any of the charged leptons. The upside-down mirror of the bottom plots should also be considered.

a_μ are taken from references [41, 42] and the EW contributions are taken from references [43, 44]. Contributions to a_e are taken from reference [45].

	QED	EW	QCD	total SM
e	$1\,159\,652\,179.88 \pm 0.23$	0.03053 ± 0.00023	1.693 ± 0.012	$1\,159\,652\,181.61 \pm 0.23$
μ	$1\,165\,847\,189 \pm 1$	1536 ± 10	$69\,390 \pm 430$	$1\,165\,918\,100 \pm 430$
τ	$1\,173\,240\,000 \pm 20\,000$	$474\,000 \pm 50\,000$	$3\,501\,000 \pm 48\,000$	$1\,177\,210\,000 \pm 50\,000$

Table 3.1: SM contributions to anomalous magnetic moment of leptons in units of 10^{-12}.

3.2 Beyond standard model contributions

Similar to the SM contributions, BSM effects can also contribute to the coupling of a fermion to photon, modifying its magnetic moment. Figure 3.3 shows one example of such a contribution from a *leptoquark* particle. Leptoquarks are hypothetical particles that couple to a lepton and a quark. They are good candidates for solving some of the theoretical problems in the SM, and can serve as one of the dark matter candidates. Although different generations of leptons and quarks are identical in SM interactions and are only differentiated by their mass, the coupling of the leptoquarks to SM fermions could depend on their generation. Therefore, the contribution of the leptoquark to a_τ could be larger compared to that of a_μ.
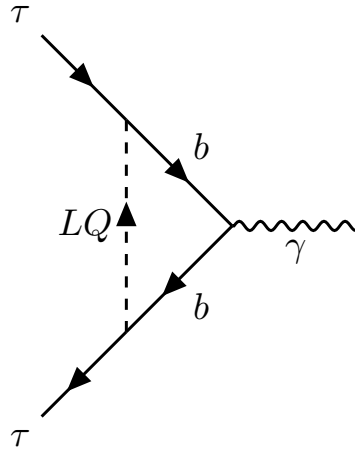
Figure 3.3: First-order contribution to the $\tau\gamma\tau$ vertex from a leptoquark coupling to the τ lepton and the bottom quark.

A composite particle obtains a larger magnetic moment compared to a similar particle with no substructure. For instance, the g-factor for a proton is 5.6, and the chargeless neutron, which should have no magnetic moment at all, has a g-factor of -3.8. Therefore, if an excess of the anomalous magnetic moment of a lepton is observed compared to the SM prediction, it can serve as evidence for the compositeness of that lepton. The contribution of compositeness to the anomalous magnetic moment of a lepton (a_ℓ) with mass m_ℓ made up of constituents of mass $m_{\text{constituent}}$ is on the order of $\mathcal{O}(\frac{m_\ell}{m_{\text{constituent}}})$ and therefore is higher for tau leptons compared to electrons and muons [46].

Supersymmetry (SUSY) is a generic characteristic of a theory which treats particles and force

carriers in the same way. As a BSM theory of particle physics, it provides a natural solution for the unification of different sectors of SM at high energy, as well as their unification with general relativity. It can also provide many dark-matter candidates as it predicts a supersymmetric counterpart for each SM particle. Similar to the leptoquarks, these supersymmetric BSM particles can also contribute to the coupling of leptons to a photon and the anomalous magnetic moment. The effect of SUSY on a_ℓ can be quantified by the difference with the prediction of the SM $\delta a_\ell = a_\ell - a_\ell^{\mathrm{SM}}$, which for a SUSY particle with mass M_{S} increases by $\delta a_\ell \sim \frac{m_\ell^2}{M_{\mathrm{S}}^2}$ [47]. Therefore, the contribution of SUSY to δa_ℓ is $\frac{m_\tau^2}{m_\mu^2} \approx 280$ times higher for tau leptons than muons.

The contributions of BSM to a_ℓ and to the coupling of leptons and photons modify both the kinematics of the lepton and the total coupling strength, which results in a higher cross section for this interaction. These effects can be modeled with two methods. In the first method, the *matrix element* of the vertex, which is used to calculate the probability amplitude mentioned in chapter 2, is generalized to accommodate BSM contributions. For instance, the generalized form of the $\tau\gamma\tau$ vertex between a tau lepton with an incoming momentum of p and an outgoing momentum of p', coupled with a photon with momentum of q and a polarization vector of $\epsilon_\mu(q)$ can be parameterized as [48]

$$-ie\bar{u}(p') \times \{F_1(q^2)\gamma^\mu + iF_2(q^2)\sigma^{\mu\nu}\frac{q_\nu}{2m_\tau} + F_3(q^2)\gamma^5\sigma^{\mu\nu}\frac{q_\nu}{2m_\tau}\} \times u(p)\epsilon_\mu(q) \qquad (3.4)$$

The three functions F_1, F_2, and F_3 are the *form factors* corresponding to the charge, anomalous magnetic moment, and electric dipole moment of the tau lepton, respectively. These observables are related to the form factors as

$$e_\tau = eF_1(0), \qquad (3.5)$$

$$a_\tau = eF_2(0), \qquad (3.6)$$

$$d_\tau = -\frac{e_\tau}{2m_\tau}F_3(0). \qquad (3.7)$$

Another approach to accommodate BSM effects on the anomalous magnetic moment is the use of effective field theories (EFT) [49]. In the EFT approach, the SM Lagrangian is generalized by adding new terms which respect the SM symmetries, and are scaled down with normalization factors corresponding to the *new physics* scale. For large enough energy scales of the new physics, the added Lagrangian terms vanish and the theory converges to the SM.

3.3 Measurement of $a_{\mathbf{e}}$

The anomalous magnetic moment of the electron is the most precisely measured quantity in the history of physics. Its current best measurement was performed recently [50] using the *Penning trap* technique, in which a single electron is trapped with a homogeneous magnetic field and a quadrupole electric field. Due to the presence of the magnetic field (B), the electron with mass m and charge e circulates with a cyclotron frequency (ω_{C}) of

$$\omega_{\mathrm{C}} = \frac{e}{m}B. \qquad (3.8)$$

It also exhibits a Larmor precession of its spin around the magnetic field with a frequency (ω_S) of
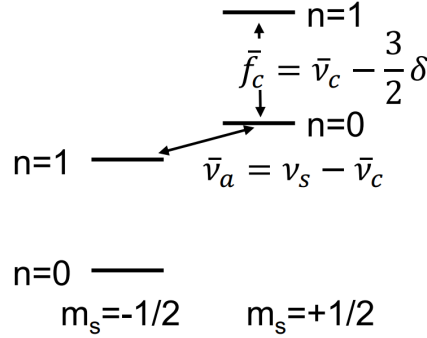
$$\omega_S = g\frac{e}{2m}B. \tag{3.9}$$

Their difference, denoted by ω_a, is a measure of the anomalous magnetic moment as

$$\omega_a = \omega_S - \omega_C = \frac{g-2}{2}\frac{e}{2m}B = \frac{g-2}{2}\omega_C = a_e\omega_C. \tag{3.10}$$

The electron is cooled to a temperature of $50\,\mathrm{mK}$. Its quantum energy levels can be written as

$$E = \hbar\omega_S m_S + \hbar\omega_C(n + \frac{1}{2}), \tag{3.11}$$

with $m_S = \pm\frac{1}{2}$ corresponding to the spin of the electron along the direction of magnetic field, and n determining the energy level.

Figure 3.4: Quantum energy levels for an electron in a Penning trap with a cyclotron frequency of $\nu_C = \frac{\omega_C}{2\pi}$ and a precession frequency of $\nu_S = \frac{\omega_S}{2\pi}$. Figure taken from reference [50].

The electron is excited from $n = 0$ to $n = 1$ of the cyclotron energy levels by driving the transitions using precisely tuned microwave radiation. The jump to the higher spin energy level (change of the spin sign) is achieved by modifying the magnetic field. While the two input energies are fixed, by varying the magnetic field, a resonance can be observed when the input energies match ω_C and ω_a, resulting in a precise measurement of these two frequencies. The anomalous magnetic moment of electron can be found using equation 3.10.

Figure 3.5 shows the current measurements of the anomalous magnetic moment of the electron, compared to the most updated SM predictions using two measurements of the fine-structure constant with Rubidium [51] and Cesium [52] as input.

3.4 Measurement of a_μ

There has been a great effort to measure the anomalous magnetic moment of the muon, a_μ, since 1959 [53]. This includes the measurement reported by Brookhaven National Laboratory (BNL) in 2004 [54] based on data recorded in 2001, and recent measurements by Fermi National Accelerator Laboratory (Fermilab), from the Run1 [55] and Run2 [56] data of a similar experiment.

In these experiments, beams of $3.09\,\mathrm{GeV}$ longitudinally-polarized muons are injected into a $7.112\,\mathrm{m}$ storage ring. The stored muon beam is transversely focused using electrostatic
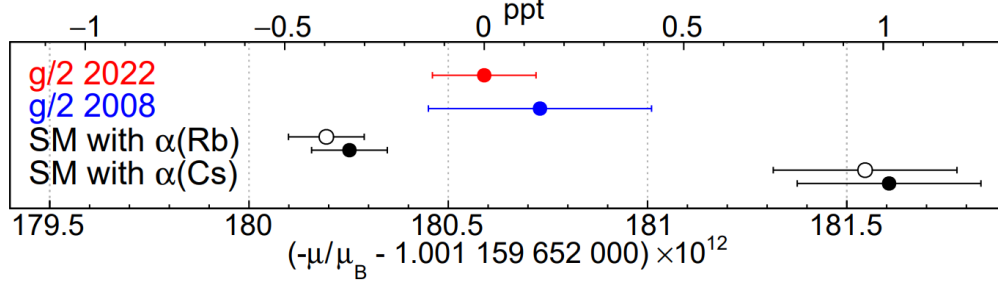
Figure 3.5: Measurements of the electron $\frac{g}{2}$. The most recent measurement is shown in red, and a similar measurement from 2008 is shown in blue. White and black hollow points show the SM predictions for slightly different contribution of 10th-order QED. The QED contribution depends on the measured value of the fine-structure constant, and a discrepancy is observed between the measurements of α with Rubidium and Cesium. Figure taken from reference [50].

quadrupoles. The cyclotron and Larmor precession frequencies of the muons can be defined in a similar manner to equations 3.8 and 3.9, and in this setup, they are around $6.7\,\text{MHz}$ and $6.93\,\text{MHz}$, respectively.

Similar to the case of electron, the difference between these two frequencies is a measure of the anomalous magnetic moment as

$$\omega_\text{a} = \omega_\text{S} - \omega_\text{C} = \frac{g-2}{2}\frac{e}{2m}B = \frac{g-2}{2}\omega_\text{C} = a_\mu\omega_\text{C}. \tag{3.12}$$

For a non-zero ω_a, the angle between the spin and momentum of the polarized muons slowly oscillates with a frequency of about $230\,\text{kHz}$. In these three equations, we have overlooked the relativistic corrections from the boost of electric fields present in the laboratory to the muon rest frame. These corrections vanish for muons stored at the *magic momentum* of $3.09\,\text{GeV}$, making ω_a proportional to, but not exactly equal to $a_\mu\omega_\text{C}$.

The longitudinally-polarized positive muons that circulate in the cyclotron have a lifetime of $2.2\,\mu s$ in their rest frame and will dominantly decay through the weak interaction to a positron, the neutrino of the electron, and the antineutrino of the muon. Due to the characteristics of the weak interaction, in the muon rest frame the positron is emitted parallel to the muon spin. This means that the positron energy in the lab frame is relatively higher when the spin is aligned with the muon momentum, and lower when they are antiparallel. The energy of the emitted positrons is measured over time and the number of high-energy positrons oscillates with a frequency of ω_a, which is precisely measured.

Having ω_a in hand, one could measure a_μ if a precise measurement of the magnetic field and therefore ω_C was in hand. However, the precision in measuring the magnetic field of a cyclotron is poor, and an alternative approach is taken in which a_μ is found by

$$a_\mu = \frac{g_\text{e}}{2}\frac{\mu_\text{p}}{\mu_\text{e}}\frac{m_\mu}{m_\text{e}}\frac{\omega_\text{a}}{\omega_\text{p}}, \tag{3.13}$$

where μ_p and μ_e are the magnetic moments of the proton and the electron defined in equation 3.1, m_μ and m_e are the muon and electron masses, and ω_p is the precession frequency of the proton which can be precisely measured in the same magnetic field using pulsed nuclear magnetic resonance (NMR) probes. While the last fraction represents the two precisely measured quantities from this experiment, the first three are known from other precise measurements of a_e, bound-state QED, and muonium hyperfine splitting, respectively.

Figure 3.6 shows the current measurements of the anomalous magnetic moment of the muon.

Results are shown for the BNL experiment as well as the first three runs of the ongoing Fermilab experiments. The current experimental world average is $a_\mu = 116\,592\,059(22) \times 10^{-11}$ with 0.19 ppm precision, which is statistically dominated.

As explained in section 3.1, the dominant source of uncertainty in the calculation of the SM prediction for the anomalous magnetic moment comes from the QCD contributions which cannot be perturbatively calculated. This contribution can be estimated either by using the cross-section results of hadron pair production in electron-positron collisions, or by using lattice QCD calculations. A comprehensive prediction for the SM value of the muon magnetic anomaly was compiled by the Muon g-2 Theory Initiative in 2020 [57] using the former method, which shows a $5.1\,\sigma$ tension with the current experimental average a_μ. However, some other theoretical calculations, including the QCD lattice methods, predict an a_μ closer to the experimentally measured value [58–61].
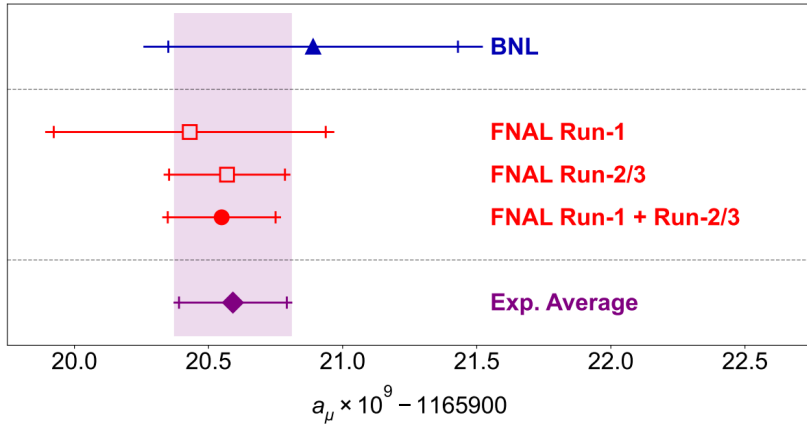
Figure 3.6: Measurements of the anomalous magnetic moment of muon. Figure taken from reference [56].

3.5 Measurement of a_τ

While the anomalous magnetic moment of the electron and the muon are two of the most precisely measured observables of nature, the anomalous magnetic moment of the tau lepton has not been measured with a similar precision. This is due to the short lifetime of the tau lepton of the order of 10^{-13} s, which makes it impossible to measure its magnetic moment through precession experiments. Instead, a_τ can be measured by studying the kinematics and cross section of tau production in collisions of charged objects that emit photons. Section 3.5.1 reviews the current best limits on a_τ obtained by the DELPHI experiment. Section 3.5.2 discusses the potential for improving these limits in hadron colliders. As discussed in section 3.2, the contributions of BSM interactions to a_τ are larger than to a_μ. The higher sensitivity to BSM interactions and the lack of a precise current measurement strongly motivates the pursuit of improved measurements of a_τ.

3.5.1 DELPHI

The current best measurement of a_τ has been done by the DELPHI collaboration using the data collected by the DELPHI experiment at LEP2 during the years 1997-2000 and corresponding to an integrated luminosity of 650 pb^{-1} [48]. As this measurement shares some general strategies

with that of this thesis analysis, as explained in chapters 5 and 6, a summary will be given in this section.

In order to measure a_τ, DELPHI made use of photon-photon collisions that also occur in electron-positron collisions. This process was first observed by the OPAL collaboration [62] and subsequently studied by the L3 collaboration [63]. Figure 3.7 shows the dominant diagram for this process, called the multiperipheral process. Each of the two photons emitted from the electrons has a non-zero invariant mass, which makes them *virtual* or *off-shell*. While the initial-state and final-state particles in a process must be *real* or *on-shell*, intermediate particles are allowed to have an invariant mass different from their true mass. The virtuality of the photons in this process is low, and hence they are called *quasi-real* photons.
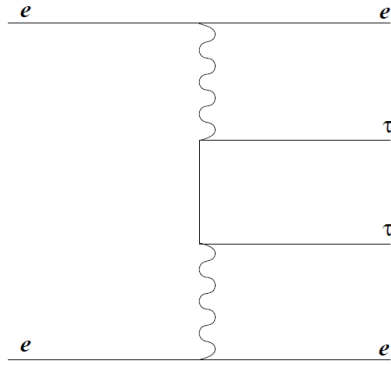
Figure 3.7: The dominant diagram for the reaction $e^+e^- \rightarrow e^+e^-\tau^+\tau^-$. Figure taken from reference [48].

The study of multiperipheral tau production is interesting in multiple ways. First, it provides a deep test of QED at the level of the fourth order in α. Moreover, the $\gamma\tau\tau$ vertex is sensitive to both the anomalous magnetic moment and electric dipole moment, and the cross section of multiperipheral tau production $e^+e^- \rightarrow e^+e^-\tau^+\tau^-$ depends on these moments. Therefore, measurements of this cross section can be translated to limits on the anomalous magnetic moment and the electric dipole moment.

To select such events, one has to detect the decay products of the tau leptons since the scattered electrons are too forward to be within the detector acceptance. In the chosen decay channel, to suppress the background, one tau lepton was selected to decay to an electron and neutrinos and the other to a non-electron (hadron or muon). An event is selected if it satisfies the following criteria:

- To suppress the background from fermion pair production, two oppositely charged tracks are required with the (sub)leading track having a transverse momentum perpendicular to the beam, p_T, above $300(100)$ MeV, with the vector sum of the two tracks less than 30 GeV.

- To suppress backgrounds with no neutrinos, the acoplanarity of two tracks, defined by $1 - \Delta\phi/\pi$ is required to be greater than 0.0278 and the p_T of the two-track system greater than 0.5 GeV.

- To select events with a high trigger efficiency, the transverse energy of the two-track system defined by $E_t = E_1 \sin\phi_1 + E_2 \sin\phi_2$ must be greater than 2 GeV.

- To ensure the balance of transverse momentum of the $\gamma\gamma$ system, no energy deposition in the forward electromagnetic calorimeters above 60% of the beam energy is allowed.

The object identification is done by a dE/dx measurement using a Time Projection Chamber (TPC) with muon, electron, kaon, and proton hypotheses. While the efficiency of particle identification with the TPC is about 83%, some residual background events from the $e^+e^- \to e^+e^-q\bar{q}$, $e^+e^- \to e^+e^-e^+e^-$, and $e^+e^- \to e^+e^-\mu^+\mu^-$ processes remain due to misidentification. Other sources of background include the non-multiperipheral $e^+e^- \to e^+e^-\tau^+\tau^-$ events and the $e^+e^- \to \tau^+\tau^-$ process.

The main source of systematic uncertainty in this analysis is from the dE/dx categorization, followed by track selection criteria, event selection criteria, and the limited number of simulated Monte Carlo (MC) events.

The cross section (σ) is calculated using $\sigma = \frac{N_{\text{obs}} - N_{\text{bg}}}{\epsilon_{\text{sel}}\epsilon_{\text{trig}}\mathcal{L}}$ where N_{sig} is the number of observed events, N_{bg} is the number of background events assuming that the background and signal events have the same trigger efficiency, ϵ_{sel} is the selection efficiency, ϵ_{trig} is the trigger efficiency, and $\mathcal{L}$ is the integrated luminosity.

To model the contribution of non-SM effects, the matrix element of the $\gamma\gamma \to \tau^+\tau^-$ process at leading order in QED [64] is translated to the cross section of the $e^+e^- \to e^+e^-\tau^+\tau^-$ process using the Equivalent Photon Approximation (EPA) [65]. Figure 3.8 shows the calculated cross section after subtracting the SM cross section for a range of a_τ values. Fits to the measured cross section were performed for different values of a_τ. Figure 3.9 shows the profile of χ^2 of the fits as a function of a_τ. As a result, a 95% range of allowed values of a_τ were extracted, and found to be $-0.052 < a_\tau < 0.013$. The result expressed in the form of a central value and uncertainty is $a_\tau = -0.018 \pm 0.017$.
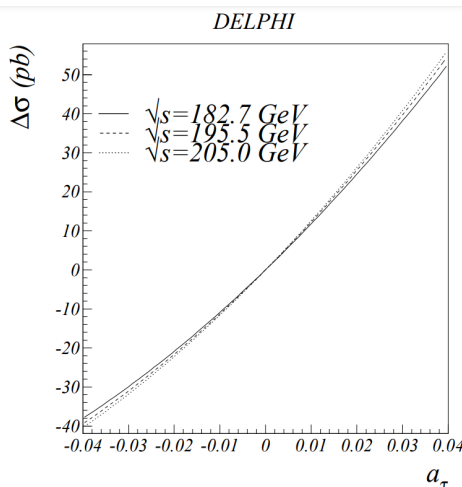
Figure 3.8: Total cross section change as a function of the anomalous magnetic moment for the three collision energies of the recorded data. Figure taken from reference [48] using the calculation from reference [64].

3.5.2 Measurement at LHC using PbPb collisions

Due to the role of measurements of the anomalous magnetic moment as a precision test of the predictions of QED, EW theory, and QCD, and given that the precision of the current best measurement of a_τ from DELPHI is an order of magnitude away from the theoretical SM prediction, it is important to seek alternative approaches to measure a_τ.

In 1991, it was suggested that pairs of tau leptons produced via photon fusion in ultraperipheral collisions of heavy ions from the $\text{PbPb} \to \text{Pb}(\gamma\gamma \to \tau^+\tau^-)\text{Pb}$ (figure 3.10) process could
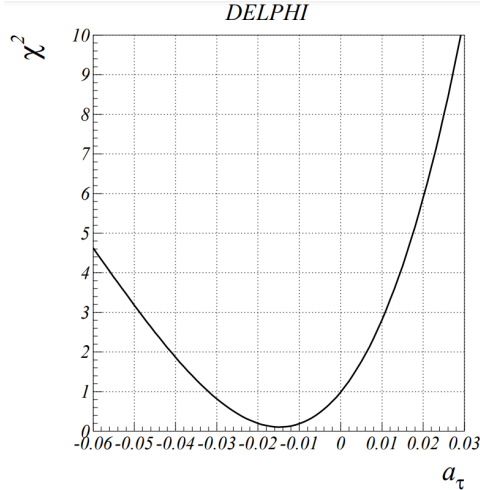
Figure 3.9: χ^2 as a function of anomalous magnetic moment. Figure taken from reference[48].

provide sensitivity to a_τ [66]. Recent calculations using effective field theory (EFT) demonstrated that lead-lead (PbPb) collisions at the LHC could provide enough sensitivity to supersede LEP measurements [67, 68]. The electromagnetic field of the Pb ions is represented by quasi-real photons with an invariant mass of 0.06 GeV. At the LHC, the two quasi-real photons from the Pb ions are quite forward with maximum energy of 80 GeV, but p_T of only about 30 MeV. Therefore, the two tau leptons are expected to be back-to-back in azimuthal angle, balanced in p_T, and soft.

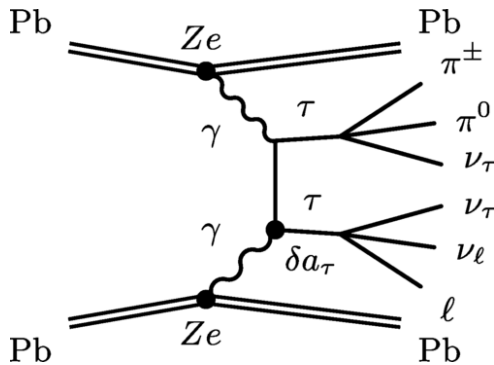The cross section of the $\gamma\gamma \to \tau^+\tau^-$ process shown in figure 3.10 is enhanced by Z^4. Therefore, despite PbPb datasets having a factor of a million lower integrated luminosities than proton-proton datasets, the cross section for $\gamma\gamma \to \tau^+\tau^-$ is 4.5 million times higher, leading to similar event yields. With the $1.8\,\text{nb}^{-1}$ collected so far, the LHC has already produced more than a million $\gamma\gamma \to \tau^+\tau^-$ events.

Figure 3.10: Pair-production of tau leptons from ultraperipheral lead ion (Pb) collisions in two of the most common decay modes: $\pi^\pm\nu_\tau\pi^0$ and $\ell\overline{\nu}_\ell\nu_\tau$. New physics can modify tau-photon couplings that affect the magnetic moment by δa_τ. Figure taken from reference [67].

In ultraperipheral PbPb collisions, only the electromagnetic fields of the Pb ions interact, leaving the Pb ions themselves intact. These events do not contain QCD interactions that generate high particle multiplicities and so they are relatively clean and are identified experimentally by having low forward activity. Given the softness of the generated tau leptons, the low background of UPCs in general, and the negligible number of additional simultaneous interactions, PbPb collisions of the LHC provide a clean environment for the proposed analysis.

The measurement of a_τ is based on the sensitivity of the $\gamma\tau\tau$ coupling in figure 3.10 to

a_τ, affecting both the cross section and the kinematics of the tau leptons and their decay products. Figure 3.11 shows the sensitivity of the p_T distributions of the tau decay products to a_τ, while figure 3.12 shows the sensitivity of the PbPb $\rightarrow$ Pb($\gamma\gamma \rightarrow \tau^+\tau^-$)Pb process to a_τ. Experimentally, by fitting the observed kinematic distributions in the data with these theoretically-calculated ones, in both shape and normalization, one can measure the value of a_τ.

Figure 3.13 shows the expected measurement of a_τ from LHC experiments compared to the current best measurement from DELPHI, as well as theoretical predictions. Expected limits are shown for various scenarios of integrated luminosity and systematic uncertainties. The integrated luminosity of PbPb collisions during Run2 of the LHC is $2\,\mathrm{nb}^{-1}$, while $10\,\mathrm{nb}^{-1}$ is expected in Run 3.
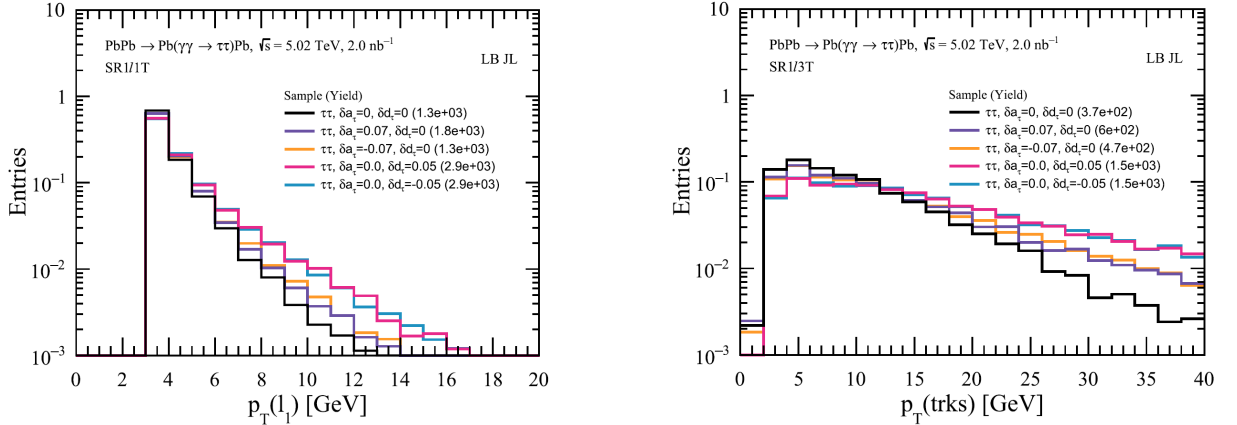
Figure 3.11: Left: Distribution of p_T for the lepton from a leptonically decaying tau lepton in PbPb collisions at $\sqrt{s_{NN}} = 5.02\,\mathrm{TeV}$. Right: Distribution of vector sum p_T of the three-track system when the hadronic tau has exactly three charged pions among its decay products. Distributions are shown for reference signals with various δa_τ and δd_τ couplings. These are normalized to the unit integral to illustrate shape changes with variations of δa_τ and δd_τ. Figure is taken from reference [68].
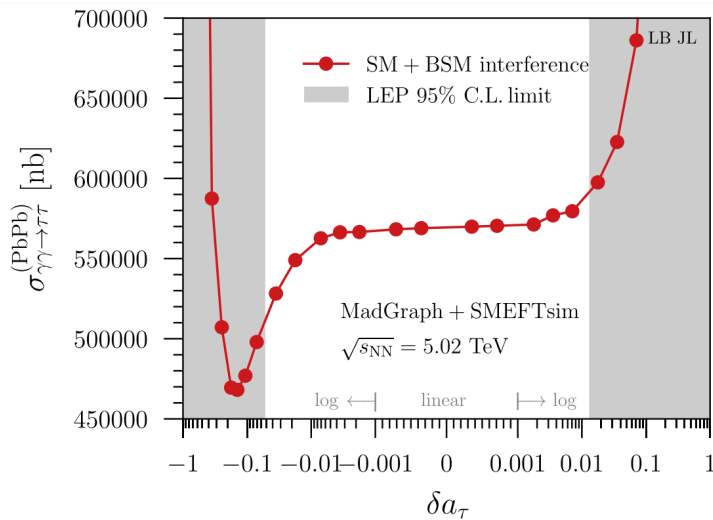
Figure 3.12: Generator-level cross section of $\gamma\gamma \rightarrow \tau^+\tau^-$ with the photon flux implemented in MADGRAPH5_aMC@NLO [69] interfaced with SMEFTSIM [70] for BSM couplings. The cross section is shown as a function of a_τ with gray regions denoting the 95% C.L. exclusion by DELPHI. The horizontal axis is on a linear scale for $\delta a_\tau \in [-0.001, 0.001]$ and is logarithmic elsewhere. Figure is taken from reference [68].
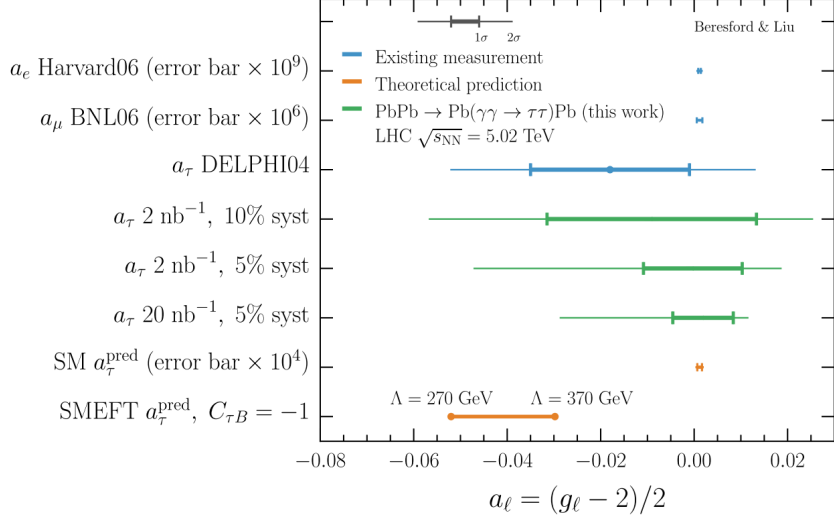
Figure 3.13: Summary of lepton anomalous magnetic moments $a_\ell = (g_\ell - 2)/2$. Existing single-experiment measurements of a_e [71], a_μ[54], and a_τ [48] are in blue. The benchmark projections of reference [68] (green) assume $2\,\mathrm{nb}^{-1}$ and $20\,\mathrm{nb}^{-1}$ for 5% and 10% systematic uncertainties. For visual clarity, we inflate $1\,\sigma$ error bars on a_e (a_μ) measurements by 10^9 (10^6), and 10^4 for the SM prediction a_τ^{pred} (orange). Collider constraints have thick (thin) lines denoting 68% C.L., $1\,\sigma$ (95% C.L., $\approx 2\,\sigma$). A SM effective field theory prediction with $C_{\tau B} = -1$ and BSM scales $270 < \Lambda < 370$ GeV is shown in thick orange. The figure is taken from reference [68].

25

4 The Large Hadron Collider and The Compact Muon Solenoid

4.1 The Large Hadron Collider

The Large Hadron Collider (LHC) is the largest and most powerful accelerator ever built. It is a synchrotron located on the border of Switzerland and France near Geneva and with a circumference of about 27 km that accelerates two oppositely circulating beams of hadrons and collides them at four collision points. The collisions at these four points are studied by four experiments: CMS, ATLAS, ALICE, and LHCb. As shown in figure 4.1, the LHC is part of CERN's accelerator complex. It accelerates and collides protons and lead ions, in addition to short test runs with xenon ions and partially stripped lead ions.

4.1.1 Proton beams

The proton acceleration starts from a bottle of hydrogen gas. Hydrogen atoms are stripped of their electrons and accelerated up to 50 MeV by a LINear ACcelerator called LINAC2. These protons are then injected into the Proton Synchrotron Booster (PSB) to be accelerated to 1.4 GeV and injected into the Proton Synchrotron (PS) where they are accelerated to 25 GeV. They are then injected into the Super Proton Synchrotron (SPS), which accelerates them to 450 GeV before they are injected into the LHC.

Bunches of protons from SPS with a bunch spacing of 25 ns are injected into two oppositely
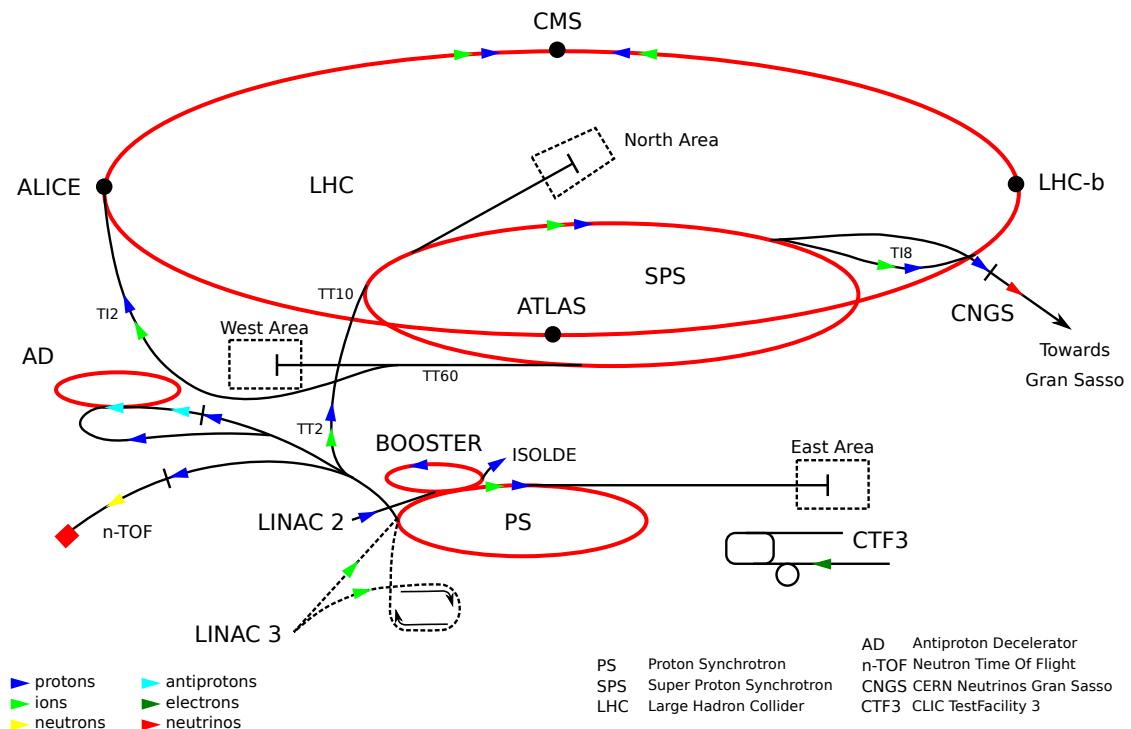

Figure 4.1: CERN's accelerator complex. Taken from [72].

circulating pipes within the LHC over the course of 4 minutes and 20 seconds and they start circulating inside the LHC's chain of dipole magnets, which span most of its circumference. Over a 20-minute period, the two beams of protons are synchronously accelerated using Radio Frequency (RF) cavities up to an energy of 6.5 TeV per beam. At each of the four collision points serving the four experiments, oppositely circulating bunches are led to collide with each other, leading to a center-of-mass energy that was 13.0 TeV during the period 2015 to 2018 referred to as "Run2", and 13.6 TeV from the start of "Run3" beginning with 2022.

At the LHC, hadrons are accelerated and collided in bunches to increase the total number of collisions. Therefore, possibly more than one collision occurs at each bunch crossing. The number of interactions per bunch crossing is referred to as "pileup". Figure 4.2 shows the pileup distribution during the Run2 period. While the increase of pileup results in a larger event rate for processes of interest, it introduces challenges for the detection of outgoing particles from the collisions that must be mitigated in order to make use of the extra events.
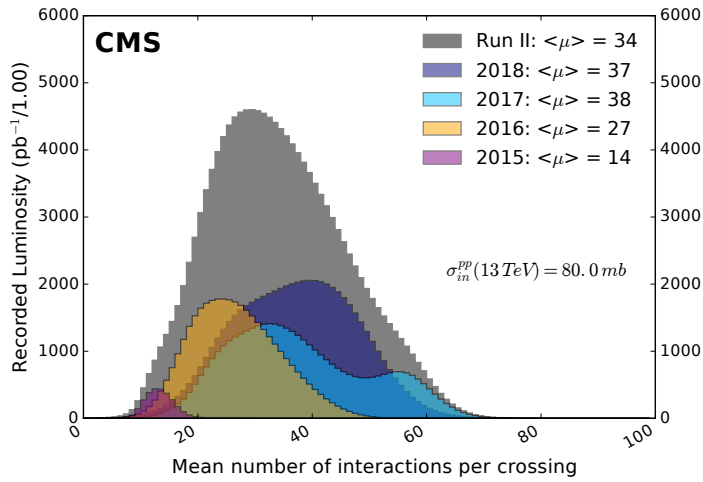
Figure 4.2: Distribution of the number of pp interactions per bunch crossing, assuming an inelastic cross section of 80 mb. Figure taken from [73].

4.1.2 Lead beams

Besides proton-proton (pp) collisions, during Run2 of the LHC there were two periods of lead-lead (PbPb) collisions in 2015 and 2018, each approximately one month long, and a one-month period of proton-lead (pPb) collisions in 2016. To produce the beam of lead ions, a 500 mg piece of lead is heated to 500 °C to get a gas of lead atoms. A few electrons are then stripped from each lead atom using an electrical current. The lead ions are accelerated by a linear accelerator, the LINAC3, up to an energy of 45 MeV per nucleon and more electrons are removed from them. They are then injected into the Low Energy Ion Ring (LIER) shown by dashed lines in figure 4.1, and accelerated to 72 MeV per nucleon. They are then injected into the PS where they are accelerated to 5.9 GeV per nucleon and all remaining electrons are stripped. The accelerator chain is the same for Pb ions and protons starting from the PS. Lead ions are injected into the SPS and accelerated to 177 GeV per nucleon, before going to the LHC.

The collision data used in this dissertation are taken in the PbPb collision period of 2015 and 2018 with a center-of-mass energy of $\sqrt{s_{NN}} = 5.02$ per nucleon. Similar to the proton beams, lead ions also collide in bunches which are spaced 25 ns apart, but the average pileup is much smaller than 1, meaning that most bunches pass each other without any collision, and it

is rather unlikely to have two collisions at the same bunch crossing. The lower beam intensity of Pb beams is due to higher charge of Pb ions which makes them harder to squeeze and the higher beam energy compared to proton beams, which poses risks for the accelerator machine at high beam intensities.

4.1.3 Luminosity

In order to study rare processes, the LHC needs to produce a large number of hadron collisions. The LHC is the most intense hadron collider ever built [74]. The intensity is represented by the instantaneous luminosity ($\mathcal{L}$) that quantifies the collision rate per second per beam area and is defined as [13, p. 533]:

$$\mathcal{L} = \frac{N_1 N_2 f}{A}, \tag{4.1}$$

where f is the frequency of bunch crossing (40 MHz for LHC), N_1 and N_2 are the number of hadrons in each colliding bunch (1.15×10^{11} for pp and 7×10^7 for PbPb), and A is the cross sectional area of each bunch, which is squeezed at each collision point to a size of about $16 \times 16 \, \mu m^2$ to increase the instantaneous luminosity. When reporting the luminosity of hadron collisions, it is common to use the unit of *barn* (b) for the area, which is equivalent to 10^{-24} cm^2. Figure 4.3 shows the distribution of peak instantaneous luminosity of each week (day) for pp (PbPb) collisions delivered by LHC to the CMS collision point in 2018.
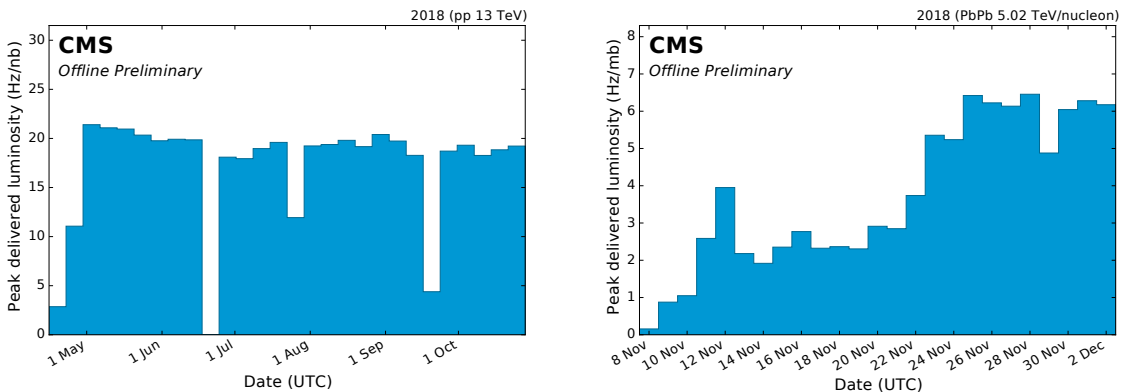
Figure 4.3: Left (right) plot shows the distribution of peak instantaneous luminosity of each week (day) for pp (PbPb) collisions delivered by LHC to the CMS collision point in 2018. Figures taken from [73].

The total size of the collision dataset is represented by *integrated luminosity L*, which is defined by:

$$L := \int\limits_{\text{data period}} \mathcal{L}(t) \mathrm{d}t, \tag{4.2}$$

and is in units of inverse area. Figure 4.4 shows the distribution of integrated luminosity for heavy-ion periods during Run2 of the LHC. It also shows the *proton-equivalent* integrated luminosity, which is obtained by multiplying the luminosity by the atomic mass of the particle that comprises each colliding beam.

As mentioned in section 4.1.2 and shown in figure 4.3, the intensity of the collision, represented by either the average number of collisions per bunch crossing or the instantaneous luminosity,
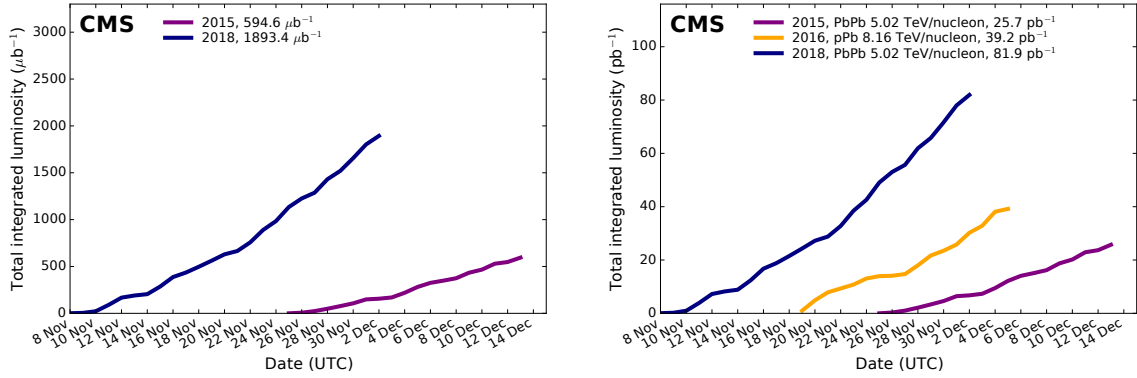
Figure 4.4: Distribution of integrated luminosity of heavy ion collisions delivered by LHC to the CMS collision point in different years. Left: PbPb collisions of 2015 and 2018. Right: Proton-equivalent luminosity for all heavy-ion periods of Run2. Figures taken from [73].

is lower in heavy-ion collisions than proton collisions. This is because some heavy-ion collisions produce a significantly larger number of particles than those of proton collisions, and would be impossible to reconstruct in presence of pileup. However, if the impact parameter of the two Pb ions is greater than the sum of their radii, the hadronic interactions will be less frequent than head-on collisions. In these interactions, referred to as *ultraperipheral collisions* (UPC), a quasireal photon from one Pb ion can interact with another quasireal photon from the other Pb ion, or with a pomeron emitted by the other Pb nucleon. In the latter case, referred to as a *photonuclear* interaction, the photon from the first Pb ion interacts hadronically with the second Pb ion, which breaks the ion. In the former case of ultraperipheral photon-photon collisions, the lead ions are left intact most of the time, but the interaction can excite one or both Pb ions, resulting in the emission of one or more neutrons by each excited Pb ion. While the cross section of hadronic PbPb interactions at the center of mass energy of $\sqrt{s_{NN}} = 5.02$ per nucleon is 7.66 ± 0.03 b [75], the ultraperipheral PbPb collisions have a cross section of 276 b [76], making them 36 times more frequent. For the peak instantaneous luminosity of 6 Hz/mb shown in figure 4.3, the collision rate of UPC events is about 46 kHz. Compared to the LHC bunch spacing of 25 ns corresponding to 40 MHz, an ultraperipheral PbPb collision is expected every 870 bunch crossings.

4.2 The Compact Muon Solenoid

The Compact Muon Solenoid (CMS) is a multipurpose hermetic detector at one of the interaction points of the LHC, 100 m underground (see figure 4.1). It detects most of the final-state particles from hadron collisions to precisely study the Standard Model and look for BSM physics signatures. The CMS detector is an approximately cylindrical detector with a length of 21.5 m and a diameter of 14.6 m. As shown in Fig. 4.5, the onion-shaped CMS detector consists of multiple layers of subdetectors to measure the energy and momentum of particles coming from the collision point. These layers are stacked around each other in a cylindrical form in the *barrel* section of the detector. To ensure hermetic coverage, the *endcap* section extends the coverage with disk-shaped layers of subdetectors stacked next to each other along the beam axis. A detailed description of the CMS detector can be found in reference [77].

The conventional coordinate system of CMS is defined in Fig. 4.6. The origin is set to the
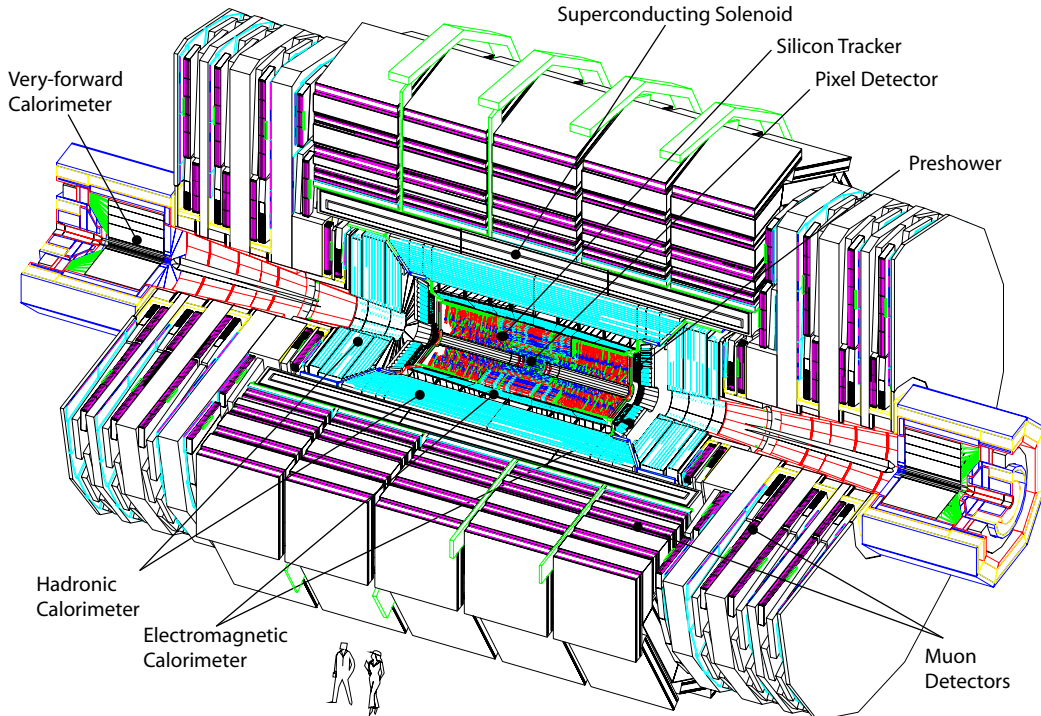
Figure 4.5: The CMS detector. Taken from [77].

center of the detector. The x-axis points to the center of the LHC ring. The y axis points upwards towards the sky perpendicular to the LHC ring. The z axis is tangent to the anticlockwise beam when viewed from above. The azimuthal angle, $\phi \in [0, 2\pi)$, is the cylindrical angle of the x-axis in the xy plane. The polar angle, $\theta \in [0, \pi)$, is measured with respect to the z axis and can be used as a measure of how forward or central a particle is. However, in inelastic hadronic collisions, it is common to use *pseudorapidity*, defined as:

$$\eta = -\log \frac{\tan \theta}{2}. \tag{4.3}$$

The pseudorapidity is 0 in the transverse plane perpendicular to the beam. It goes to $\eta = \infty$ along the positive direction of the z-axis and goes to $\eta = -\infty$ along the negative direction of the z-axis. The difference between the pseudorapidity of two vectors is Lorentz invariant under the boost in the z axis. Moreover, the distance in the η-ϕ plane between two vectors is defined as:

$$\Delta R = \sqrt{(\Delta\phi)^2 + (\Delta\eta)^2}, \tag{4.4}$$

and is used as a Lorentz-invariant measure of the angle between them. Finally, the momentum vector of particles can be projected onto the transverse (x-y) plane and the z axis. The corresponding vectors are called transverse momentum (p_T) and longitudinal momentum (p_z), respectively.

The onion-shaped CMS detector consists of multiple layers of subdetectors in both *barrel* and *endcap* sections in order to identify and measure the properties of the outgoing particles from the interaction point. As shown in figures 4.5 and 4.7, starting from the interaction point outward, the subdetectors are the *tracking system* to measure the charge and momentum of the charged particles, the *electromagnetic calorimeter* (ECAL) to measure the energy of the electrons and photons, the *hadronic calorimeter* (HCAL) to measure the energy of the hadrons,
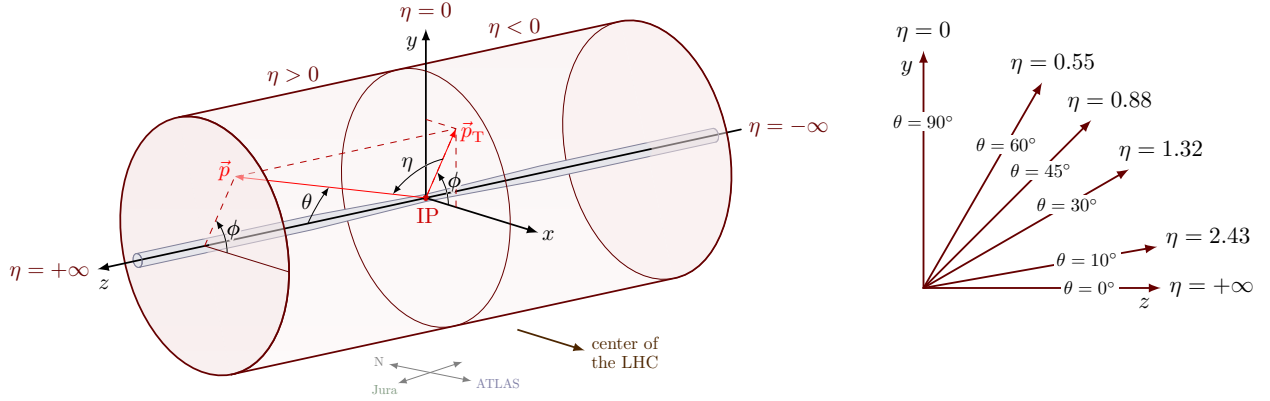
Figure 4.6: Left: The conventional coordinate system of CMS with momentum vector $\vec{p}$. Taken from [78]. **Right**: Pseudorapidity. Taken from [79].

and the *muon system* to measure the charge and momentum of the muons. A magnet and flux-return yoke is used to bend the trajectory of the charged particles, enabling the measurement of their momentum in the tracking and muon systems. In the range of $3 < |\eta| < 5$ in both $+z$ and $-z$ directions sit two *forward hadron calorimeters* (HF).
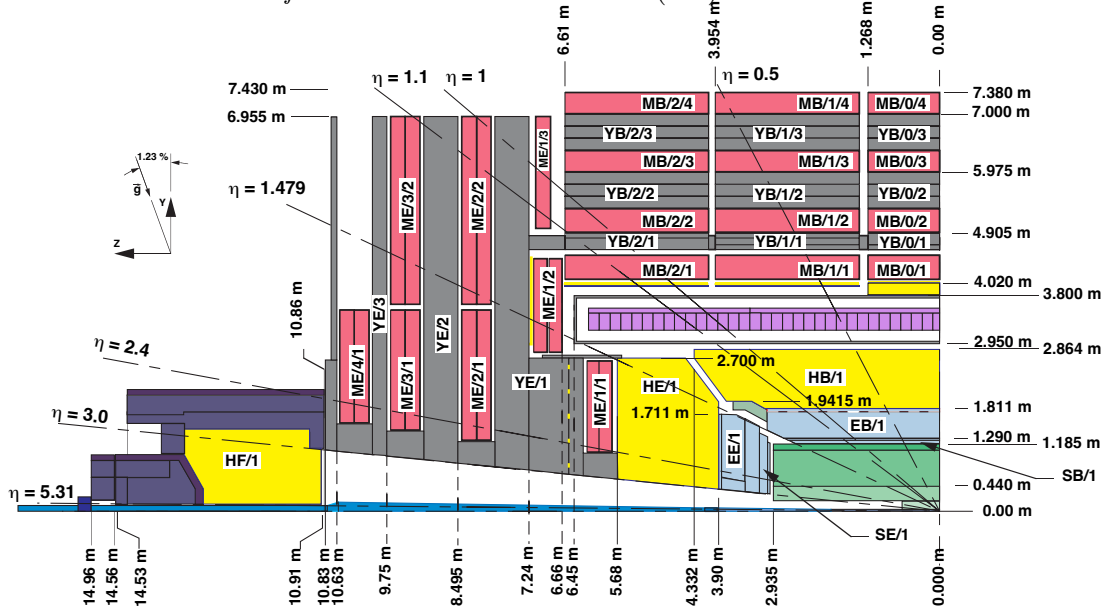
Figure 4.7: Schematic of one quadrant of the CMS detector in the positive zy-plane. The tracker is shown in green, the ECAL in light blue, the HCAL in yellow, the muon stations in red, the solenoid magnet in purple, and the iron flux-return yoke in dark gray. Adapted from reference [80].

4.2.1 Magnet

The magnetic field is provided by a wide-aperture superconducting thin solenoid. It is a 12.5 m long cylinder with a diameter of 6 m. The magnet is placed between the HCAL subdetector and the muon system and provides a rather homogeneous magnetic field inside the solenoid of 3.8 T, which bends the trajectory of the charged particles. The bending radius (r) correlates with p_T and magnetic field (B) as:

$$r[\text{m}] = \frac{p_T[\text{GeV}]}{0.3\,B[\text{T}]}. \tag{4.5}$$

Therefore, the transverse momenta of particles can be determined by measuring the trajectory of the ionization deposits left by minimum-ionizing charged particles in the tracking and muon systems. Their charge is determined by the bending direction.

Outside the solenoid, layers of iron are used in between the muon tracking layers as a flux-return yoke [81] that returns about two thirds of the magnetic field inside the detector. This adds to the bending power in the muon system and improves the homogeneity of the field inside the solenoid. The iron layers also serve as absorbers in the muon system.

4.2.2 The tracking system

The CMS tracker is the closest subdetector of the CMS experiment to the beam and is designed to find the trajectories corresponding to charged particles bent inside the magnet. The trajectories are generically helically shaped with a circular projection in the transverse plane. The charged particles deposit energy while passing through the segmented silicon layers of the tracker, leaving a cluster of charge or *hit* that is stored to be read out for events of interest. The best fitted helix trajectory passing through these hits is taken as the measured track, and its transverse radius determines the p_T of the track, as can be deduced from equation 4.5.

The tracking system is composed of two sections, highlighted in green and pink in figure 4.8. The inner section close to the collision point is called the *pixel tracker* or the *pixel detector*. It is enclosed by an outer subsystem called the *strip tracker* or the *strip detector*.
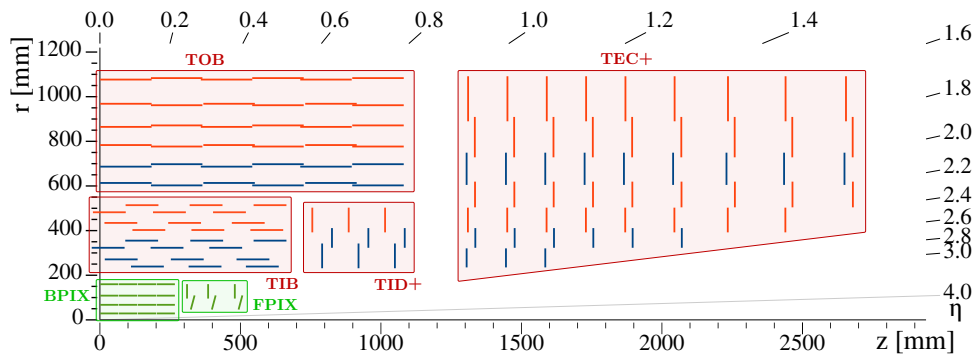
Figure 4.8: Schematic view of the CMS tracking system. The pixel detector is shown in green, and corresponds to the Phase1 pixel detector, while the strip detector is shown in pink. Adapted from [82].

4.2.2.1 The pixel detector

The pixel detector is composed of layers of small silicon pixel cells of the size $100 \times 150 \, \mu\text{m}^2$. Charged particles passing through each layer deposit minimum ionizing charges in one or more pixels, which are grouped together as a cluster or *hit* whose charge-averaged position in both ϕ and η is taken as the reconstructed hit position of that layer. The position resolution of hits generally improves with a smaller pixel pitch size. The charge deposited in the silicon pixels is collected by a readout system with pixels bonded to the silicon pixels. Groups of pixels form a pixel module composed of a pixelated silicon sensor and the corresponding readout chip. A set of modules can then form a layer of a barrel or a disk of an endcap. Hits from multiple layers of the pixel detector and tracker system as a whole that are consistent with the helical trajectory of a charged particle in a magnetic field are group together and referred to as the *track* associated to that particle.

As shown in figure 4.8, the barrel section of the pixel detector (BPIX) is composed of concentric cylinders and the endcap/forward section of the pixel detector (FPIX) is composed of disks perpendicular to the beam axis. The CMS Phase0 pixel detector, in operation between 2010 and 2016, was composed of 1440 sensor modules with a total of 66 million silicon pixels comprising three BPIX layers and two FPIX disks on each side. This detector was replaced in the long shutdown of 2017 with the Phase1 pixel detector, comprised of four BPIX layers and three FPIX disks on each side, for a total of 1856 modules and 124 million pixels [83, 84]. The Phase1 BPIX achieves a hit position resolution of approximately $10\,\mu m$ in the $r - \phi$ direction and 20-30 μm along the z direction. Figure 4.9 compares these two layouts. The extra layer in BPIX, extra disk in FPIX, and the closer placement of the innermost layer to the collision point all contribute to a more precise measurement of the track parameters. The improved tracking also contributes to a better measurement of the 3D position of the collision vertex, which is the common vertex of the multiple tracks produced in a single interaction. This is necessary for dealing with the increased number of pp collisions provided in Run2 in each bunch crossing [85, 86]. It also helps to measure secondary vertices associated with B mesons, which travel approximately one millimeter before decaying.
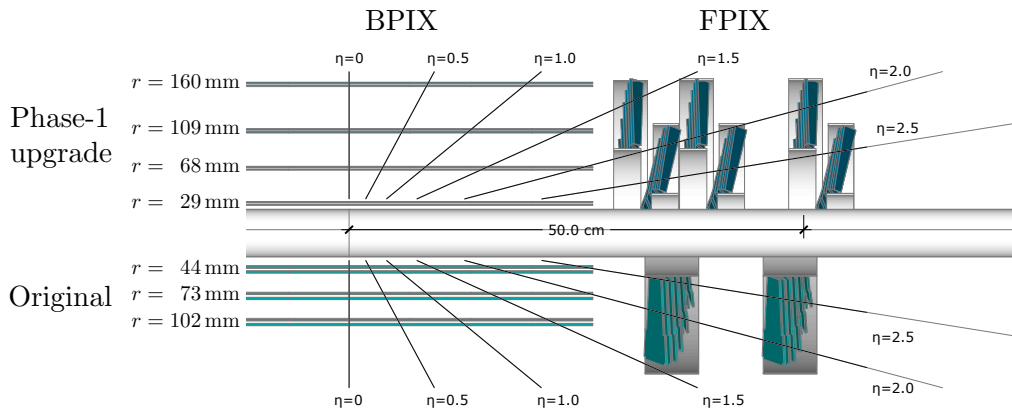
Figure 4.9: Comparison between the layout of the Phase0 and Phase1 pixel detectors. The beam pipe is narrowed down to make room for the first layer of the Phase1 barrel pixel detector, which is 29 mm from the beam. Adapted from [84].

4.2.2.2 The strip detector

The pixel detector is enclosed by the outer layer of the tracking system, referred to as the strip detector. It follows a tracking concept similar to that of the pixel detector and extends from a radius of 20 cm out to 116 cm. Since the occupancy decreases as a function of distance from the collision point, relatively larger silicon microstrips are used in the strip detector, which consist of 15148 modules in total with 9.3 million silicon strips. The length of each strip varies from $80\,\mu m$ to $205\,\mu m$, but the ratio of the strip pitch to the strip width is 0.25 for all types. As shown in figure 4.8, the silicon strip detector is divided into tracker inner barrel (TIB) and tracker outer barrel (TOB) parts in the barrel region with concentric cylindrical layers. The endcap region consists of the *tracker inner disk* (TID) and *tracker endcap* (TEC) subdetectors, which extend the $|\eta|$ coverage up to 2.5.

4.2.3 The electromagnetic calorimeter

The *electromagnetic calorimeter* subdetector is designed to stop and measure the energy of photons, electrons, and positrons. The ECAL consists of 75848 PbWO$_4$ crystals, and is split into a barrel section of $|\eta| < 1.48$, and an endcap section that further extend to $|\eta| < 3$. The most precise energy measurement is carried out in the region $|\eta| < 2.6$. Incoming photons and electrons interact with the dense material of the crystals and form electromagnetic showers, which is the consecutive production of electrons and positrons from the photons and the bremsstrahlung radiation of photons from electrons and positrons, as the two dominant interactions for high energy photons and electrons, respectively. The photons are then collected at the back side of each crystal by a silicon avalanche photodiode (APD) in the barrel region and a vacuum phototriode (VPT) in the endcap region. The collected energy of the scintillated photons is a representative of the energy of the incoming photon or electron. PbWO$_4$ is a fast scintillator, has a short radiation length and a small Moliere radius. Therefore, the electromagnetic showers can be contained in short crystals that fit into the small designated area for calorimeters before the magnet. Furthermore, due to the short Moliere radius, small crystals with a face size of approximately $22 \times 22\,\text{mm}^2$ can contain 90% of the shower in one crystal and 95% in a 3×3 matrix. This fixed crystal face size translates to a granularity of $\Delta\eta \times \Delta\phi = 0.0175 \times 0.0175$ in the barrel region and a maximum granularity of $\Delta\eta \times \Delta\phi = 0.05 \times 0.05$ in the endcap region. The small granularity ensures a precise measurement of ϕ and η of the incoming photon or electron. The crystal length can contain approximately 26 radiation lengths in its length of about 23 cm. In the endcap, a crystal length of 22 cm is used due to the presence of a *preshower* layer, consisting of a thin lead conversion plate before the ECAL that allows collimated photon pairs from the decay of neutral pions to be distinguished from singly produced photons.

The energy resolution of the ECAL subdetector can be parameterized as a function of energy [87]:

$$\left(\frac{\sigma_E}{E}\right)^2 = \left(\frac{S}{\sqrt{E}}\right)^2 \oplus \left(\frac{N}{E}\right)^2 \oplus C^2, \tag{4.6}$$

with a stochastic term S, noise N, and constant term C. Figure. 4.10, shows a measurement of these terms using electron beams with various energies.

The good energy resolution of the ECAL, as well as its high granularity and precise angular measurement, allowed CMS to achieve small mass resolutions of around 1% for the invariant mass of Higgs boson candidates decaying to two photons. The technical design report [87] describes the ECAL in more technical detail.

4.2.4 The hadron calorimeter

The *hadron calorimeter* is situated outside the ECAL and within the magnet solenoid. Similar to the functionality of ECAL for electrons and photons, the HCAL stops the hadrons and measures their energy as they produce hadronic showers. The HCAL is a sampling calorimeter consisting of layers of brass absorbers, which contain the shower within the HCAL length and increase the rate of hadronic showering, and plastic scintillators that sample the induced, electromagnetic part of the shower, and whose light is guided to hybrid photodiode detectors (HPDs) by fibers. Similar to the energy resolution of ECAL, the energy resolution of HCAL [89] can be parameterized as
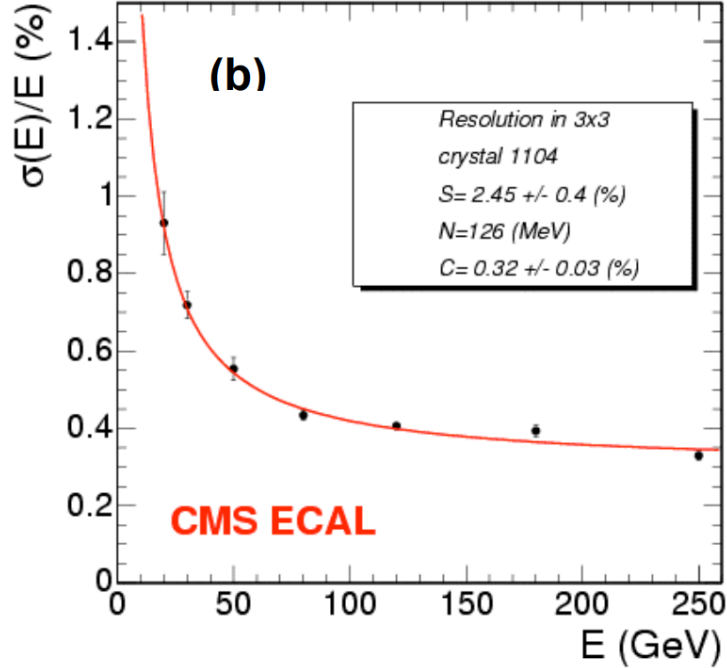
Figure 4.10: Energy resolution of a 3×3 ECAL matrix measured with electron beams with various energies. The stochastic term S, the noise term N, and the constant term C are derived. Figure taken from [88].

a function of energy as:

$$\left(\frac{\sigma}{E}\right)^2 = \left(\frac{115\%}{\sqrt{E}}\right)^2 \oplus \left(\frac{5.5\%}{E}\right)^2. \tag{4.7}$$

4.2.5 The forward hadron calorimeter

The *forward hadron calorimeter* is an extension of the HCAL in the forward region of $3 < |\eta| < 5.2$ and is positioned $11.2\,\mathrm{m}$ from the interaction point. It is a radiation-hard sampling calorimeter, composed of steel absorbers, with quartz fibers along the beam as active material, and read out with photomultipliers. It has a granularity of $\Delta\eta \times \Delta\phi = 0.175 \times 0.175$ per tower. Each tower serves as one calorimeter unit and contains long and short quartz fibers. While long fibers cover the full $165\,\mathrm{cm}$ depth of the tower, short fibers start after $22\,\mathrm{cm}$ from the front face of the detector. This allows two independent measurements of the energy released in the detector in order to evaluate both the electromagnetic and hadronic components of the shower energy. While the hadronic component is present in both fibers, the electromagnetic component of the shower releases its energy in the first part of the calorimeter, measured by the long fiber, and releases only a negligible amount of energy beyond $22\,\mathrm{cm}$ in the short fiber.

4.2.6 The muon system

The muon system is the outermost subdetector of the CMS and is positioned outside the solenoid magnet. Muons and neutrinos are the only two Standard Model particles expected to pass beyond the magnet of CMS. Therefore, hit and track detection with the muon system is a reliable identification criterion for muons. Furthermore, the muon tracks in the muon system can be extended to the tracks in the tracker system, improving the measurement of muon p_{T}.

The combined p_T resolution can be roughly parameterized as:

$$\left(\frac{\sigma_{p_T}}{p_T}\right)^2 = (A \cdot p_T)^2 \oplus C^2, \tag{4.8}$$

where A, and C are constants determined by the hit resolution and multiple scattering, respectively [90]. At high p_T, the resolution increases with momentum, as the track becomes more straight, which increases the uncertainty in its curvature. At low p_T, the resolution is dominated by the multiple scattering of muons by the detector material.

The muon tracking system is composed of three types of gas-ionizing detectors: Drift Tube (DT) champers, Cathode Strip Chambers (CSC), and Resistive Plate Chambers (RPC). The muon system relies on a redundancy between these three technologies, so that in each η-ϕ region of the detector there are two independent measurements of the muon charge and p_T. The barrel muon system consists of 4 concentric shells of drift tube chambers covering $|\eta| < 1.2$. The RPC technology has been chosen in both the barrel and the endcap in the range $|\eta| < 1.6$ as dedicated trigger detectors to identify and record collision events containing muons. Due to their fast response and good time resolution ($\sigma < 1.5\,\text{ns}$), they guarantee a precise bunch crossing assignment of the muon tracks. The CSC chambers cover the endcap region of $0.9 < |\eta| < 2.4$, providing precise time and position measurements. The detailed technical design report can be found in reference [91].

4.2.7 The zero degree calorimeters

Two *zero degree calorimeters* (ZDC) called $\text{ZDC}_{\text{minus}}$ and ZDC_{plus} are installed $140\,\text{m}$ away from the interaction point of CMS along both beam directions. They are segmented and completely cover the region of $|\eta| > 8.3$. They are made of quartz fibers and plates embedded in tungsten absorbers to collect Cerenkov light. The ZDC plays an important role in the study of *forward physics* which offers constraints on the modeling of the underlying event in hadron collisions and measures the nucleon structure.
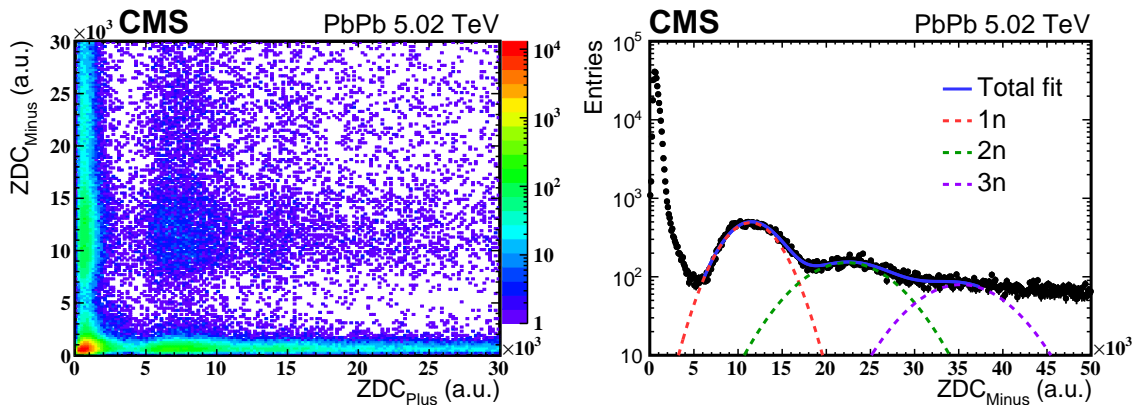
Figure 4.11: The left panel shows the correlation between energy distributions of the Minus and Plus ZDC detectors (one entry per event), while the right panel shows a multi-Gaussian function fit to the Minus ZDC energy distribution. Figure taken from [92].

In the study of PbPb collisions, in which forward neutrons are expected to be emitted by the Pb ions, the total deposited ZDC energy on each side can be used to determine the number of emitted neutrons. Figure 4.11 (left) shows the distribution of the total energy measured in in the $\text{ZDC}_{\text{minus}}$ versus total energy measured in the ZDC_{plus} for ultraperipheral PbPb collisions

producing two muons via the PbPb $\rightarrow$ Pb($\gamma\gamma \rightarrow \mu^+\mu^-$)Pb process. The plot on the right shows a logarithmic one-dimensional distribution of the total energy measured in $\mathrm{ZDC_{minus}}$. Each peak corresponds to a specific number of neutrons emitted from the excited Pb ion, and increases with lower impact parameters of the two Pb ions.

4.2.8 Trigger

At LHC, the *bunch spacing* is 25 ns, equivalent to a collision rate of 40 MHz, which is too high to read out all subdetectors, as well as for other parts of the data acquisition and data storage chain. As a result, a two-tier trigger system is employed to identify and store the collision events that are more interesting for physics studies. In the first tier referred to as the *Level-1* (L1) trigger, information from the calorimeters and muon system is provided to hardware-based event selection boards. The resulting event rate from L1 is about 100 kHz. In the next tier, known as the *high-level trigger* (HLT), a complete reconstruction of the event from the raw data of the sub-detectors is performed by software algorithms running on a farm of processors. These algorithms are optimized to be fast, yet with just enough precision to decide whether the event should be stored on disk or not. On average, events pass HLT at a rate of approximately 400 Hz and their raw information is stored on disk, and then fully reconstructed offline. A detailed description of the CMS trigger system can be found in reference [93].

4.2.9 Particle identification and reconstruction

The CMS detector is capable of identifying and reconstructing the properties of the particles that are stable enough to pass through it before decaying and which deposit sufficient energy while being isolated enough from other particles. As seen in figure 4.12, some Standard Model particles including electrons, photons, muons, protons, and pions live long enough to go through one or multiple layers of the CMS detector, while particles like the W, Z, and H bosons decay before reaching the first layer of the CMS inner tracker and whose properties have to be inferred using measurements of their stable decay products. Moreover, a kaon can sometimes live long enough to decay while in flight in the detector, leaving a kinked track in the tracking system.

The stable particles that reach the CMS detector can then be identified by their trace in one or more subdetectors of the CMS. As illustrated in figure 4.13, muons are identified by leaving a track in the muon system, the electrons and photons both deposit energy in the ECAL, while electrons can be distinguished by also having a track in the tracking system. The same identification applies for the neutral and charged hadrons showering in the HCAL. Neutrinos are the only Standard Model particles that are expected to go through the whole CMS detector without interacting. Some particles may be too close to the beam or outside the acceptance of the CMS detector and not be reconstructed.

4.2.9.1 Particle-flow algorithm

The CMS detector employs a particle flow (PF) algorithm [96, 97] to fully reconstruct collision events by combining the measurements in individual CMS subsystems. Tracks in the inner tracker or muon system are built iteratively from hits, using the *Kalman-filter* (KF) *technique* [98, 99]. In the calorimeters, the nearby segments are clustered to give the total energy of a shower. Each track in the tracking system, track in the the muon system, energy deposition in the ECAL, or energy deposition in the HCAL is considered a PF element. These elements can
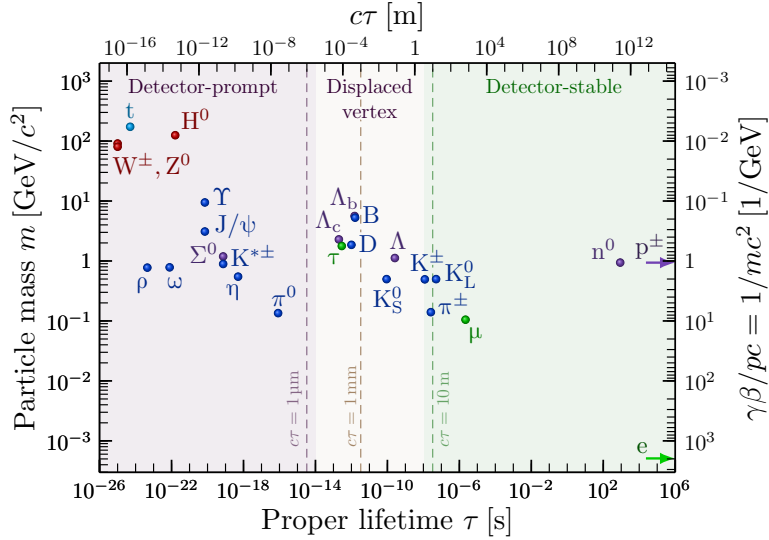
Figure 4.12: Mass versus lifetime τ of many composite and fundamental SM particles, divided in different regions of stability in the context of the CMS experiment. The decay length is given by $L = \gamma\beta c\tau$, with $\gamma\beta = p/mc$. Adapted from [94].

be assembled based on their proximity in η and ϕ. The algorithm starts with the muons as they produce a clear signature by having a track in the muon system. The corresponding track in the tracking system is merged with the one in the muon system, and both are removed from the list of PF elements in the event. Energy deposition in the ECAL will be associated with a photon if no matching track is found in the tracking system, and an electron if such a consistent track is found. The sign of track curvature determines the charge of the particle. The same approach is taken with HCAL for the identification of neutral and charged hadrons. In each step, the PF elements assigned to the reconstructed particles are removed iteratively from the list.

Once particles have been identified, the events can be analyzed in order to study specific processes or search for new or yet unseen phenomena. Some particles produced in collisions decay quickly, and must be reconstructed from the particles they decay into. One such particle is the tau lepton, the subject of the next few chapters.
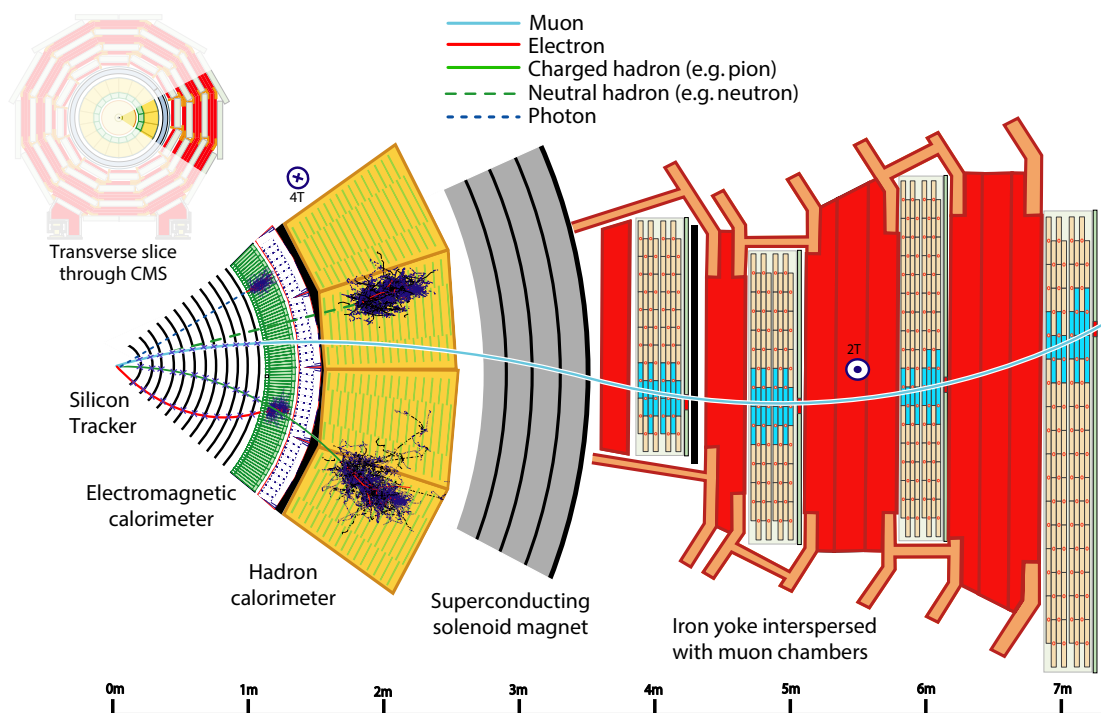
Figure 4.13: Particles in the CMS detector. Identification of a particle is based on the set of subdetectors in which it leaves a trace. Adapted from reference [95].

5 Observation of the $\gamma\gamma \to \tau^+\tau^-$ process in heavy-ion collisions and extracting limits on a_τ

In chapter 3, the measurement of the anomalous magnetic moment of the tau lepton, a_τ, using the PbPb collision data collected during the Run2 of the LHC was motivated. As mentioned in chapter 4, there were two PbPb runs during Run2 in 2015 and 2018, with the 2018 dataset being more than three times larger. Here in this chapter, we will review our analysis using the 2015 PbPb dataset collected by the CMS, which resulted in the first observation of the process and first measurement of a_τ at the LHC. A more sophisticated analysis is currently ongoing at CMS using the 2018 dataset, and will be discussed in chapter 6.

This analysis [100] uses the 2015 dataset of ultraperipheral PbPb collisions at $\sqrt{s_{\mathrm{NN}}} = 5.02\,\mathrm{TeV}$, corresponding to a total integrated luminosity of $404\,\mu\mathrm{b}^{-1}$ collected by the CMS experiment. The process under study is $\mathrm{PbPb} \to \mathrm{Pb}(\gamma\gamma \to \tau^+\tau^-)\mathrm{Pb}$, with two quasi-real photons emitted from the Pb ions converting to two tau leptons, as shown in figure 5.1. A Monte Carlo simulation of the signal process is generated [67] with MADGRAPH5_aMC@NLO (v2.6.5) [101], PYTHIA8 (v2.1.2) [102] is used for hadronization and decay, and GEANT4 [103] is used to emulate the full response of the CMS detector.

In the decay channel studied in this analysis, one tau lepton decays to a muon and two neutrinos. The other tau lepton decays to three charged pions, a neutrino, and any number of neutral pions. This decay channel, referred to as μ+3prong, provides the cleanest signature for the $\gamma\gamma \to \tau^+\tau^-$ process, since muons have the clearest signature for identification at CMS, and the three charged pions coming from the same vertex and having an invariant mass expected from a tau lepton decay are unlikely to originate from background processes. This ensures a high signal-to-background ratio and a relatively easy observation of the $\mathrm{PbPb} \to \mathrm{Pb}(\gamma\gamma \to \tau^+\tau^-)\mathrm{Pb}$ process, which was convenient for a first-step analysis using the smaller 2015 dataset.
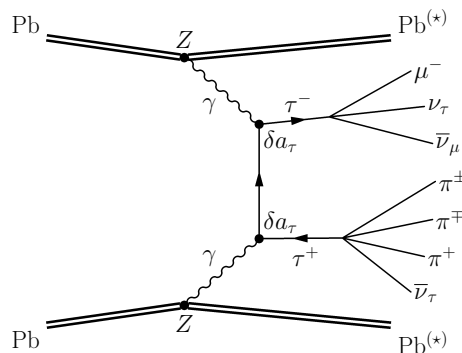
Figure 5.1: Feynman diagram of the $\mathrm{PbPb} \to \mathrm{Pb}(\gamma\gamma \to \tau^+\tau^-)\mathrm{Pb}$ process in the μ+3prong decay channel.

5.1 Reconstruction and event selection

5.1.1 Online event selection

The events are selected online by a Level-1 trigger, which requires a muon with at least two muon stations fired and which has no p_T threshold requirement. It is also required for the interaction to happen in an occupied bunch. In the HLT, the trigger selects ultraperipheral PbPb collisions by requiring that at least one side of the HF calorimeter has no signal above the noise threshold. It also requires at least one pixel track that must have a minimum p_T of $0.1\,\mathrm{GeV}$.

5.1.1.1 Trigger efficiency

The trigger efficiency is estimated using a tag-and-probe (TnP) method applied to both the data and MC simulation. The idea is to look for events expected to have two muons, identify or *tag* one of the muons, and then estimate the conditional efficiency of identifying or *probing* the other muon with the trigger. Here, we look for events containing a J/ψ that decays to two muons. The procedure starts by selecting events containing a *tag* muon that already satisfies or *fires* a trigger requiring a single muon, and a *probe* muon candidate with a track in the tracker system, while also requiring that the mass of the muon and the track be close to that of the J/ψ. The efficiency of our trigger would therefore be measured by the fraction of such events in which the *probe* muon independently fires our trigger.

The TnP method is applied to both the data and simulated MC events. The efficiency of the simulated muon trigger in MC is not necessarily equal to the one in data taking, and therefore the events in MC have to be weighted with a set of scale factors (SFs) to correct for the difference in trigger efficiency between data and MC simulations. The SF is calculated by taking the ratio of the trigger efficiency obtained by the TnP method for data over the efficiency of the simulated trigger. The SFs are calculated as a function of $|\eta|$ and p_T of the muon and are applied accordingly later, when weighting simulated signal events.

The p_T binning of the efficiency and SF measurement is coarse enough so that a fit function can be applied in order to account for the limited event count. The $|\eta|$ binning is chosen such that it differentiates between regions of the CMS detector with different efficiencies due to different detector technologies, while taking into account the limited size of the available data as the driving source of statistical uncertainty.

The single-muon trigger efficiencies are shown in figure 5.2 as a function of muon p_T for three different $|\eta|$ sections of the detector and in figure 5.3 as a function of muon $|\eta|$. For most of the phase space, very good agreement is found between the data and MC simulation, except as expected for the low-p_T ($< 3\,\mathrm{GeV}$) and ultralow-p_T ($< 2\,\mathrm{GeV}$) cases where SFs are found to be about 90% and 80%, respectively. As shown in figure 5.4, a p_T-dependent statistical (2-5%) and systematic (1-2%) uncertainty is estimated using pseudo-experiments and varying the nominal TnP fit settings, signal and background parametrization, and tag selection.

5.1.2 Offline event selections

To suppress background processes such as hadronic PbPb collisions and non-collision events, several exclusive selection criteria are imposed. First, it is required that the primary vertex of the events pass a filter designed for PbPb collision events, which ensures that the analyzed events have valid vertices. In addition, the shapes of the clusters in the pixel detector are required to be
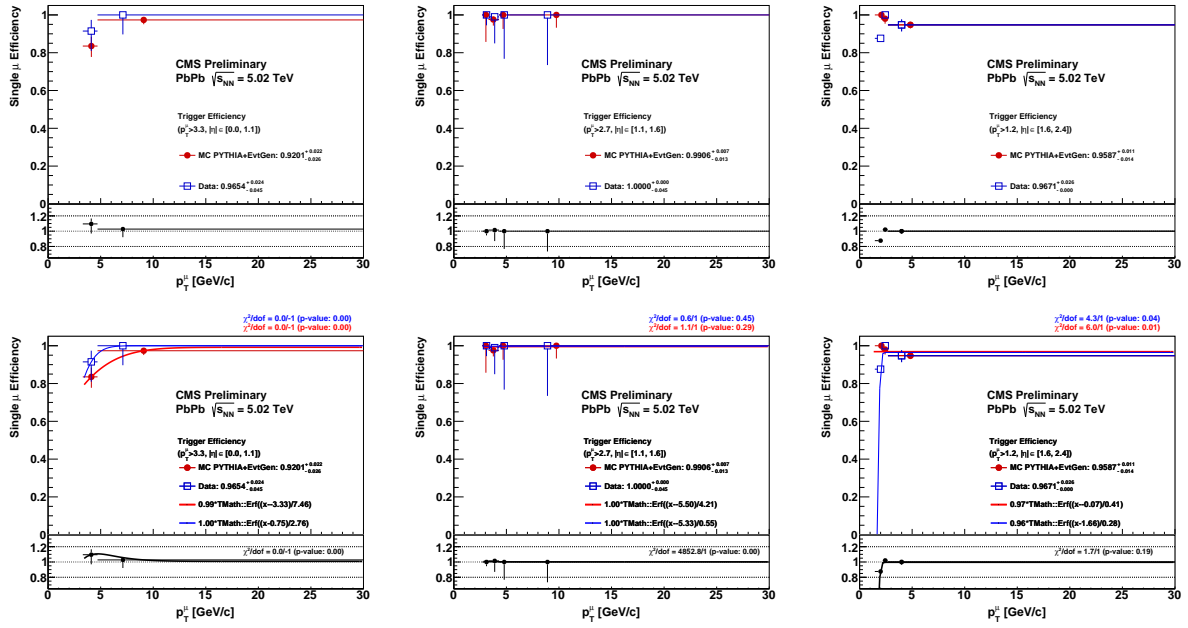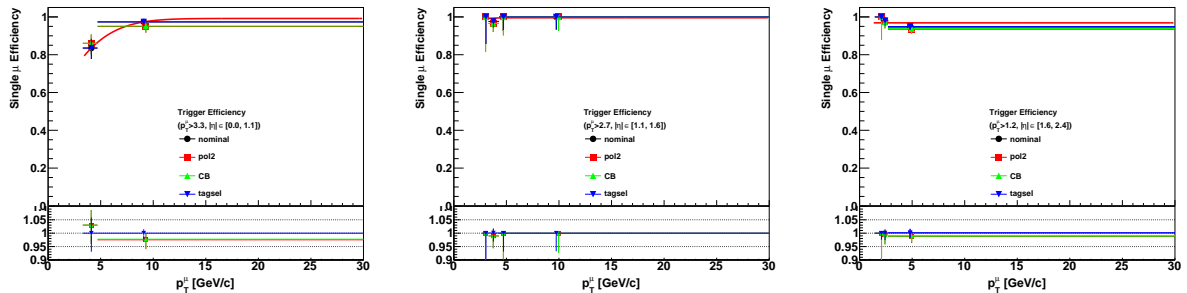
Figure 5.2: Top: Muon trigger efficiency in data (blue) and MC (red) as a function of the muon p_T for the most central and the most forward of the three rapidity regions in which SFs are calculated. Bottom: The same graph after performing fits in muon efficiencies. The minipanel in each figure shows the ratio of the data to the MC efficiencies with black points.

compatible with the shapes expected from a heavy ion collision to suppress non-collision events. To suppress inclusive hadronic interactions, the recorded energy of each HF tower must be lower than the noise thresholds in HF. Therefore, the energy of the leading tower in energy is required to be below $4\,\mathrm{GeV}$ in both the plus and minus ends. The leading tower energy distributions in HF can be seen in figure 5.5, where the signal (red histogram) and $\gamma\gamma \to c\bar{c}$ (green histogram) background MC samples are superimposed. For this plot, all signal selections discussed later are applied, except for the HF requirement.

The τ lepton has a mean lifetime of 3×10^{-13} seconds, which means it would decay before reaching the first CMS tracking layer. Its decay products and their respective branching ratios are listed in reference [104]. In the first analysis, the electron decay mode was not examined, due to the challenges involved in the reconstruction of low-p_T electrons, especially electrons with
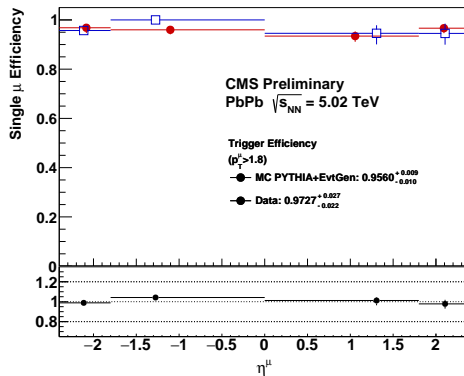
Figure 5.3: Muon trigger efficiency in data (blue) and MC (red) as a function of muon η for muons with $p_T > 1.8\,\mathrm{GeV}$.

Figure 5.4: Muon trigger efficiency versus muon p_T for the most central and the most forward of the three rapidity regions in which SFs are calculated with nominal and alternative selections. The minipanel in each figure shows the ratio of nominal efficiencies to the efficiencies obtained with alternative selections.
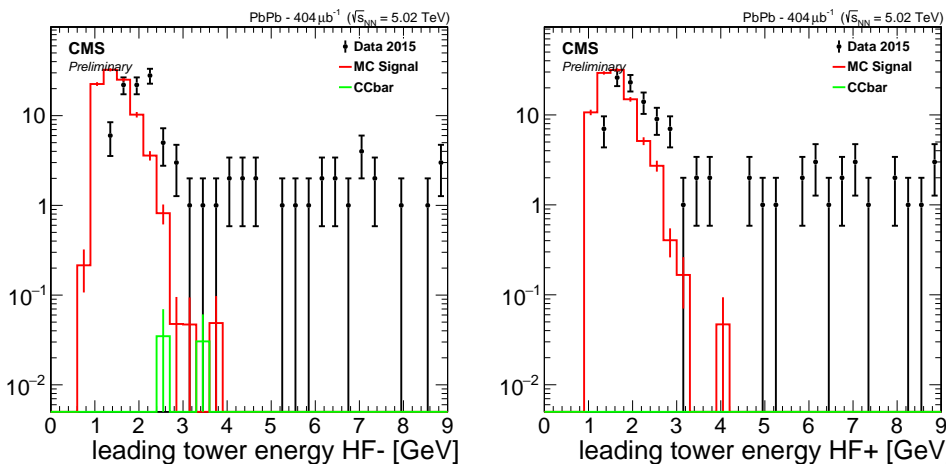
Figure 5.5: Leading tower energy in minus (left) and plus (right) HF. The $\gamma\gamma \to c\bar{c}$ MC sample is superimposed for reference. The MC simulated samples are normalized to the luminosity of data.

$p_T < 5\,\text{GeV}$. The decay into a muon and neutrinos is experimentally easier to study, as muons from the process are expected to pass through all tracker detector layers, leaving clusters in the muon spectrometer, facilitating their efficient and background-free identification. However, this decay channel is only required for one of the τ leptons in the events as having two muons and four neutrinos resembles the $\text{PbPb} \to \text{Pb}(\gamma\gamma \to \mu^+\mu^-)\text{Pb}$ process which has been extensively studied in the past [105], and is considered as a background process for the $\text{PbPb} \to \text{Pb}(\gamma\gamma \to \tau^+\tau^-)\text{Pb}$ process. As a result, the decay channel with two muons is expected to have a low sensitivity. Therefore, one has to look for the 1-prong or 3-prong decays of the second τ lepton. The 1-prong decays have a total branching ratio of 49.46% while the 3-prong decays have a total of 14.57%. Even though the 1-prong decays have a higher yield, this decay is prone to having many backgrounds, as any track can be a 1-prong tau candidate, while the 3-prong decay is almost background-free, thus providing a higher sensitivity.

As the two τ leptons are reconstructed in the 3-prong and muonic final states, only events with exactly three charged pion candidates and exactly one muon candidate are considered. The efficiency of selecting exactly three charged pions is 93% for pions satisfying the detector acceptance. The distribution of the number of charged pion candidates (N_{ch}) is shown in figure 5.6. For this plot, all analysis selections except the number of charged pions are applied.

The muon from the tau decay is referred to as the visible part of the muonic tau, τ_μ. Its
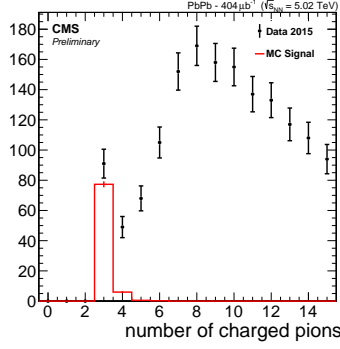
Figure 5.6: Number of charged pion candidates per event for data compared to a MC simulation of the signal process reconstructed with a simulation of CMS detector material and response.

pseudorapidity is required to be $|\eta| < 2.4$. The reconstruction quality tag of the muon is required to be *soft*, as described in reference [106]. The requirement for the transverse momentum of the muon varies, depending on its $|\eta|$, and is $p_{\mathrm{T}} > 3.5$ GeV for $|\eta| < 1.2$ and $p_{\mathrm{T}} > 2.5$ for $|\eta| \geq 1.2$ because muons with less curvature can still reach this region of the muon detectors. This selection is based on the acceptance and efficiency performance of soft muons shown in figure 5.7 and the increase in signal sensitivity as deduced from the left plot of figure 5.8. The misidentification efficiency ("fake rate") of a hadron misidentified as a prompt muon is expected to be at the 0.2–0.5% level depending on the hadron species [106], hence the impact on the analysis is not significant.

Kinematic distributions of the selected muons (p_{T}, η, ϕ) are shown in figure 5.8 for data (black) compared to the MC simulation of the signal (red) stacked on a data-driven background estimate described in section 5.2 (green). The MC simulation of the signal is corrected with identification (ID), standalone identification in muon chambers, and inner tracking SFs of the muon as a function of muon p_{T} and η. In contrast to the inner tracking SFs, a slight dependency of $\approx 2\%$ is seen for the ID SFs (figure 5.9) evaluated by fitting the SFs to a first-order polynomial. The effect of the SF application is shown in figure 5.10.
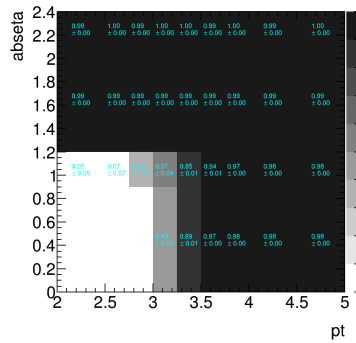
Figure 5.7: Reconstruction efficiency for muons satisfying the soft ID requirements.

The candidate vertex with the largest sum over the p_{T}^2 of its assigned physics objects is taken to be the primary interaction vertex. The tracks to form the $\tau_{3\mathrm{prong}}$ are required to be within the acceptance of the tracker system ($|\eta| < 2.5$) and to be close to the primary vertex of the events ($\Delta z < 0.25$ cm). Tracks are considered only if they are identified as charged pions by the PF algorithm described in chapter 4. Each track must have a minimum of three hits in the tracker system with normalized $\chi^2 < 100$. The transverse momentum of the pion track is required to be above 0.5 GeV for the leading and above 0.3 GeV for the two subleading ones after
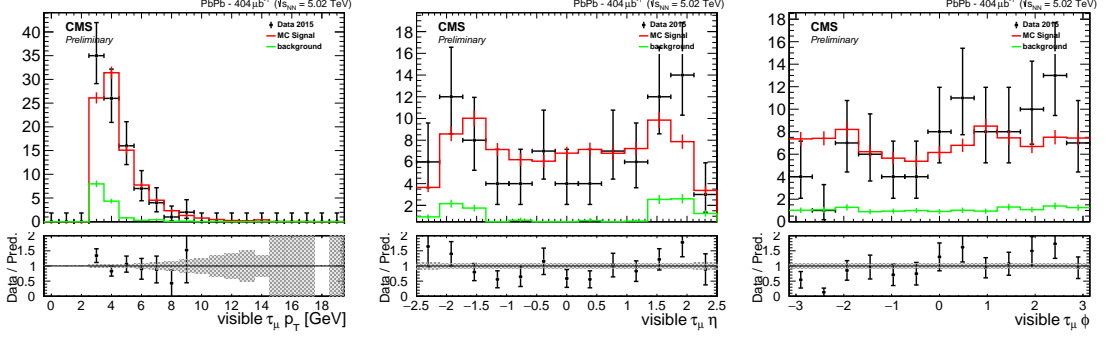
Figure 5.8: Kinematic distributions for muon from the τ lepton decay. The distribution in data (black) is compared to the MC simulation of the signal (red) stacked on a data-driven background estimate described in section 5.2 (green).
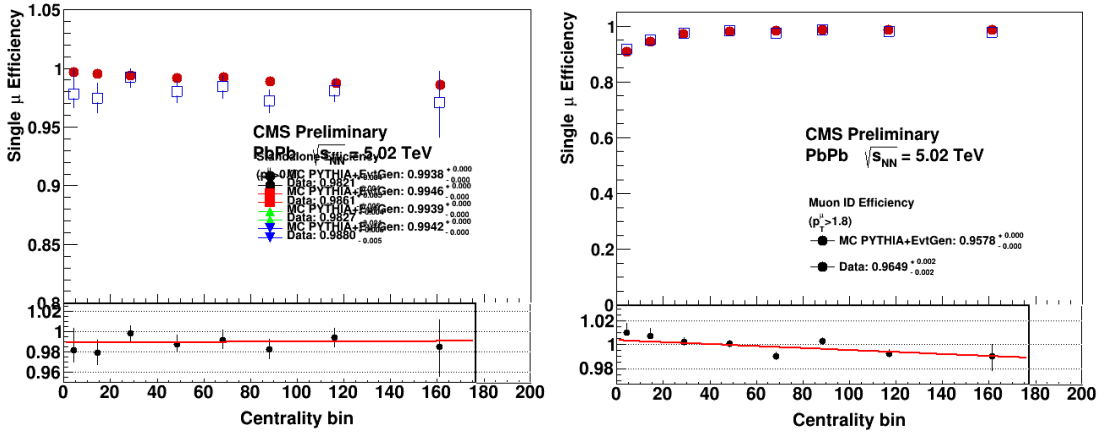
Figure 5.9: Centrality dependence of the muon inner tracking (left) and *hybrid* soft ID (right) SFs. The SFs are fit to a first order polynomial.

ordering in p_T. The selected tracks are also required to be identified as *high purity* [107] tracks. These requirements ensure high quality of tracks and the rejection of background processes. This is shown in figure 5.11, where the pion kinematic distributions from data are compared with the signal MC distributions stacked on the data-driven background estimates. The tracking reconstruction efficiency as a function of p_T and η and the comparison between the generated and reconstructed pion p_T are shown in figure 5.12. The MC simulation of the signal is corrected by tracking SFs as a function of pion p_T and η.

The selected tracks are grouped to form the $\tau_{3\mathrm{prong}}$ candidate. The three-track system is required to have opposite charge with respect to the selected muon and have a $p_T^{\mathrm{vis}} > 2\,\mathrm{GeV}$, where p_T^{vis} is the vector sum of the p_T of the three charged pions. The vertex probability of the three tracks is required to be greater than 0.5%. In addition, the visible invariant mass is required to be $m_{\tau_{3\mathrm{prong}}}^{\mathrm{vis}} < 1.5\,\mathrm{GeV}$. The kinematic comparison between data and MC of the reconstructed $\tau_{3\mathrm{prong}}$ is shown in figure 5.13. Further comparisons between data and predictions from signal MC and the data-driven background for the di-τ candidate and combinations of the τ muon and pions from the $\tau_{3\mathrm{prong}}$ candidate are shown in figures 5.14–5.16. All signal selections are summarized in table 5.1.

45
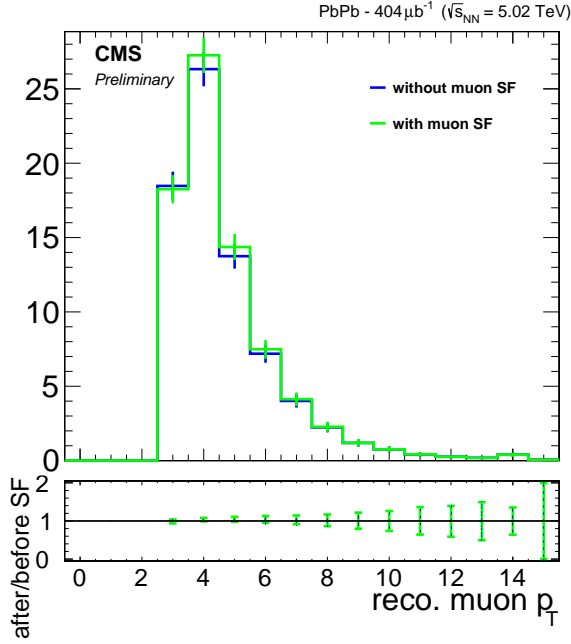
Figure 5.10: Comparison of the muon p_T distribution from signal MC before (blue) and after (green) applying the muon SFs.

Table 5.1: A summary of signal selection requirements.

Event level	trigger - `HLT_HIUPCSingleMuNotHF2Pixel_SingleTrack`
	HF tower less than $4\,\mathrm{GeV}$
	3 charged tracks and 1 muon reconstructed
For the μ	$p_T > 3.5\,\mathrm{GeV}$ for $|\eta| < 1.2$
	$p_T > 2.5\,\mathrm{GeV}$ for $1.2 < |\eta| < 2.4$
	soft muon ID
For the pions	$p_T^{\mathrm{leading}} > 0.5\,\mathrm{GeV}$ & $p_T^{\mathrm{subleading}} > 0.3\,\mathrm{GeV}$ for the (sub-)subleading
	$|\eta| < 2.5$
	PF with $\pi^{\pm}$ pdg id
	3 tracker hits with normalized χ^2 less than 100
For the $\tau_{3\mathrm{prong}}$	$p_T^{\mathrm{vis}} > 2\,\mathrm{GeV}$ and $m_\tau^{\mathrm{vis}} < 1.5\,\mathrm{GeV}$
	$\Delta z(\tau, \mathrm{PV}) < 2.5$ mm
	vertex probability $> 0.5\%$
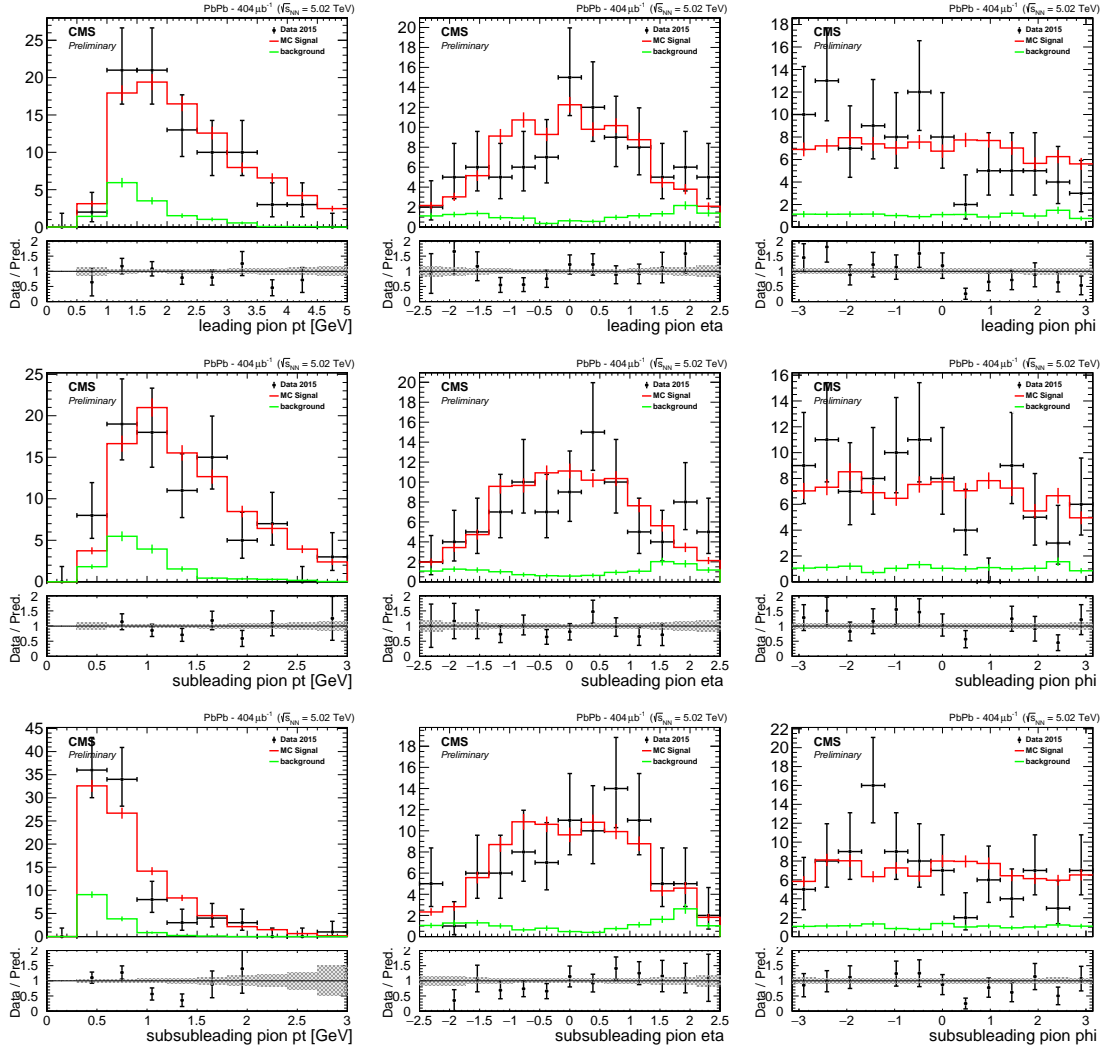
Figure 5.11: Kinematic distributions for leading- (top), subleading- (middle), and subsubleading-p_{T} (bottom) pions. The distribution in data (black) is compared to the MC simulation of the signal (red) stacked on a data-driven background estimate described in section 5.2 (green).
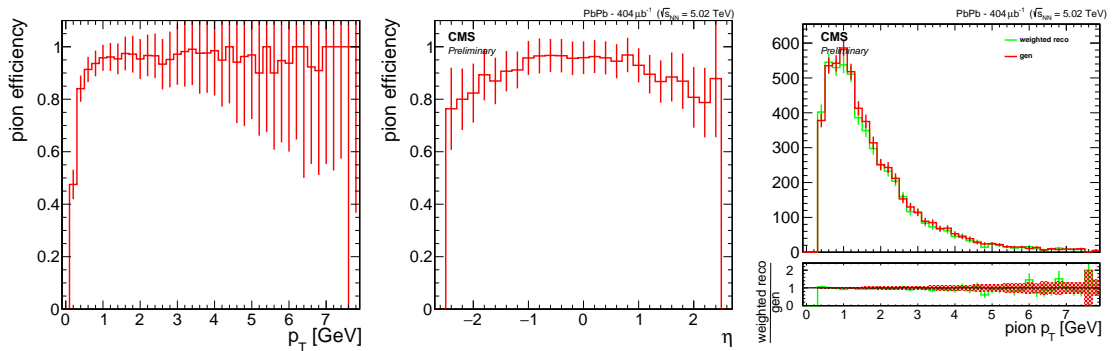
Figure 5.12: Tracking reconstruction efficiency as a function of p_{T} (left) and η (middle), determined from the signal MC. On the right, the comparison between generated (red) and reconstructed (green) pion p_{T} weighted with 1/efficiency is shown.
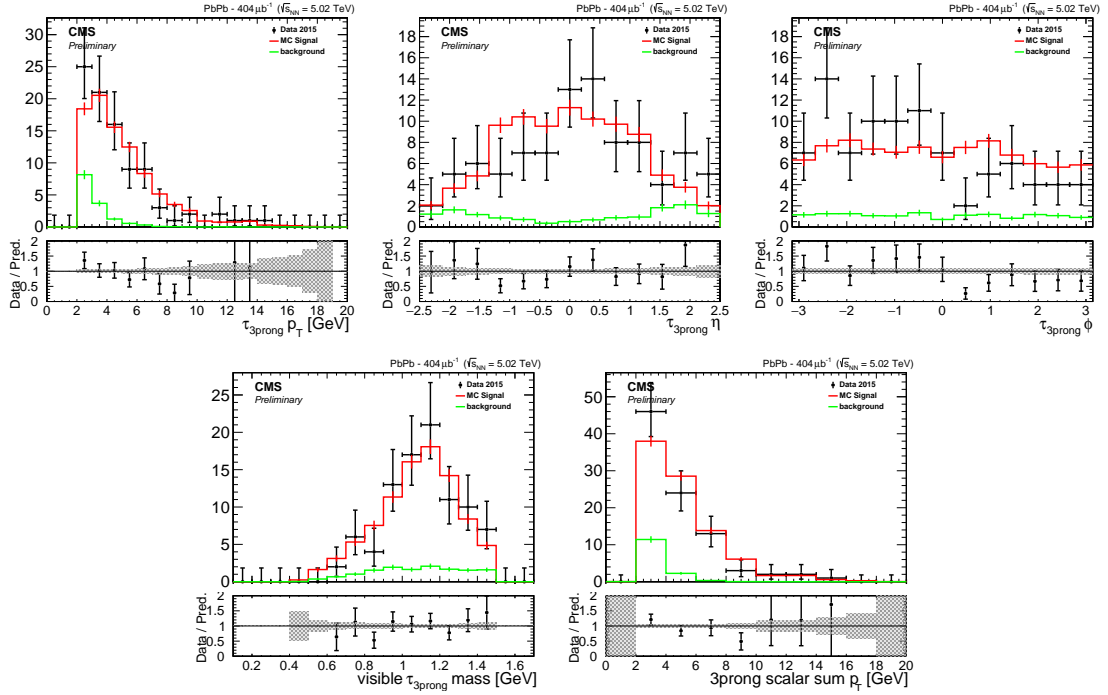
Figure 5.13: Kinematic distributions of the $\tau_{3\mathrm{prong}}$ (top), with the $\tau_{3\mathrm{prong}}$ scalar p_{T} sum and its invariant mass being displayed at the bottom. The distribution in data (black) is compared to the MC simulation of the signal (red) stacked on a data-driven background estimate described in section 5.2 (green).
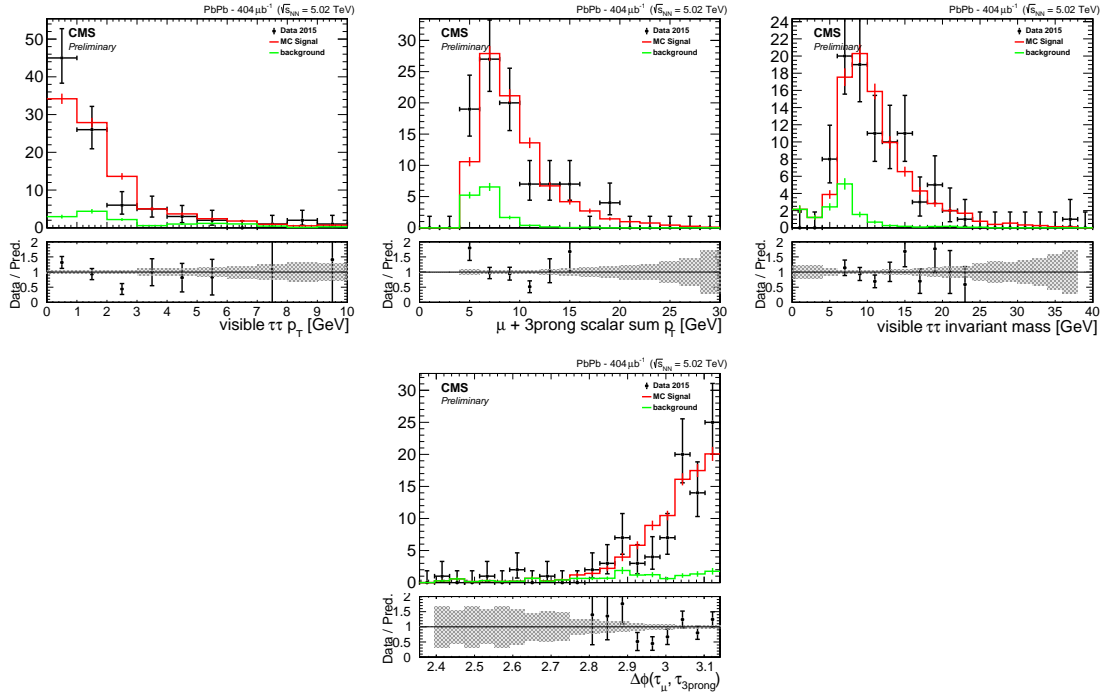
Figure 5.14: Distributions of the visible di-τ system: its vector p_{T} sum (top left), scalar p_{T} sum (top middle), invariant mass (top right), and difference in opening azimuthal angle between the τ_{μ} and $\tau_{3\mathrm{prong}}$ leptons, $\Delta\phi(\tau_{\mu}, \tau_{3\mathrm{prong}})$ (bottom). The distribution in data (black) is compared to the MC simulation of the signal (red) stacked on a data-driven background estimate described in section 5.2 (green).
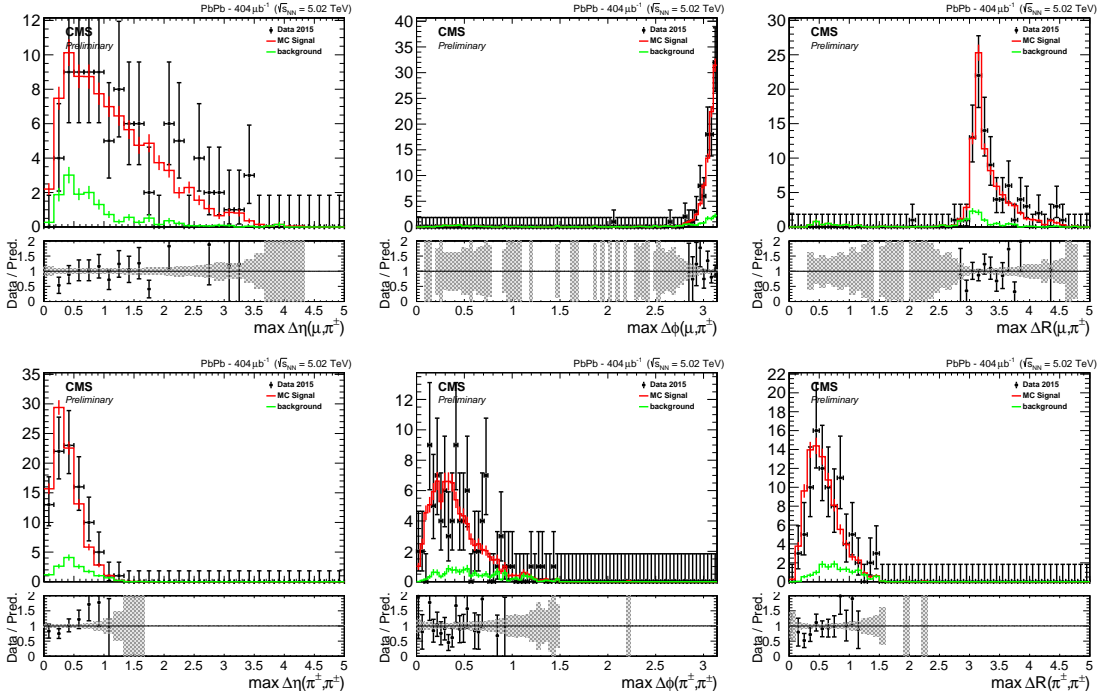
Figure 5.15: Kinematic distributions for the maximum difference in η (left), ϕ (middle), and $R = \sqrt{\eta^2 + \phi^2}$ (right) between the τ muon and pions from the $\tau_{3\mathrm{prong}}$ candidate (top) and between pions from the $\tau_{3\mathrm{prong}}$ candidate (bottom). The background is determined using control phase space regions in data (see section 5.2).
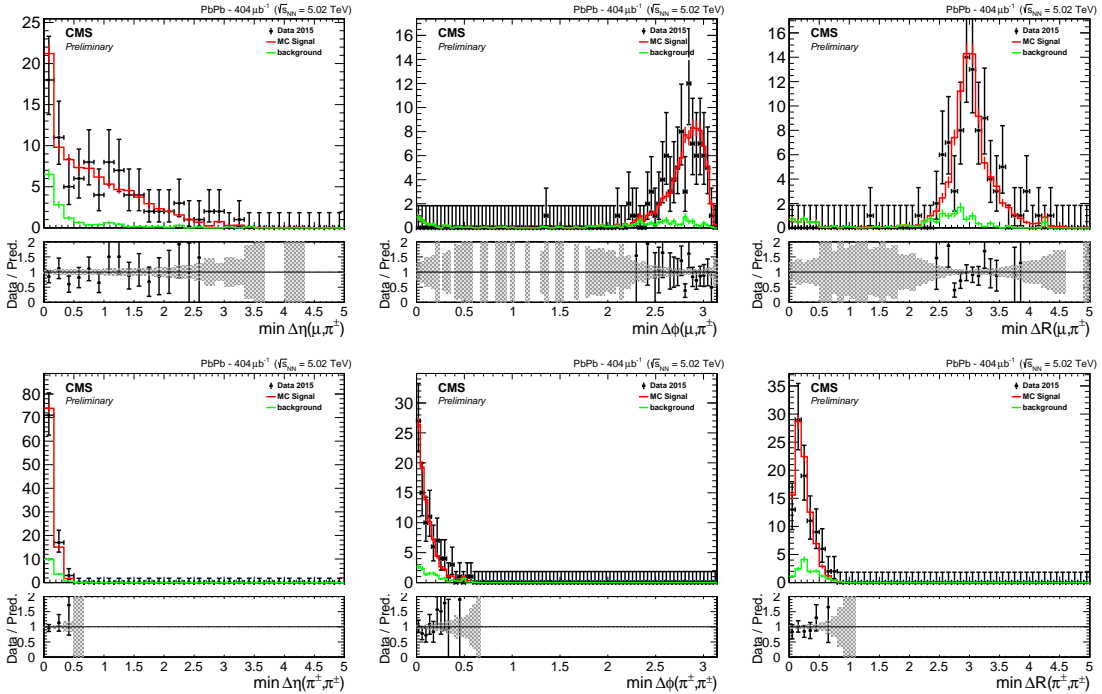
Figure 5.16: Kinematic distributions for the minimum difference in η (left), ϕ (middle), and $R = \sqrt{\eta^2 + \phi^2}$ (right) between the τ muon and pions from the $\tau_{3\mathrm{prong}}$ candidate (top) and between pions from the $\tau_{3\mathrm{prong}}$ candidate (bottom). The distribution in data (black) is compared to the MC simulation of the signal (red) stacked on a data-driven background estimate described in section 5.2 (green).

5.2 Background estimation

Background contamination is estimated in a data-driven way, using an *ABCD method* in which four phase-space regions (*categories*) are split based on their expected signal and background contamination. In our case, we make use of the number of charged pion candidates per event (N_{ch}, see figure 5.6) and the HF activity. Specifically, the ABCD categories are defined as

- A: high-N_{ch} and high-HF
- B: low-N_{ch} and high-HF
- C: high-N_{ch} and low-HF
- D: low-N_{ch} and low-HF.

The low-N_{ch} region is $N_{\text{ch}} = 3$ whereas for the high region $5 \leq N_{\text{ch}} \leq 8$. For HF, the low and high regions correspond to the leading tower energy being below and above $4\,\text{GeV}$, respectively. Consequently, region D is the signal region, and the background distribution in D is estimated by the formula B $\times$ C/A, while multiplication and division are performed bin by bin for each kinematic distribution. The $\Delta\phi(\tau_\mu, \tau_{\text{3prong}})$ distributions for all regions are shown in figure 5.17. The background MC samples are associated with a high number of track multiplicity, and hence we find no events remaining after applying the selection criteria in the signal-dominated category. For reference and as a closure test, they are displayed in the background-dominated categories.
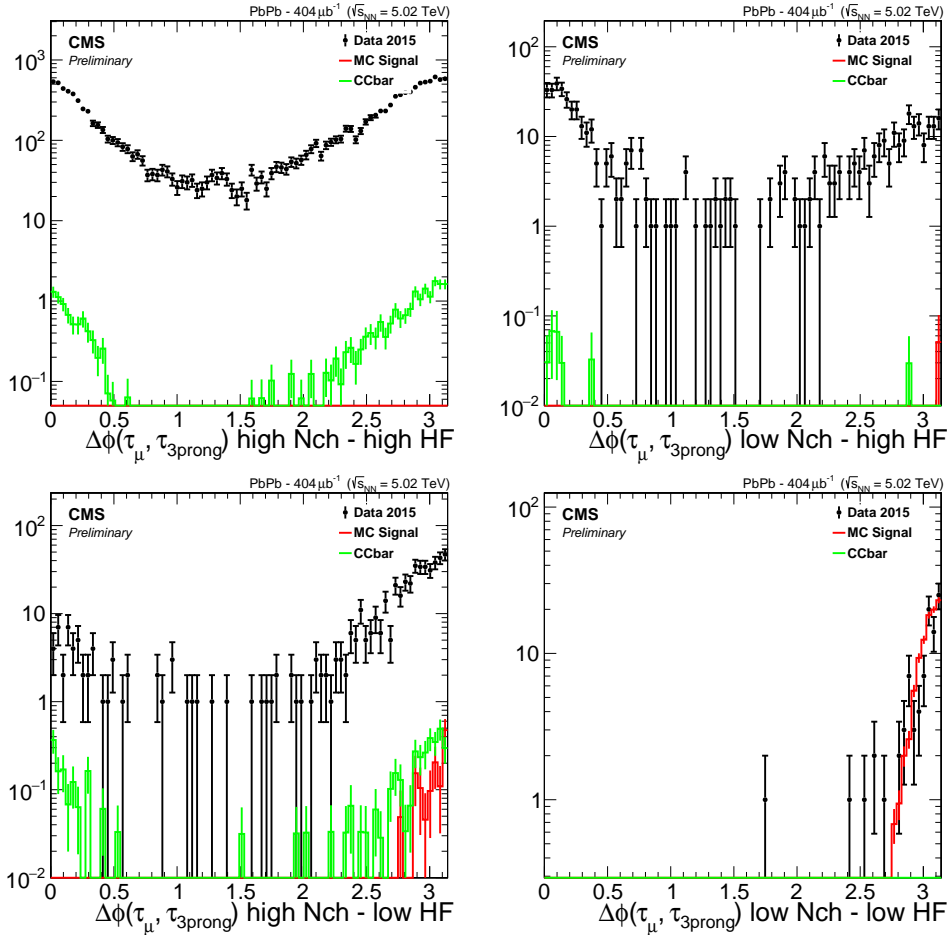
Figure 5.17: The four regions of the ABCD method. Top left (A), top right (B), bottom left (C) and bottom right (D). The region D is the signal region.

To validate the assumed linearity in the ABCD method, the control region A with the highest statistics is divided into 4 subcategories. These are defined by applying the selections on N_{ch} to be $5 \leq N_{ch} \leq 6$ and $7 \leq N_{ch} \leq 8$ and on the HF leading tower, $4 \leq HF_{leading} \leq 20 \, GeV$ and $HF_{leading} > 20 \, GeV$. The distributions of $\Delta\phi(\tau_\mu, \tau_{3prong})$ corresponding to 4 subcategories are shown in figure 5.18 (left). To validate the linearity between regions, for each N_{ch} subcategory, the distribution with $4 \leq HF_{leading} \leq 20 \, GeV$ is divided by the corresponding distribution with $HF_{leading} > 20 \, GeV$. As seen in figure 5.18 (right), the two resulting distributions match well, which confirms the linearity between regions.
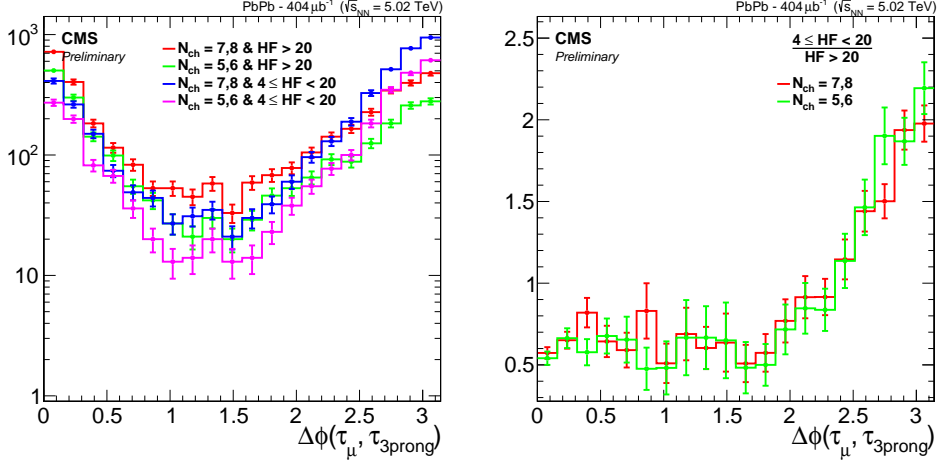
Figure 5.18: The "A" category of the ABCD method divided into 4 subcategories (left). The linearity between the regions in the ABCD method is validated (right).

5.3 Signal yield extraction

To compare the compatibility of the data with the background-only and signal plus background hypotheses, where the signal is allowed to be scaled by some factor r, we construct the test statistic $\tilde{q}_r$ [108] based on the profile likelihood ratio:

$$q_0 = -2 \ln \frac{\mathcal{L}(\text{data}|r, \hat{\theta}_r)}{\mathcal{L}(\text{data}|\hat{r}, \hat{\theta})}, \qquad \text{with a constraint, } 0 \leq \hat{r} \leq r, \qquad (5.1)$$

where $\hat{\theta}_r$ refers to the conditional maximum likelihood estimators of θ given the signal strength parameter r, and "data" which refers to the actual experimental observation. The pair of parameter estimators $\hat{r}$ and $\hat{\theta}$ correspond to the global maximum of the likelihood.

The lower constraint $0 \leq \hat{r}$ is dictated by physics, as the signal rate is nonnegative, while the upper constraint $\hat{r} \leq r$ is imposed by hand to guarantee a one-sided confidence interval. Physics-wise, this means that upward fluctuations of the data with $\hat{r} > r$ are not considered as evidence against the signal hypothesis, but rather that the signal strength is r.

The pre-fit distributions of the variable that the fit is performed on is shown in figure 5.19. The background distribution has 14.3 events, and the signal distribution contains 77 events. The *Higgs combine* [109] tool is used for the fit.

The best-fit value of the signal strength is obtained by minimizing the negative likelihood, which results in $r = 0.993^{+0.163}_{-0.143}$ and corresponds to $N^{\tau\tau}_{sig} = 77 \pm 12$ signal events, and 14.1 background events. The post-fit $\Delta\phi(\tau_\mu, \tau_{3prong})$ distribution is shown in figure 5.20 (left), whereas the post-fit impact on the background $\Delta\phi(\tau_\mu, \tau_{3prong})$ template from the considered
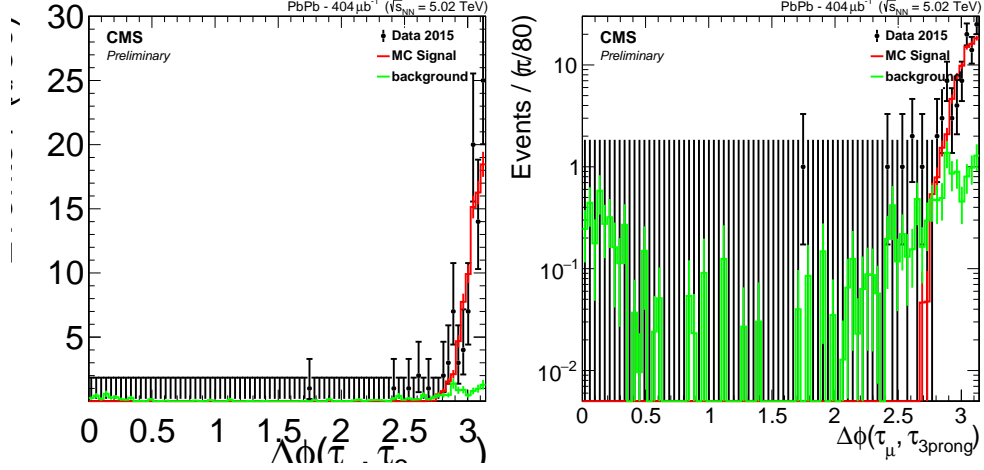
Figure 5.19: Pre-fit distribution of $\Delta\phi(\tau_\mu, \tau_{3prong})$ variable in linear (left) and log-Y scale (right). Data are displayed with black points, while signal MC with red line and background with green.

sources of systematic uncertainty described in section 5.4 is shown in figure 5.20 (right). The summary of the impacts and pulls of the most significant nuisance parameters is shown in figure 5.21. The left panel shows the post-fit pull (value and uncertainty) of each nuisance parameter, meaning what fraction of its uncertainty it is pulled away from the nominal, assumed value of the parameter, while the right panel displays the estimated impact on the signal strength of the fit, meaning the change in the signal strength parameter that would be expected for a 1-sigma variation of the nuisance parameter. Only the thirty most dominant nuisance parameters are displayed, with their name shown in each row of the plots.
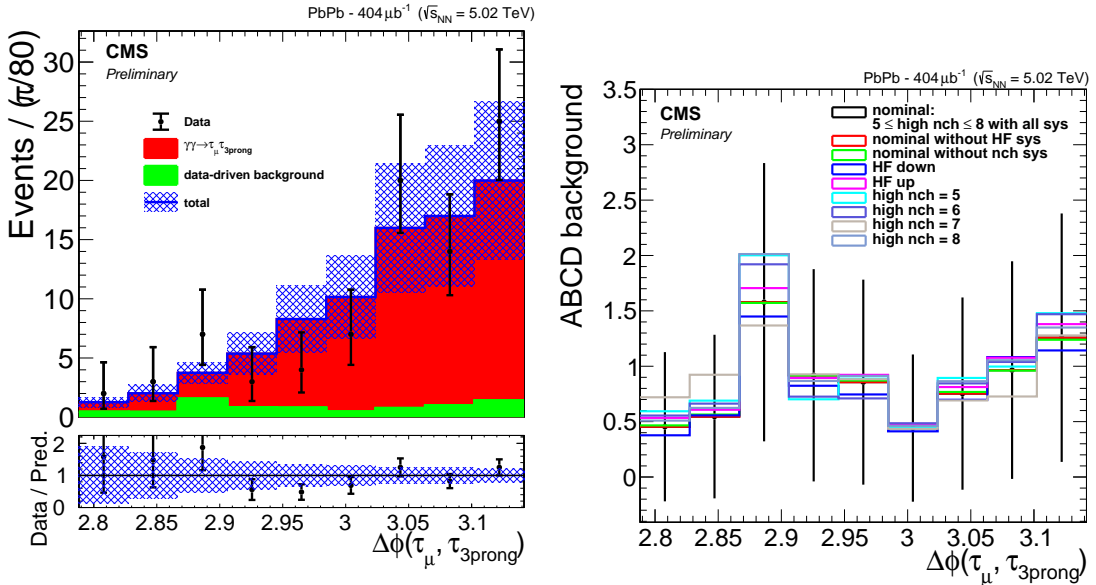
Figure 5.20: Left: Difference in opening azimuthal angle between the τ_μ and τ_{3prong} leptons. The data are represented by the points with the vertical bars showing the statistical uncertainties. The solid red histogram shows the signal contribution, which is stacked on the green background. The total is displayed by a blue line and the shaded area shows its uncertainty. Right: The post-fit impact on the background $\Delta\phi(\tau_\mu, \tau_{3prong})$ template from the considered sources of systematic uncertainty.

The Kolmogorov-Smirnov test, applied to the data and the signal plus background shapes
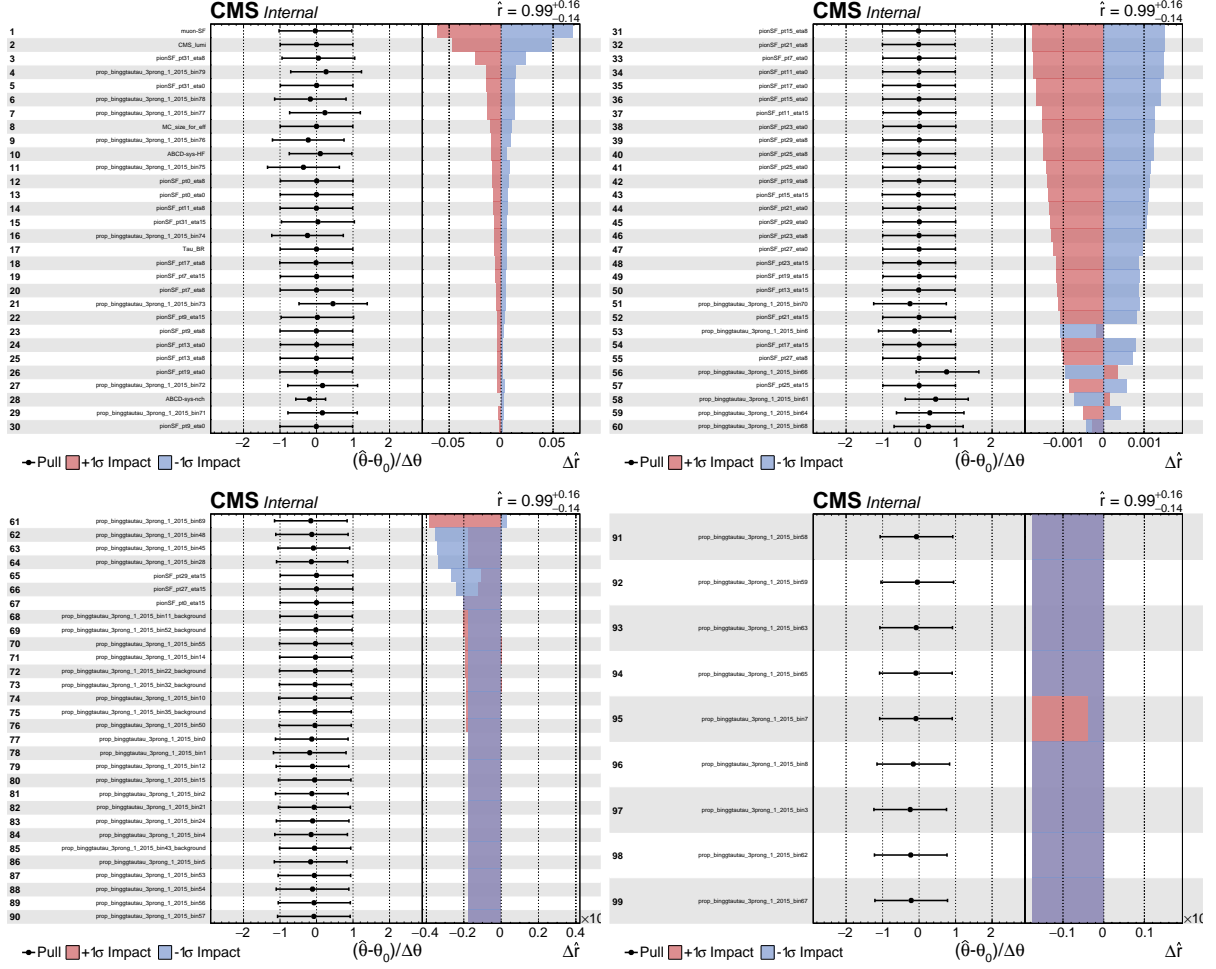
Figure 5.21: Left: Post-fit pull (value and uncertainty) of each nuisance parameter considered in the fit. Right: the estimated impact on the fit for the signal strength.

after the fit application, returns the value of 0.91. The bias of the result is checked with a pull study, shown in figure 5.22. The Gaussian fit to the calculated pulls results in a mean bias of $\mu = -0.05 \pm 0.01$, with a standard deviation of $\sigma = 0.95 \pm 0.01$, which shows an unbiased signal extraction.

The presence of the signal is quantified by the background-only p-value, i.e. the probability for the background to fluctuate and give an excess of events as large or larger than the observed one. This requires the definition of a test statistic and the construction of its sampling distribution. The test statistic used is $q0$, where

$$q_0 = -2 \ln \frac{\mathcal{L}(\text{data}|0, \hat{\theta}_0)}{\mathcal{L}(\text{data}|\hat{r}, \hat{\theta}_0)} \qquad \text{and } \hat{r} \geq 0. \tag{5.2}$$

The constraint $\hat{r} \geq 0$ gives an accumulation of the test statistic at zero for events with downward fluctuations, since we are not interested in interpreting a deficit of events with respect to the expected background as being on an equal footing as that of an excess. Following the frequentist convention for treatment of nuisance parameters, we then build the distribution $f(q_0|0, \hat{\theta}_0^{\text{obs}})$ by generating pseudo-data for nuisance parameters around $\hat{\theta}_0^{\text{obs}}$ using event counts following Poisson probabilities under the assumption of the background-only hypotheses. From such a distribution, one can evaluate the p-value corresponding to a given experimental observation q_0^{obs} as follows:
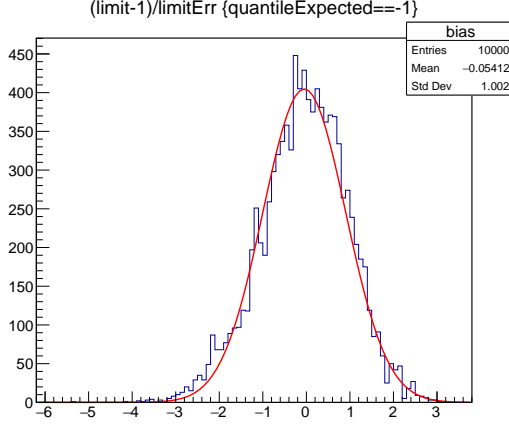
Figure 5.22: Bias study of signal extraction procedure, studying pulls. The result of the toys are shown with the blue histogram. The fitted Gaussian function shows an unbiased procedure.

$$p_0 = P(q_0 \geq q_0^{\text{obs}}) = \int_{q_0^{\text{obs}}}^{\infty} f(q_0|0, \hat{\theta}_0^{\text{obs}}) dq_0. \qquad (5.3)$$

To convert the p-value into a significance Z, we adopt the convention of a *one-sided Gaussian tail*

$$p = \int_{Z}^{\infty} \frac{1}{\sqrt{2\pi}} \exp(-x^2/2) dx = \frac{1}{2} P_{\chi_1^2}(Z^2), \qquad (5.4)$$

where $P_{\chi_1^2}$ stands for the survival function of a χ^2 with one degree of freedom. The 5σ significance $(Z = 5)$ would correspond in this case to $p_b = 2.8 \times 10^{-7}$. The significance of the observation of the PbPb $\to$ Pb$(\gamma\gamma \to \tau^+\tau^-)$Pb process in this analysis is $14.2\,\sigma$ while a significance of $14.5\,\sigma$ was expected. Figure 5.23 shows $-2\Delta \ln \mathcal{L}$ as a function of the signal strength r. The signal strength values with $-2\Delta \ln \mathcal{L}$ of 1 and 4 correspond to confidence level ranges of 63% and 95%, respectively.
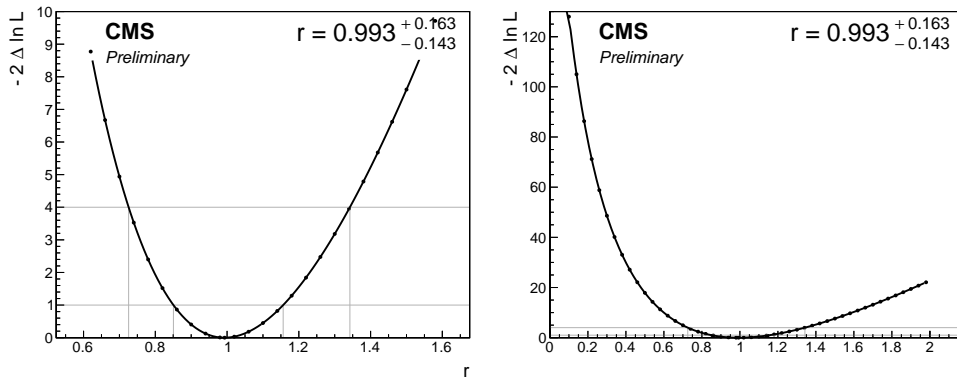
Figure 5.23: Likelihood ratio zoomed (left) and full range (right).

5.4 Systematic uncertainties

The HF requirement of 4 GeV is used both for the selection of signal and for the estimation of the ABCD background. An uncertainty of 10% [110] is assigned to the HF scale, which translates to a negligible effect on the number of signal events, but a change in the ABCD background

shape and normalization factor that changes the signal estimation by 0.9%. An additional systematic uncertainty coming from the background shape and yield estimation is considered by reevaluating the background using the ABCD procedure, but changing the high N_{ch} parameter to 5, 6, 7 and 8 separately. The maximum variation with respect to the central value comes from $N_{\text{ch}} = 5$, resulting in a 0.2% variation on the fiducial cross section measurement which will be described in section 5.5.

The uncertainty in the measurements of the τ lepton branching fraction results in a 0.6% [104] change in the signal cross section. The uncertainty in the muon reconstruction scale factors including the trigger response, identification, and tracking efficiency has an impact of 6.7%. The uncertainties in the pion tracking SF are taken into account independently per each p_{T} and η bin, with a total impact of 3.6%. The uncertainty in the integrated luminosity is 5.0% [111] and directly affects the normalization of simulated signal process. Finally, the uncertainty coming from the limited MC sample size affects the signal efficiency by 1.1%, calculated as a weighted binomial uncertainty, and by 3% for the statistical bin-by-bin variations of the templates. The uncertainties described above are summarized in table 5.2. The total is their sum in quadrature, taking into account their correlation, and is found to be 9.7%.

Table 5.2: Postfit contributions to the systematic uncertainty of the $\sigma(\gamma\gamma \to \tau^+\tau^-)$ measurement, in percent. The last row gives the sum in quadrature of all components.

Source	Relative uncertainty (%)
Muon SF	6.7
Luminosity measurement	5.0
pion SF	3.6
MC sample size (bin by bin)	3.0
MC sample size (efficiency)	1.1
HF scale effect on background shape	0.9
τ lepton branching fraction measurement	0.6
Effect of chosen N_{ch} on background shape	0.2
Total	9.7

5.5 Cross section

The cross section is measured in the fiducial volume of the CMS detector, following its geometric acceptance, which is summarized in table 5.3. The formula used to calculate the cross section is $\sigma(\gamma\gamma \to \tau^+\tau^-) = N_{\text{sig}}^{\tau\tau}/(2\epsilon\,\mathcal{L}_{\text{int}}\,\mathcal{B}_{\tau_\mu}\,\mathcal{B}_{\tau_{3\text{prong}}})$, where $N_{\text{sig}}^{\tau\tau}$ is the number of signal events, ϵ is the total analysis efficiency, $\mathcal{L}_{\text{int}}$ is the total luminosity, $\mathcal{B}_{\tau_\mu}$ is the branching ratio of muonic tau decay, and $\mathcal{B}_{\tau_{3\text{prong}}}$ is the branching ratio of 3-prong tau decay. The factor of two is used to account for the two combinations of tau lepton decays that result in the considered final state.

$N_{\text{sig}}^{\tau\tau}$ is the signal yield that is measured by the number of events that pass the analysis cuts as described in section 5.1, after subtracting the estimated background described in section 5.2. The integrated luminosity corresponds to $\mathcal{L}_{\text{int}} = 404\ \mu\text{b}^{-1}$. The branching fractions are taken from the PDG [104] and are equal to $\mathcal{B}_{\tau_\mu} = 17.39\%$ and $\mathcal{B}_{\tau_{3\text{prong}}} = 14.55\%$.

The efficiency is the convolution of the pion and muon reconstruction efficiencies, the trigger efficiency, and the analysis selection efficiency. The efficiency is estimated using a simulated MC

Table 5.3: Definition of the fiducial phase space for the $\sigma(\gamma\gamma \to \tau^+\tau^-)$ measurement.

For the μ	$p_T > 3.5\,\text{GeV}$ for $|\eta| < 1.2$
	$p_T > 2.5\,\text{GeV}$ for $1.2 < |\eta| < 2.4$
For the pions	$p_T^{\text{leading}} > 0.5\,\text{GeV}$ & $p_T^{\text{subleading}} > 0.3\,\text{GeV}$ for the (sub-)subleading
	$|\eta| < 2.5$
For the $\tau_{3\text{prong}}$	$p_T^{\text{vis}} > 2\,\text{GeV}$ and $m_\tau^{\text{vis}} < 1.5\,\text{GeV}$

signal sample, by calculating the ratio of reconstructed events that pass the selection analysis criteria to the number of generated events that pass the fiducial cuts described in table 5.3. It is found to be $\epsilon = 78.55\%$.

The fiducial cross section is then fit and found to be $\sigma(\gamma\gamma \to \tau^+\tau^-) = 4.8 \pm 0.6\,(\text{stat}) \pm 0.5\,(\text{syst})\,\mu\text{b}$. This result, summarized in figure 5.24, is compared to the leading-order QED predictions [67, 112]. Given that reference [112] provides an analytical description and not a generator-level sample on which to apply the analysis selections, we obtain its central value by applying a scaling factor of 20% to account for the systematically higher cross section compared to the calculations derived from reference [67]. In both cases, a theoretical uncertainty of 10% is considered [113].
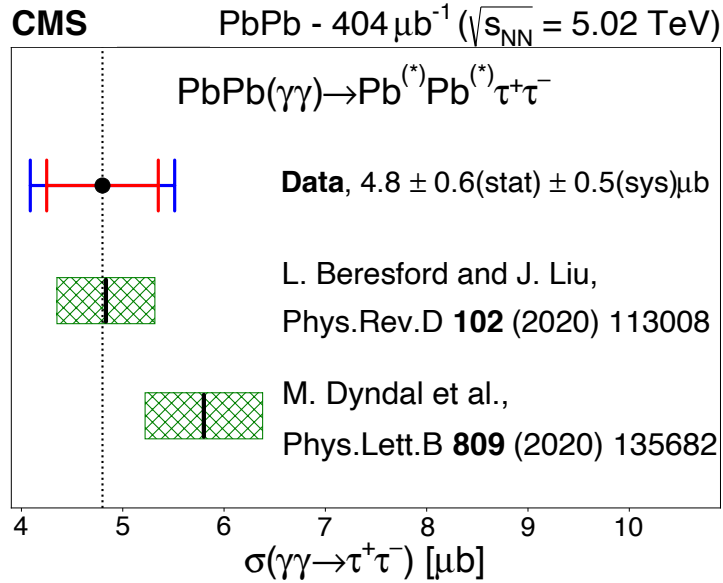
Figure 5.24: The cross section measured in a fiducial phase space region at $\sqrt{s_{\text{NN}}} = 5.02\,\text{TeV}$. The theoretical predictions are computed with leading-order accuracy in QED [67, 112].

5.6 Limits on anomalous magnetic moment

Assuming that the factors applied to extrapolate the fiducial cross section measurement from the phase space defined in table 5.3 to the full phase space are linear, we can translate our cross section measurement of the fiducial phase space to the inclusive phase space. Using the dependence of the BSM cross sections on a_τ as described in reference [67], we can derive limits on a_τ of $(-8.8 < a_\tau < 5.6)\times 10^{-2}$ with 68% confidence level. This is visually displayed on the left of figure 5.25. This range is in agreement with previous results from LEP experiments [62, 63, 114].

A comparison of the limits obtained from this analysis and the most tight constraint from LEP is shown on the right of figure 5.25.
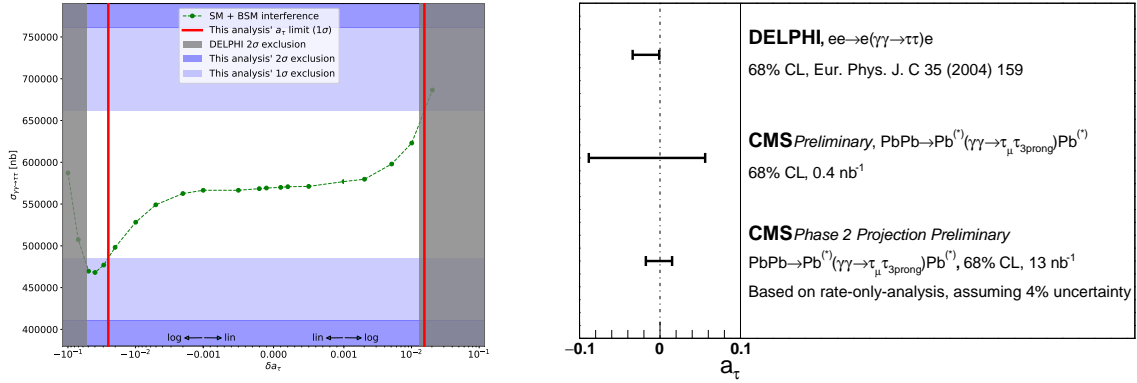
Figure 5.25: Left: Generator-level cross sections for $\gamma\gamma \rightarrow \tau\tau$ sourced by the implementation of the Pb photon flux in MadGraph, as described in Ref. [67]. This is interfaced with SMEFTsim for BSM coupling variations in $\delta\alpha_\tau$, fixing $\delta d\tau = 0$ at $\sqrt{s_{NN}} = 5.02\,\text{TeV}$. Right: Comparison of the constraints on α_τ from DELPHI and this analysis. The projected uncertainty due to expected increases in integrated luminosity is included.

6 Improved limits on a_τ using LHC PbPb collisions recorded in 2018

6.1 Introduction

In chapter 5, we reviewed an analysis to measure the anomalous magnetic moment of the tau lepton using the dataset of PbPb collision data taken during the 2015 PbPb run of the LHC. This analysis served as a stepping stone for the one discussed in this chapter, which uses the 2018 PbPb collision data of the LHC that has more than three times the luminosity and the same center-of-mass energy of $5.02\,\text{TeV}$ per nucleon. The 2015 analysis was aimed at cleanest decay channel referred to as μ+3prong of two tau leptons, having one muon on one side and three charged pions on the other. The ongoing analysis of the 2018 dataset targets additional channels of μ+1prong, e+3prong, and μ+e.

Figure 6.1 reviews the branching ratios (BR) of a single tau lepton and a pair of tau leptons. As mentioned in chapter 5, the μ+3prong channel is the cleanest channel since the identification of a muon in CMS is based on a clean signature, and the background processes resembling a three-prong decay of a tau lepton are suppressed. The μ+1prong channel has a more than three times larger BR, and its study is crucial in the currently statistically limited measurement of a_τ. However, this channel is prone to a relatively larger contribution from background processes, which will be discussed in section 6.3. The study of the e+3prong channel is similar to that of the μ+3prong, but the expected number of signal events is lower due to the higher trigger thresholds on electrons in CMS. The μ+e channel has the lowest background contamination among all possible channels, but suffers from a low BR. While my colleagues are studying the latter two channels, I will summarize my studies on the μ+3prong and μ+1prong channels in sections 6.2 and 6.3, respectively. The event selection for these two channels is performed independently as two separate analyses.
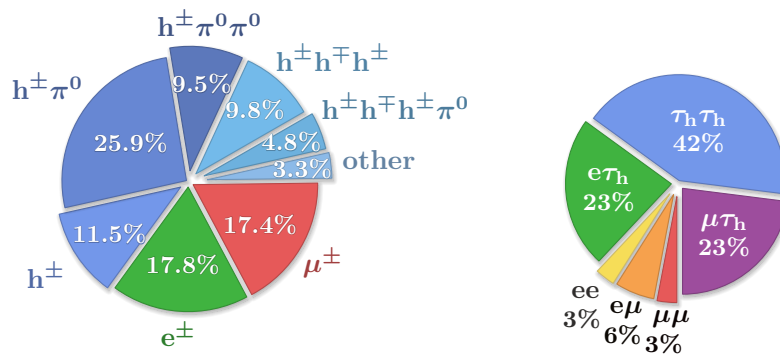
Figure 6.1: Pie charts of branching fractions. **Left**: τ lepton decay. **Right**: Decay channels of a pair of τ leptons. Numbers from PDG [13, p. 28].

For both decay channels, only a subset of the 2018 dataset corresponding to a luminosity of $425\,\mu\text{b}^{-1}$ is used, which will be referred to as *data*. This is less than one-third of the full 2018

dataset and is similar to the size of the 2015 dataset. This approach was taken to ensure the analysis selections are blinded to the full dataset, preventing biased over-tuning of the selection cuts.

The signal PbPb $\rightarrow$ Pb($\gamma\gamma \rightarrow \tau^+\tau^-$)Pb process has been simulated using multiple generators, including MADGRAPH5_aMC@NLO (v2.6.5) [101], SuperChic [115], Upcgen [116], and gamma-UPC [117]. The hadronization and decay of tau leptons are performed using the PYTHIA8 (v2.1.2) [102] generator. The resulting particles are reconstructed using CMSSW software which includes a complete simulation of the material and the electronic response of the CMS detector using GEANT4 [103]. While good agreement was observed between various generators, gamma-UPC will be used in this chapter as the default signal generator, due to the advanced treatment of the photon flux and higher order QED effects.

While the trigger and reconstruction performance of the CMS detector is simulated in the MC samples, the corresponding efficiencies are not always the same between the data and MC simulations. To correct for such mismodelings, the simulated events are weighted by a set of scale factors (SF) which generically depend on p_T and η, in the manner explained in chapter 5. The SF is defined as the ratio of efficiency in the data over that of the MC simulation. The online trigger is the same for both μ+3prong and μ+1prong channels, and its efficiency depends on the muon p_T and η. The SFs corresponding to the reconstruction of the muon tracks and the muon identification efficiency are applied to the simulated events. A SF corresponding to the reconstruction of the charged-pion tracks is also applied to the charged-pion candidates of the MC in both decay channels.

6.2 μ+3prong decay channel

6.2.1 Event selection

The analysis of this decay channel using the 2018 dataset is based on the one discussed in chapter 5 using the 2015 dataset. However, the event selection has to be readjusted. This is due to two main changes in detector performance in 2018 in tracking and calorimetry, which will be discussed in section 6.2.1.1. The full μ+3prong decay process can be written as $(\tau^-) + (\tau^+) \rightarrow (\mu^- + \nu_\tau + \overline{\nu}_\mu) + (\pi^\pm + \pi^\pm + \pi^\mp + \overline{\nu}_\tau + n\pi^0)$, with n as an arbitrary number of neutral pions. Events are selected online by requiring a muon in the muon system and an additional track in the tracker, while HF activity is allowed only on one side of HF. Offline, events are reconstructed by requiring exactly one muon and exactly three charged pions identified by the PF algorithm. The visible three-prong tau-lepton candidate is reconstructed by summing up the four-vectors corresponding to the three charged pions.

6.2.1.1 Changes with respect to the 2015 analysis

As explained in chapter 4, an additional layer was added to the CMS pixel detector in 2018, improving tracking performance and providing the possibility to reconstruct tracks with relatively lower p_T. This could translate to the addition of lower p_T pions and muons and provide higher statistics. However, the thresholds on the muon p_T as a function of η are primarily based on the geometric limits imposed by the placement of the muon system and thus are not affected by the extra layer of the pixel detector. Furthermore, since the muon and the tau lepton formed by the three charged pions are almost balanced, and the thresholds on the charged pion p_T were

already low in 2015, no significant improvement in the sensitivity of the analysis can be expected by lowering the p_T thresholds.
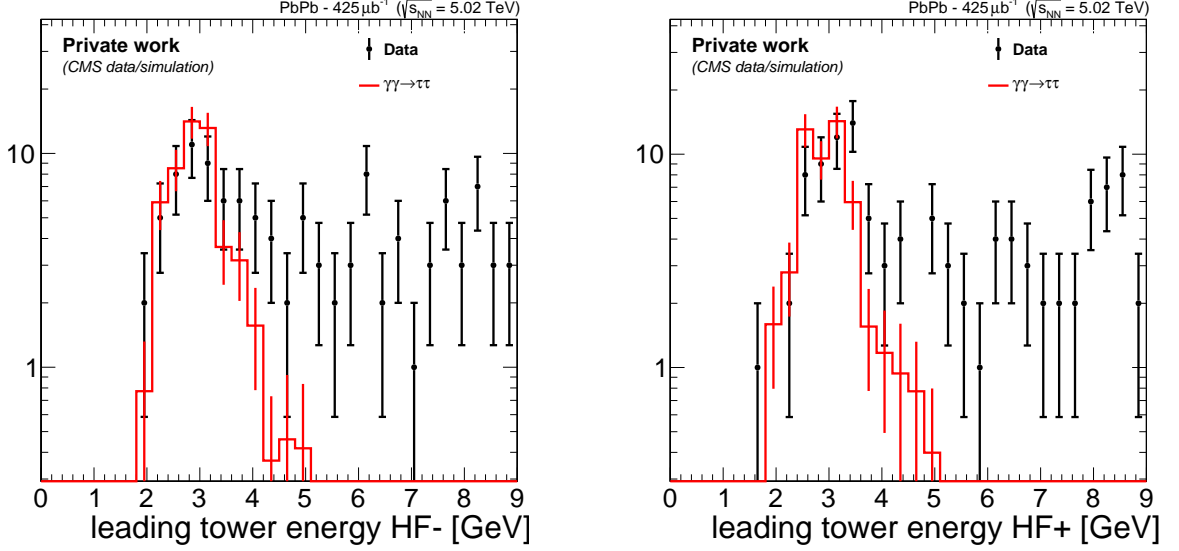
Figure 6.2: The distribution of energy of the leading-energy tower for HF− (left) and HF+ (right) detectors in the μ+3prong channel.

The major adjustment in the 2018 analysis of the μ+3prong channel is related to the HF thresholds. Due to the degradation of the calorimeters over time, the noise levels in the hadronic calorimeters and specifically the HF are higher in 2018 than in 2015. Figure 6.2 shows the distribution of the leading tower energy for two sides of the HF separately, for data and the simulated MC sample of the signal PbPb → Pb($\gamma\gamma \to \tau^+\tau^-$)Pb process after applying all signal-selection criteria except on the plotted variable. The leading tower energy is a good measure of the exclusivity of events. In ultraperipheral $\gamma\gamma \to \tau^+\tau^-$ collisions of PbPb, no extra particle is expected to be produced, and hence any activity in the HF detectors is a signature of hadronic background processes and needs to be rejected. However, due to the noise-induced activity in HF, this requirement will also remove the signal events. The HF upper threshold has to be set to a level that keeps about 99% of empty events with no collision, and is chosen to be 6 GeV for the 2018 analysis, compared to the 4 GeV threshold used in the 2015 analysis. The higher the noise level, the higher this threshold needs to be, which leads to more contamination from hadronic background events. Therefore, the contribution of hadronic background events in 2018 is expected to be higher.

6.2.2 Background modeling

The background is modeled in a similar way as in the 2015 analysis using the ABCD method with the four regions below, defined based on the energy of the leading energy HF tower ($E_{\mathrm{max}}^{\mathrm{HF}}$) and the number of charged pions (N_{ch}).

- A: $E_{\mathrm{max}}^{\mathrm{HF}} > 6\,\mathrm{GeV}$ & $N_{\mathrm{ch}} = 5, 6, 7, 8$
- B: $E_{\mathrm{max}}^{\mathrm{HF}} > 6\,\mathrm{GeV}$ & $N_{\mathrm{ch}} = 3$
- C: $E_{\mathrm{max}}^{\mathrm{HF}} < 6\,\mathrm{GeV}$ & $N_{\mathrm{ch}} = 5, 6, 7, 8$
- D: $E_{\mathrm{max}}^{\mathrm{HF}} < 6\,\mathrm{GeV}$ & $N_{\mathrm{ch}} = 3$

Region D is the signal region and the background distribution of each kinematic variable in the signal region is estimated from the corresponding distributions in the three control regions by $\frac{B \times C}{A}$, performed bin by bin.

Figure 6.3 shows an example of the ABCD application using the kinematic distributions of $\Delta\phi$ between the muon and the three-prong tau lepton candidate. Distributions are shown for regions A to D, followed by a fifth distribution for the ABCD background estimation in region D.

6.2.3 Agreement of data with the signal plus background model

To validate the modeling of the background, one has to ensure the background-subtracted data can be represented by the $\gamma\gamma \rightarrow \tau^+\tau^-$ signal. This can be achieved by comparing the kinematic distributions of data with those of the signal plus background model. These distributions have to agree for the muonic tau, hadronic tau, and the ditau lepton system.

Figure 6.4 shows the distribution of muon p_{T}, pseudorapidity (η), and azimuthal angle (ϕ) for data, MC simulation of the signal process, and the ABCD background prediction in the signal region, with the latter two stacked on top of each other. Good agreement is found between the data and the signal plus background model, which ensures that the excess of muons in data over the background is indeed coming from the $\gamma\gamma \rightarrow \tau^+\tau^-$ signal.

Figure 6.5 shows the kinematic distributions of the three charged pions separately, with a good agreement between the data and the signal plus background model. Figure 6.6 shows the invariant mass of these three pions, which shows good agreement of the excess data with the expected visible tau lepton mass from the MC simulation of the signal. The kinematics of the reconstructed 3-prong tau lepton candidate is shown in figure 6.7.

The final check, after ensuring that the visible parts of both muonic and hadronic taus kinematically match the signal prediction, is to check the total p_{T} and invariant mass of the visible ditau system, as well as the opening azimuthal angle ($\Delta\phi$) between the two tau candidates, as shown in figure 6.8. The good agreement of the excess of data over the background estimate with the signal prediction in all kinematic variables of the muonic tau, hadronic tau, and ditau lepton system provides solid validation that this excess is indeed from the $\gamma\gamma \rightarrow \tau^+\tau^-$ signal process.
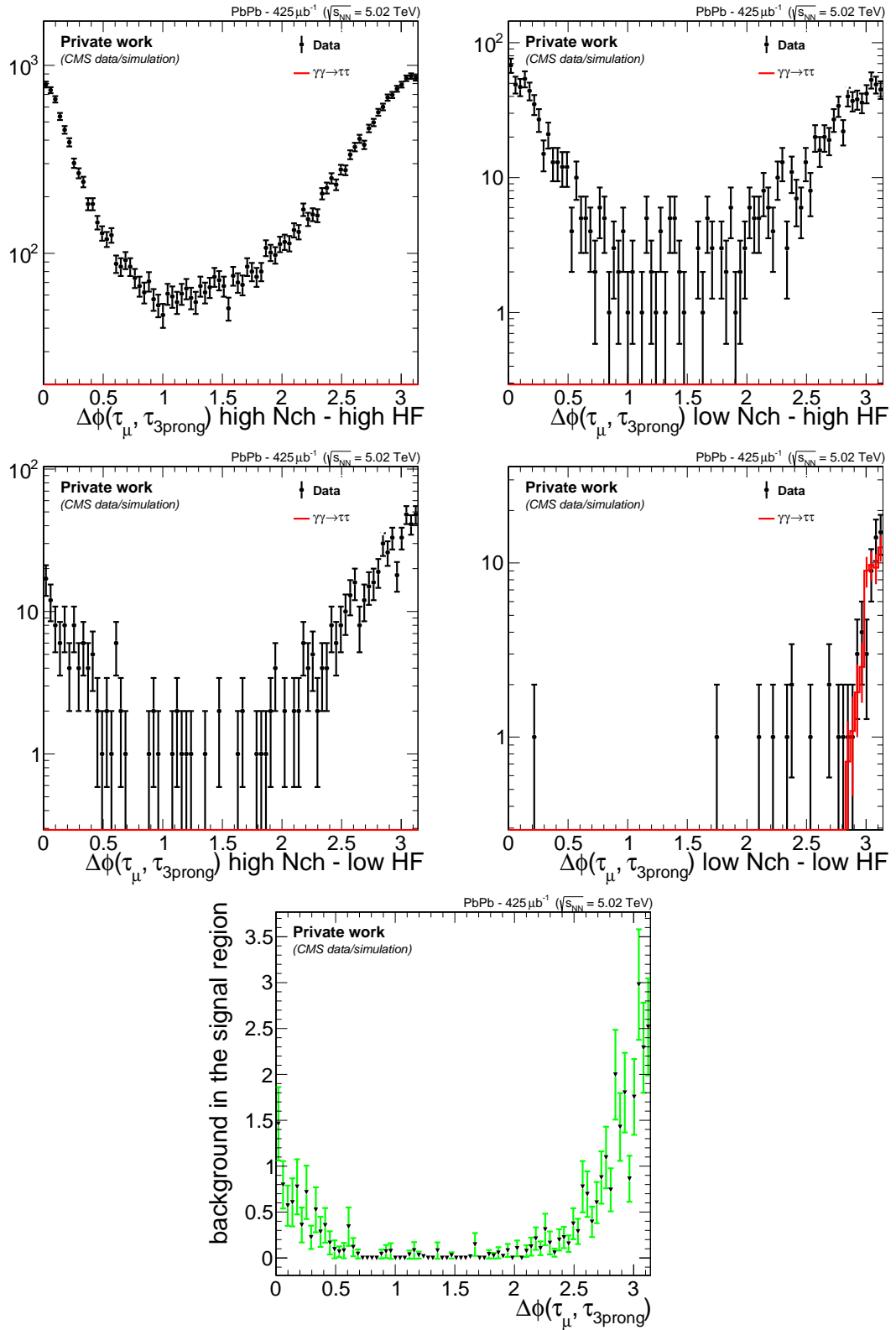
Figure 6.3: Distribution of $\Delta\phi$ between the muon and the visible three-prong tau candidate for regions A to D, and the estimated background for region D using the ABCD method.
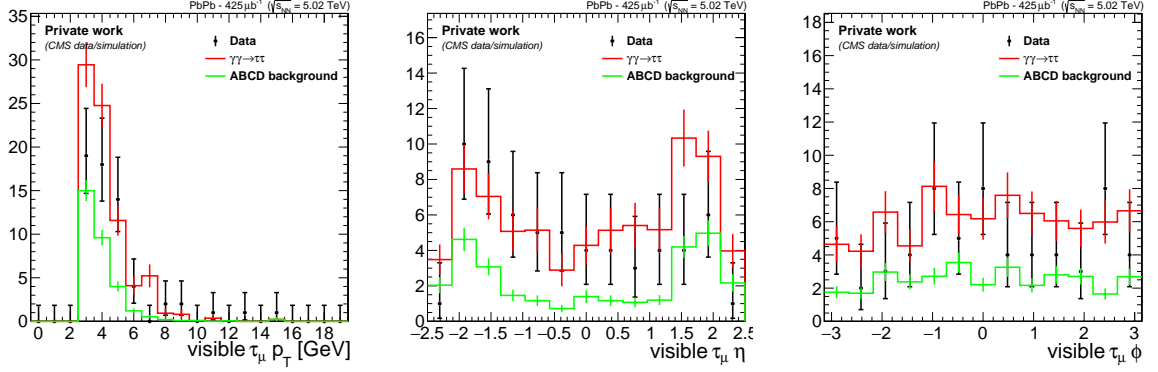
Figure 6.4: Distributions of p_T, pseudorapidity, and azimuthal angle of the muon candidates in the μ+3prong category. Signal distributions (red) are stacked on top of the ABCD background prediction (green) and compared with data (black).
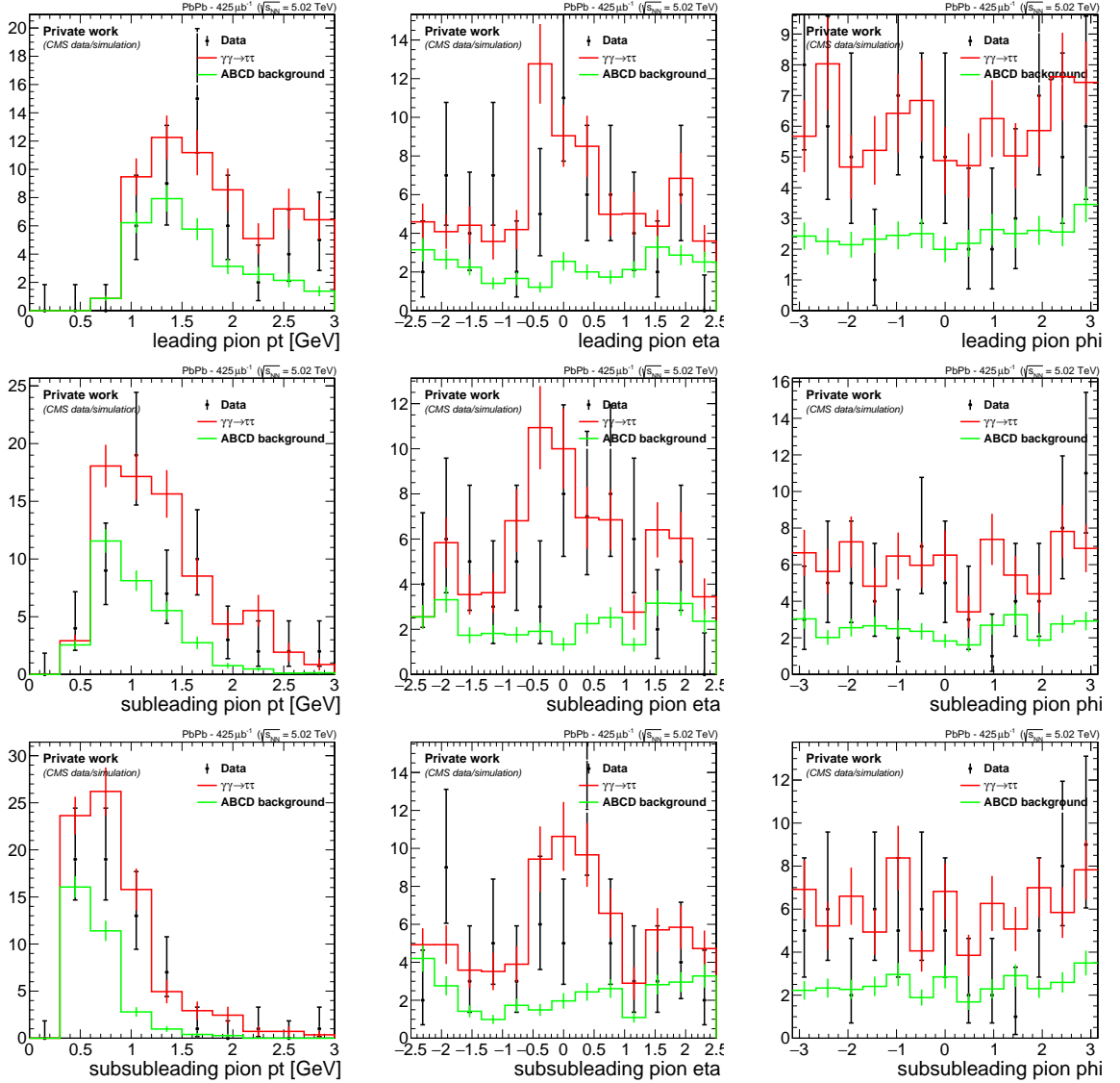
Figure 6.5: Distributions of p_T (left), pseudorapidity (middle), and azimuthal angle (right) of the leading (top), subleading (middle), and sub-subleading (bottom) charged pion candidates in the μ+3prong category. Signal distributions (red) are stacked on top of the ABCD background prediction (green) and compared with data (black).
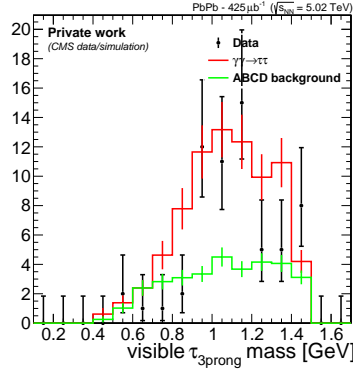
Figure 6.6: Distribution of the invariant mass of the hadronic tau lepton candidate reconstructed from the three charged pion candidates in the μ+3prong category. Signal distributions (red) are stacked on top of the ABCD background prediction (green) and compared with data (black).
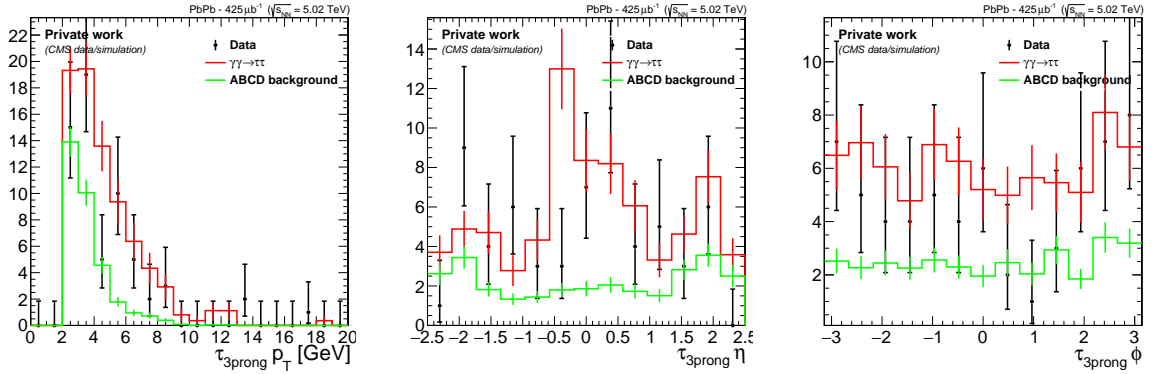
Figure 6.7: Distributions of p_T (left), pseudorapidity (middle), and azimuthal angle (right) of the hadronic tau lepton candidate in the μ+3prong category. Signal distributions (red) are stacked on top of the ABCD background prediction (green) and compared with data (black).
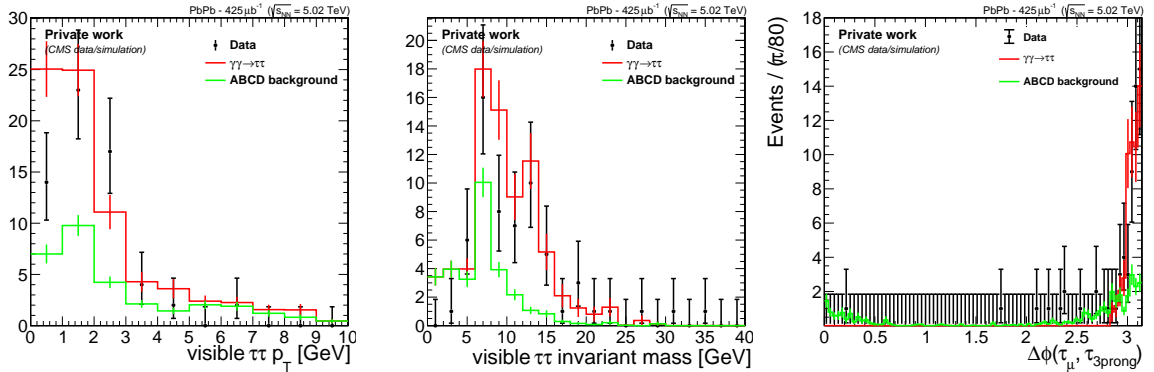
Figure 6.8: Distributions of total p_T (left), invariant mass (middle), and opening azimuthal angle of the two visible tau lepton candidates in the μ+3prong category. Signal distributions (red) are stacked on top of the ABCD background prediction (green) and compared with data (black).

6.3 μ+1prong decay channel

In this final state, the decay of two tau leptons to a muon, a charged pion, neutral pions that decay to photons, and neutrinos is under study. The full decay channel can be written as $(\tau^-) + (\tau^+) \rightarrow (\mu^- + \nu_\tau + \overline{\nu}_\mu) + (\pi^\pm + \overline{\nu}_\tau + n\pi^0)$, with $n \geq 0$ the number of neutral pions. Events are triggered online by having a muon, an extra track in the pixel detector, and low activity in at least one of the two HF detectors. Offline, events with exactly one muon and exactly one particle flow candidate corresponding to a charged pion are selected, while events with any HF tower with energy above $6\,\mathrm{GeV}$ are rejected to ensure exclusivity.

As mentioned earlier, this ditau-lepton decay channel is expected to have the highest number of signal events among the *semileptonic* final states, due to the efficiency of low-p_T muon triggers and the high BR of 1-prong tau lepton decays. However, the study and modeling of backgrounds is more challenging compared to the μ+3prong final state discussed in section 6.2.

6.3.1 Background processes; modeling and veto

One of the main sources of background in this final state is dimuon photoproduction with an emitted FSR photon from one of the muons. The process is written as $\gamma + \gamma \rightarrow \mu^+ + \mu^- + \gamma$ with the two photons emitted from Pb ions as depicted in figure 6.9. If one of the two muons in the final state does not reach the CMS muon system, it will be reconstructed as a charged pion, given it only leaves a track in the tracker system and not the muon system. Therefore, both $\gamma + \gamma \rightarrow \mu^+ + \mu^-$ and $\gamma + \gamma \rightarrow \mu^+ + \mu^- + \gamma$ processes can resemble the signal μ+1prong final state if one of the muons does not have enough p_T to reach the muon systems, which is likely given the kinematics of ultraperipheral PbPb collisions. The two quasi-real photons from the Pb ions have a p_T of around $30\,\mathrm{MeV}$ in $5.02\,\mathrm{TeV}$/nucleon PbPb collisions at the LHC, and therefore, in the case of the $\gamma + \gamma \rightarrow \mu^+ + \mu^-$ process, the background is easily removable considering the fact that the two final-state muons are completely back-to-back as opposed to the μ+1prong signal process which has invisible particles in the final state such that the two visible tracks are relatively less back-to-back. However, the $\gamma + \gamma \rightarrow \mu^+ + \mu^- + \gamma$ background cannot be easily removed, as the emitted FSR photon will lower the balance of the two tracks in the final state, making it resemble the signal μ+1prong process.
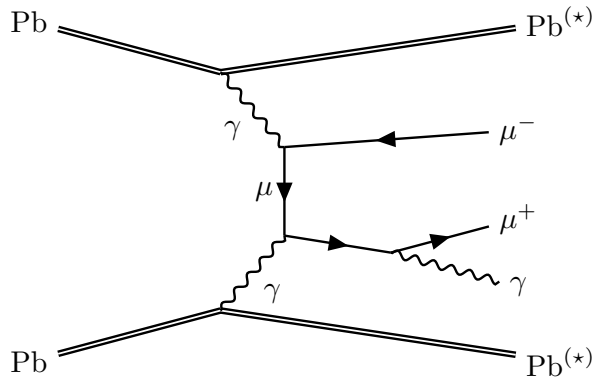
Figure 6.9: Feynman diagram of the $\gamma + \gamma \rightarrow \mu^+ + \mu^- + \gamma$ process in ultraperipheral PbPb collisions. The star in Pb* indicates the possible excitation of the lead ion.

To veto the $\gamma + \gamma \rightarrow \mu^+ + \mu^- + \gamma$ background, one can use the fact that in this process the system of two tracks and the FSR photon is expected to be fully balanced in the transverse plane. Therefore, if an event contains a photon that is back-to-back to the two-track system

in azimuthal angle and has the same p_T, this event is considered background and is removed. Since the noise in the calorimeters is higher than the energy of the FSR photons, the veto requirements must be tuned carefully to ensure that signal events with noise-generated photons are not removed. Moreover, due to the possible presence of one or a few π^0 mesons in the signal μ+1prong process, the FSR photon candidate in the event might actually be a real photon from the signal process. However, in both cases of noisy photons and π^0 photons, the chance of having a matching p_T with the two-track system and being in the exact opposite azimuthal angle is relatively low compared to that of FSR photons.

Figure 6.10 shows the difference in p_T between the two-track system and the FSR photon candidate. To select the FSR photon candidate from the photons within an acoplanarity of 0.05 of the two-track system or the visible ditau candidate, the one with the highest p_T is chosen. In the $\gamma + \gamma \rightarrow \mu^+ + \mu^- + \gamma$ background process, the p_T of the FSR photon is expected to be close to that of the visible ditau, as shown in the left plot using generator-level photons in the described back-to-back acoplanarity cone. After the addition of detector level reconstruction, as shown in the right plot, the distribution still has a peak for the $\gamma + \gamma \rightarrow \mu^+ + \mu^- + \gamma$ process, with a tail on the left side corresponding to the mismatched or noise-initiated photons. Therefore, events in the range of $\pm 0.5\,\mathrm{GeV}$ of this distribution are rejected as background.
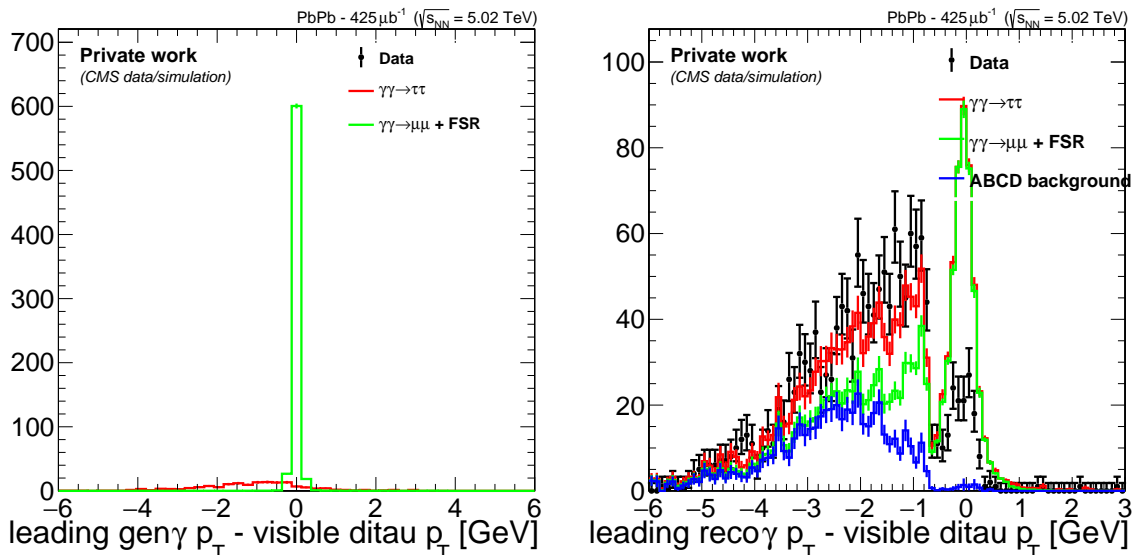
Figure 6.10: Difference in p_T between the two-track system and the leading photon found in the opposite ϕ selection window. On the left, the generator-level photon is used and on the right, the reconstructed-level photon. The acoplanarity between the photon and the two-track system is less than 0.05. Simulated processes are normalized with their corresponding cross sections.

Since two-muon final states with one low-p_T muon faking a charged pion can be a background for the μ+1prong decay channel, the production of mesons such as J/ψ and Ψ(2S) decaying to two muons should be considered as background processes. These mesons are produced in the photonuclear interaction of a photon from one Pb ion with a pomeron from the other Pb ion. Compared to the quasi-real photons in photon-photon interactions, the pomeron has a larger initial transverse momentum. Therefore, these mesons, as well as the two-track system of their decay products, are not fully balanced in the transverse plane, mimicking the signal final state. Compared to the $\gamma + \gamma \rightarrow \mu^+ + \mu^- + \gamma$ background process, the transverse boost of the two-track system cannot be matched to a reconstructed object to veto this background. However, as both decay products of these mesons are reconstructed and the mass of the charged pion is similar to

that of the muon, the invariant mass of the two-track system peaks at the mass of these mesons. Hence, this background can be removed rather efficiently.

Another source of background in the study of the exclusive $\gamma\gamma \to \tau^+\tau^-$ process is the presence of non-exclusive events. As discussed in section 6.2, while nonexclusive events can be rejected by requiring low activity in the HF detectors, the relatively higher noise in these detectors compared to 2015 translates to a reduced background reduction power. Moreover, the nonexclusive background in the μ+1prong decay channel is higher compared to the μ+3prong decay channel, as the requirement of three tracks with an invariant mass in the range corresponding to the visible tau cleans the latter decay channel from background contamination.

In nonexclusive background processes, one or both Pb ions interact hadronically and break up. Emissions from the Pb ions are forward and can be detected by both ZDC and HF detectors. Therefore, for nonexclusive photonuclear events, the ZDC activity is correlated with the HF activity. As discussed in chapter 4, the ZDC activity can be categorized according to the number of neutrons emitted from each Pb ion. While the nonexclusive events are dominant in ZDC categories with a higher number of neutron emmisions, it was shown in figure 4.11 for the $\text{PbPb} \to \text{Pb}(\gamma\gamma \to \mu^+\mu^-)\text{Pb}$ process that UPC events have predominantly zero or small ZDC activity.

Since the $\text{PbPb} \to \text{Pb}(\gamma\gamma \to \mu^+\mu^-)\text{Pb}$ process is quite similar to the $\text{PbPb} \to \text{Pb}(\gamma\gamma \to \tau^+\tau^-)\text{Pb}$ signal process, it can be used as a proxy to study ZDC activity as a function of dilepton invariant mass. The dilepton invariant mass depends on the quasi-real photon flux at each impact parameter of the Pb ions. Similar ZDC activity is expected for these two processes for the same impact parameter, or invariant mass of the two quasi-real photons, which is also the invariant mass of the resulting two leptons. The probability of each ZDC category as a function of dilepton invariant mass and rapidity is obtained from the study of the $\text{PbPb} \to \text{Pb}(\gamma\gamma \to \mu^+\mu^-)\text{Pb}$ process in the 2018 PbPb data. This enables us to split the simulated $\text{PbPb} \to \text{Pb}(\gamma\gamma \to \tau^+\tau^-)\text{Pb}$ signal events into various ZDC categories based on the generator-level ditau invariant mass and rapidity, even though the ZDC material and response are not simulated in our signal samples. A similar approach can be taken to split the events in the simulated sample of the $\gamma + \gamma \to \mu^+ + \mu^- + \gamma$ process.

Given the difference between the signal and nonexclusive background events in the ZDC activity, we divide the signal region into several categories according to the number of neutrons emitted in the ZDC, which allows us to apply different signal selection criteria in each category. Specifically, as the HF activity of the nonexclusive events is correlated with the ZDC activity, we require a tighter HF veto in the regions with ZDC activity. The energy of the leading-energy HF tower is required to be less than $6\,\text{GeV}$ in the 0n0n ZDC category with no neutrons emitted on any side, and less than $5\,\text{GeV}$ if any neutron is observed.

Following the approach taken in chapter 5 and section 6.2, the remaining nonexclusive background is modeled by an ABCD method based on the number of charged pion tracks (N_{ch}) and the energy of the leading-energy HF tower ($E_{\text{max}}^{\text{HF}}$). Four regions of phase space are formed as follows:

- A: $E_{\text{max}}^{\text{HF}} > 8\,\text{GeV}$ & $N_{\text{ch}} = 2, 3$
- B: $E_{\text{max}}^{\text{HF}} > 8\,\text{GeV}$ & $N_{\text{ch}} = 1$
- C: $E_{\text{max}}^{\text{HF}} < 5, 6\,\text{GeV}$ & $N_{\text{ch}} = 2, 3$
- D: $E_{\text{max}}^{\text{HF}} < 5, 6\,\text{GeV}$ & $N_{\text{ch}} = 1$

The D region represents the signal region, while the A, B, and C regions represent three control regions. At least one HF tower above 8 GeV is required in the A and B regions. The 8 GeV threshold ensures minimal noise contamination and avoids the turn-on region of 6-8 GeV for nonexclusive events, as seen in figure 6.15. The HF requirement depends on the ZDC category in regions C and D, as discussed above. The nonexclusive background in region D is estimated by the formula B × C/A, while multiplication and divisions are performed bin by bin for each kinematic variable. Figures 6.11 and 6.12 show two examples of the ABCD method performed on $\Delta\phi$ between the muon and the charged-pion candidate and the invariant mass of the pair. The corresponding distributions are shown for regions A to D and the background in region D.

The ABCD method assumes the absence of any correlation between HF activity and track multiplicity. This assumption does not hold when a process favors a specific region among the four regions. For instance, the J/ψ production discussed above is not present in regions A and C with high track multiplicity. Compared to other background processes, the fraction of events in region D with low HF activity to region B with high HF activity is higher for J/ψ production. Therefore, as seen in figure 6.12, the ABCD method fails to predict about half of the J/ψ events at an invariant mass of 3.1 GeV. While the J/ψ background can be removed based on its fixed invariant mass, similar dimuon events with one low-p_T muon faking a charged pion face the same challenge. In such events with a muon faking a charged pion, the other muon is highly likely to have a low p_T as well. Therefore, the ABCD prediction should be corrected for events containing a low-p_T muon.

Figure 6.13 shows the distribution of acoplanarity between the muon and the charged pion, defined as $\alpha = 1 - \Delta\phi/2\pi$. Distributions are shown separately for events with muon p_T below and above 3.5 GeV. As signal events are expected to have low acoplanarity, events with acoplanarity greater than 0.35 are merged into a single bin, which is used as a control region to scale the ABCD background. For events containing a high-p_T muon, there is good agreement between the signal plus background model and data, whereas for events with a low-p_T muon, the ABCD prediction needs to be scaled up by a factor of approximately 2, to achieve a good agreement in the high-acoplanarity control region. This factor will be used later to scale the ABCD prediction for events containing a low-p_T muon.

In addition to the background processes discussed above, there are some events reconstructed in the $(\tau^-) + (\tau^+) \to (\mu^- + \nu_\tau + \overline{\nu}_\mu) + (\pi^\pm + \overline{\nu}_\tau + n\pi^0)$ signal region that match other decay channels of the $\gamma\gamma \to \tau^+\tau^-$ signal sample at the generator level, especially the μ+3prong decay channel that can resemble the μ+1prong decay channel when the tracking system misses two tracks. The kinematic distributions corresponding to these events will not be plotted separately in sections 6.3.2 and 6.3.4, since they are partially reconstructed signal candidates. Hereafter, these events are treated as part of the signal events in the μ+1prong channel.

6.3.2 Signal selection

Using the data from PbPb collisions of the CMS experiment in 2018, we select events triggered online by a single muon and an extra track in the pixel detector, and low activity in at least one of the two HF calorimeters. Offline, events are required to have exactly one muon matching the *soft* muon quality requirements [106], with $p_\mathrm{T} > 3.5$ GeV for $|\eta| < 1.2$ and $p_\mathrm{T} > 2.5$ GeV for $|\eta| > 1.2$, following the acceptance of the muon detector system. In addition to the muon, exactly one PF candidate identified as a charged pion is required with a p_T greater than 0.3 GeV.

The two-track system representing the visible decay products of the ditau decay $(\tau^-) + (\tau^+) \to$
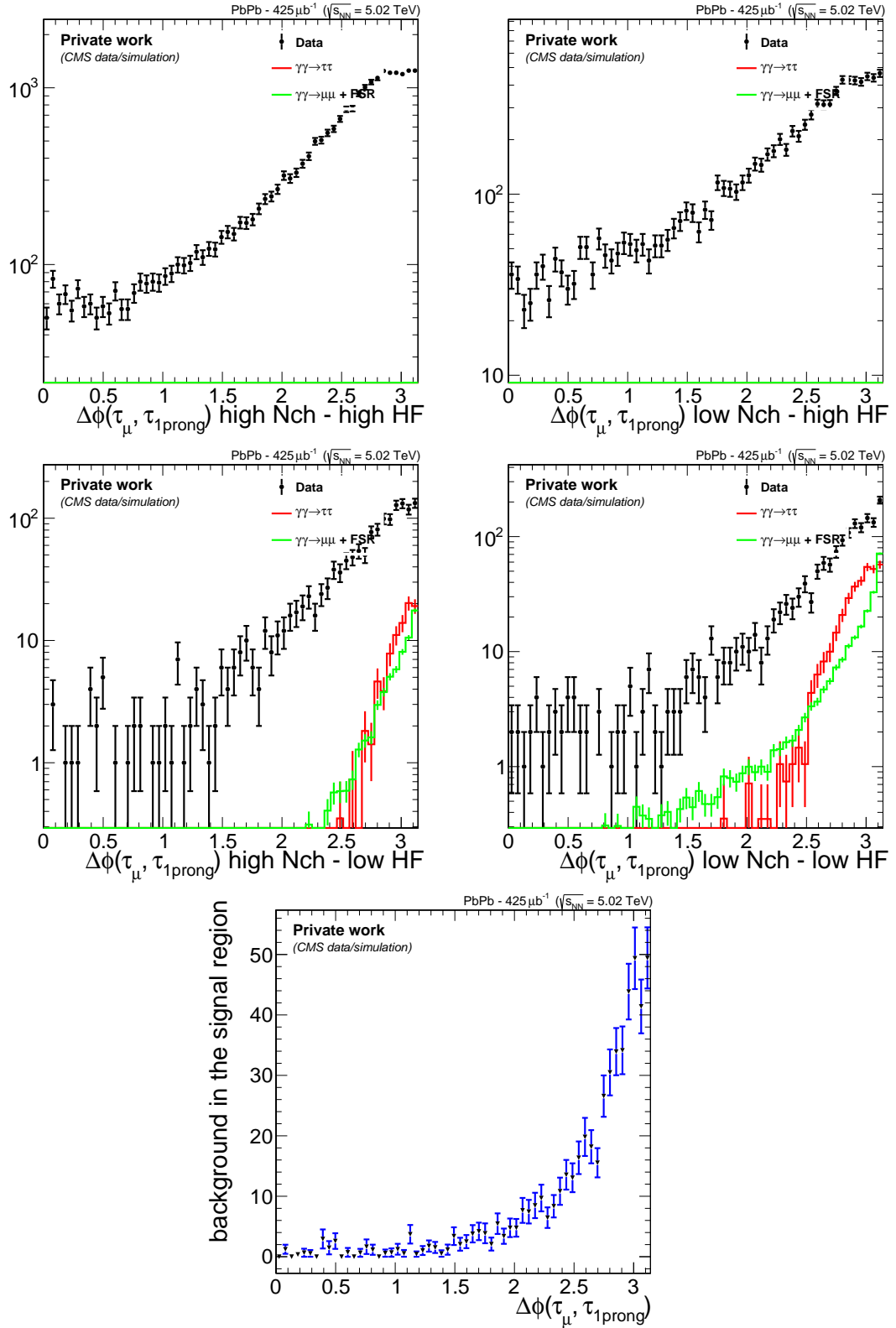
Figure 6.11: Distribution of $\Delta\phi$ between the muon and the charged pion candidate for regions A (top left), B (top right), C (middle left), and D (middle right), and the estimated background (bottom) for region D using the ABCD method.
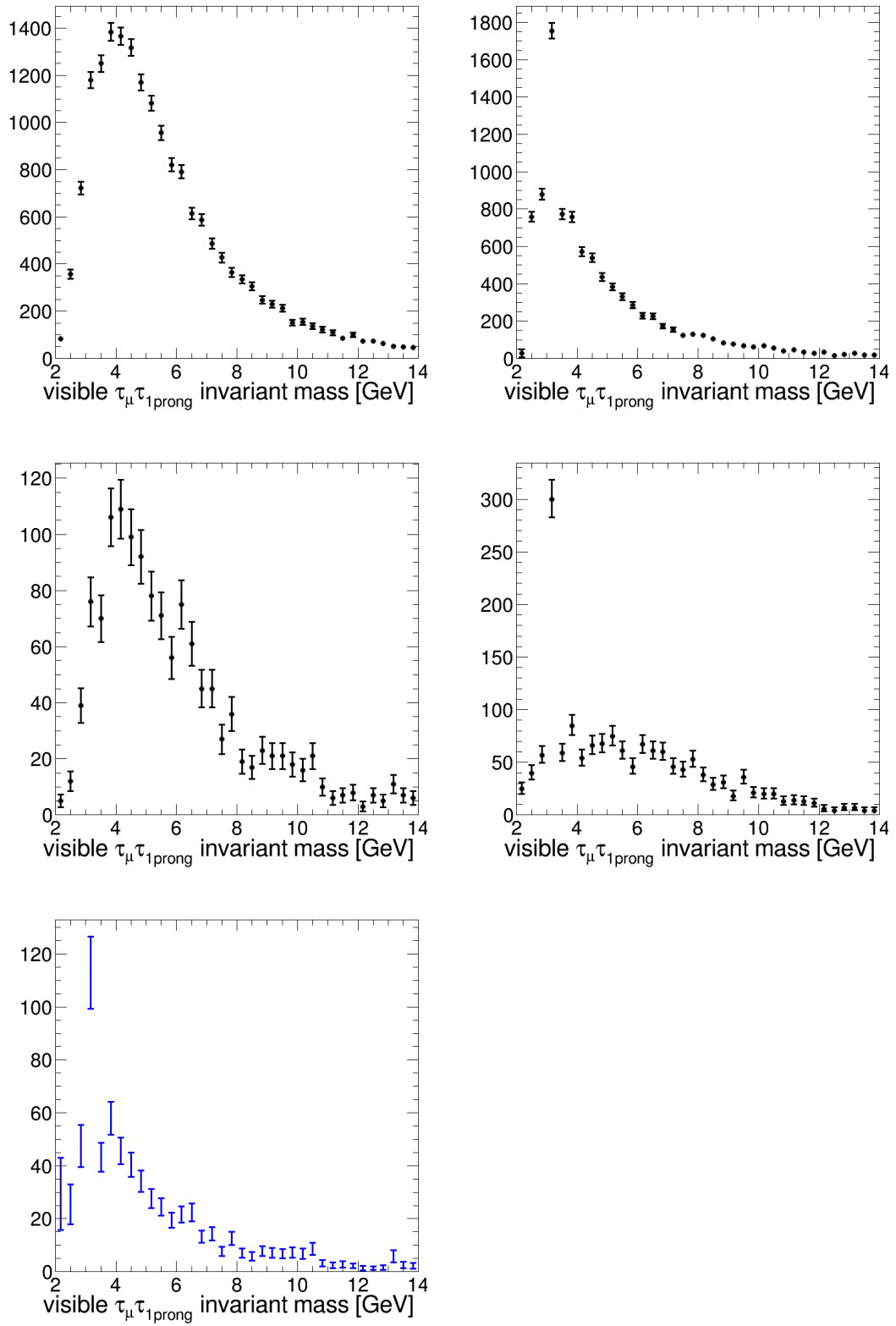
Figure 6.12: Distribution of the invariant mass of the muon and charged pion candidate for regions A (top left), B (top right), C (middle left), and D (middle right), and the estimated background (bottom) for region D using the ABCD method.
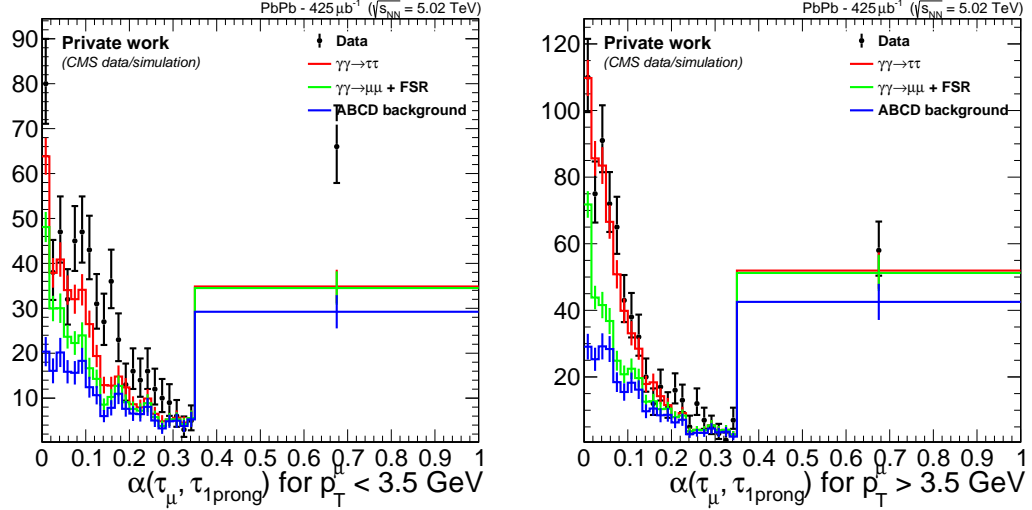
Figure 6.13: Distribution of acoplanarity between the muon and the charged pion for muons with p_T below (left) and above (right) $3.5\,\text{GeV}$.

$(\mu^- + \nu_\tau + \overline{\nu}_\mu) + (\pi^\pm + \overline{\nu}_\tau + n\pi^0)$ and referred to hereafter as visible ditau, is required to have a p_T greater than $0.75\,\text{GeV}$ to completely remove the back-to-back $\gamma + \gamma \to \mu^+ + \mu^-$ background process and a large fraction of the $\gamma + \gamma \to \mu^+ + \mu^- + \gamma$ background process. Figure 6.14 (left) shows the distribution of the visible ditau pt for the ABCD background, $\gamma + \gamma \to \mu^+ + \mu^- + \gamma$ background process, with signal stacked on top, compared to the distribution for the data. By applying a minimum p_T of $0.75\,\text{GeV}$, the background-dominated region of this phase space will be removed. Next, events with a visible ditau mass below $4\,\text{GeV}$ are removed. As shown in figure 6.14 (right), the region below $4\,\text{GeV}$ is contaminated by J/ψ and $\Psi(2S)$ mesons produced in photonuclear events and decaying to two muons, while one muon does not reach the muon system and fakes a charged pion. As explained in section 6.3.1, these backgrounds can be removed efficiently by vetoing events with a visible ditau invariant mass close to the mass of the J/ψ and $\Psi(2S)$ mesons, both below $4\,\text{GeV}$.
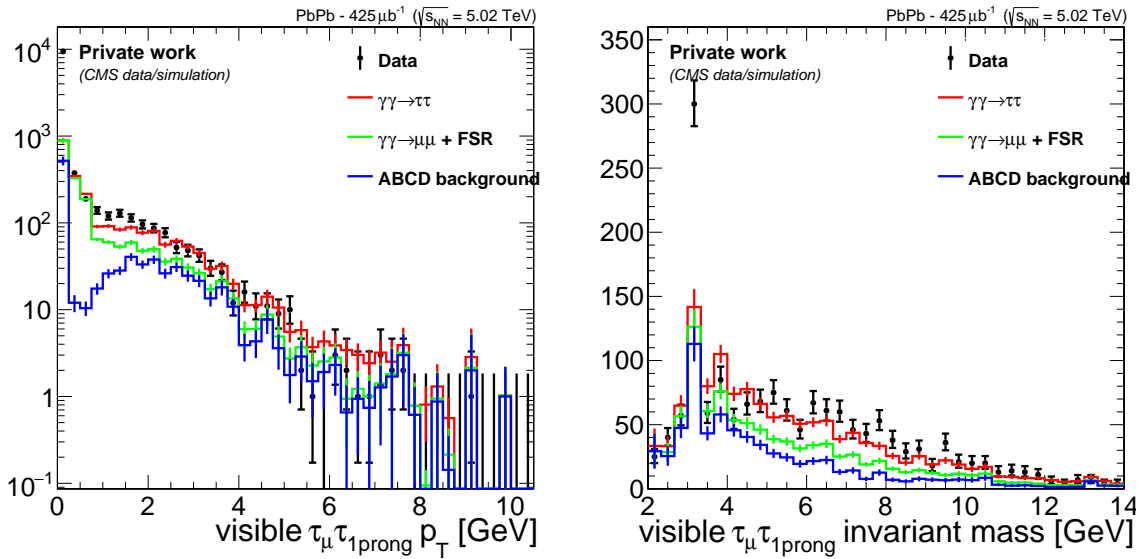
Figure 6.14: The p_T (left) and invariant mass (right) distributions of the two-track final state.

Figure 6.15 shows the energy distribution of the leading energy tower of the HF$-$ and HF$+$ detectors. Since it is unlikely that either the signal process or the $\gamma + \gamma \to \mu^+ + \mu^- + \gamma$ background

71

process deposit energy in the HF detectors, the distributions shown for these processes represent the simulated noise in the HF detectors for 2018 and this is found in general to match that of the data. As explained in section 6.3.1, to reduce the nonexclusive background, events with an HF tower with energy above 6 GeV are rejected. Although a fraction of nonexclusive background events remain after this veto, given the higher noise level of the HF detector in 2018 compared to 2015, the 6 GeV limit serves as the best compromise to ensure high signal efficiency. As discussed in section 6.3.1, the requirement on $E_{\max}^{\mathrm{HF}}$ is lower (5 GeV) for events with ZDC activity. This is justified in figure 6.16, which demonstrates a higher activity in the HF detector above the noise level, if and only if activity in the ZDC detector of the same side is detected.
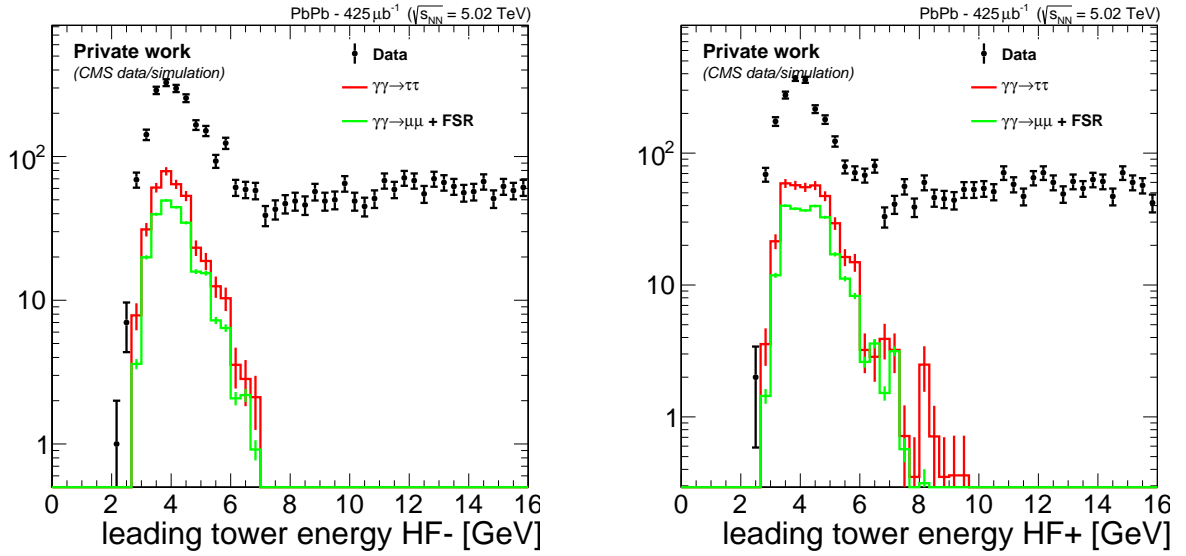
Figure 6.15: The distribution of energy of the leading-energy tower for the HF− (left) and HF+ (right) detectors in the μ+1prong channel.
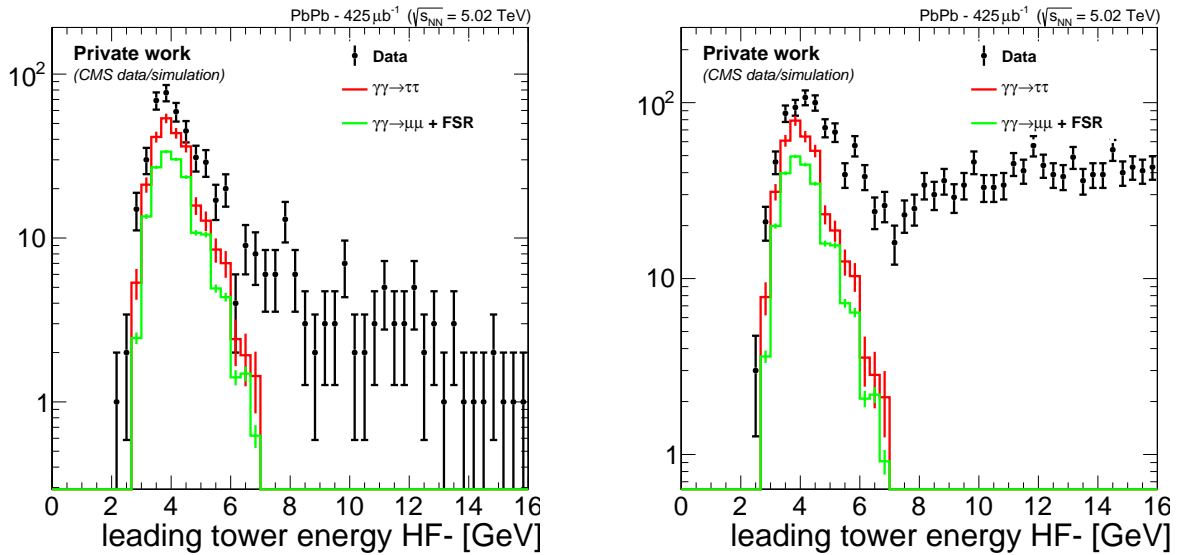
Figure 6.16: The distribution of energy of the leading-energy tower of the HF− detector in the μ+1prong channel when no (left) and some (right) activity is seen in the ZDC$_{\mathrm{minus}}$.

6.3.3 Reconstruction of neutral pions

Relative to the total $16.62\,\%$ BR of the $(\tau^-) + (\tau^+) \rightarrow (\mu^- + \nu_\tau + \overline{\nu}_\mu) + (\pi^\pm + \overline{\nu}_\tau + n\pi^0)$ decay channel, $24.1\,\%$ of this final state does not contain a π^0 meson, $54.3\,\%$ contains exactly one π^0 meson, $19.5\,\%$ contains exactly two π^0 mesons, and $2.2\,\%$ contains exactly three π^0 mesons [13]. The presence of a π^0 is a signature of the signal process against the background processes discussed in section 6.3.1. As seen in the left of figure 6.17, the π^0 mesons produced in the signal process are mostly below $3\,\mathrm{GeV}$ in p_T, with their photon decay products having a p_T of lower than $1.5\,\mathrm{GeV}$. Such low-p_T photons from the π^0 decay have never been observed in CMS, let alone using the 2018 detector in which the noise level, defined as the energy threshold to remove 99% of noise-generated calorimeter activity, is a few GeV. Therefore, the reconstruction of π^0 mesons from the $(\tau^-) + (\tau^+) \rightarrow (\mu^- + \nu_\tau + \overline{\nu}_\mu) + (\pi^\pm + \overline{\nu}_\tau + n\pi^0)$ final state is challenging and requires a dedicated, innovative selection method.

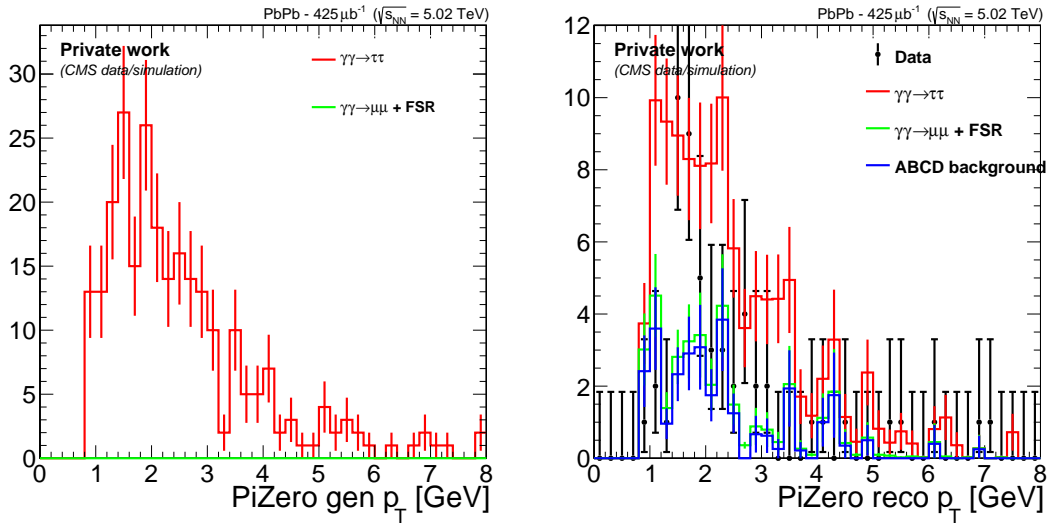**Figure 6.17:** p_T of the π^0 candidates at generator (left) and reconstructed (right) level.

Due to the high level of noise in the electromagnetic calorimeters, there are typically 20-30 photon candidates with energies below $2\,\mathrm{GeV}$ in each event, making it rather impossible to choose the correct combination initiated from the π^0 meson. Applying the energy thresholds typically utilized in CMS analyses will also remove all the photon candidates as the energy of the signal photons are below the noise level. However, if one restricts the search for photons to parts of the detector that the photon is expected in, the probability of having a noise-initiated photon in the small part of the detector is significantly reduced, and the noise thresholds can be reduced effectively.

To reconstruct the π^0 candidates from the $(\tau^-) + (\tau^+) \rightarrow (\mu^- + \nu_\tau + \overline{\nu}_\mu) + (\pi^\pm + \overline{\nu}_\tau + n\pi^0)$ process, two photon candidates are to be selected. In the first step, a loose requirement is applied to the photon p_T to be greater than $0.4\,\mathrm{GeV}$ and the pseudorapidity to be less than 2.1. Although the p_T threshold is lower than the noise levels, it is sufficient to reduce the number of photon pair candidates that will be further scrutinized in the next steps. As seen in the left plot of figure 6.18, the $\Delta\phi$ between the photons coming from the π^0 candidate and the charged pion, all at generator level, is lower than 1. Therefore, the reconstructed-level photons are required to be within this $\Delta\phi$ range around the charged pion, to partially reduce the background from noise-generated photons. As seen in the right plot of figure 6.18, at reconstructed level, the FSR photon from the $\gamma + \gamma \rightarrow \mu^+ + \mu^- + \gamma$ process also lies within this $\Delta\phi$ range around the
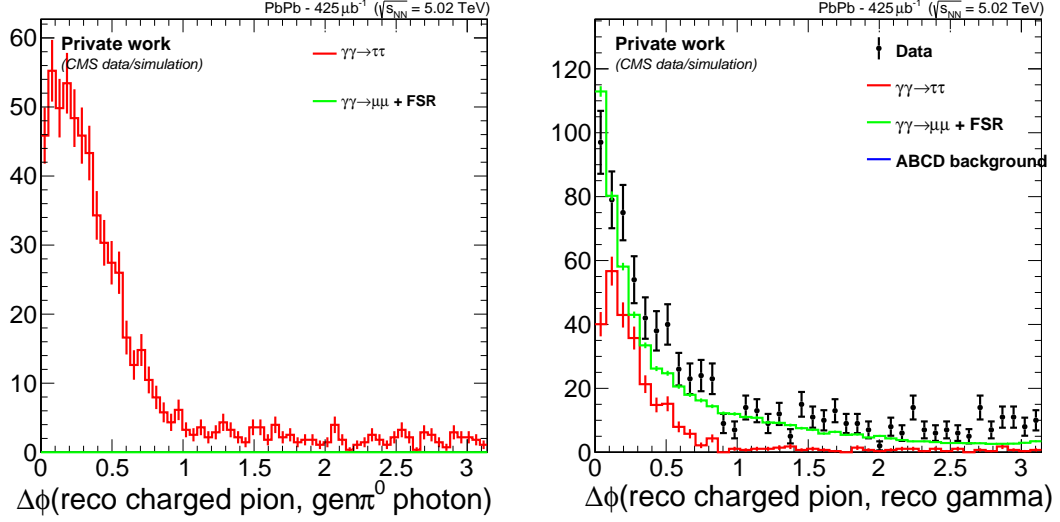
Figure 6.18: The $\Delta\phi$ between the charged pion and the photons at generator (left) and reconstructed (right) level. At generator level, the photons are ensured to be from the π^0 meson.

charged pion. However, by requiring both photons to be within this range and since only one of the photons from the $\gamma + \gamma \to \mu^+ + \mu^- + \gamma$ process at reconstructed level is real and the other noise-induced, this background will also be reduced.
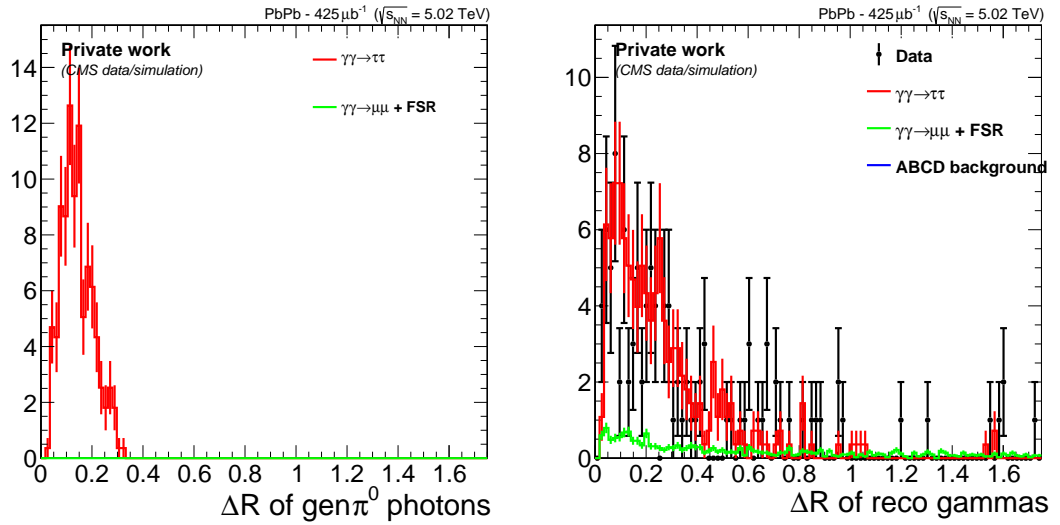
Figure 6.19: The ΔR between the two photons at generator (left) and reconstructed (right) level. Photons are ensured to be from π^0 at generator level.

As seen in figure 6.19 (left), the two photons initiated from the π^0 candidate at the generator level are expected to have a ΔR of less than 0.3. This requirement is applied to the reconstructed photon candidates, and as seen in figure 6.19 (right), it can veto the noise-induced photon pairs.

From each of the photon pairs that remain in the event, a π^0 candidate is reconstructed. Figure 6.17 (left) shows the p_T of the generated-level π^0 mesons remaining after the aforementioned selections. Based on this figure, a lower cut of $0.8\,\mathrm{GeV}$ is applied on the π^0 mesons from the reconstructed-level photon candidates. The p_T distribution of the reconstructed π^0 mesons is shown in figure 6.17 (right).

Figure 6.20 shows the invariant mass distributions of π^0 candidates after subtracting the PDG mass of π^0 [13]. A peak at zero is observed as expected for the signal π^0 mesons. The distributions for signal and background models are stacked on top of each other after normalization by

their corresponding cross section but do not show good agreement with the data. This is due to the relatively lower reconstruction efficiency in the data compared to simulations at low photon p_{T}, as seen also in the right of figure 6.17 showing reconstructed p_{T} of π^0 candidates and in the right of figure 6.10 for the residual p_{T} of the reconstructed FSR photon. However, after taking into account the relative scale factor for photon efficiency observed in figure 6.10 and scaling down the signal, good agreement is achieved, which demonstrates the good performance of the π^0 reconstruction method itself and opens up the opportunity to loosen other signal selections for events with a reconstructed π^0 meson or to introduce a separate decay channel for events containing one or more π^0 mesons.
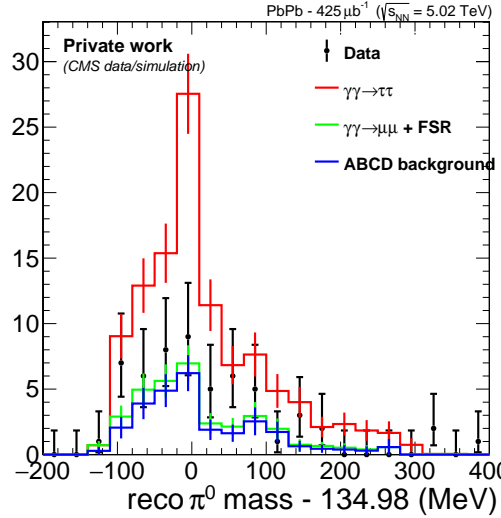
Figure 6.20: Invariant mass of all π^0 candidates in the event after the subtraction of the PDG mass of the π^0. A peak at zero is expected for real π^0 mesons. Distributions are normalized to cross section and stacked on top of each other. No contribution from the ABCD background estimator is predicted.
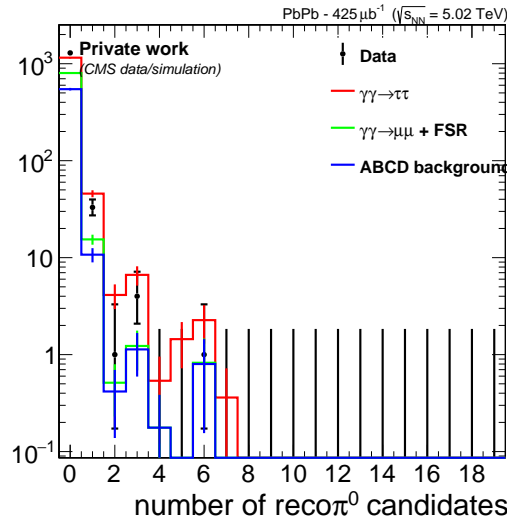
Figure 6.21: Number of π^0 candidates in each event passing the π^0 selection method.

Figure 6.21 shows the number of reconstructed π^0 candidates for data and the signal plus background model. Based on the signal distribution and taking into account the BR of $(\tau^-) + (\tau^+) \rightarrow (\mu^- + \nu_\tau + \overline{\nu}_\mu) + (\pi^\pm + \overline{\nu}_\tau + n\pi^0)$ decays with one or two π^0 mesons, one finds the

efficiency of reconstructing one π^0 meson to be around 23 % and the efficiency of reconstructing two π^0 mesons to be around 6 %, which is close to $(0.23)^2$, confirming that these π^0 mesons are indeed from the signal channel.

6.3.4 Agreement of data with the signal plus background model

To validate the presence of the signal process in data, the kinematic distributions in data should agree with those of the signal plus background model. Similar to the discussion in section 6.2.3, we check this agreement separately for the muonic tau, hadronic tau, and the ditau system.

Figure 6.22: Distributions of p_T, pseudorapidity, and azimuthal angle of the muon candidates in the μ+1prong category. Signal distributions (red) are stacked on top of the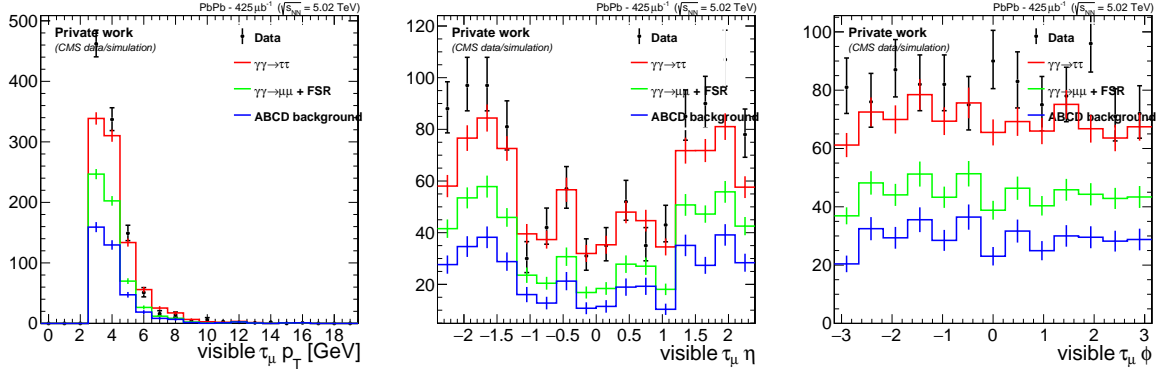 $\gamma + \gamma \to \mu^+ + \mu^- + \gamma$ background (green) and the ABCD background prediction (blue) and compared with data (black).

Figure 6.22 shows the distribution of p_T, pseudorapidity (η), and azimuthal angle (ϕ) of the muons in data, compared to the stacked distribution of signal, $\gamma + \gamma \to \mu^+ + \mu^- + \gamma$ background process, and the ABCD background prediction. An agreement within uncertainties is seen, which indicates that the excess of data over the background comes from the $PbPb \to Pb(\gamma\gamma \to \tau^+\tau^-)Pb$ signal process. For muons with $2.5 < p_T < 3.5$ GeV, which, based on the muon selections are in the endcap region, a small excess of data over the signal plus background model is observed which indicates that the background modeling needs to be improved for processes involving forward and low-p_T muons.

As discussed in section 6.3.1, the ABCDpredicted is corrected by defining a control region based on the acoplanarity of the muon and the charged pion, and scaling the predicted ABCD background by a factor of about 2, for events containing a muon with $p_T < 3.5$ GeV. Figure 6.23 shows the p_T distribution of the muon for data and the signal plus background model, after applying this correction on the ABCD prediction. The agreement between the signal and the excess of the data over the background is significantly improved. While this correction improves all kinematic distributions, it is not applied to other kinematic variables yet, as only the muon p_T distribution will be used for signal extraction, and the categorization of the muon p_T distribution based on muon p_T is trivial.

Figure 6.24 shows a similar comparison for charged pions. The agreement between data and signal plus background modeling ensures that the excess data events over the estimated background come from the charged pions in the signal process.

Following the agreements observed for the muonic and hadronic tau leptons, figure 6.25 shows the kinematic distributions of the ditau system for data and the signal plus background model. The visible ditau system is reconstructed by adding the 4-vectors of the muon and the charged

Figure 6.23: Distributions of muon p_T in the μ+1prong category, with corrected ABCD prediction discussed in the text. The signal distribution (red) is stacked on top of the $\gamma + \gamma \to \mu^+ + \mu^- + \gamma$ background (green) and the corrected ABCD background prediction (blue) and compared with data (black).
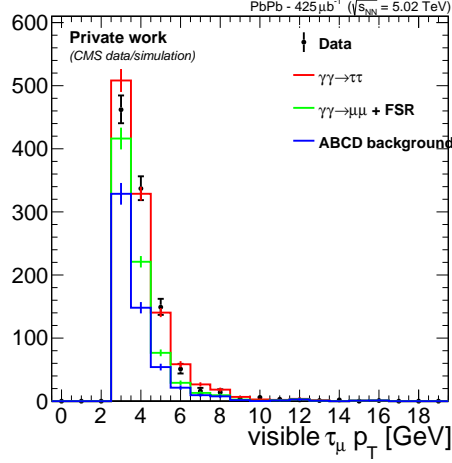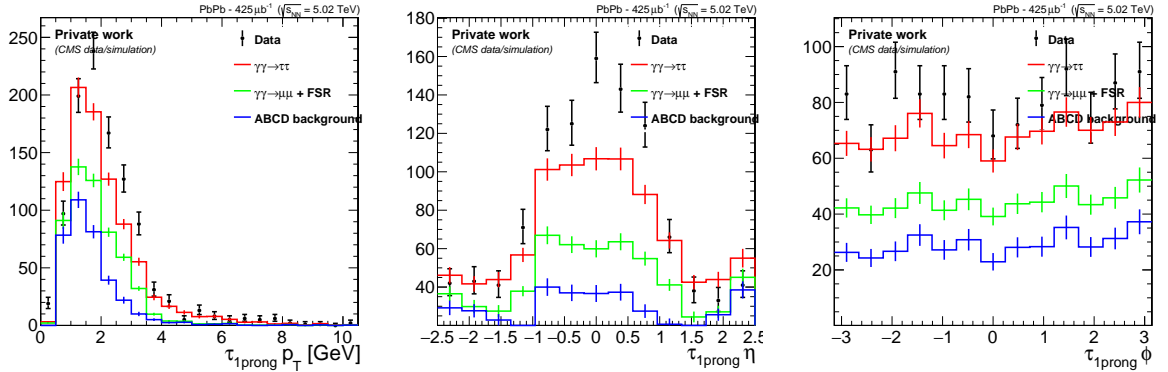

Figure 6.24: Distributions of p_T, pseudorapidity, and azimuthal angle of the charged pion candidates in the μ+1prong category. Signal distributions (red) are stacked on top of the $\gamma + \gamma \to \mu^+ + \mu^- + \gamma$ background (green) and the ABCD background prediction (blue) and compared with data (black).

pion candidate. An agreement is observed in p_T and the invariant mass of the visible ditau system, as well as the opening azimuthal angle ($\Delta\phi$) between the muon and the charged pion as the visible decay products of the tau leptons. This confirms that the excess of data events over the background model is indeed from the PbPb $\to$ Pb($\gamma\gamma \to \tau^+\tau^-$)Pb signal process.

6.3.5 Signal extraction

In chapter 5, the signal extraction was performed using the distribution of opening azimuthal angle of the two visible tau leptons. The choice of this variable ensured the maximum discrimination between the signal and the background, maximizing the observation significance as the main target of that analysis. In the current analysis, the aim is to utilize the sensitivity of the tau-lepton kinematics to a_τ. A generator-level study was performed using the Upcgen generator, which can generate PbPb $\to$ Pb($\gamma\gamma \to \tau^+\tau^-$)Pb samples with arbitrary a_τ values. It was inferred that even though the sensitivity of the cross section to a_τ is still higher than the sensitivity of the tau-lepton kinematics, the muon p_T distribution has a shape dependence on a_τ, which can be utilized to improve the measurement sensitivity of a_τ.

The a_τ measurement procedure relies on the generation of MC samples using the UPCgen

Figure 6.25: Distributions of total p_T (left), invariant mass (middle), and opening azimuthal angle of the two visible tau candidates in the μ+1prong category. Signal distributions (red) are stacked on top of the $\gamma + \gamma \to \mu^+ + \mu^- + \gamma$ background (green) and the ABCD background prediction (blue) and compared with data (black).

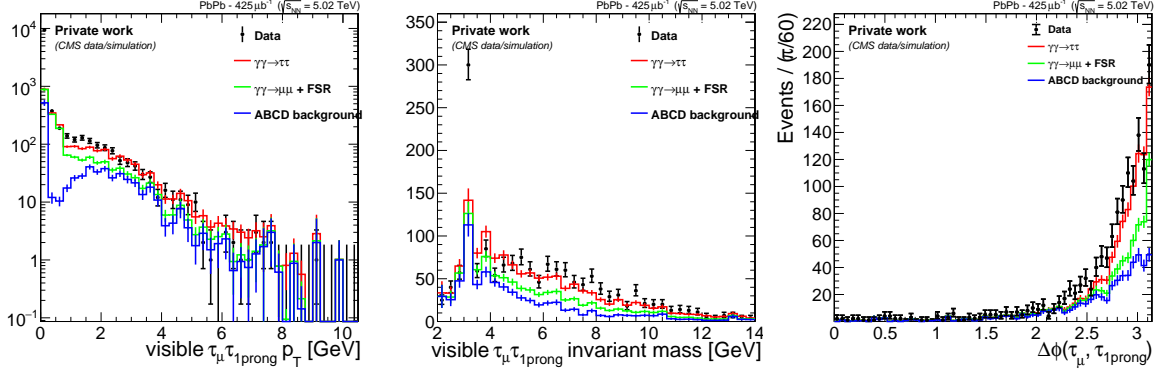generator for various values of a_τ. This provides a set of templates for that kinematic variable, such as muon p_T, at various values of a_τ. Maximum likelihood fits of the data to those templates then determine the most likely values of a_τ. To perform such fits, two main methods are under study, both of which will be discussed in the following.

In the first approach, the generated Upcgen samples are processed through the CMSSW reconstruction algorithm, which simulates the detector response. For each a_τ value, the *reconstructed-level* template of the muon p_T will be added to the background model, which consists of the corrected ABCD prediction and the $\gamma + \gamma \to \mu^+ + \mu^- + \gamma$ background for the μ+1prong channel. A maximum likelihood fit of the data to the signal plus background model will be performed for each a_τ point, with the signal yield as a free normalization parameter representing the signal cross section. Overall, the likelihood can be measured for each signal yield (cross section) and a_τ value, providing a two-dimensional measurement of cross section and a_τ limits. While the Upcgen generator is the only one capable of generating $PbPb \to Pb(\gamma\gamma \to \tau^+\tau^-)Pb$ signal samples with BSM a_τ values, the reliability of the gamma-UPC sample to replicate the kinematics of the signal in the SM is expected to be higher. Therefore, the reconstructed-level BSM kinematic templates can be generated by weighing the reconstructed-level SM distribution of gamma-UPC with weights defined by the ratio of the BSM distribution to the SM distribution in Upcgen.

In the second method, the signal is extracted by a maximum likelihood fit of the data to the signal plus background model similar to what was explained above, but only at the SM a_τ value. The extracted reconstructed-level signal is then *unfolded* to obtain the generator-level signal. This unfolded distribution can then be compared with theoretical predictions, by performing maximum likelihood fits of it to the BSM templates at generator level.

To unfold the reconstructed-level distributions to the generator-level ones, one needs to construct a mapping between these two. In the case of this analysis, one needs a mapping from the reconstructed muon p_T to the p_T of the generated mother τ lepton. A two-dimensional distribution of tau p_T and reconstructed muon p_T is filled using information from the decay of tau leptons to muons with PYTHIA8 in one of the signal samples. The unfolding procedure of a binned p_T distribution of the reconstructed muon p_T is as follows. Each bin of the muon p_T distribution has a corresponding tau p_T template that will be normalized (weighted) to the number of events in that bin. The sum of these weighted tau p_T distributions will represent the unfolded result.

The unfolded tau p_T distribution can be compared with the generator-level tau p_T distri-

bution. Trivially, if the unfolding is performed on the same sample from which the unfolding map is constructed, one expects a very good agreement of the unfolded distribution with the generated-level one. As a second step and to ensure the validity of the unfolding procedure, the unfolding is performed on a statistically independent set of events than those from which the unfolding map is extracted.
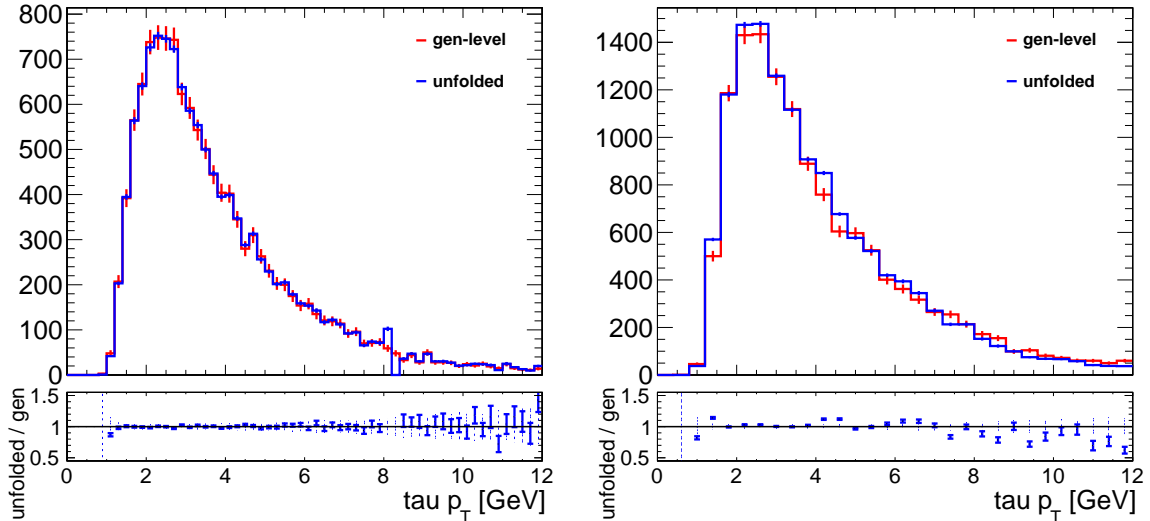
Figure 6.26: Distribution of unfolded tau p_T using the reconstructed-level muon p_T and η. The unfolding map is extracted from the same events in the left plot, whereas it is extracted from an independent set of tau decays in the right plot. The bottom pads show the ratio of the unfolded distribution to the generator-level distribution.

To enhance the precision of the unfolding procedure, one can use more than one input kinematic variable. For this analysis, an unfolding algorithm has been developed that maps the reconstructed muon p_T and η to tau p_T. The generic procedure is the same, except that the unfolding map will be three-dimensional. Figure 6.26 shows the distribution of unfolded tau p_T with the described procedure. As expected, when the map is extracted from the same tau decay events, the unfolded distribution matches perfectly with the true generated-level distribution of tau p_T. The validity of applying the unfolding procedure to data is ensured by observing a good agreement in the right plot in which an independent set of events have been used to extract the map.

The two methods described in this section to extract limits on a_τ and cross section of the PbPb $\to$ Pb($\gamma\gamma \to \tau^+\tau^-$)Pb process have their advantages and disadvantages. In the first method, a significant computational power is required to reconstruct MC samples with enough statistics to be used as fit templates of various a_τ points. If a reconstructed SM gamma-UPC sample is to be weighted with reconstructed BSM Upcgen samples, even larger statistics are required, as the statistical error will be prominent when taking the ratios. However, if the BSM templates are produced using only the generator-level information from the BSM Upcgen samples, there would be no need for large computational power to reconstruct the Upcgen samples. Although the unfolding procedure in the second method introduces a small uncertainty as observed in figure 6.26 (right), it has the advantage of providing a generator-level signal distribution that can be compared to any theoretical prediction independent of the detector effects.

6.3.6 Systematic uncertainties

There are many systematic uncertainties involved in the signal extraction and measurement of a_τ. A preliminary study has been conducted to estimate the contribution of the dominant sources of uncertainty. The *relative* uncertainty of each process given below should be normalized to the fractional contribution of that process in the signal plus background model, which will be done during the final fit.

The relative uncertainty on the muon scale factors for both the signal and the $\gamma + \gamma \rightarrow \mu^+ + \mu^- + \gamma$ background process is 4%. This includes the relative efficiency of the trigger, tracking, and identification of muons in data and simulation. For the charged pions, a tracking SF uncertainty of 2.4% is considered. The statistical uncertainty due to the limited size of the signal and $\gamma + \gamma \rightarrow \mu^+ + \mu^- + \gamma$ MC samples is 1.5% and 1.0%, respectively. The uncertainty in the luminosity measurement is measured to be 1.5%. The uncertainty in the calculation of the branching ratio of the tau-lepton decay channels is 0.6%.

The ABCD background estimation also depends on the categorization of events and therefore depends on the choice of N_{ch} categories and the precision of the HF energy threshold as the categorization criteria. The relative systematic uncertainty in the choice of the N_{ch} categorization is estimated to be 1.0%, while the HF scaling uncertainty is not well known and is under investigation. Furthermore, there is a 3-4% statistical uncertainty associated with the ABCD background estimation based on the limited number of events in the three control regions. This will decrease when using the full 2018 dataset.

The systematic uncertainties from the correction of the ABCD prediction is described in section 6.3.1, and the uncertainty on the categorization of signal events into ZDC categories based on an analysis of dimuon events is not yet accurately evaluated. The former is estimated to be about 2.5% for the full 2018 dataset, and the latter 1.8%.

Some of the systematic uncertainties can be constrained by analyzing the $\gamma + \gamma \rightarrow \mu^+ + \mu^-$ process in parallel and taking the ratio of the two channels or performing a simultaneous maximum likelihood fit. For instance, the scaling uncertainty of the MC simulation based on the luminosity measurement is the same for both processes and vanishes in the ratio. The same argument applies to the muon trigger uncertainty as well.

7 Prospects for future a_τ measurements

In this chapter, we discuss the prospects for measurements of the anomalous magnetic moment of the tau lepton (a_τ) by CMS during Run3 of the LHC and the next stage, the HL-LHC. The Run2 measurements discussed in chapters 5 and 6 are statistically limited, which motivates future measurements with significantly larger datasets of ultraperipheral PbPb collisions. Moreover, the possibility of analyzing new decay channels will further improve statistical precision. Finally, the CMS experiment, after upgrades for the HL-LHC, will offer a larger phase space of acceptance, higher reconstruction efficiency, and new possibilities to study all the decay channels of the PbPb $\rightarrow$ Pb($\gamma\gamma \rightarrow \tau^+\tau^-$)Pb process.

The significant improvement of a_τ measurements with the HL-LHC, the need for an upgraded CMS detector to handle the conditions of the HL-LHC, and specifically, the envisioned improvements in the tracking system, which will be shown in this chapter as crucial for the a_τ measurements, motivate the upgrade studies discussed in the following chapters.

7.1 Prospects for Run3 of the LHC

During the Run3 data-taking period of the LHC, three months of heavy ion collision data are envisioned over the years from 2023 to 2025, as seen in figure 7.1. With improved beam intensity, an integrated luminosity of about $2.2\,\text{nb}^{-1}$ is expected to be delivered to CMS per month [118], comparable to the total of $2\,\text{nb}^{-1}$ collected during Run2. Therefore, the size of the PbPb collision dataset from the LHC is expected to be 4 times larger by the end of Run3, halving the statistical uncertainty of the measurements.
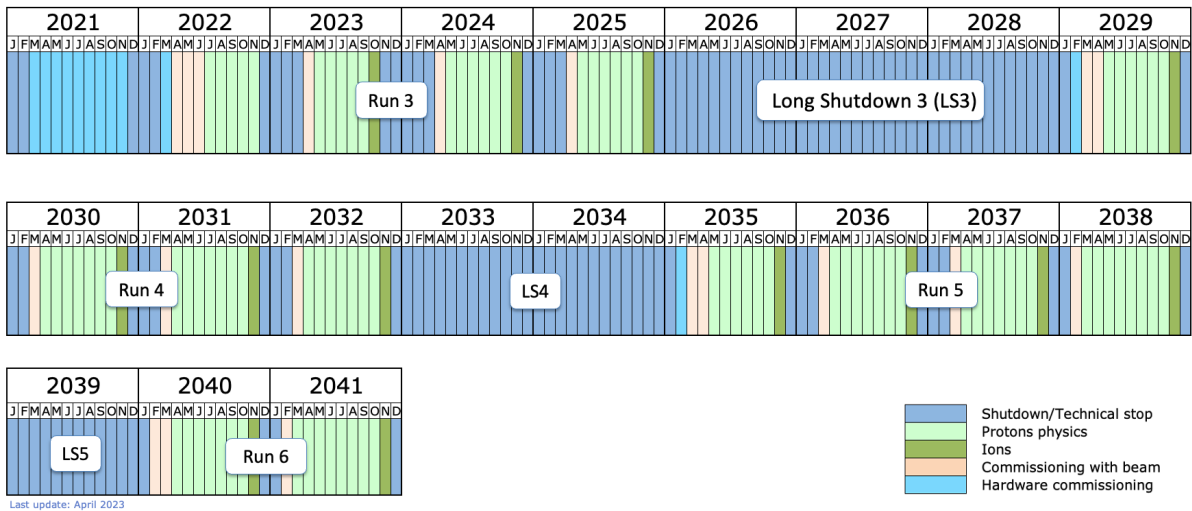
Figure 7.1: The updated schedule as of January 2022 with long shutdown 3 (LS3) to start in 2026 and to last for 3 years. HL-LHC operations are foreseen to end in 2041. A total of 12 one-month-long heavy-ion periods are scheduled. The figure is taken from reference [119].

Although no significant detector upgrade was envisioned for Run3 to improve detector accep-

tance and efficiency, improvements in the triggering system can further improve the available data size. In particular, the ZDC information is planned to be integrated into the trigger algorithm during Run3. The total energy deposited in each of the two ZDC detectors allows us to categorize the events based on the number of neutrons emitted on each side, as discussed in chapter 4, which can be used as a handle on the impact parameter of the ultraperipheral collisions. The specific target categories of neutron emission will be determined based on the available trigger bandwidth and the rate of events in each category.

Unlike *object-based* triggers, which target the decay products of the tau lepton, like the muon, *event-based* triggers like that of the ZDC target the main $PbPb \to Pb(\gamma\gamma \to \tau^+\tau^-)Pb$ process inclusively, independent of the decay channel. This allows us to record fully hadronic events in which both tau leptons decay to one or three charged pions. While fully hadronic events account for 42% of the ditau decays, they were not recorded in the Run2 dataset since tracking information was not available for Level-1 triggering, and no event-based trigger was implemented. The level of improvement in the size of dataset using the ZDC triggers is currently unknown, as the ongoing study on the trigger rates has not yet concluded on the most efficient way to trigger on the signal process using the ZDC, but with the lowest background rates.

7.2 Prospects for the high-luminosity LHC

CMS will undergo a major upgrade during the Long Shutdown 3 shown in figure 7.1, in preparation for the high-luminosity LHC (HL-LHC) era with increased beam intensity. The new detector is expected to improve in all subsystems to handle this higher intensity. The changes affecting the measurement of a_τ include an improved efficiency and acceptance of the detector that will be discussed in section 7.2.1 and new triggering possibilities which will be discussed in section 7.2.2.

7.2.1 Acceptance

The acceptance of the Phase2 CMS detector operating during the HL-LHC era will improve compared to the current Phase1 detector. This includes a new muon system that extends the pseudorapidity from $\eta < 2.4$ of the Phase1 detector to $\eta < 2.8$, a new calorimeter system that extends the pseudorapidity from $\eta < 2.4$ of the Phase1 detector to $\eta < 3.0$, and an improved tracking system that extends the pseudorapidity from $\eta < 2.5$ of the Phase1 detector to $\eta < 4.0$.

To assess improvements in the acceptance of $PbPb \to Pb(\gamma\gamma \to \tau^+\tau^-)Pb$ signal events, a MC simulation of this process generated by the SuperChic [115] generator has been used, while the tau lepton decays are simulated by PYTHIA8 [102]. The fraction of events in the accepted phase space of the Phase1 and Phase2 CMS detectors at the generator level represents the acceptance of the detector.

This study shows that the fraction of the accepted phase space of the Phase1 detector for the muon plus hadron decay channels discussed in chapter 6 is about 0.0038. Assuming that there is no improvement in the p_T thresholds for the Phase2 detector, and by only extending the pseudorapidity coverage, the acceptance improves by 15% to 0.0044. However, the Phase2 detector is able to reconstruct relatively lower-p_T muons and tracks, due to improvements in detector technology and the extension of the pseudorapidity coverage. Taking into account the expected p_T thresholds of the Phase2 detector, the acceptance of the muon plus hadronic channels reaches 0.0143 which is 3.8 times higher than the current Phase1 acceptance.

7.2.2 Track trigger

Figure 7.2 shows one of the results of this generator-level analysis. In this graph, the fraction of accepted PbPb $\rightarrow$ Pb($\gamma\gamma \rightarrow \tau^+\tau^-$)Pb signal events is shown assuming different p_T thresholds on the various decay products of the tau lepton. The muon and electron show similar behavior as a result of having similar branching ratios. Events with at least one object above the threshold of the object are accepted. While the acceptance decreases by applying a higher p_T threshold for all four objects, charged pions show a relatively higher acceptance at any fixed threshold. This motivates the development of *track triggers* to record events that contain charged pions without the need for a muon or electron trigger. For instance, it can be seen from the plot that the requirement of a 2 GeV charged pion gives the same acceptance as the requirement of a 1.2 GeV muon or electron.
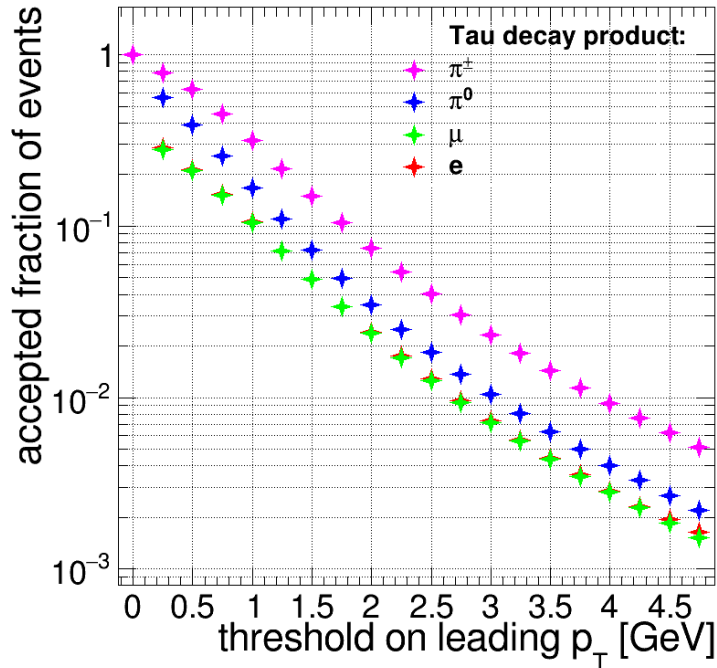
Figure 7.2: Fraction of events from the PbPb $\rightarrow$ Pb($\gamma\gamma \rightarrow \tau^+\tau^-$)Pb process with at least one tau-lepton decay product above the threshold, for various choices of decay products and thresholds.

A Level-1 track trigger will be implemented for the Phase2 CMS detector [120]. Each layer of the Phase2 outer tracking system consists of double-layered modules. In these modules, hits on the back and front layer are combined to from a 2-point vector called a *stub* with a position and a direction. Based on the stubs found in each layer, the angle of the track crossing the module can be determined. Assuming that the particle trajectories originate from the collision point, the p_T of the tracks can be estimated by each stub with a precision not quite as good as that of the full track reconstruction, but sufficient for triggering. Due to limitations in the number of track patterns that can be verified with the trigger system, and the fact that the number of patterns increases exponentially at low pt, the system is configured to only detect tracks with $p_T > 2$ GeV. If a track above this threshold is detected, it sends the information to the Level-1 triggering system to record the event.

Figure 7.3 (right) shows the efficiency of the Phase2 Level-1 track trigger for charged pions in the PbPb $\rightarrow$ Pb($\gamma\gamma \rightarrow \tau^+\tau^-$)Pb signal process. Signal events are generated with the
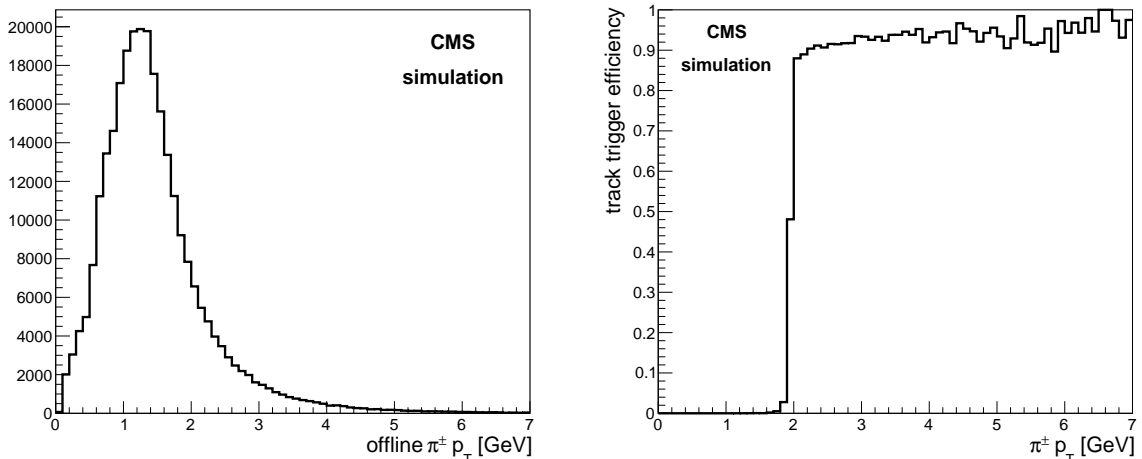
Figure 7.3: Left: Simulated p_T distribution of the offline reconstructed charged pion tracks using the Phase2 tracking system, for charged pions from the decay of tau leptons produced in one million PbPb $\rightarrow$ Pb($\gamma\gamma \rightarrow \tau^+\tau^-$)Pb events generated by Upcgen [116]. Right: Efficiency of the Level-1 track trigger to reconstruct and trigger on these tracks.

Upcgen [116] generator with the SM value of a_τ and the decay of tau leptons is simulated by PYTHIA8 [102]. A full simulation of the Phase2 detector material, geometry, and response provided by the CMSSW software is used to reconstruct particle objects and emulate the Level-1 track trigger of the Phase2 detector. The efficiency is calculated in each bin of p_T by dividing the number of tracks with that p_T that pass the Level-1 track trigger emulator and match an offline reconstructed track of a charged pion, by the number of reconstructed tracks with that p_T labeled as a charged pion.

The availability of track triggers opens the door for the measurement of fully hadronic decay channels of the PbPb $\rightarrow$ Pb($\gamma\gamma \rightarrow \tau^+\tau^-$)Pb signal process that has a total of a 42% branching fraction. Furthermore, the acceptance of muon plus hadron and electron plus hadron events will increase with the introduction of track triggers, as events with a charged pion above 2 GeV and a muon or electron below the trigger threshold for muons and electrons will be recorded. Based on the generator-level study mentioned above, and by adding track triggers with a 2 GeV threshold, the acceptance of the Phase2 CMS detector is estimated to be 0.027, which is 7 times greater than the acceptance of the current Phase1 detector for muon plus hadronic channels.

7.3 Sensitivity projection

In this section, the information obtained from the breakdown of uncertainty of the finalized CMS analysis described in chapter 5 is combined with the estimation of the improvements in Run3 and HL-LHC discussed in this chapter to obtain an approximate projection for future measurements in Run3 and HL-LHC. The statistical uncertainty on the measurement of the cross section and some dominant systematic uncertainties will be projected. Finally, projected limits on a_τ will be derived.

7.3.1 Statistical uncertainty

The statistical uncertainty of the measurement depends purely on the size of the dataset, making it easy to extrapolate. The relative statistical uncertainty scales with $\frac{1}{\sqrt{N}}$ for N signal events.

This uncertainty will be improved by increasing the total luminosity, adding new decay channels, and enlarging the accepted kinematic phase space.

As seen in figure 7.1, three periods of heavy-ion data taking during Run3 and nine additional periods during HL-LHC are scheduled. A minimum integrated luminosity of $2.2\,\text{nb}^{-1}$ is expected for each period [118]. Therefore, the total integrated luminosity of Run3 is expected to be 17 times higher than that of the 2015 dataset.

While the tolerated rate of the ZDC trigger has not yet been concluded, if they are 10% efficient in recording events with at least one emitted neutron, about 3% of $\text{PbPb} \to \text{Pb}(\gamma\gamma \to \tau^+\tau^-)\text{Pb}$ can be recorded, as determined by the neutron emission expected from the STARlight MC generator. As event-based triggers have no p_T threshold on the tau-lepton decay products, the ZDC trigger would then record about 3% of fully hadronic events and improve the efficiency of muon and electron triggers. Therefore, an increase as much as 4-fold in the acceptance and efficiency of events in Run3 compared to Run2 could be possible. Considering all the factors discussed, the statistical uncertainty in the cross section in Run3 would then be as much as 8 times smaller than the 12% statistical uncertainty obtained in the 2015 analysis.

According to the studies discussed in section 7.2 on the improvements in the Phase2 CMS detector, the fraction of signal events recorded with the HL-LHC would be seven times greater than the number of muon plus hadron events in Run2, which itself is four times larger than the number of μ+3prong events. It can be deduced from the left plot of figure 7.3 that, in the signal process, most charged pions are below the $2\,\text{GeV}$ threshold of the Level-1 track trigger and will not be recorded especially in the fully hadronic channel. Therefore, event-based triggers, such as the ZDC trigger, can also be crucial during the HL-LHC era. Overall, the expected statistical uncertainty for the HL-LHC dataset could be as much as 25 times lower than the 12% statistical uncertainty obtained in the 2015 analysis.

7.3.2 Systematic uncertainty

In the measurements of the $\text{PbPb} \to \text{Pb}(\gamma\gamma \to \tau^+\tau^-)\text{Pb}$ cross section using muon plus hadronic channels, the dominant sources of uncertainty are uncertainties in the muon scale factors, tracking scale factors, luminosity, and statistical uncertainty in the background model driven by data. All these sources of systematic uncertainty are rooted in the limited size of the dataset used to estimate them. Therefore, they can be scaled down similarly to the statistical uncertainties.

Improvements in the algorithms and detectors used to estimate these sources can further reduce the systematic uncertainty. For instance, the uncertainty in the measurements of luminosity should decrease by the inverse square root of luminosity as the size of the dataset if the measurement technique remains the same. Therefore, as the uncertainty on the luminosity of the 2015 dataset was 5%, this uncertainty for the 2018 dataset could be expected to be $\frac{5\%}{\sqrt{3}} = 3\%$. However, due to improvements in measurement tools and techniques, this uncertainty is 1.5% for the 2018 dataset.

Another contributing factor in reducing the systematic uncertainty of the cross-section measurement is taking the ratio of the number of events from the signal process to the number of events from another precisely measured process in the signal phase space. For instance, if the ratio of events from the $\text{PbPb} \to \text{Pb}(\gamma\gamma \to \tau^+\tau^-)\text{Pb}$ process to the $\text{PbPb} \to \text{Pb}(\gamma\gamma \to \mu^+\mu^-)\text{Pb}$ process is taken, the luminosity as a common scale for both processes cancels and the systematic uncertainty in luminosity is removed. A similar approach can be taken to some extent for muon and track uncertainties, especially the muon trigger uncertainty as the dominant contribution

to the muon scale factor uncertainty. The statistical uncertainty of the data-driven background models are not expected to reduce significantly using this method, but they can be almost entirely removed if a reliable simulation of the background processes is developed for future analyses.

Without improvements in the analysis techniques and measurement tools of systematic sources, the systematic uncertainties of the cross section measurements in Run3 and HL-LHC are expected to be lower than the 10% systematic uncertainty of the 2015 analysis by factors of up to 8 and 25, respectively, similar to the statistical uncertainty. However, the sources of systematic uncertainty discussed here will most likely be negligible compared to the statistical uncertainty of the measurement given the future improvements discussed above. Therefore, the dominant sources of systematic uncertainty are likely not statistically driven during the late stages of HL-LHC. These include the uncertainties on the branching ratio of tau decays and more importantly the theoretical uncertainties affecting the kinematic distributions in the $PbPb \rightarrow Pb(\gamma\gamma \rightarrow \tau^+\tau^-)Pb$ simulations, including the uncertainties on the form factors of the Pb ions and their photon flux.

7.3.3 Limits on a_τ

Both the cross section and the kinematics of tau leptons in the $PbPb \rightarrow Pb(\gamma\gamma \rightarrow \tau^+\tau^-)Pb$ process depend on a_τ. In the finalized 2015 analysis discussed in chapter 5, only the sensitivity to the cross section was utilized to translate the limits on the cross section to the limits on a_τ. However, a similar analysis using the ATLAS experiment with a similar uncertainty in the cross section for the same decay channel achieved three times better limits on a_τ [121].

As discussed in section 7.3.1, the statistical uncertainty of the cross section measurement in Run3 (HL-LHC) could be as much as 8 (25) times lower than the 12% statistical uncertainty of the 2015 analysis. This estimation will become more clear with the near-future developments of the event-based triggers like the ZDC trigger. As the current dominant sources of systematic uncertainty are statistically driven, they are expected to decrease by the same factor. However, the effect from these sources will most likely be negligible with new analysis techniques and tools for evaluating the uncertainty, and the dominant systematic sources would mainly come from limitations in the theory. Overall, a conservative estimate of the systematic uncertainty in the cross section measurement in Run3 (HL-LHC) is 8 (25) times lower than the 10% systematic uncertainty of the 2015 analysis.

Taking into account potential improvements in the statistical and systematic uncertainties, the total uncertainty of the cross section measurement in Run3 (HL-LHC) could be as small as 19 (6) per mil. Assuming a linear sensitivity of cross section and kinematic shapes on a_τ for small values of a_τ, the uncertainty on a_τ considering both sensitivities would then be estimated to be $a_\tau = (1 \pm 3) \times 10^{-3}$ for Run3 and $a_\tau = (12 \pm 9) \times 10^{-4}$ for the HL-LHC. Should no BSM effects occur, this measurement would still allow an approximate verification of the dominant correction to a_τ from the one-loop QED effect, which is $\frac{\alpha}{2\pi} \approx 0.00116$.

8 The CMS Phase2 Pixel Detector

In order to maintain and even improve its performance in tracking and vertexing in conditions with up to 200 pileup interactions, the CMS tracking system, and in particular the CMS inner tracker or pixel detector, will have to be completely replaced before the start of the HL-LHC. The target specification for the design of this detector will be discussed in section 8.1. In section 8.2, the pixel modules as the building block of the detector consisting of sensors and readout chips are discussed. In addition to the final specifications of the pixel modules, the prototypes that were studied and the options for the sensor pitch size, sensor bias scheme, and readout are discussed.

8.1 Detector design

The upgraded detector will have a six-fold increase in granularity, which will reduce the occupancy of individual channels and improve the resolution of cluster hits in both the ϕ and z directions, resulting in improved tracking and vertexing. The upgraded detector must withstand a radiation dose of 1.9 Gy and a hadron fluence of 3.5×10^{16} neq/cm^2 for a total integrated luminosity of $4000\,\mathrm{fb}^{-1}$. Therefore, it must be designed to be resistant to radiation, with the possibility of replacing degraded parts, especially the first layer which receives the highest dose of radiation. The acceptance of the improved detector in the forward region will increase in $|\eta|$ from the current ≈ 2.5 up to ≈ 4, which improves the measurement of forward objects such as jets that can be mis-reconstructed due to pileup, and enlarges the accepted phase space of many future measurements. This detector will also contribute to the luminosity measurements in real time by means of hit counting.
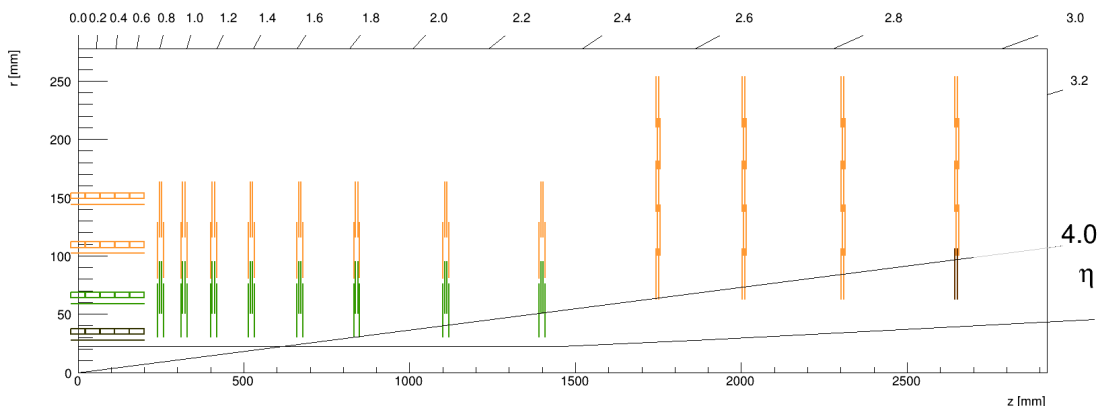
Figure 8.1: Sketch of one quarter of the pixel detector layout in the r-z view. Green lines correspond to modules made up of two readout chips (1×2) and orange lines represent larger modules with four chips (2×2). The figure is taken from reference [120].

As shown in figure 8.1, the detector consists of a four-layer barrel section (referred to as the Tracker Barrel Pixel Detector, TBPX), eight small double discs per end (referred to as

the Tracker Forward Pixel Detector, TFPX), and four large double discs per end (referred to as the Tracker Endcap Pixel Detector, TEPX). In the TBPX, the pixel modules are arranged in "ladders". In each layer, adjacent ladders are staggered in radius to achieve r-ϕ overlap between ladders. The modules of a ladder do not overlap in z. A projective gap at $\eta = 0$ is avoided by mounting an odd number of modules along z and by splitting the barrel mechanics in z into slightly asymmetric halves. In the TFPX and TEPX, the modules are arranged in concentric rings. Each double disc physically consists of two discs, which allows the modules to be mounted in four planes, with overlaps in r and r-ϕ. Each disc is split into two halves and these D-shaped structures are called "dees". The TEPX will provide the required luminosity measurement capability through an appropriate implementation of the readout architecture. The complete pixel detector will have an active area of about $4.9\,\text{m}^2$. The number of layers crossed by particles originating from the luminous region is shown in figure 8.2, both for the inner tracker alone and for the entire tracker.
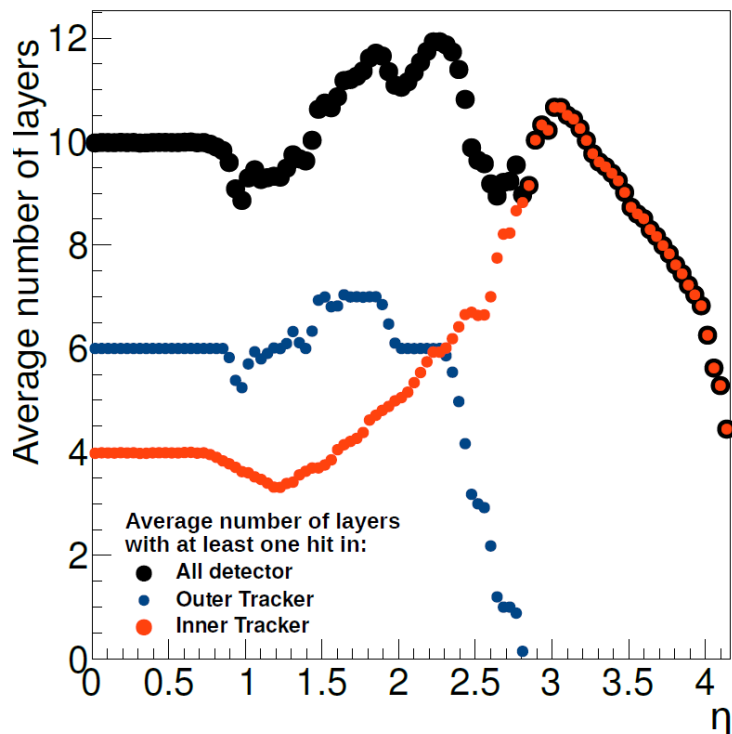
Figure 8.2: Average number of module layers traversed by particles, including both the inner tracker (red) and the outer tracker (blue) modules, as well as the complete tracker (black). Particle trajectories are approximated by straight lines, using a flat distribution of primary vertices within $|z_0| < 70\,\text{mm}$, without including the effects of multiple scattering. The figure is taken from reference [120].

8.2 Pixel Modules

A pixel module consists of a pixel sensor, several readout chips, a flex circuit, and a mechanical support. It constitutes the basic unit of the pixel detector. The sensors are bump-bonded to the readout chips. A thin, high-density flex circuit, also known as a high-density interconnect (HDI), is glued onto the sensor and wire-bonded to the readout chips. It transmits the data of the pixel module to the circuit board containing a chain of pixel modules, provides clock, trigger, and control signals, and distributes power to the readout chips. The final design of the CMS readout chips, called the CROC, has an active area of $21.7 \times 18.6\,\text{mm}^2$. Each pixel module

will consist of either 2 CROCs in a 1×2 format or 4 CROCs in a 2×2 format. The choice of using 1×2 or 2×2 modules is based on the expected data rates, and is depicted in figure 8.1.

8.2.1 Pixel Sensors

Different sensor options were considered and studied for use in different parts of the detector. The main options were two different pixel sizes, both with the same area, and the choice between planar and 3D sensors. Thin planar n-in-p type silicon sensors provide good hit resolution, tracking, and vertexing while being relatively radiation hard. The silicon sensors have a pitch size of $50 \times 50 \, \mu m^2$ or $25 \times 100 \, \mu m^2$, while the long side of the pixels in the latter geometry points along z in the barrel and along r in the endcaps. The factor of six reduction in the pixel size from the $100 \times 150 \, \mu m^2$ used in the Phase0 and Phase1 pixel detectors allows low occupancy and improved track separation in dense environments such as high-p_T jets.

In addition to the study of planar sensors, an alternative was explored using 3D silicon sensors, which offer intrinsically higher radiation resistance due to a shorter charge-collection distance [120].

Several studies have been carried out to compare the options of square pixels ($50 \times 50 \, \mu m^2$) and rectangular ($25 \times 100 \, \mu m^2$) pixels [122]. Figure 8.3 shows the drawing of two adjacent pixels in the $25 \times 100 \, \mu m^2$ and $50 \times 50 \, \mu m^2$ pitch designs and how they can be bonded to the readout chip with a $50 \times 50 \, \mu m^2$ pitch size. Although they generally show similar performance in tracking, there is a trade-off between primary vertex discrimination, where the square sensors with higher granularity in z perform better, and the resolution in the impact parameter, where the rectangular sensors with better granularity in ϕ perform better.

One of the factors involved in the comparison of $50 \times 50 \, \mu m^2$ and $25 \times 100 \, \mu m^2$ pitch size options is the charge induction into neighboring pixels, which is higher for the $25 \times 100 \, \mu m^2$ pitch size option and will be discussed in chapter 10. Moreover, towards the edges of the barrel layers, especially for the first layer, square pixels would result in very long clusters. The tracks in that region are more parallel to the pixel surface and therefore, their effective path is close to the pitch of the sensor along z, while perpendicular tracks with low pseudorapidity pass through the $150 \, \mu m$ thickness of the sensor. Therefore, the path of the track inside the $50 \times 50 \, \mu m^2$ sensors is just over $50 \, \mu m$ compared to $100 \, \mu m$ for $25 \times 100 \, \mu m^2$ sensors, which would limit the range of the operational threshold of the chip and increase the rate of broken clusters after radiation. In addition, such long clusters would require a larger bandwidth to read out the data. Overall, it has been decided to use only the $25 \times 100 \, \mu m^2$ pitch size in all sections of the pixel detector.
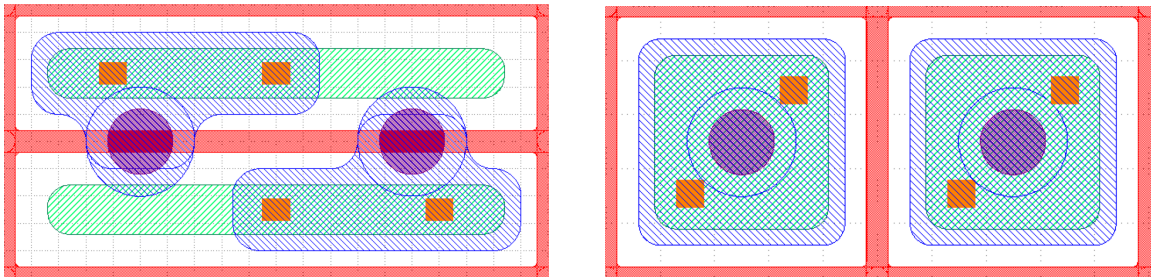

Figure 8.3: Drawing of two adjacent pixel cells for sensors from the HPK submission with pixel size $25 \times 100 \, \mu m^2$ (left) and $50 \times 50 \, \mu m^2$ (right). The n+ implants are shown in green, the metal layers in blue, the p-stop areas in red, the contacts in orange, and the bump bond pads in purple. The figure is taken from reference [120].

8.2.1.1 Planar

While thicker silicon sensors have an initial advantage of higher charge deposition, after enduring high radiation doses of up to 1.9 Grad and 3.5×10^{16} neq/cm^2 for a luminosity of 4000 fb^{-1}, the effective charge collected by silicon sensors begins to decrease significantly for thick sensors due to the effects of charge trapping, which prevents the ionized electrons from drifting to the collection wells. Therefore, the silicon sensors for the CMS Phase2 pixel detector will have an active thickness as low as 150 μm compared to 270-285 μm for the Phase0 and Phase1 detectors. In addition to higher charge collection after radiation and therefore higher efficiency, thin planar sensors require lower bias voltages, reducing overall power consumption and leakage current. Figure 8.4 shows a schematic of the planar sensors with n$^+$ wells for the collection of ionized electrons in the bulk, as well as p-stop regions for the isolation of the n$^+$ wells.

One consideration in designing planar sensors is that they require bias voltages of up to 800V to maintain an acceptable efficiency after irradiation during the HL-LHC. Therefore, it is important to ensure that any sparking between the detector components is prevented at such bias voltages.
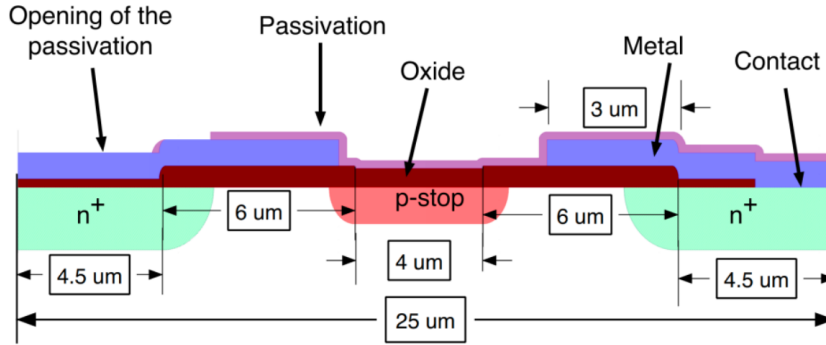
Figure 8.4: Schematic of the HPK planar sensors with n$^+$ wells and p-stop regions for the isolation of the n$^+$ wells.

Planar sensors from various vendors have been thoroughly tested in various designs and with different irradiation doses to ensure that they meet the requirements in terms of efficiency after radiation, spatial resolution, and leakage current. In particular, 6-inch wafers of planar silicon sensors from Hamamatsu Photonics K.K. (HPK) [123] and Fondazione Bruno Kessler (FBK) [124] companies, as well as 8-inch wafers from LFoundry [125] have been tested, with the latter expected to be more cost-effective due to the larger wafer size, and offering more flexibility in the sensor design due to the use of passive CMOS technology, which is widely used in industry.

8.2.1.2 3D

In the 3D sensor design, the bias voltage is applied through vertical p$^+$ columns within the silicon volume that reach the biased backside of the sensor, as seen in figure 8.5. This reduces the effective distance between the electrodes and decouples this distance from the sensor thickness, allowing for relatively lower depletion voltages, less charge trapping, higher charge collection, and lower power consumption. The ionized electrons are collected by n$^+$ columns inside the volume that serve as readout electrodes and stop 25-30 μm above the backside.

Although 3D sensors are relatively more radiation-hard compared to planar sensors, the
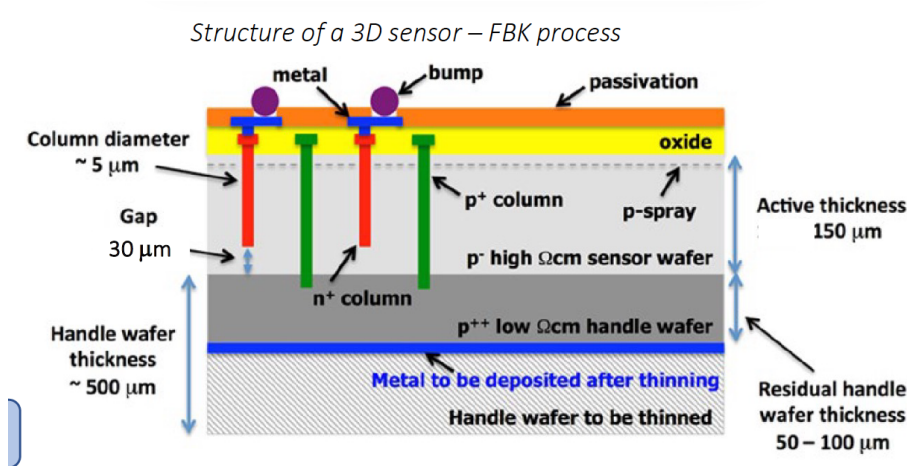
Figure 8.5: Schematic of the FBK 3D sensors with n^+ columns for the collection of ionized electrons in the bulk, and deep p^+ columns reaching the backside and providing the bias voltage inside the silicon volume.

complexity of their production procedure results in lower yields and higher production cost. Therefore, they will be utilized only in the first layer of the TBPX that receives the highest dose of radiation.

8.3 Pixel detector readout chip

In order to read out charge from the pixel detectors, a radiation-hard readout chip called the CROC (CMS ReadOut Chip) is bump-bonded directly to the sensors. The signal induced by ionized electrons in the silicon sensor is collected by the n-in-p implants as shown in figure 8.4 for planar and figure 8.5 for 3D sensors, and is carried out through the bump bonds to the readout chip. This analog signal is amplified, and the time over threshold (ToT), defined as the time during which the signal is above a certain threshold, is digitized into 4 bits per bunch crossing (at 40 MHz). The ToT provides a measure of the amplitude of the signal. Each CROC has an active area of $21.7 \times 18.6 \, \text{mm}^2$ with a periphery of $21.7 \times 2 \, \text{mm}^2$, and is manufactured using 65 nm CMOS technology.

The readout chip has an internal charge injection circuit that plays a crucial role in the characterization of the chip in terms of ToT digitization, noise, threshold measurement, threshold equalization across the pixel array, and charge-to-ToT calibration.

The readout chips are designed and developed by the RD53 Collaboration for both CMS and ATLAS Phase2 detectors. The first prototype of this chip was called RD53A and consisted of three Front Ends (FE) named synchronous, linear, and differential [126]. It was thoroughly studied for about 4 years in many lab and test beam measurements in terms of noise, threshold equalization, radiation hardness, power distribution, and data loss, and other measures of performance. The CROC is designed based on the RD53A implementation of the linear FE and tuned to the specific requirements of CMS. It benefits from many improvements, particularly in threshold equalization, ToT digitization, noise, and flexibility in the readout of both small and large signals.

Since the readout chip must operate under high-rate conditions of the HL-LHC, it uses a high-intensity, low-power CMOS technology with a low supply voltage of 1.2 V and a current of
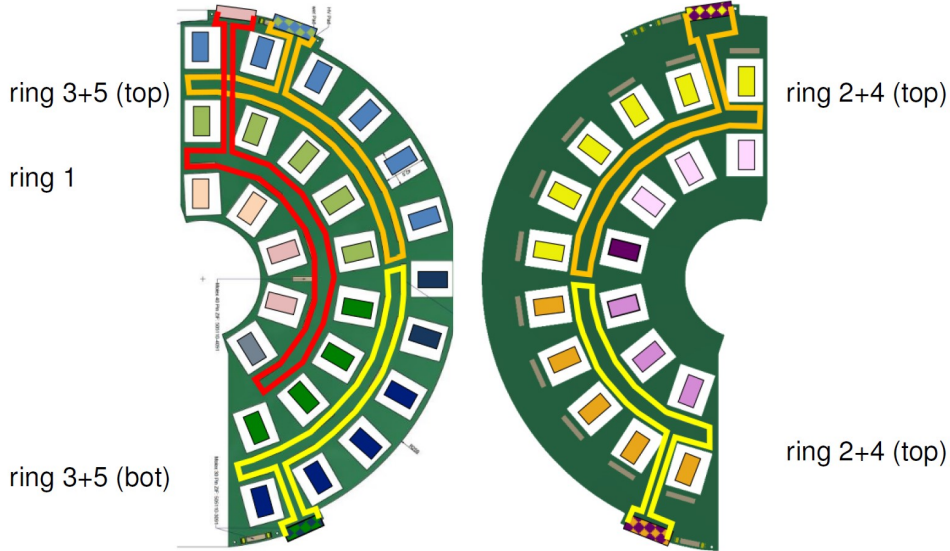
Figure 8.6: Serial-powering chains of the TEPX disk for the half disk incorporating rings 1, 3, and 5 (left) and the half disk incorporating rings 2 and 4 (right). The longest chain consists of 11 2×2 pixel modules, 5 in ring 3 and 6 in ring 5.

2 A per chip [127]. The classical parallel powering system is not suitable for such high currents, and DC-DC converters are not stable enough to operate at such high radiation doses. Therefore, a serial powering system is employed where the 2 A current per chip (8 A for quad modules with 4 parallel chips) is supplied to chains of up to 11 pixel modules, as shown in figure 8.6 for the TEPX. Each of the two analog and digital Shunt-LDO regulators in a chip is composed of a shunt current regulator and a low-dropout (LDO) regulator. Each Shunt-LDO takes the input 1 A and regulates the voltage to the required 1.2 V. While this powering system has many advantages in terms of radiation hardness and material budget, if a full pixel module is broken and creates an open circuit, the entire chain of pixel modules would not be functional. However, various tests show that the chips are often still conductive even after being broken, and if even one chip from a pixel module is conductive, which is much more likely than a complete breakdown, the remaining chips and certainly the chain of pixel modules would not suffer.

In order to decide on the specifications of the CROC module including the powering scheme, front end, and the tuning handles, many prototypes of pixel modules with RD53A and CROC readout chips and various design options have been tested both in the lab and using beams of charged particles. These studies will be explained in more detail in chapters 9, 10, and 11.

9 Characterization of the readout chip

As a research and development (R&D) campaign to identify designs that meet the requirements of CMS at the HL-LHC, the CMS tracker upgrade group designed, characterized, and tested various prototypes of pixel modules with $50 \times 50 \, \mu\mathrm{m}^2$ and $25 \times 100 \, \mu\mathrm{m}^2$ silicon sensor pitch sizes read out by the RD53A chip as the first prototype of CMS and ATLAS Phase2 readout chips (ROC), and the CMS readout chip (CROC) as the final ROC to be used in the CMS Phase2 pixel detector.

The RD53A prototype chip consists of three front ends (FE) named synchronous, linear, and differential. CMS has chosen the linear FE after a thorough performance study of the three FEs in tuning and operation, and it is used as the FE of the CROC. After a brief description of the linear FE in section 9.1, the characterization and tuning procedure of the readout chip will be discussed in section 9.2.

9.1 The linear front end

A schematic diagram of the linear FE is shown in figure 9.1. The readout chain of a pixel begins with a low-power charge sensitive amplifier (CSA) that features a Krummenacher feedback circuit in order to cope with the increased leakage current of the sensor after irradiation. The output of the CSA is digitized using a high-speed current comparator and transimpedance amplifier, and is then processed by the digital pixel logic including a 4-bit Time-over-Threshold (ToT) counter (not shown in the figure). The global threshold for all pixels is applied to the V_{th} input of the comparator. A 4-bit binary weighted digital-to-analog converter (DAC) allows for per-pixel threshold adjustment (trimming DAC, TDAC). All pixels of the RD53A chip are equipped with an individual charge injection circuit for testing and calibration purposes.

9.2 The characterization procedure

The general testing procedure of the RD53A pixel modules consists of the following steps. First, the pixel modules are prepared in a process that includes bump-bonding the silicon pixels to the RD53A readout chip, and wire-bonding the RD53A chip to the designated printed circuit board (PCB) shown in figure 9.2, which facilitates the user interaction with the chip in both power distribution and readout.

Secondly, the chip's global settings are tuned using the PCB and a data acquisition (DAQ) system. There are two DAQ softwares developed to characterize the RD53A chip and readout, and interpret the data, and each is accompanied by its corresponding FPGA and hardware. The results discussed here are obtained with the BDAQ53 software [128], while CMS has developed a dedicated CMS DAQ system called Ph2_ACF [129] for prototype development studies, as well as for readout of the final pixel modules of the CMS Phase2 tracker.
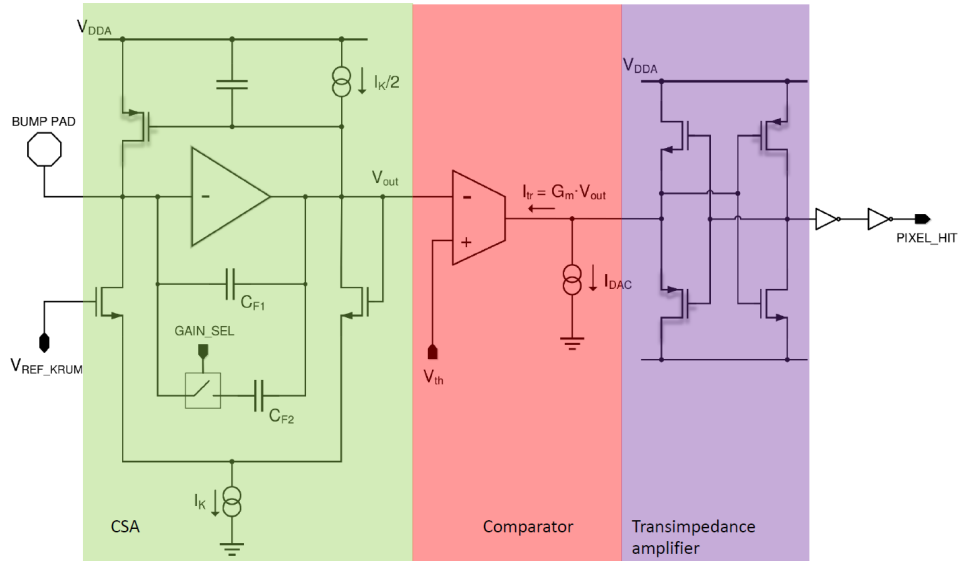
Figure 9.1: Schematic diagram of the RD53A Linear Front-end. Figure taken from reference [126].

9.2.1 Tuning global chip parameters

The RD53A ROC is designed for serial powering, which is the chosen powering scheme for the CMS inner tracker Phase2 upgrade. However, the RD53A chip also offers the possibility of bypassing the internal power regulator to directly supply the bias voltages from external power supply units. The input voltage required to start the RD53A chip is 1.2 V for both the analog and digital sections. This voltage can be supplied directly, but there is also the possibility of using the low dropout (LDO) regulator of the chip, activated by using jumpers on the PCB, which inputs a fixed voltage of 1.8 V and regulates it to values around 1.2 V. After establishing communication with the chip, this regulated voltage can be fine-tuned by modifying one of the digital-to-analog converter (DAC) settings of the chip. Starting up and establishing a communication with irradiated modules is relatively harder, and in practice, a larger input analog voltage, preferably through the direct mode, helps with successfully establishing a connection. After establishing the connection, the values of the reference current (I_{ref}) and voltage (V_{ref}) must be tuned to 4 μA and 0.9 V, respectively, using the corresponding jumpers on the PCB. These values have to be monitored and re-tuned after each modification of the input voltages, especially the digital input voltage.

9.2.2 Efficiency measurement and dead pixel masking

The efficiency of a pixel module is defined as the number of pixel hits read out over the total number of expected hits within its acceptance. The RD53A pixel module is equipped with an internal charge injection circuit for each pixel, which allows the evaluation of the efficiency for both digital and analog sections separately.

A healthy pixel is expected to detect and return a hit if and only if an adequate charge has been injected into it. If a pixel does not detect a digital or analog hit, it would be tagged as a dead pixel and removed from the set of available pixels for further characterization tests. This set is saved in a file called the *mask file*, which includes some pixel-to-pixel DAC values and whether a pixel is *enabled* for charge injection and readout, or otherwise *masked*. If a pixel returns a hit irrespective of the injected charge into it, which could be either due to noise,
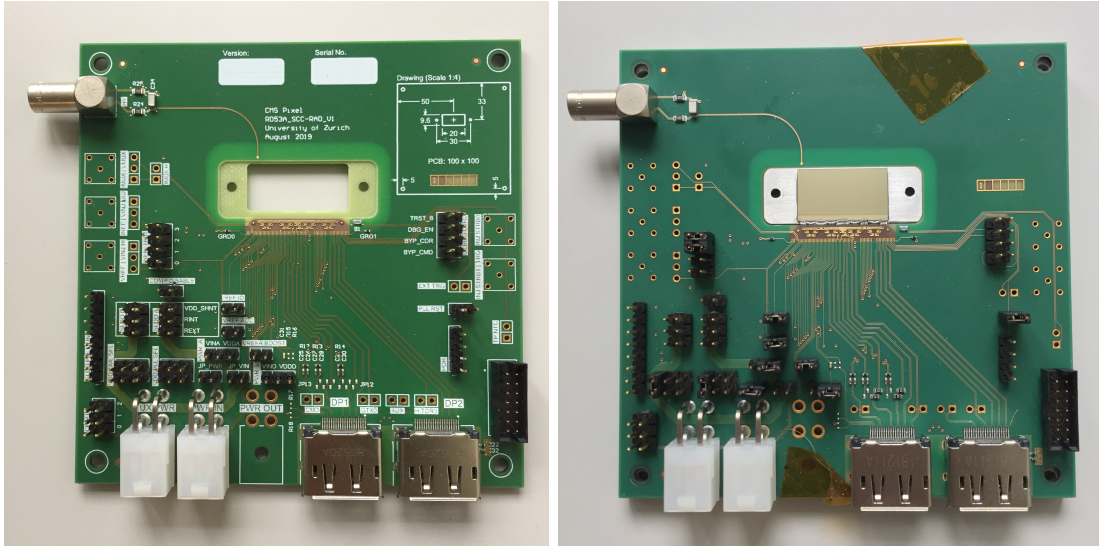
Figure 9.2: The PCB designed for readout, tuning, and power distribution of RD53A pixel modules. Left: The empty PCB. Right: After mounting an RD53A module wire-bonded to the PCB.

especially in irradiated pixel modules or being stuck, it will also be masked out for further tests to make sure it does not fill up the readout bandwidth and hence lower the efficiency of other pixels.

9.2.2.1 Digital scan

After tuning the global chip configurations, the first pixel-to-pixel scan is the digital scan, which injects charge into the digital sector of the ROC pixels and reads out the digital hits to evaluate the efficiency. This measurement is quite fast as the efficiency of individual pixels is not measured one by one, but rather follows an injection pattern that ensures that the injection and readout of neighboring pixels do not affect the measurement, while maximizing the number of pixels being simultaneously measured. As this scan only corresponds to the digital sector of the ROC, there is no need to apply a bias voltage to the sensor beforehand and can be done even with *bare* ROCs without any silicon sensor attached. The output of this scan is the average occupancy or efficiency of the pixel module. In addition, dead or stuck pixels will be marked in the mask file as disabled. User-specified DAC values are sent to the chip at the beginning of each scan, possibly modifying I_{ref} from the set value in section 9.2.1. Therefore, following the first scan, usually the digital scan, I_{ref} should be monitored using the jumpers on the PCB, and re-tuned by the DAC configurations in the software if needed.

9.2.2.2 Analog scan

If the result of the digital scan is satisfactory, for the pixels enabled in the output mask file of the digital scan, the next step is to inject charge into the analog sector of the ROC pixels and evaluate their efficiency. Similar to the digital scan, charge injections follow injection patterns to minimize the measurement time.

The amount of injected charge can be set by the user in units of calibration voltage (VCAL). The injected charge, ΔVCAL, is determined after subtracting the reference VCAL value, $\mathrm{VCAL_{ref}}$. There is a linear conversion between ΔVCAL and the number of injected electrons, whose slope and offset depend on V_{ref}. Therefore, to ensure a consistent and comparable characterization

procedure for all pixel modules, the V_{ref} should be equal for all of them. Furthermore, since the ground of the ROC should not be affected by the sensor, enough bias voltage needs to be applied to the sensor to deplete it before the analog scan, to reduce the capacitance between the ROC and sensor and the resulting fluctuation of the ROC ground.

After the analog scan, the efficiency of individual pixels is determined and the mask file is updated with new dead and stuck pixels. Moreover, the analog scan returns the time-over-threshold (TOT) representing the amplitude of the signal for each injection and each pixel. The TOT is digitized into values of 0 to 14 for the RD53A readout chip. It is recommended to calibrate the gain of the ROC by modifying the Krumenacher current, driving the slope of the return to the baseline. In this way, an average TOT of 6 is achieved for an injected charge of 10,000 electrons, the most probable number of ionized electrons for a minimum ionizing particle passing through a $150\,\mu m$ thick silicon sensor. This is to make sure that the most probable amount of deposited charge in the sensor is well within the accepted TOT range. The injected charge should be lower for irradiated modules, as the most probable number of electrons collected from an irradiated sensor is lower due to radiation-induced defects that trap drifting charges.

9.2.3 Threshold measurement

As seen in figure 9.1, the signal amplitude in the linear FE is compared to a threshold voltage called V_{th}. The global threshold voltage for all pixels in the linear FE is set using the *Vthreshold_LIN* DAC setting. To measure this threshold in units of ΔVCAL or equivalently electrons, one needs to perform a threshold scan.

The threshold scan consists of a chain of analog scans with various amounts of injected charge specified by the user with a range and step length of ΔVCAL. For each pixel, the analog scan with a very low amount of injected charge results in 0 efficiency, and for high enough injected charges, the efficiency is 1. When increasing the amount of injected charge, one expects a turning point around the injected charge corresponding to the threshold voltage, in which the efficiency goes from 0 to 1. In practice and due to the presence of noise, the dependence of efficiency of an individual pixel as a function of injected charge follows an error function (S-curve), the 50% level of which is used to determine the threshold in units of ΔVCAL or electrons.

Figure 9.3 (left) shows the overlaid S-curves corresponding to all pixels in the linear FE with a specific global threshold voltage. After fitting an error function to each S-curve, the distribution of the charges corresponding to a 50% threshold value is obtained and can be seen in figure 9.3 (right). The measured threshold charges show pixel-to-pixel variations which can be mitigated to some extent and will be explained in section 9.2.4.

While the S-curve of a pixel is in the range of 0% to 100% for healthy pixels, it does not always cover the full range of occupancy. For instance, a *dead* or *stuck* pixel does not detect any amount of injected charge and its S-curve stays at 0%. On the other hand, noisy pixels can be triggered and detect a fake signal even without charge injection or an over-threshold amount of charge. Therefore, the occupancy of such pixels can go above 100%. If the noise is too high, the bandwidth of the pixel readout can be full, increasing the dead time of the pixel and lowering the chance of detecting new signals. If the detected charge stays above the threshold for a long time, the readout will assume a long and strong signal and will not detect the new ones. Therefore, noise can also lower the effective occupancy, resulting in S-curves with a plateau at an occupancy between 0% and 100%. The chance of having dead, stuck, and noisy pixels is higher in irradiated modules, as seen in figure 9.4, and require a more careful masking
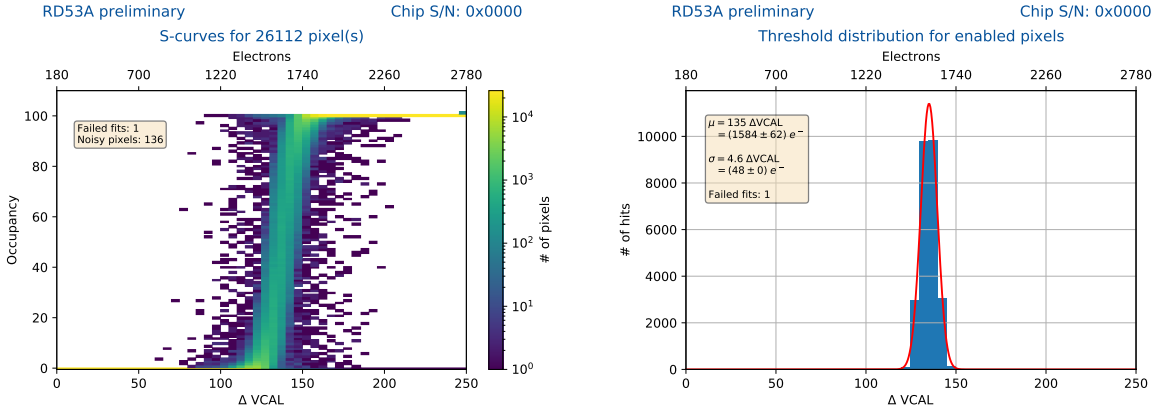
Figure 9.3: Left: S-curves corresponding to the pixels in the linear FE of an unirradiated RD53A pixel module. The occupancy increases from 0% at low injected charge, ΔVCAL, to 100% at high charges following an error function centered on the corresponding threshold of the pixel. Right: The distribution of *threshold*, defined as the charge corresponding to the 50% occupancy of each pixel. The 50% point for each pixel is found after fitting an error function to its corresponding S-curves in the left plot.

and tuning procedure. Another cause of fake occupancy is the charge induction into neighboring pixels which will be discussed in chapter 10.
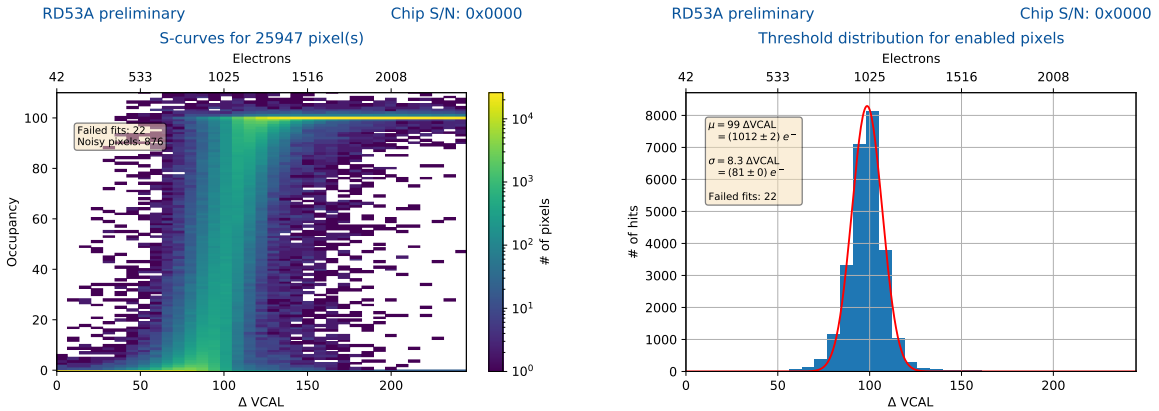
Figure 9.4: S-curves and threshold distribution for an RD53A pixel module irradiated to the fluence of 8.6×10^{15} neq/cm^2, which is expected for the first layer of TBPX after a luminosity of $1000\,\mathrm{fb}^{-1}$, which will be delivered by the early years of the Run5 of the LHC.

In addition to the pixel-to-pixel variations of the threshold, for each value of injected charge, the output signal amplitude represented by the TOT can also vary from pixel to pixel. However, this does not affect the S-curve, which is based merely on the occupancy and not the amplitude of the signal. The dependence of the TOT on the injected charge will be further discussed in section 9.2.6.

9.2.4 Threshold equalization

The average threshold charge for all pixels of the linear FE can be modified by the *Vthreshold_LIN* DAC setting. However, as seen in figure 9.3, the real threshold charge is in practice different from pixel to pixel. This variation can be problematic because it means that given a certain amount of charge deposited in the sensor, the possibility of detecting this signal, represented by the efficiency, is different from pixel to pixel, resulting in a non-homogeneous response

in the detector. The threshold is expected to be tuned as low as possible to increase the global efficiency of the detector, while being high enough to remove the noise in the detector. Having large pixel-to-pixel variations of the threshold means that while some pixels with low effective threshold are filling the tolerable bandwidth for occupancy, the global threshold is still not low enough to reach the desired efficiency for the detector.

To mitigate pixel-to-pixel variations of the threshold compared to the global V_{th}, a 4-bit trimming DAC (TDAC) is assigned to each pixel, which allows fine-tuning of the threshold. A DAC configuration of the RD53A called *LDAC_LIN* sets the least significant bit of the in-pixel threshold TDAC. In other words, the threshold for each individual pixel is the global V_{th}, plus the corresponding TDAC value of the pixel weighted by LDAC_LIN, which is set globally by the user. The effective step length determined by LDAC_LIN also depends on chip settings such as I_{ref}, which should be set consistently for all studied ROCs. It also depends on temperature, which means that for irradiated modules typically running in a cold box, relatively higher values of LDAC_LIN have to be set by the user.

The equalization of the threshold values within the pixels starts with a threshold scan with all TDAC values in the middle of the TDAC range (7 for the RD53A linear FE with a 4-bit TDAC) to obtain the S-curves and 50% points corresponding to the threshold charges. It is then followed by an iterative procedure to obtain a set of optimized TDAC values for individual pixels, which minimizes the standard deviation of the threshold distribution. There are two iterative methods to get the optimized TDAC values and both follow a binary search in the TDAC range.

The first method uses a predefined set of steps to increase or decrease the TDAC. Starting from the mid-range TDAC, pixels with higher threshold than the average are given higher TDAC values, and vice versa. Next, another threshold scan is taken to get the new 50% points from the fits to the S-curves, the TDAC step is shortened, and the same procedure is followed until the optimized TDAC value for a pixel is found, which gives the closest threshold for that pixel to the average threshold. The TDAC steps for a 4-bit TDAC range can be set as {4,2,1,1}, giving the possibility to start from the TDAC of 7 and reach any TDAC value between 0 and 15.

The second method, which is designed to be much faster, does not take threshold scans in each step. Instead, a single analog scan is taken for each pixel to measure its efficiency at the average threshold point determined from the initial threshold scan or at a user-defined target threshold. If the efficiency is lower than 50%, the TDAC will increase for that pixel following a binary search in the TDAC range and vice versa. While the second method is much faster, it relies on a strictly increasing S-curve. Therefore, it is prone to noise-related variations, especially for irradiated modules. However, no noticeable effect in the performance of the tuning is observed, and this method, implemented in the Ph2_ACF software, is chosen as the baseline.

The TDAC value corresponding to each pixel will be updated in the mask file. Figure 9.5 shows the untuned and tuned distribution of the TDAC values for all pixels in the linear FE of an RD53A ROC, as well as the threshold distribution corresponding to each TDAC distribution. It is recommended to first perform the threshold equalization for high global thresholds of a few thousand electrons and then fine-tune the TDAC values at lower thresholds. If one attempts to perform the threshold equalization directly at the desired low threshold, the pixels with TDAC values far below the average have a lower effective threshold during the first S-curve measurement, resulting in high noise, high fluctuations in their S-curve, and possible failure in measuring their 50% point.
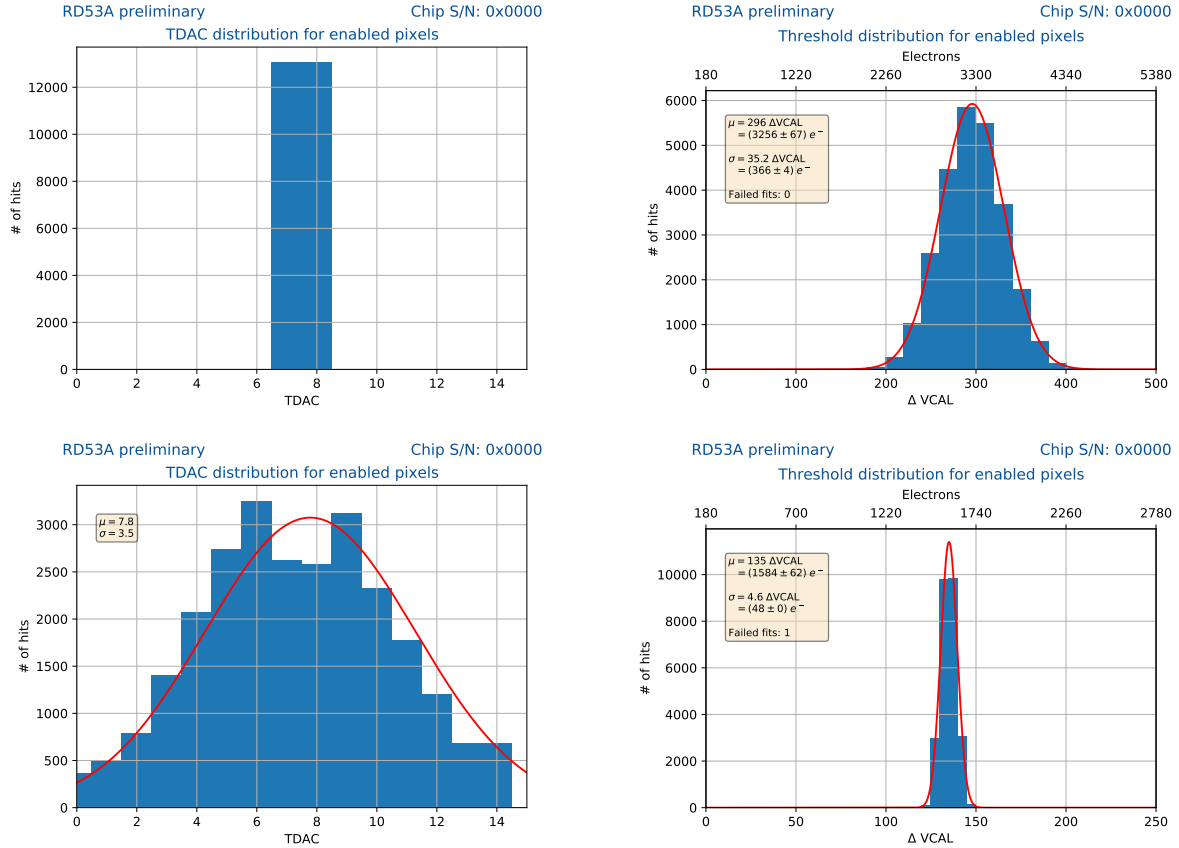
Figure 9.5: Distribution of TDAC (left) and the corresponding threshold distribution (right) for an unirradiated RD53A pixel module. The top plots correspond to the starting point of threshold equalization with a mean threshold of 3256e and a standard variation of 366e while the bottom plots show the equalized threshold with a mean of 1584e and a standard deviation of 48e.

Choosing the value of LDAC_LIN is an important practical consideration during module tuning. Generally, as LDAC_LIN determines the weight of the TDAC bits, if too high of a LDAC_LIN value is chosen, the precision in fine-tuning the threshold is lost. On the other hand, if LDAC_LIN is too low, pixels with thresholds far from the average or target threshold cannot be tuned, as the TDAC bits are not sufficiently weighted. In practice, one has to monitor the TDAC distribution as the output of the threshold equalization algorithm and make sure that the number of pixels in the overflow and underflow of this distribution is on the order of a few percent of the total number of pixels. This would be harder to achieve for irradiated modules with many noisy or defective pixels that would need a higher LDAC_LIN to bring their threshold close to the average.

9.2.5 Noise measurement

The study of noise in a pixel detector is one of the crucial characterization steps. Noisy pixels increase the occupancy and hit rate and can fill the tolerable bandwidth for data readout. In addition, if a noisy pixel is close to the trajectory of the impinging particle, the error in cluster position reconstruction and tracking increases. Therefore, it is crucial to evaluate the increased occupancy due to noise, the number of noisy pixels, the distribution of the charge created by noise, and to carefully remove the noisy pixels without affecting efficiency significantly.

The charge distribution of the noise can be obtained from a threshold scan. The main reason

that the S-curve from a threshold scan is not a step function at the threshold value but rather a wide error function is the presence of noise in the CSA of the linear FE. This noise is simulated to be 87 electrons for a detector capacitance of 50 fF [126]. Therefore, the noise in each pixel coming from the amplifier can be estimated by measuring the width of its corresponding S-curve. As this noise depends on the capacitance of the detector, the attached sensors should be fully depleted to ensure consistent and realistic measurement for all pixel modules.

Figure 9.6 shows the distribution of the noise charge extracted from the width of the S-curves. The average noise charge slightly increases with irradiation. It has negligible dependence on the sensor bias voltage after depletion, given that the sensor capacitance stays the same, confirming that the source of this noise is mostly the readout chip and not the sensor. On the other hand, the noise charge shows a larger increase when the temperature increases, which also increases the leakage current of the sensor.
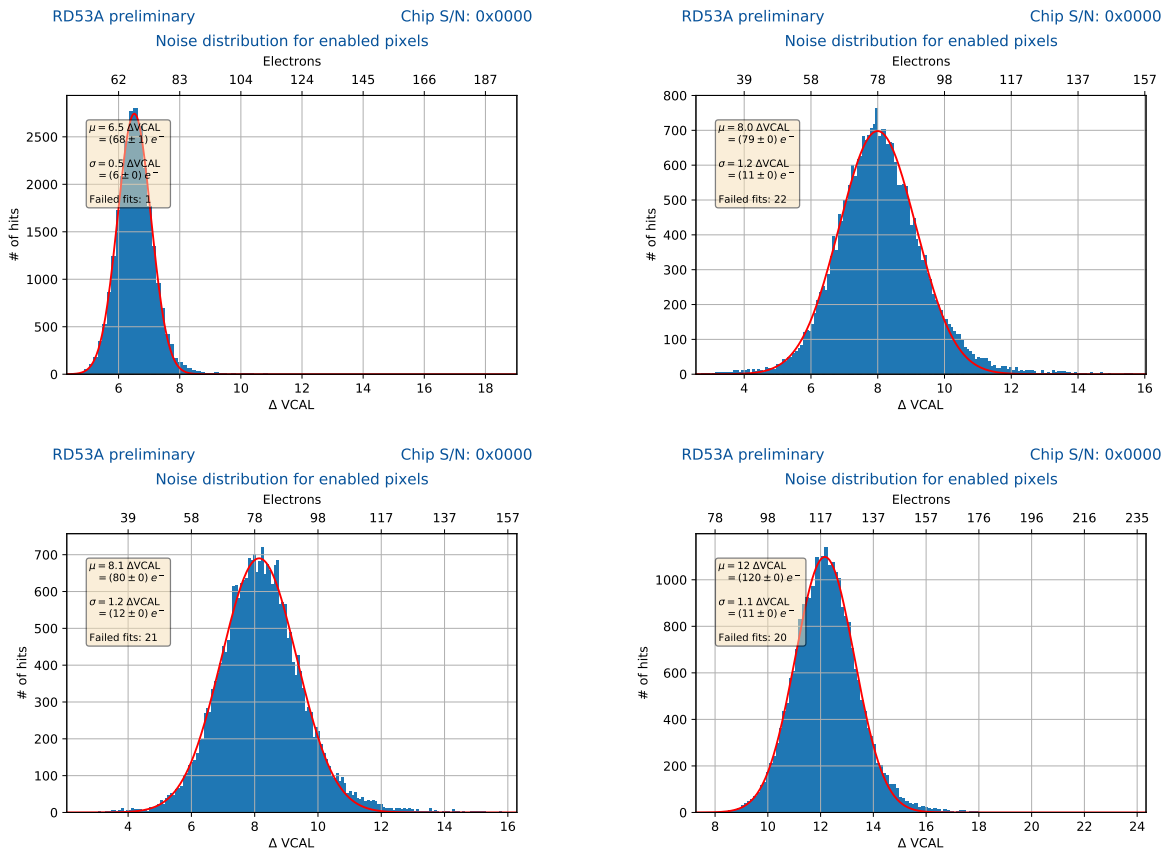
Figure 9.6: Distribution of noise derived from the width of the S-curves. The top left plot corresponds to an unirradiated RD53A pixel module, while the other three correspond to a module irradiated to 8.6×10^{15} neq/cm^2. For the top right plot, the sensor is biased to 500 V with a leakage current of 25 μA. For the bottom left plot, the sensor is biased to 1095 V with a leakage current of 100 μA. For the bottom right plot, the sensor is biased to 500 V with a leakage current of 500 μA due to higher sensor temperature compared to the previous two conditions.

In addition to fluctuations in the amplifier, noise can be initiated from the sensor itself, especially for irradiated sensors. The variation of this charge is larger than that of the CSA and creates spikes in a set of noisy pixels with large occupancy. These noisy pixels have to be identified and masked off. This is done using a *noise scan* in which a user-defined number of readouts from all pixels are performed without the presence of injected or deposited charge, and therefore no occupancy is expected. Pixels showing an occupancy higher than a user-defined

limit are identified as noisy and removed. For instance, while the noise charge is the same for the top right and bottom left plots of figure 9.6, corresponding to irradiated pixel modules at low temperature with two different bias voltages, the number of noisy pixels detected by the noise scan is larger at the bias voltage of 1095 V compared to 500 V.

The list of noisy pixels identified by a noise scan can vary by changing the bias voltage or temperature, or even moving the module. Therefore, after any change of the module configurations and environment, a new noise scan has to be performed starting from a fresh mask file from previous scans with a tuned threshold distribution. However, for irradiated modules, an iterative chain of noise scans is required when increasing the bias voltage of the sensor. Generally, the higher the bias voltage, the higher the number of noisy pixels and their charge and occupancy. If a fresh noise scan is performed at a high bias voltage for an irradiated module, the rate of triggers from the noisy pixels is so high that it fills the readout bandwidth, and effectively no occupancy is detected and no noisy pixels will be identified. Therefore, the highly noisy pixels have to be identified at lower bias voltages when their occupancy is still relatively low and tolerable by the readout bandwidth. Then by increasing the bias voltage step by step, the new noisy pixels can be masked.
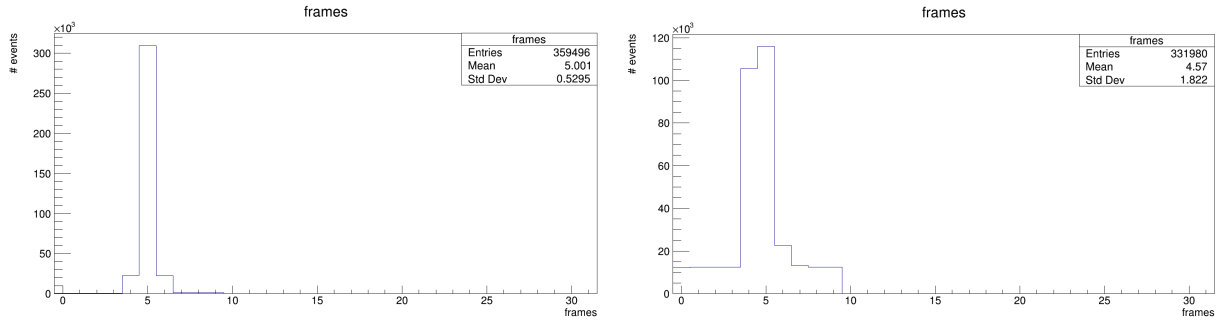

Figure 9.7: Distribution of bunch crossing frame in the online monitor during the data taking for fresh (left), and irradiated (right) RD53A pixel modules with a 3D sensor.

When testing the pixel modules with a beam, a signature of hits from the noisy pixels is that they are not generated at the same bunch crossing as the real hits. During the data taking in a beam test, a window of bunch crossings is allowed to make sure the trigger latency of the hits is accommodated. While the real hits are triggered at the same relative latency and create a peak in the trigger latency distribution, the noisy hits are triggered at random times that are not correlated with the crossing of the bunches in the beam. Therefore, the level of noise occupancy can be evaluated. Figure 9.7 shows the distribution of bunch crossing frame in the online monitor during data taking in a beam test. For fresh modules (left), signals occupy one or two bins of the distribution, as their relative time of arrival with respect to the bunch crossing is similar. For irradiated modules (right), a flat background is added to the distribution that corresponds to the randomly distributed time of arrival of noise-generated signals. A loose noise masking procedure is performed on the irradiated module. The noisy pixels should be masked to the level that the bandwidth is not filled in order to lower the efficiency but tolerated otherwise to keep the randomly noisy pixels that could recover during the test. Further masking of noisy pixels can be done offline during the analysis of beam test data and by studying the pixel occupancy.

9.2.6 Calibration of TOT vs. ΔVCAL

The time period in which the analog signal generated by the incoming charge into the ROC stays above the comparator threshold is referred to as TOT (time over threshold). It is digitized and used as a representation of the signal strength. For each pixel, the TOT is an increasing function versus the collected charge. However, the dependence of the TOT to the collected charge is not fully linear, and, more importantly, the dependence differs from pixel to pixel. Therefore, the TOT values for each pixel need to be calibrated so that a fixed amount of deposited charge in each pixel of the detector is read out to be equal. This would ensure that the characterization measurements such as the evaluation of interpixel crosstalk explained in chapter 10 and the operational measurements such as the cluster position are reliable.

To calibrate the TOT values with the corresponding collected charges for each pixel, one can inject certain amounts of charge to the pixel and find the mapping of the TOT as a function of charge. From each pixel in an analog scan with N charge injections, a number of hits are read out, which can be different from N. For instance, if the injected charge is below the threshold, the read-out hits are decreased, or if there is noise it can increase the number of readout hits, especially for irradiated modules. To find the mapping of TOT as a function of charge, I have developed an algorithm to clean the read-out TOT values from low-amplitude noise and get an average TOT from the N injection of a specific injected charge. Although individual TOT values for each injection are digitized, the average TOT is a real number.
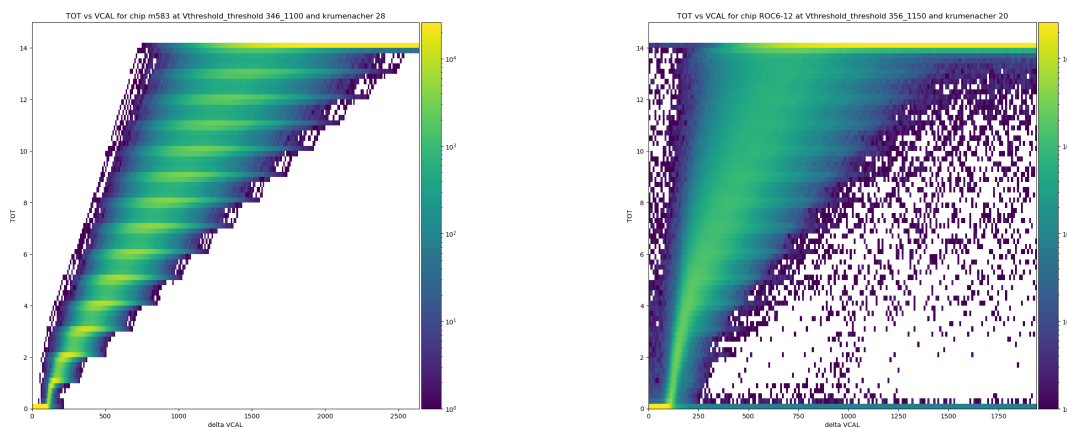
Figure 9.8: Mapping of TOT as a function of ΔVCAL for a non-irradiated (left) and an irradiated (right) pixel module. The y-axis shows the average TOT value for each pixel after cleaning noisy TOTs, while the x-axis is the injected charge in units of ΔVCAL. The charge in electrons is about 10 times the ΔVCAL value.

Figure 9.8 shows two sample mappings of TOT as a function of charge (ΔVCAL) overlaid for all pixels of the linear FE. The mapping is calculated using a threshold scan in the ΔVCAL range of the x-axis, as the threshold scan is essentially a chain of analog scans in a range of injected charge with specific steps. The left plot corresponds to a nonirradiated pixel module and the right plot to a pixel module irradiated to 7.5×10^{15} neq/cm^2. After the irradiation, some pixels fail to return any TOT or return a lot of low-TOT noise, such that the average TOT is lowered. This effect is mitigated after the noise cleaning but is still present, as seen in the right plot. In both plots, the average TOT starts to be nonzero only after a certain injected charge slightly higher than the operating threshold, an expected effect given the definition of TOT and

the fact that it is digitized. Note that since the time over threshold of the signal depends on both the comparator threshold and the Krumenacher DAC setting, a new mapping is required for each setting of these two DAC values or following the equalization of the threshold.

After obtaining the mapping of the average TOT as a function of charge (ΔVCAL) for each pixel, the mapping is reversed to obtain the most probable injected charge corresponding to each integer TOT value for each pixel. The reversed mapping will be useful to convert the per-pixel charge from the beam tests or real data taking, which is in units of TOT, to the corresponding charge value in units of ΔVCAL or electrons for each individual pixel, leading to a more reliable position measurement.
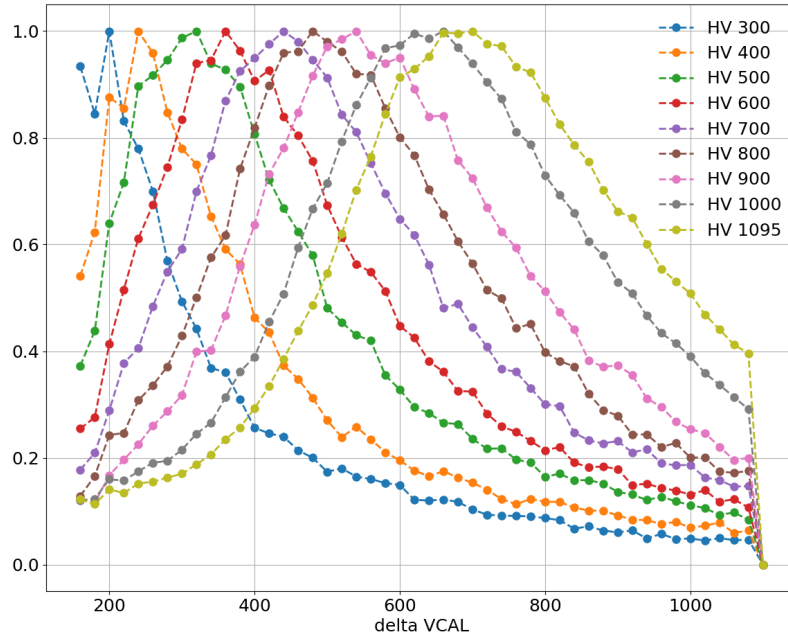
9.2.7 Source scans

The closest characterization procedure in the lab to that of a test with beams of charged particles is done using radioactive sources and is called a *source scan*. The radioactive source is a ^{90}Sr isotope undergoing a beta decay that produces an electron with an energy of up to 2.2 MeV. The produced electrons deposit charge in the bulk of the silicon sensor, and the ionized electrons are collected by the ROC, providing a more realistic test than the previous characterization steps with charge injection directly into the ROC pixels.

An internal self-trigger procedure is utilized in the source scan. For any collected signal above the comparator threshold, the RD53A chip sends a trigger, which is received by the readout hardware and sent back again to the chip to record the event. As opposed to beam tests in which the external trigger is sent from scintillators or other pixel modules, the internal self-trigger is prone to relatively higher levels of noise. For irradiated modules, the threshold has to be lowered step by step while iteratively removing noisy pixels, and a lower cut has to be applied on the collected charge to reduce the noise, especially when the sensors are not fully depleted.

Figure 9.9 shows the normalized distributions of collected charge for an RD53A pixel module with a planar sensor, irradiated to the fluence of 8.6×10^{15} neq/cm^2. The charge is shown in units of ΔVCAL after pixel-to-pixel calibration of the collected TOT values, while the charge in electrons is about 10 times the value in ΔVCAL. The readout chip threshold is tuned to an average of 1073 electrons. The charge distributions are shown for various values of bias voltage applied on the sensor that go as high as 1095 V, the highest bias voltage ever applied on a pixel module with n-in-p sensors in high-energy physics applications. While the bias voltages at beam tests are limited to 800 V, such lab measurements can shed light on charge multiplication effects at higher bias voltages. At low bias voltages, the distributions contain lower statistics despite the same exposure time to the source, which is due to the saturation of the bandwidth with noisy pixels that have charges similar to the deposited ones.

Figure 9.10 shows the dependence of the collected charge as a function of the bias voltage. Each distribution in figure 9.9 is fitted with a Landau function convoluted with a Gaussian. The Landau function represents the charge deposition in the silicon bulk [130], while the Gaussian represents the following detector and readout noise. The most probable value of the Landau distribution is taken as the representative of the charge for each bias voltage, shown in figure 9.10.

delta VCAL distribution for chip m586i at VTH_threshold 353_1073 with krumenacher 20

Figure 9.9: Distribution of charge in units of ΔVCAL obtained by a source scan for a pixel module irradiated to the fluence of 8.6×10^{15} neq/cm^2, tuned to a threshold of 1073 electrons, and biased to various levels of bias voltage shown in the legend. The charge distribution corresponding to each bias voltage is averaged over all active pixels, using the TOT vs ΔVCAL mapping of individual pixels.

delta VCAL vs HV for chip m586i at VTH_threshold 353_1073 with krumenacher 20
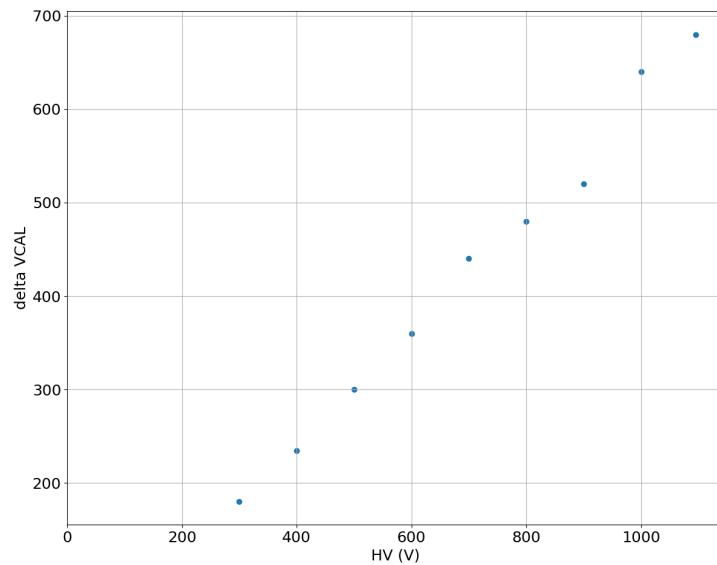
Figure 9.10: The collected charge versus bias voltage obtained from the graphs in figure 9.9 for a pixel module irradiated to the fluence of 8.6×10^{15} neq/cm^2 and tuned to a threshold of 1073 e.

10 Crosstalk

10.1 Description of the crosstalk effect

The RD53A readout chip [126], developed by the RD53 collaboration as the prototype readout chip (ROC) for the CMS and ATLAS pixel detectors, has a pitch size of $50 \times 50 \, \mu\mathrm{m}^2$. As mentioned in chapter 8, two geometries of $50 \times 50 \, \mu\mathrm{m}^2$ and $25 \times 100 \, \mu\mathrm{m}^2$ were studied for the sensors during the R&D process. In the geometry with a $25 \times 100 \, \mu\mathrm{m}^2$ cell size, the layout of the aluminum pad, which overlays the neighboring implant, can cause interchannel charge induction or *crosstalk* between the pixels paired by these pads, as seen in figure 10.1. The crosstalk effect is more pronounced between these pairs, but a small amount of charge can also be induced in other neighboring channels. Quantitatively, the crosstalk value between two channels is defined as the amount of induced charge over the total charge. Crosstalk causes two main complications. It increases the number of pixels with an over-threshold charge, which leads to higher data-rates, and it increases the error on cluster position reconstruction, and subsequently track reconstruction.

After implementation of the crosstalk effect in the CMS offline software (CMSSW), I studied the effect of crosstalk on cluster size and hit position resolution, both of which will be discussed in section 10.2. I have also pioneered the measurements of the crosstalk both in lab and beam tests, which are discussed in section 10.3. Finally, my studies on the mitigation of crosstalk will be discussed in section 10.4.
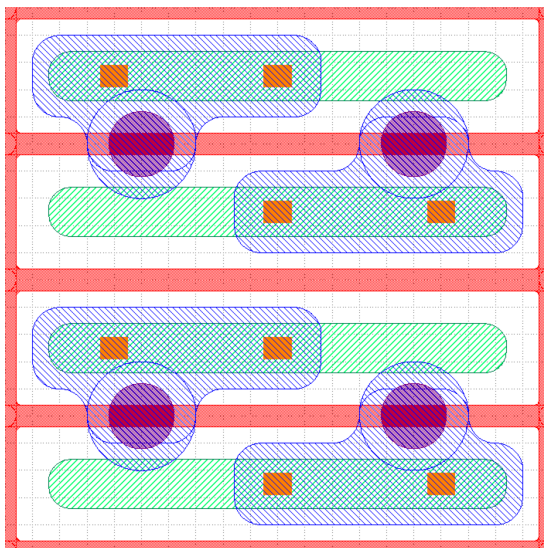
Figure 10.1: Aluminum pads (blue) are needed to establish an electrical contact and transfer the charge from the pixel n$^+$ implant (green) with a $25 \times 100 \, \mu\mathrm{m}^2$ pitch to the bump bond pad (purple) with a $50 \times 50 \, \mu\mathrm{m}^2$ pitch. The pad of one cell overlays the neighboring implant for *paired* pixels, increasing the total input capacitance. In this figure, the first and second pixels form a pair in terms of crosstalk, and the third and fourth pixels form another pair. The second and third pixels are considered *unpaired*. The figure is adapted from reference [120].

10.2 Simulation of crosstalk effect with CMSSW

The CMSSW software contains a complete simulation of the CMS detector material, as well as the electronic response. In this regard, the crosstalk effect as one of the parameters affecting the detector performance is implemented in CMSSW to study its effect on data rates and the performance of the tracking algorithm.

As one of the validation steps in the implementation, figure 10.2 depicts the effect of various crosstalk values on the cluster width in layer one of the pixel detector for perpendicular tracks. Here, the crosstalk value between coupled pixels for which crosstalk is expected is set to 0%, 10%, and 20%, while it is set to zero for uncoupled pixels. A white hollow box shows the position of one pixel.

As validated by the output of the CMSSW simulation, for the no-crosstalk scenario, when impinging in the center of a pixel, the charge is largely contained in that pixel, and hence the cluster width is close to one. When the track passes close to one of the borders of the pixel, part of the track may pass through the neighboring pixel and the created charge in the neighboring pixels is more probable to be over the readout threshold. Therefore, the width of the cluster increases to around two. After the introduction of crosstalk between a pixel and one of its neighbors, when the track passes close to their borders, the number of pixels with over-threshold charges is still two. However, when the track passes close to the border with an uncoupled pixel, the two pixels close to the track position still have over-threshold charges, while part of the charge from the main pixel is also induced into its paired neighbor far from the track position. Therefore, the cluster width gets close to three. The vertical symmetry in these plots is a result of measuring the cluster width along the x-axis and not the total number of pixels in a cluster (cluster size).

The increase in the number of over-threshold pixels translates to a higher number of channels being read out per each bunch crossing, and hence increases the data rate. Implementing the crosstalk effect in the full detector simulation facilitates a more realistic evaluation of data rates in various parts of the detector for each design.

In addition to the effect on data rates, crosstalk can also affect the precision in cluster position and track reconstruction. After implementing crosstalk in the CMSSW software, these effects could also be evaluated under various conditions to determine the affordable margins of crosstalk in the sensor and readout design.

The cluster position reconstruction error can be measured in the CMSSW software by comparing the reconstructed hit position (recHit) and the true position of the simulated impinging particle (simHit). Figure 10.3 shows the distribution of this difference in the local X direction of the $25 \times 100 \, \mu\text{m}^2$ pixels, along the $25 \, \mu m$ side where the crosstalk is expected to have an effect, for three scenarios of no crosstalk, 10% crosstalk, and 20% crosstalk. The particles are impinged perpendicularly into the pixels. The standard deviation of the fitted Gaussian function is called *position resolution* and worsens as the crosstalk value increases, as expected. Figure 10.4, shows similar distributions in the local coordinate Y along the $100 \, \mu m$ side of the $25 \times 100 \, \mu\text{m}^2$ pixels for the 0% and 20% crosstalk values. The flat part of the distribution represents tracks passing through the center of the pixel, which are detected by only one pixel in the Y direction and hence lead to a binary flat position resolution error.
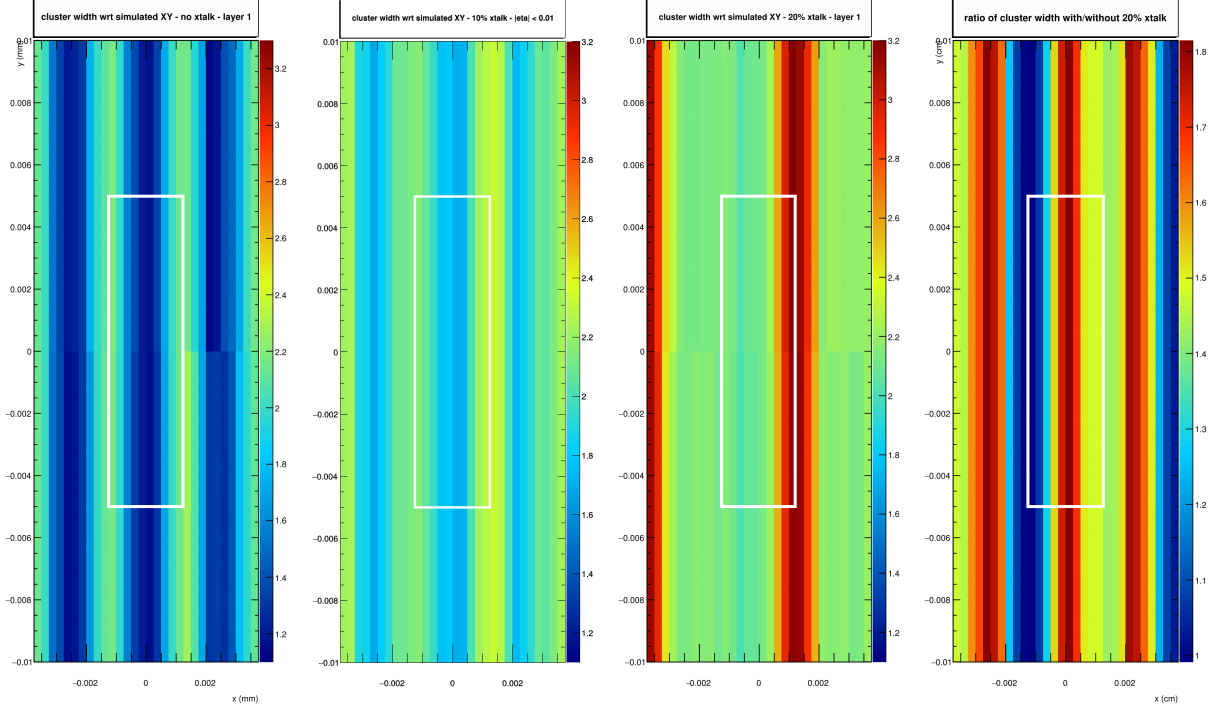
Figure 10.2: Cluster width as a function of track position for crosstalk ("xtalk") values of 0%, 10%, and 20%, repectively from left to right. A white box shows the position of a pixel. After the introduction of crosstalk, an increase in cluster width is seen when the track passes close to the border of a pixel with its uncoupled neighbor. The rightmost plot shows the ratio of the 20% map to the 0%.

## 10.3 Measuring crosstalk

10.3.1 Lab measurements

As mentioned in chapter 9, the RD53A readout chip has an internal charge injection circuit by which the S-curves can be obtained and the threshold values can be measured. For example, take two pixels that are paired by a certain value of crosstalk, called pixels A and B. Starting from small values of charge and by injecting more and more charge into pixel A and reading out both pixels, at some injected charge around the threshold of pixel A, the occupancy goes from 0% to 100%, as seen in figure 10.5 (top left) and in chapter 9. Now if we continue to increase the injected charge, bearing in mind that some of the injected charge in A would end up in B due to crosstalk, at some point the induced charge in B is higher than its threshold value and the occupancy goes from 100% to 200%.

Figure 10.5 shows this behavior for an RD53A pixel module with $25 \times 100 \, \mu\text{m}^2$ pitch sensors. On the left, the single S-curve and its corresponding threshold distribution is obtained by injecting a charge in the range of 0 to 300 ΔVCAL (3300 electrons). On the right plots, charges up to 22500 electrons are injected, resulting in two overlaying S-curves, one for the main injected pixel, which is just a zoomed-out version of the left plot, and one for the paired neighboring pixel. The two S-curves are plotted separately on the same figure, and the overall occupancy at charges above 10 ke goes to 200%. Such a behavior is only observed when reading out the paired neighbor of the injected pixel and can only exist in the presence of crosstalk. The lower the value of crosstalk, the higher the required injected charge to observe the second S-curve. Both
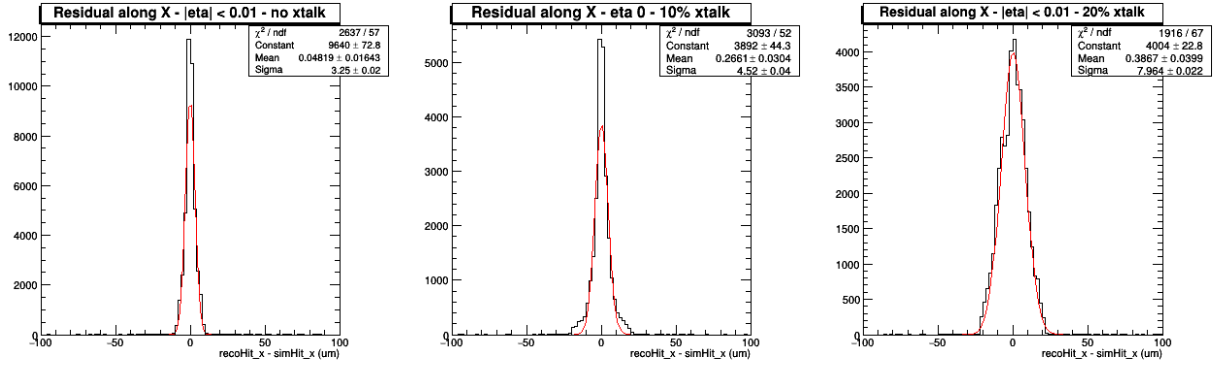
Figure 10.3: Residual distribution of the reconstructed cluster position along the short side of the $25 \times 100\,\mu\mathrm{m}^2$ pixels compared to the real impinged position for crosstalk values of 0% (left), 10% (middle), and 20% (right). Distributions are obtained using a particle gun simulated in the CMSSW software, impinging a muon on the first layer of the pixel detector at $|\eta| < 0.01$.
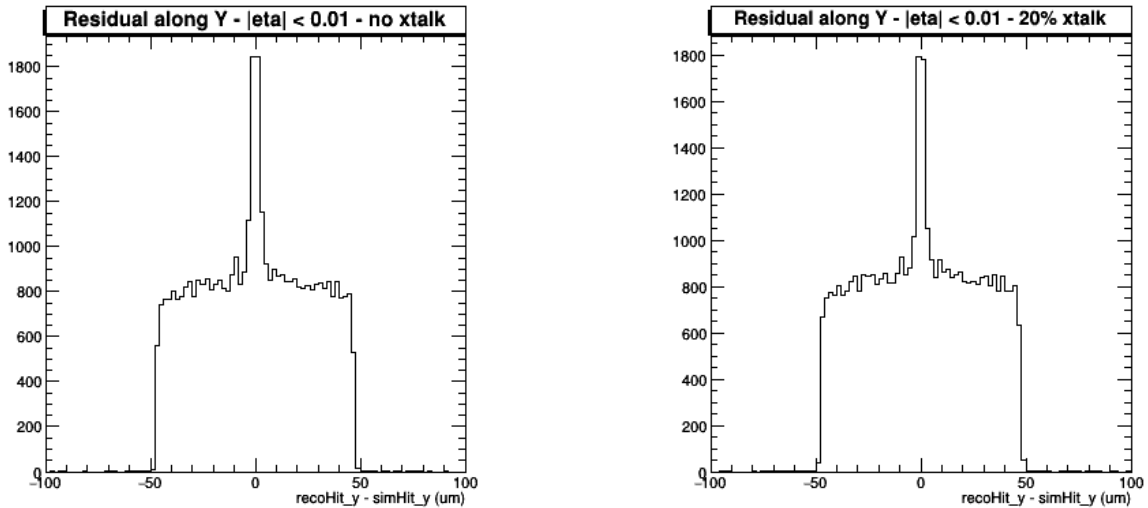
Figure 10.4: Residual distribution of the reconstructed cluster position along the long side of the $25 \times 100\,\mu\mathrm{m}^2$ pixels compared to the real impinged position for crosstalk values of 0% (left) and 20% (right). Distributions are obtained using a particle gun simulated in the CMSSW software, impinging a muon on the first layer of the pixel detector at $|\eta| < 0.01$.

the threshold and the crosstalk can vary from pixel to pixel and pair to pair, which explains the width of these threshold distributions especially for the second S-curves.

For each pair of pixels, a first ($thr1$) and a second ($thr2$) 50% threshold are measured corresponding to the charges in which the occupancy of the main pixel and its neighboring pixel are at 50%, respectively. With these two measurements per each pair of pixels, one can measure the crosstalk value between them. Assuming that crosstalk between two paired pixels is x, a value between 0 and 1 showing the ratio of induced charge to total, by injecting c amount of charge in pixel A as the main pixel, $x \times c$ is induced in the neighboring pixel B and $(1 - x) \times c$ remains in A. When $c_1 = thr1$, the remaining charge is enough to be detected by pixel A and when $c_2 = thr2$, the induced charge is enough to be detected by pixel B. Assuming that the amount of charge to fire a pixel is roughly similar, which is achieved after equalizing the thresholds for a module, one infers that:

$$(1 - x) \times c_1 = x \times c_2 \implies thr1 \times (1 - x) = thr2 \times x \implies x = \frac{thr1}{thr1 + thr2} \qquad (10.1)$$
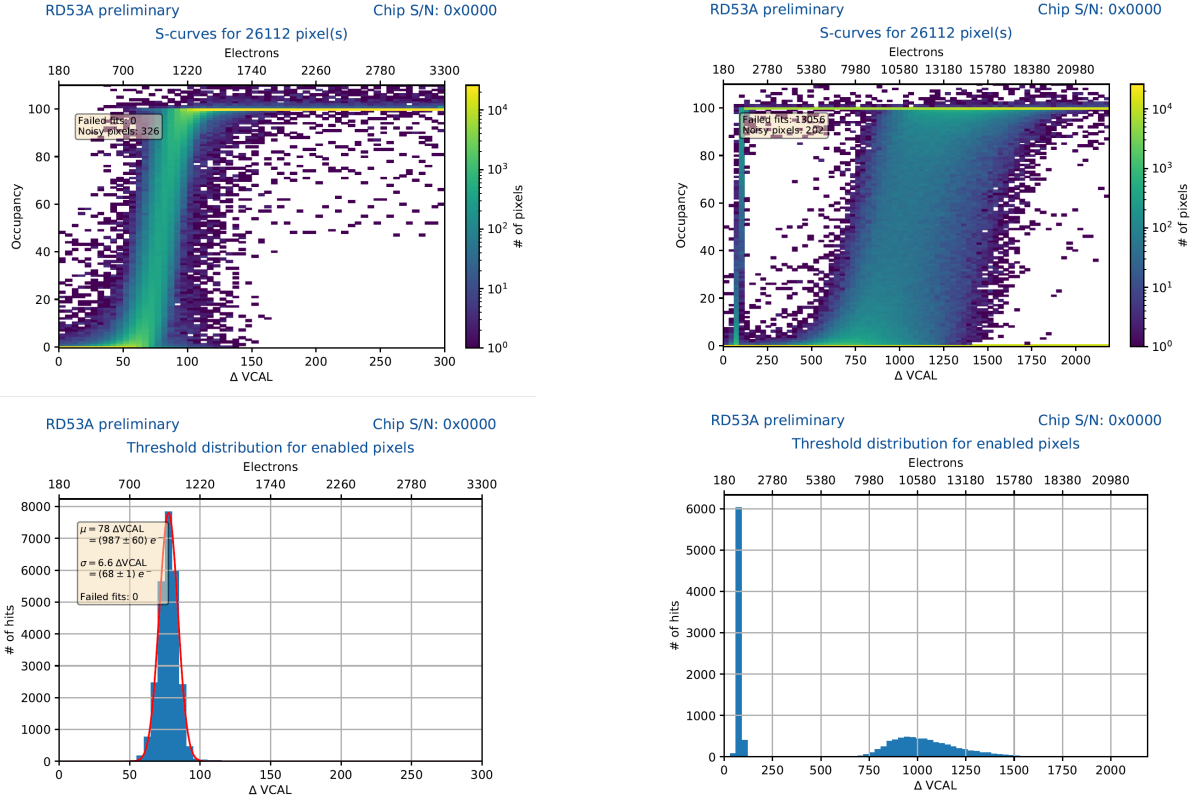
Figure 10.5: S-curves (top) and the corresponding 50% threshold values (bottom) for an RD53A pixel module with a $25 \times 100\,\mu\text{m}^2$ pitch sensor. The S-curves corresponding to the main pixels into which the charge is injected and neighboring pixels into which the charge is induced due to crosstalk are overlaid, with a total occupancy of 200% for sufficiently high injected charge. The plots on the left are the zoomed-in versions to clearly see the first peak corresponding to the main pixels.

By defining

$$r = \frac{thr2}{thr1}, \tag{10.2}$$

we calculate the crosstalk as:

$$x = \frac{1}{1+r} \tag{10.3}$$

Therefore, we can measure the value of crosstalk between each individual pair of pixels using the two corresponding thresholds measured for that pair. The crosstalk value can be reported in the range of $[0, 1]$ or equivalently in $[0\%, 100\%]$.

Figure 10.6 shows the distribution of the crosstalk value in percentage for all paired pixels of the linear FE of an HPK RD53A module with $25 \times 100\,\mu\text{m}^2$ pitch sensor. The left plot shows the distribution before irradiation, and the right plot shows the distribution for the same module after irradiation to a fluence of $8.6 \times 10^{15}\,\text{neq/cm}^2$. Irradiation is expected to lower the crosstalk effect to some extent, as the ionized charges in the pixels are trapped and the pixel charges are too low, in general, to have a secondary induction effect. Also, the capacitance between pixel pairs is reduced after irradiation.

Figure 10.7 shows the 2D map of crosstalk for each pixel and its pair as a function of its row and column, for the same module before and after irradiation. A dependency on the column number of the linear FE is observed in all the tested modules, which was not expected
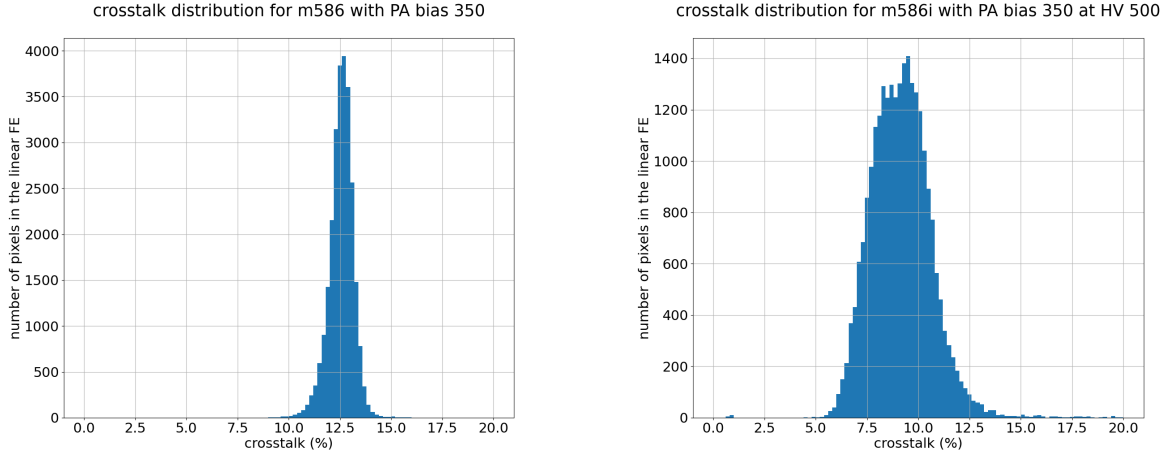
Figure 10.6: Distribution of the crosstalk percentage for individual pairs of a fresh (left) and irradiated (right) RD53A pixel module with a $25 \times 100\,\mu\mathrm{m}^2$ pitch sensor.
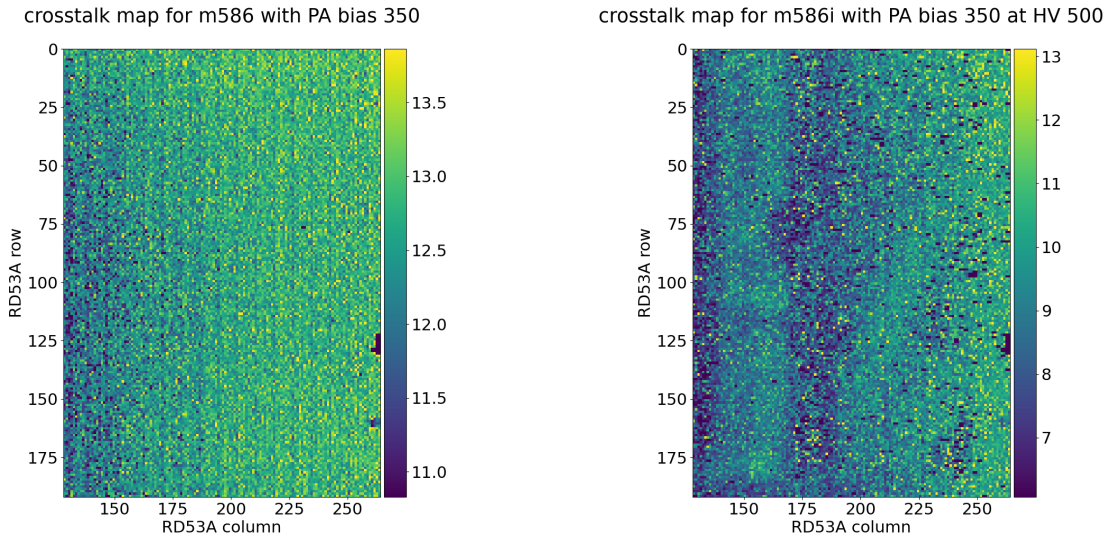
Figure 10.7: 2D map of the crosstalk percentage in the linear FE of a fresh (left) and an irradiated (right) RD53A pixel module with a $25 \times 100\,\mu\mathrm{m}^2$ pitch sensor. The dependency of crosstalk on the column number is observed in all tested RD53A pixel modules.

from the initial design, but can be explained by a dependency of the crosstalk on readout chip configurations like the preamplifier (PA) bias. This will be discussed in more detail in section 10.4.2.

10.3.2 Beam measurements

The crosstalk effect can be observed and measured using a beam of particles that impinge on the sensor. Although the conditions might not be as controlled as in the lab, and the measurements are not as precise, validating the effect of crosstalk and a rough quantitative estimation of its value in a more real-life condition is fruitful.

After impinging a beam of particles into the sensor, the charge in each pixel of the sensor can be measured after converting the measured TOT into ΔVCAL for each pixel, using the maps obtained by the TOT calibration explained in chapter 9. In particular, one can take clusters with exactly two neighboring pixels and calculate the ratio of the lower charge to the total charge of

the cluster, that is, the sum of the two pixels. Assuming that there is no crosstalk between the two neighboring pixels, by plotting the distribution of such a ratio for all clusters, a rather flat distribution is expected. The effect of having a pixel threshold and digitization of the TOT will modify the ratio distribution, so that it goes from a flat to a monotonically rising distribution.
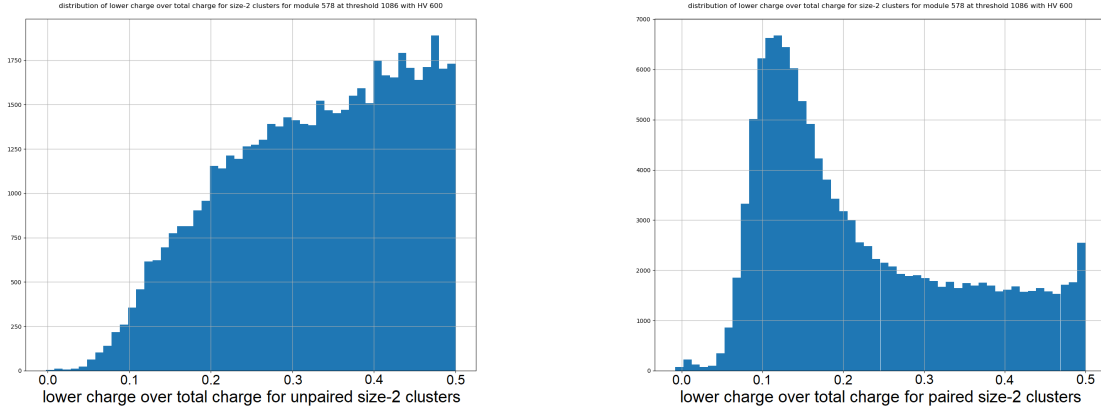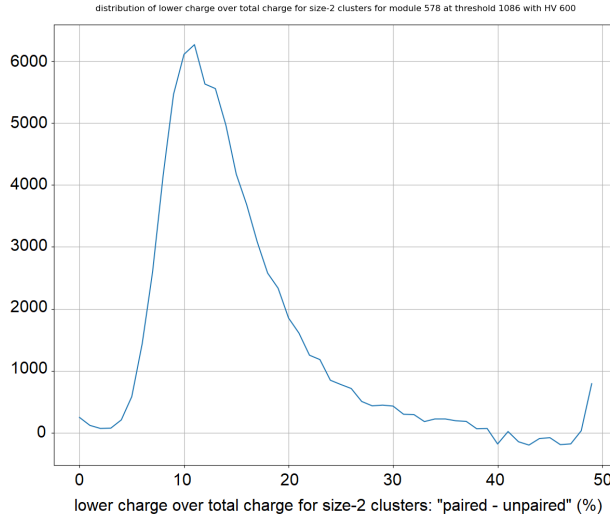

Figure 10.8: Distribution of the ratio between the lower charge over total charge, for clusters with two unpaired pixels (left) and two paired pixels (right). Clusters are formed after a beam of minimum ionizing charged particles passes through an irradiated RD53A pixel module with a $25 \times 100 \, \mu m^2$ pitch sensor.

Figure 10.8 (left) shows such a distribution of the ratio, for clusters of two unpaired pixels for an HPK RD53A module with a $25 \times 100 \, \mu m^2$ pitch sensor irradiated to a fluence of 5.0×10^{15} neq/cm^2. The rising behavior is due to the effect of threshold. Low values of the ratio correspond to clusters with two pixels and an unbalanced distribution of charge, which is less probable, as in such cases the pixel with the lower charge has a charge lower than its threshold.

Figure 10.8 (right) shows the same distribution for the same module and clusters with two neighboring pixels, but by choosing paired pixels for which the crosstalk effect is expected. If no crosstalk was present, these two distributions would be expected to be similar apart from statistical fluctuations, as is observed for other modules with no crosstalk. If the impinged particle passes through the central parts of a pixel and therefore should result in a cluster with one pixel, in the presence of x% crosstalk, x% of its charge would go to the neighboring paired pixel and, hence, the ratio of the lower charge to total charge should be around x%. Therefore, for clusters with paired pixels, one expects a peak around the crosstalk value on top of the main distribution.

This peak is better observed and measured if one subtracts the unpaired distributions from the paired ones, as depicted in figure 10.9, from which a crosstalk value of around 11% can be estimated.

One of the main errors in such a measurement comes from applying a threshold and the fact that there are usually below-threshold ionization charges in the neighboring paired pixels already before the crosstalk charge induction, which means that the peak seen in the ratio distribution is slightly overestimating the crosstalk value. The other factor is the effect of digitization. In measurements with a beam, charges are readout in limited units of TOT values, and hence the ratio is not as precise as in lab measurements that have a much better handle over the injected charges. As mentioned in chapter 9, the TOT values should be calibrated for each individual pixel to obtain a consistent charge value. Therefore, the ratio distributions shown above are

distribution of lower charge over total charge for size-2 clusters for module 578 at threshold 1086 with HV 600

lower charge over total charge for size-2 clusters: "paired - unpaired" (%)

Figure 10.9: Subtraction of the unpaired distribution in figure 10.8 from the paired one to obtain a clear peak representing the crosstalk percentage.

all taken after converting the TOT to ΔVCAL for individual pixels. Overall, the qualitative observation and quantitative measurement of crosstalk using a beam of particles is a crucial validation step to confirm that the effects measured in the lab are also observed in more realistic conditions with ionized electrons collected from the sensor.

## 10.4 Mitigating crosstalk

10.4.1 Online Mitigation

The effect of crosstalk on the measurement of the cluster position and, therefore, the tracking reconstruction can be mitigated by the reconstruction algorithm itself in some cases. This mitigation algorithm was implemented in the CMSSW software and assumed a constant and linear crosstalk effect with only one of the neighbors. Given an arbitrary cluster of pixels, for each pixel and its corresponding pair with actual deposited charges of d_1 and d_2, and a value of x for their crosstalk, the measured charges m_1 and m_2 will be:

$$\begin{pmatrix} m_1 \\ m_2 \end{pmatrix} = \begin{pmatrix} 1-x & x \\ x & 1-x \end{pmatrix} \begin{pmatrix} d_1 \\ d_2 \end{pmatrix}, \tag{10.4}$$

Therefore, the effect of crosstalk can be modeled by an application of a crosstalk matrix

$$X = \begin{pmatrix} 1-x & x \\ x & 1-x \end{pmatrix}, \tag{10.5}$$

The mitigation algorithm reverses the crosstalk matrix to obtain a correction matrix of $C = X^{-1}$ and applies it to the measured charges for the paired pixels. In practice, this has to be applied only for the marginal pixels of a cluster, as the position reconstruction of the CMSSW software only utilizes the marginal pixels to obtain the charge-weighted position of the pixels. Moreover, if the pair of a marginal pixel is not inside the cluster and its corrected charge is calculated to be over the threshold, the paired pixel is added to the cluster, and a new central position is defined for the cluster.
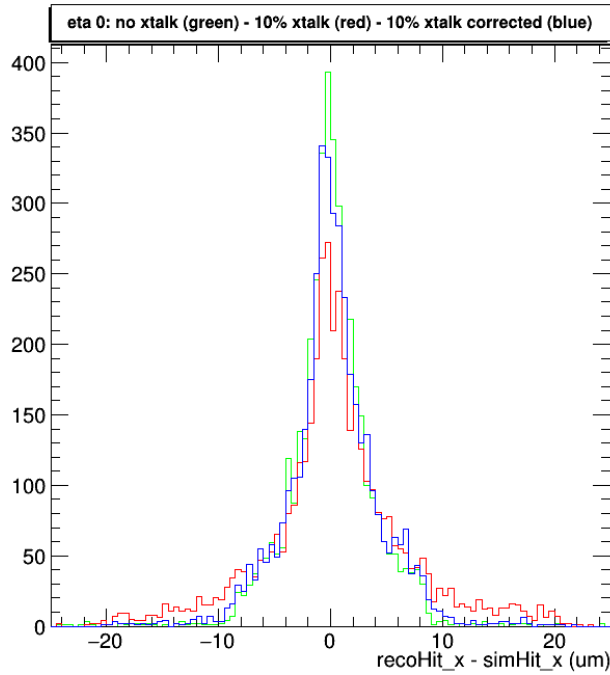
Figure 10.10: Position resolution along the short side of the $25 \times 100\,\mu\mathrm{m}^2$ pitch pixels for perpendicular tracks. Resolution worsens when going from 0% (green) to 10% crosstalk (red), and partially recovers after applying the offline crosstalk mitigation algorithm (blue).

The presence of a threshold and digitization of the pixel charges can worsen not only the performance of the main position reconstruction algorithm itself but also the correction algorithm. This is more prominent when the charges are just below the threshold with a measured charge of zero. However, in some configurations of the threshold value and digitization granularity, the correction algorithm can be fruitful. Figure 10.10 shows a distribution of position resolution for perpendicular tracks. The resolution gets worse after applying a 10% crosstalk compared to the 0% crosstalk scenario, while it can be reasonably improved after applying the correction algorithm.

10.4.2 Mitigation by readout chip configurations

After implementing the algorithms for lab measurements of crosstalk for individual pixels and investigating their distributions, it was understood that some DAC parameters of the readout chip can affect the value of crosstalk. In particular, an increase in the preamplifier (PA) bias voltage of the RD53A chip results in a lower average crosstalk as depicted in figure 10.11. By increasing the PA bias voltage from its default value of 350 at the time, to 500, the distribution of the crosstalk value shifted towards lower percentages.

As shown in figure 10.12, an interesting feature of this observation was the shift in 2D patterns of the crosstalk by increasing the PA bias voltage. Such shifts in the 2D crosstalk patterns were not observed for the same module after irradiation, as shown in figure 10.13.

After performing these measurements on more than 10 RD53A modules with $25 \times 100\,\mu\mathrm{m}^2$ pitch sensors, it was inferred that the increase of the PA bias reduced the mean crosstalk value in all cases, while no significant result could be inferred about the shifts in the 2D patterns apart from the fact that if such patterns exist as a function of columns as they often did for fresh modules, the increase of the PA bias shifts the patterns along the columns, which could
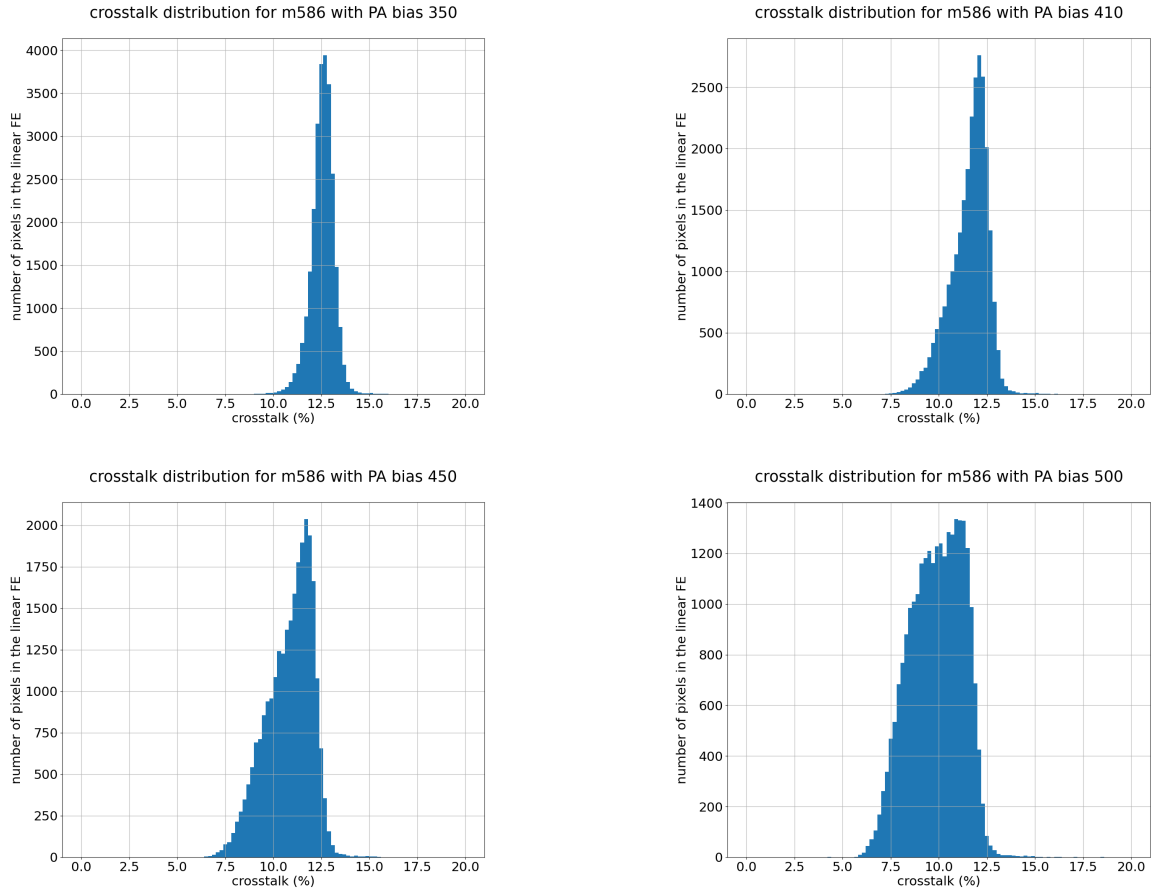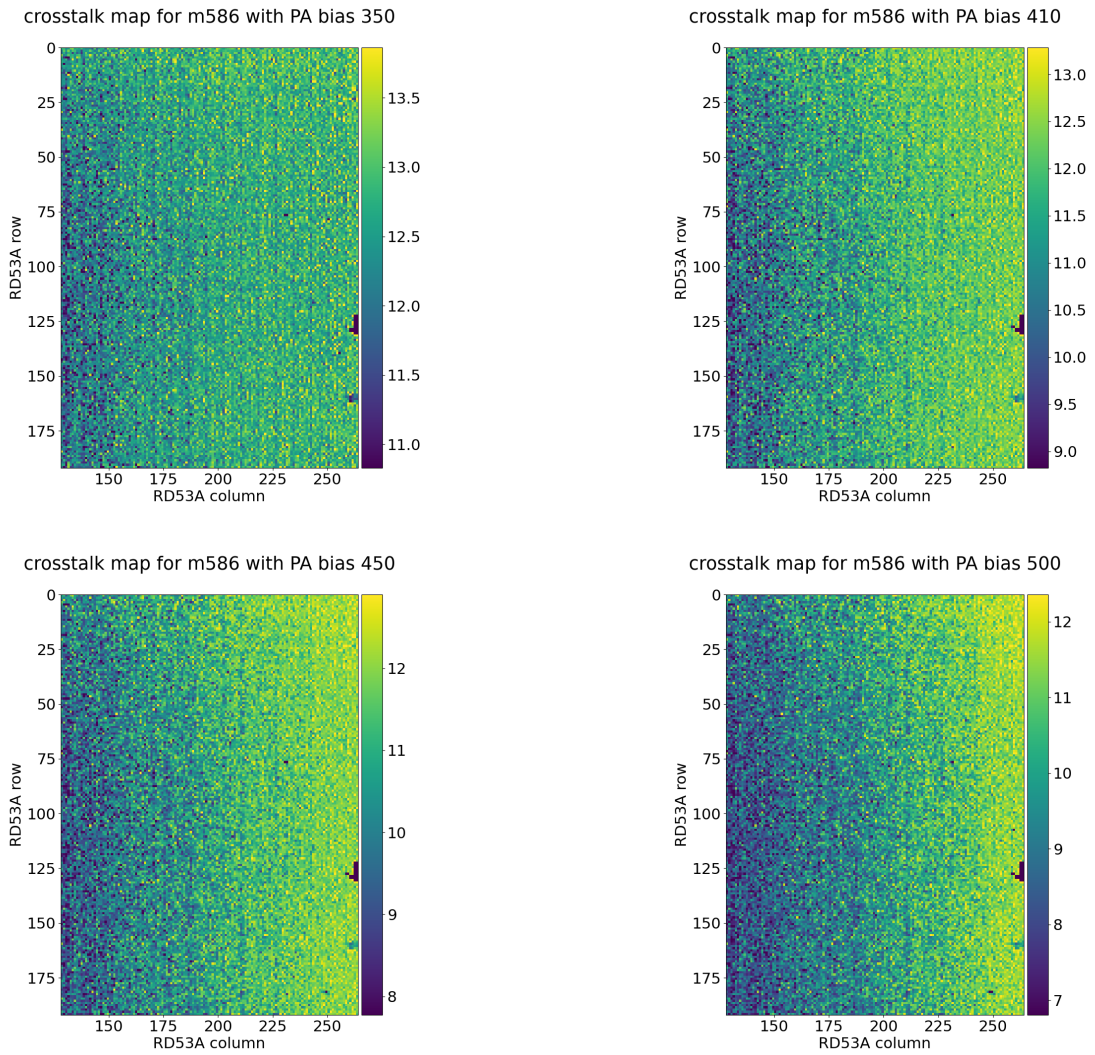
Figure 10.11: Distribution of crosstalk percentage between the paired pixels in the linear FE of a fresh RD53A module with a $25 \times 100 \, \mu\mathrm{m}^2$ pitch sensor. Distributions are shown for preamplifier (PA) bias values of 350 (top left), 410 (top right), 450 (bottom left), and 500 (bottom right).

result in a more or less homogenized 2D map. Although increasing the PA bias results in lower crosstalk values, since it also increases the power consumption of the readout chip, a compromise was required, leading to a new default value of 410.

10.4.3 Mitigation by sensor layout design

One of the most effective ways of reducing crosstalk is to tackle it from its source, which is the overlay of the aluminum under bump pad of one cell on the neighboring implant, as shown in figure 10.1. In the "bitten" pixel design as shown in figure 10.14 compared to the standard design, the implant of the neighboring pixel is cut out to remove such an overlay.

The bitten design significantly reduces the crosstalk effect and was thoroughly tested to ensure that cutting out the implant does not affect the overall efficiency of the sensor. This design has now been chosen as the default CMS design for the Phase2 pixel detector.

Figure 10.12: 2D map of the crosstalk percentage between the paired pixels as a function of row and column in the linear FE of a *fresh* RD53A module with a $25 \times 100\,\mu\mathrm{m}^2$ pitch sensor. Maps are shown for preamplifier (PA) bias values of 350 (top left), 410 (top right), 450 (bottom left), and 500 (bottom right).
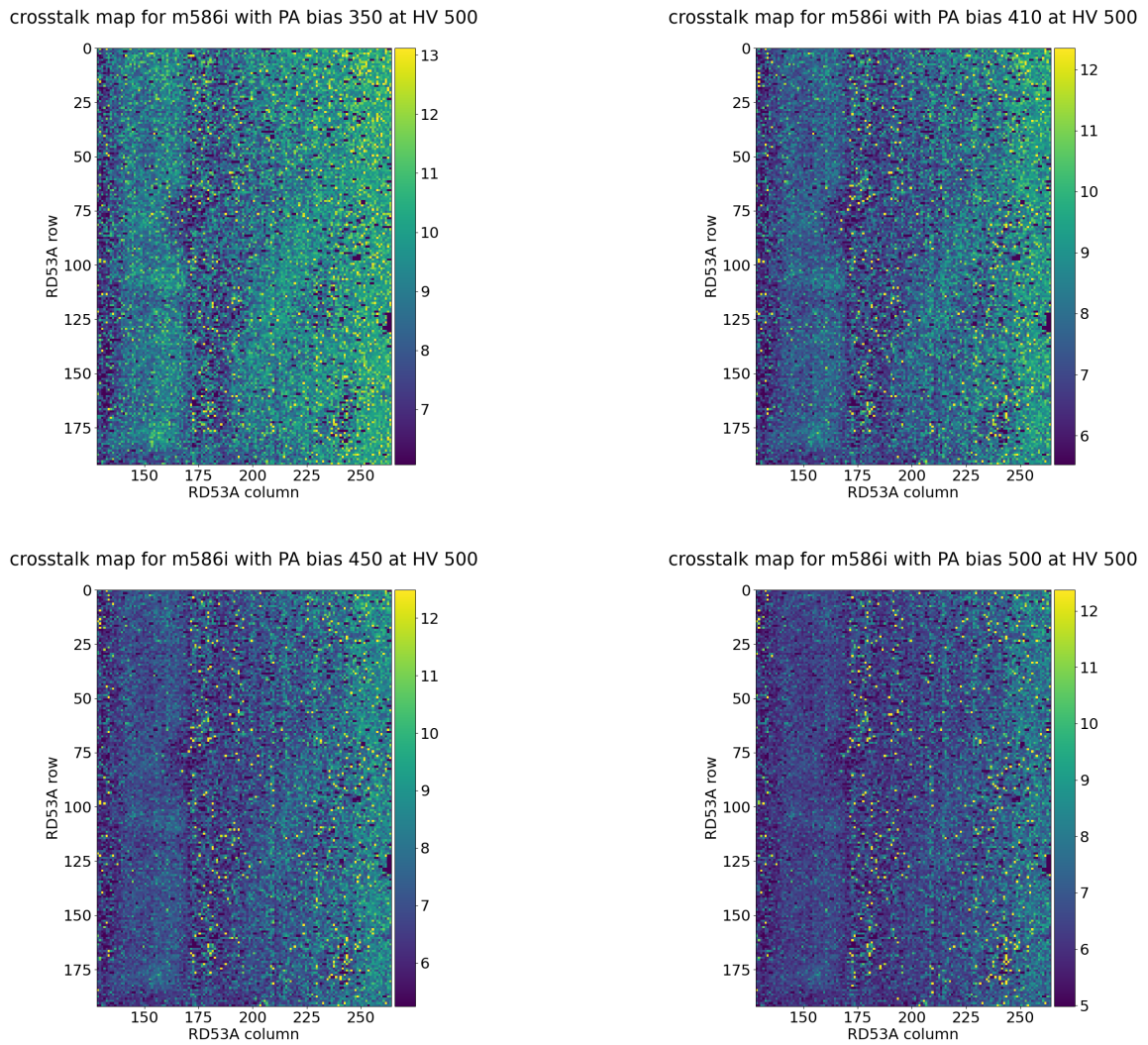
Figure 10.13: 2D map of crosstalk percentage between the paired pixels as a function of row and column in the linear FE of an *irradiated* RD53A module with a $25 \times 100 \, \mu m^2$ pitch sensor. Maps are shown for preamplifier (PA) bias values of 350 (top left), 410 (top right), 450 (bottom left), and 500 (bottom right).
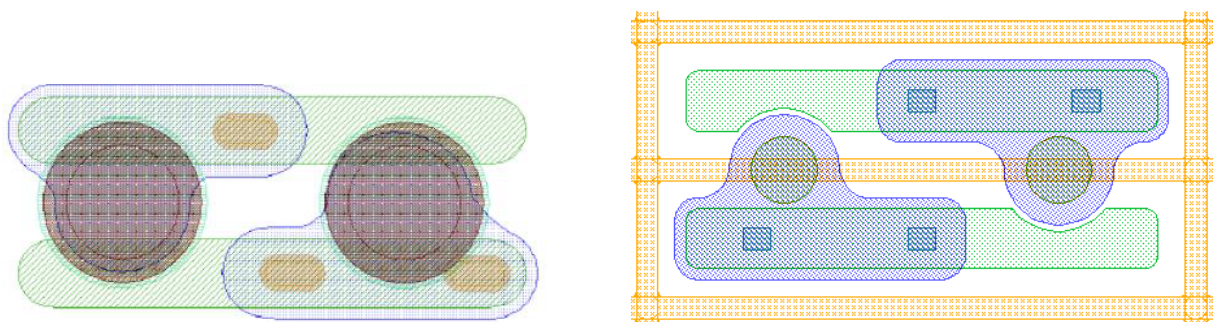
Figure 10.14: Layout of the $25 \times 100 \, \mu m^2$ pitch sensor for the standard (left) and bitten (right) design. A part of the pixel implant is cut out in the bitten design to remove the overlay with the under-bump metalization of the neighboring pixel and decrease the capacitance between the pixels.

11 TEPX

The TEPX section of the CMS Phase2 pixel detector extends the pseudorapidity coverage of the system from $|\eta| < 4$ to $|\eta| < 4$. Among many benefits for the physics analyses during HL-LHC, the extension of the coverage and the resulting decrease in the track reconstruction p_T thresholds, due to the acceptance of the more forward tracking disks, can improve the measurement of the anomalous magnetic moment of the tau lepton, as discussed in chapter 7. Furthermore, the real-time luminosity measurement of the TEPX subdetector mentioned in chapter 8 will reduce the systematic uncertainty of the luminosity that affects the majority of physics analyses. In this chapter, my contribution to the research and development (R&D) studies of the TEPX subdetector will be summarized.

11.1 R&D studies of the TEPX at UZH

R&D studies of the TEPX section of the CMS Phase2 pixel detector described in chapter 8 are performed by the UZH and PSI groups and the final TEPX detector will be constructed at UZH. The results presented in this chapter are from the first prototypes of the TEPX quad modules. These modules, consisting of 4 RD53A readout chips connected to a high-density interconnect (HDI) to read out the data and provide the power, are tested both separately while mounted on a single quad PCB, and while mounted on the first TEPX half-disk PCB.

A serial powering system will be employed in the Phase2 pixel detector. Serial powering implementation and testing is necessarily more thorough for TEPX than the other pixel sections due to the long chains of up to 11 2×2 (quad) modules, each consisting of 4 readout chips. A failure of one full quad module could result in an open circuit and failure of the entire chain, which should be strictly prevented. However, the loss of one chip in the module is tolerable and the chain should remain functional. In addition to power considerations, due to the relatively lower occupancy compared to the barrel section, the data lanes in TEPX also pass through long chains of quad modules which could potentially result in higher noise, signal deficiency, and bit errors. Therefore, they must be thoroughly studied during the R&D steps.

11.2 The half-disk PCB

Figure 11.1 shows the prototype PCB with one side of the TEPX half-disk consisting of rings 1, 3, and 5, with 5, 9, and 12 quad modules, respectively. The complementary side of the half-disk with rings 2 and 4 will be attached on the back. As only a few quad modules were available at the time, the rest of the half disk is filled with dummy modules, mimicking the electrical characteristics of the quad modules, to close the circuits. The tests are performed on ring 1 of the half disk with positions 11, 12, 13, 14, and 15 from right to left in figure 11.1. The power for ring one is supplied from the left side and the data lanes start from the RD53A chips, are routed through the HDI via a connector to the half-disk PCB, then through the PCB to a connector on the right side, through a flex on the right side, are then split by an adapter board shown in the
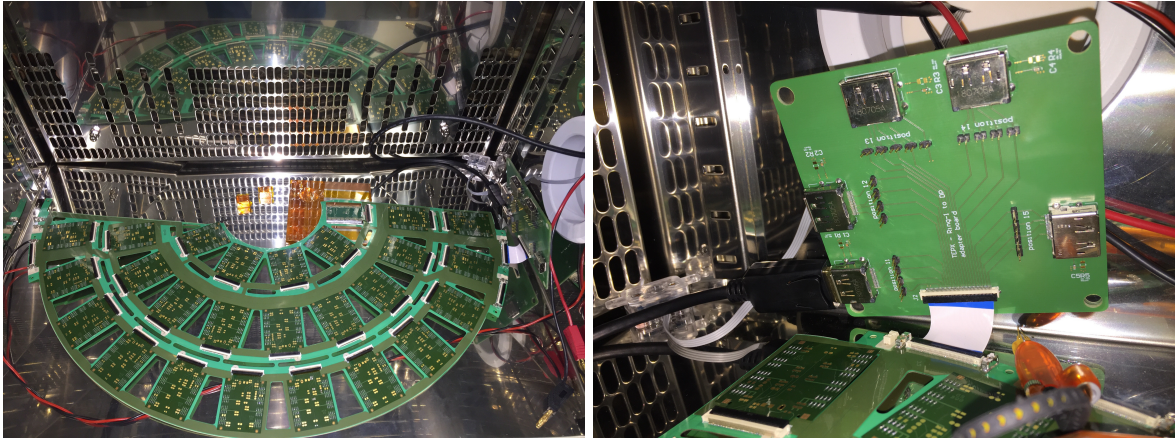
Figure 11.1: TEPX half disk in a climate chamber

right picture of figure 11.1 into 5 display ports corresponding to the 5 quads, and then connected to the readout data acquisition system shown through a fixed mobile convergence (FMC) adapter board connected to a field-programmable gate array (FPGA) shown in figure 11.2.
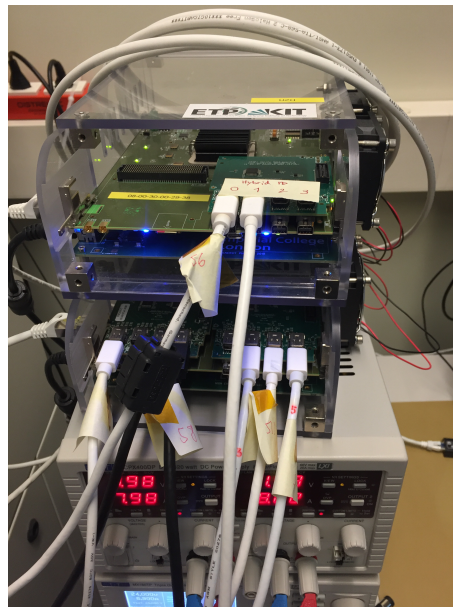
Figure 11.2: The DAQ setup used for the test of single quad modules and the TEPX half-disk. Shown are the FC7 FPGA and the dedicated FMC adapter board.

The full disk is placed in a climate chamber for cooling. Copper blocks as in figure 11.3 are used to improve the contact of the quad module with the bottom of the climate chamber. The temperature of the readout chips can be measured from a resistor on the HDI. This quantity needs to be calibrated once by turning off the module and measuring the resistance for various temperatures of the climate chamber. Once calibrated, the temperature of the chip can be monitored. This temperature is higher than the ambient temperature of the climate chamber when the chip is powered, and the difference reflects the cooling power and thermal connectivity of the cooling system.
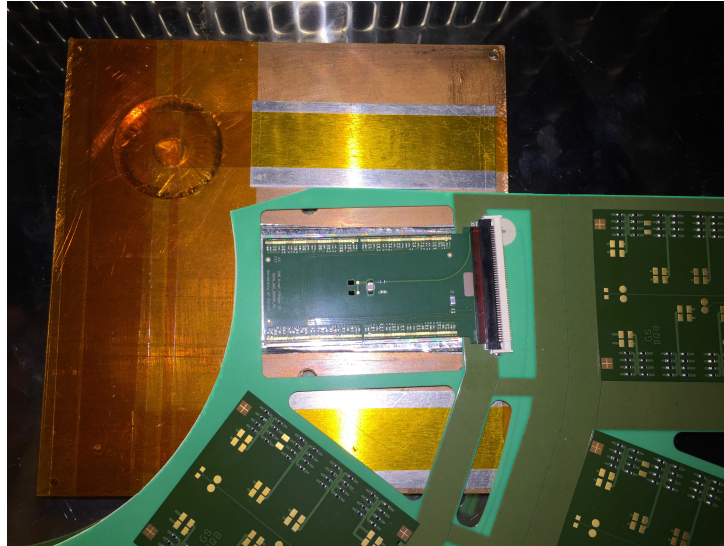
Figure 11.3: Cooling quads by a copper block in a climate chamber

11.3 Powering test of single quad modules

The Shunt-LDO regulator of the RD53A chip regulates the input current of 2.2 A to the required input voltage of 1.2 V for the analog and digital sections, denoted by VDDA and VDDD respectively. The first test that should be performed on a quad module is an IV scan to study the current regulators while disentangling the effects of the module from those of the disk. To do so, the quad module is mounted on a single quad adapter board, shown in figure 11.4 connected to a water-cooled copper block, as shown in figure 11.5.
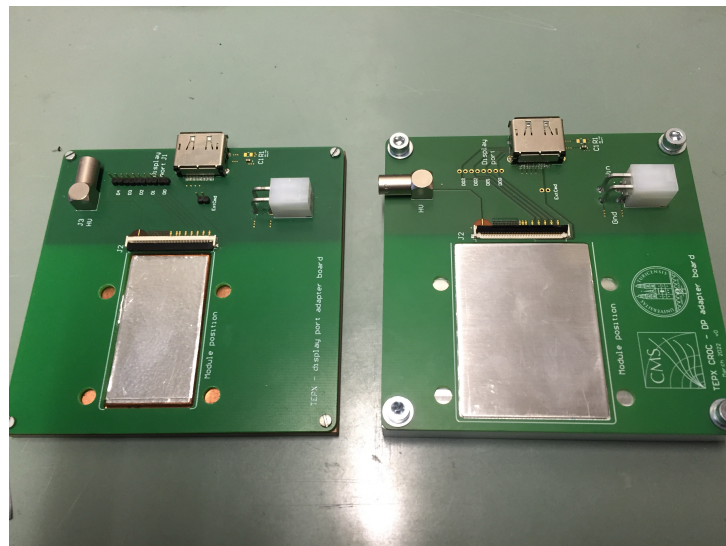
Figure 11.4: The adapter board for testing a single quad module with four RD53A (left) or CROC (right) pixel modules.

An increasing level of current is supplied to the quad module by a current source, and the regulated analog and digital input voltage for each individual chip coming from the output of its Shunt-LDO is measured from the HDI. Figure 11.6 shows the result of this IV scan for the analog and digital input voltages of each RD53A chip, as well as the corresponding voltage of the current source. The jump seen around 2.9 A corresponds to the turn-on point of the Shunt-LDO. As seen in this graph, to achieve the required 1.2 V for input voltages and establish

119
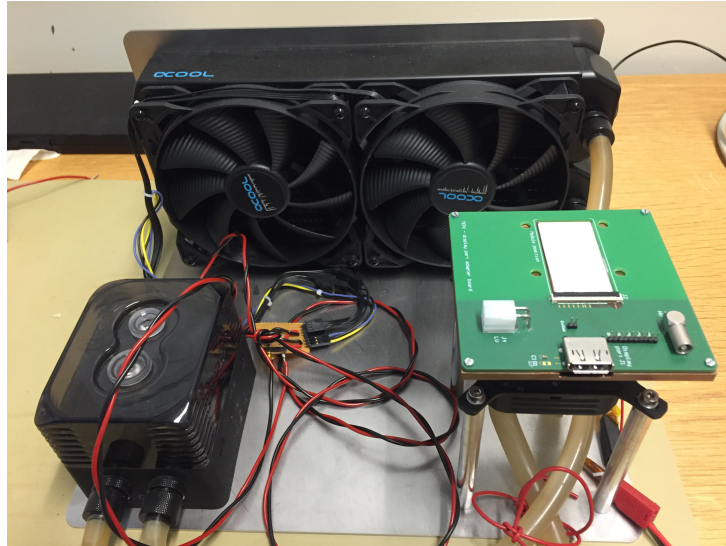
Figure 11.5: Water-cooling setup for the tests with single quad modules

communication with the chips, the input current must be above 4 A.
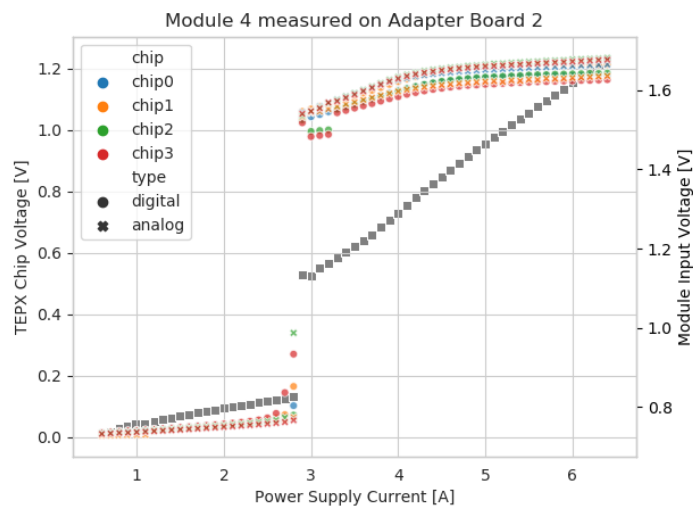
Figure 11.6: IV scans for a single quad RD53A module. Digital and analog voltages of each chip coming from the output of the Shunt-LDO, as well as the voltage of the current source are shown.

11.4 Powering test of quad modules inside the half-disk

Next, these IV scans are taken from the quad module at various positions of the half-disk as shown in figure 11.7. As the quads and their different turn-on points could potentially affect the IV scan, in the first step one quad is mounted in one of the ring-1 positions and the rest of the ring is filled with dummy modules, as shown in the left plot, and then one or a few other quad modules are mounted in the chain, as shown in the right plot.

After a thorough systematic study of the IV curve in various positions and scenarios, it was observed that the half-disk PCB has no deficiency in distributing the power. Furthermore, in some scenarios such as the one shown in the right graph of figure 11.7, one of the chips from quad 3 in the chain was not responsive in terms of both power and data readout and the input
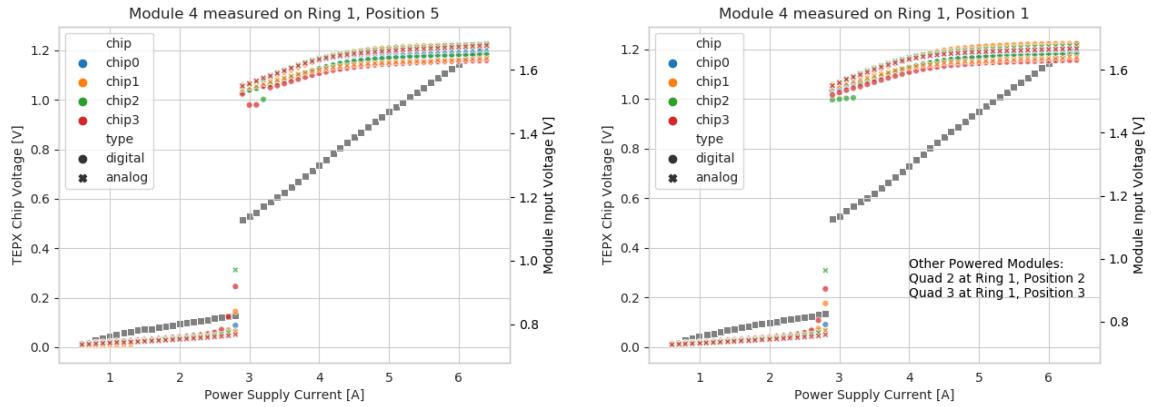
Figure 11.7: The IV curve of quad modules in different positions of ring-1 of the half-disk PCB. The left plot corresponds to a scenario with only one quad module in the chain and the rest of the chain filled with dummy modules to close the chain. The right plot corresponds to a scenario with three quad modules mounted in ring 1.

current to the quad was shared between only three chips, but no significant effect on the power or data quality of the functioning chips was observed either in the other chips of the damaged quad module or the other quad modules in the chain, demonstrating the reliability of the serial powering system.

11.5 Study of digital signals of the half-disk readout chain with an oscilloscope

Following the studies of power distribution, the data transmission through the data lanes of the half-disk PCB is tested. The clock and data signals transferred between the data acquisition firmware and the chips pass through the connecting cables, connectors, adapter board, PCB, and HDI. Any of these elements can potentially reduce signal quality. The signals at each point of connection through this data chain are probed by an oscilloscope. These measurements proved to be quite helpful for debugging data collection in the first prototype and spotting defective or broken elements.

Figure 11.8: Clock signal measured at the connector of the FPGA (left) and the connector of the quad module to the TEPX half-disk (right).

Figure 11.8 shows the clock signal sent by the readout FPGA at two ends of the readout chain, namely, at the FPGA connector and on the quad connector. The presence of a relatively good quality clock signal on both ends shows that the clock lanes in between are well connected. Figure 11.9 shows a similar measurement, but this time from the data lanes. The presence of these signals on both ends not only shows the undamaged connection between the elements of

the data chain, but also shows an established connection to the data acquisition system. This only happens after a sufficient input voltage is supplied by the Shunt-LDO of the chip.
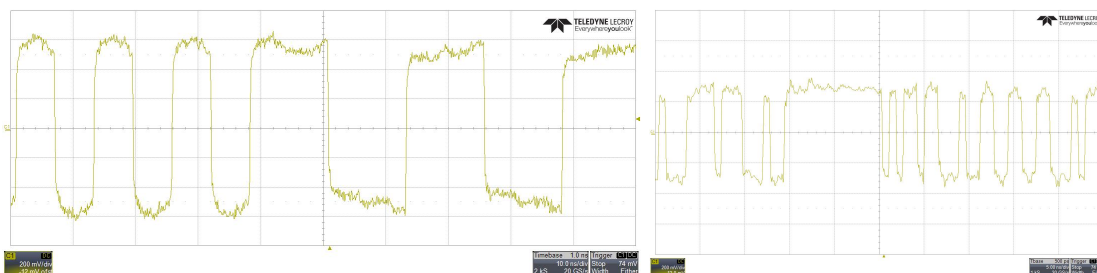
Figure 11.9: Data signal measured at the connector of the FPGA (left) and the connector of the quad module to the TEPX half-disk (right).

Although the presence of data streams on both ends of the readout chain is already a very good signature of data transmission quality, the quality of these signals can be lowered throughout the chain. An ideal digital data stream would look like a series of step functions. However, because of the dispersion of the signals, the real signals look like a series of error functions. By overlaying these signals on top of each other and sampling them with an oscilloscope, an *eye-diagram* is formed as shown in figure 11.10. In the center, the midpoint of the signal is shown where the rising and falling signals are triggered, forming the two crossing lines. While ideally these two lines should be vertical, their slope, or qualitatively the opening area of the two eye shapes in the diagram, shows the level of signal dispersion. The dispersion level seen here at the connector of the quad is acceptable and hints at an acceptable data transmission quality. High levels of signal dispersion can increase the chance of missing some bits of the data. Therefore, bit error rates will also be measured for various positions of modules within the disk.
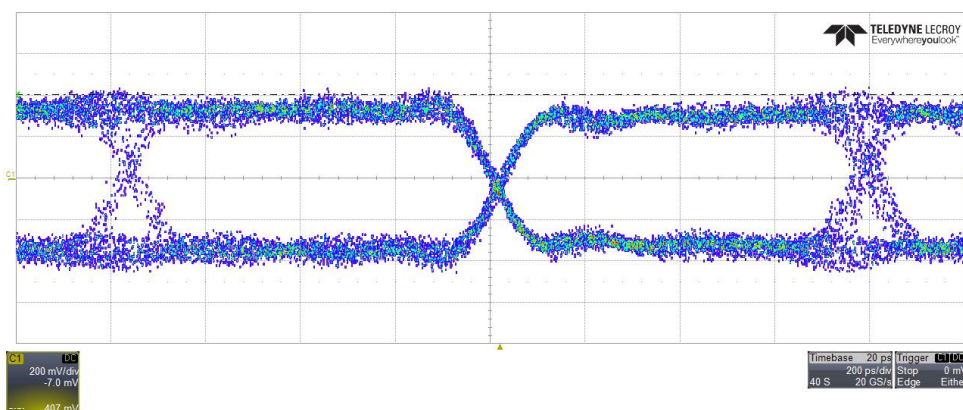
Figure 11.10: The eye diagram for a quad module in position 1-1 in a TEPX half-disk.

11.6 Characterization of quad modules

The study of digital signals with an oscilloscope is a great tool to diagnose data transmission problems and detect mismatched data lanes or broken components of the data chain. However, such tests cannot be performed systematically and automated. After debugging the data transmission setup, the RD53A chips of the quad have to go through the characterization steps described in chapter 9 to make sure the readout chips are operational and tunable, and the readout quality is the same when the quad module is mounted on the half-disk PCB and on the

single quad adapter board, as the readout from the single quad adapter board is less prone to dispersion, noise, missing bits, and power distribution issues.
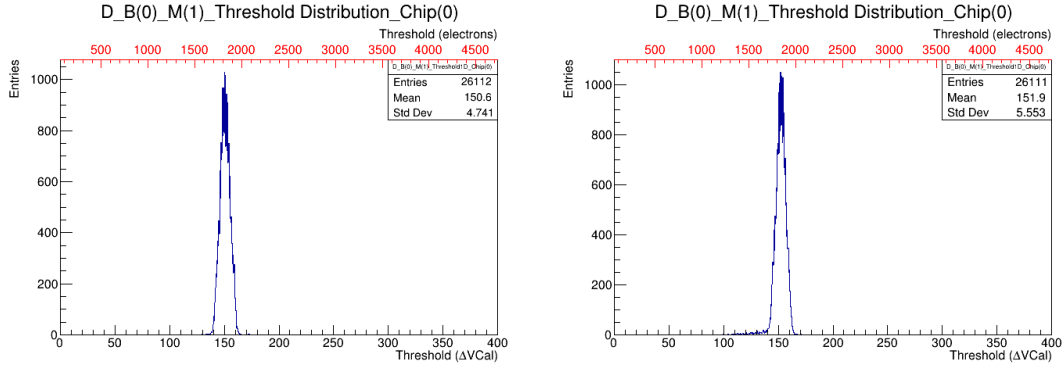
Figure 11.11: Threshold distribution of a quad module mounted on a single adapter board (left) and in ring 1 of the TEPX half disk (right). The module has been re-tuned before testing in each position.
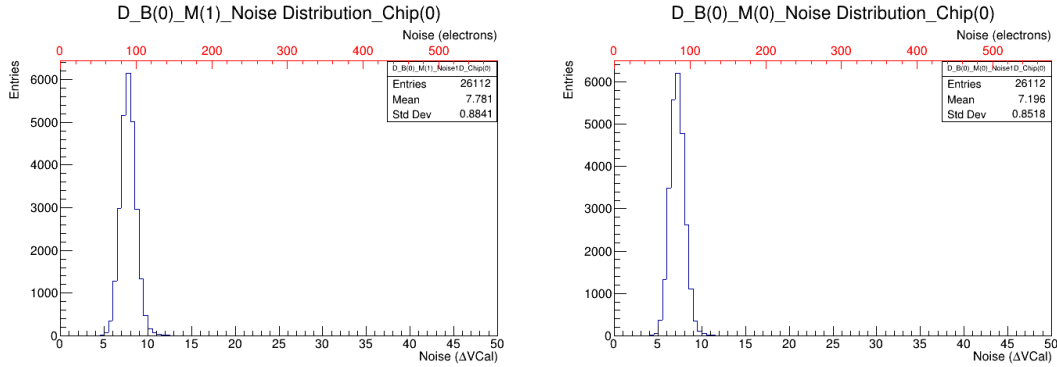
Figure 11.12: Noise distribution of a quad module mounted on a single adapter board (left) and in ring 1 of the TEPX half disk (right). The module has been re-tuned before testing in each position.

Figure 11.11 shows the threshold distribution of one of the RD53A chips of a quad module mounted on the single quad adapter board and on the half-disk PCB. The threshold equalization is performed separately for each case to mitigate the potential effects of transport of the quad module, change of temperature and cooling, and input power. The threshold distributions show similar mean and variance, hinting at a negligible deficiency from the half-disk PCB readout and serial powering. Figure 11.12 shows the noise charge distributions taken from the S-curves as described in chapter 9. Again, the similarity of the distributions proves that no noticeable extra noise has been introduced from the half-disk PCB or the adapters.

11.7 Current status of the TEPX

As mentioned in the previous chapters, my involvement in the TEPX was mainly in the early R&D studies, which took place from late 2019 to 2021. Currently, the prototyping phase of TEPX has evolved by implementing quad modules assembled with the first version of the CROC chip. This is the next version of the RD53 ASIC family, where the linear FE chosen by CMS is deployed in the entire area of the chip. The performance of the new quad modules has been tested in stand-alone mode, in terms of tunability, noise, and data merging. Moreover, the

modules have been read out in serial power mode in the disk PCB, to validate the operability of the power chain, both regarding the possible effect on noise and the data transmission. Low noise values and low data corruption levels have been found. Currently, the optical stage of the read-out is being characterized, to complete the read-out chain validation. The start of module production with the final version of the chip is foreseen for Summer 2024.

12 Summary

In this dissertation, my studies on the measurement of the anomalous magnetic moment of the tau lepton were reviewed. The first measurement at the LHC used the 2015 dataset of Pb-Pb collisions at a center-of-mass energy of $5.02\,\mathrm{TeV}$ per nucleon, recorded by the CMS experiment. This measurement was published [100] in Physical Review Letters and selected as the editor's choice. I have also presented these results at Moriond 2022 and Quark Matter 2022 conferences and published [131] them as a proceeding. An ongoing measurement aims to improve the precision of this measurement, possibly better than the current best measurement by the DELPHI Collaboration, by using the larger dataset collected in 2018, studying additional decay channels of tau leptons, reducing the systematic uncertainties, and improving the analysis methods. Specifically, I have developed several aspects of the new analysis, including a new decay channel of μ+1prong and its relatively difficult background estimate, a method for identifying and mitigating the troublesome $\gamma + \gamma \rightarrow \mu^+ + \mu^- + \gamma$ background, a method for identifying π^0s from tau lepton decay down to never-before reached p_T thresholds, and a method for unfolding the reconstructed data to the truth-level information. I also present my studies indicating the future prospects of this measurement with Run3 data and with the HL-LHC, taking advantage of new upgraded features of the Phase2 CMS experiment in order to improve signal acceptance, efficiency, and therefore statistical uncertainty, along with plans for improving systematic uncertainties to similar levels as the statistical uncertainty. Finally, my contribution to the upgrade studies of the CMS tracking system was presented. Part of this work was published as conference proceedings [132, 133]. The upgraded CMS detector is able to handle the challenging conditions of the high-luminosity LHC era and collect enough data to measure the anomalous magnetic moment of the tau lepton with an estimated central value and precision of a_τ that could be as good as $a_\tau = (12 \pm 9) \times 10^{-4}$. Assuming no BSM effects, this level of precision would allow a confirmation of the dominant correction to a_τ from the one-loop QED effect, which is $\frac{\alpha}{2\pi} \approx 11.6 \times 10^{-4}$.

References

[1] Neutelings, Izaak, "History timeline and energy scales – TikZ.net", `https://tikz.net/timeline/`, 2022. (Retrieved March 26, 2022).

[2] S. L. Glashow, J. Iliopoulos, and L. Maiani, "Weak Interactions with Lepton-Hadron Symmetry", *Phys. Rev. D* **2** (1970) 1285, `doi:10.1103/PhysRevD.2.1285`.

[3] Wikimedia Commons, "File:Standard Model of Elementary Particles.svg — Wikimedia Commons, the free media repository", `https://commons.wikimedia.org/wiki/File:Standard_Model_of_Elementary_Particles.svg`, 2023. (Retrieved Jan 13, 2023).

[4] E. Noether, "Invariante Variationsprobleme", *Nachrichten von der Gesellschaft der Wissenschaften zu Göttingen, Mathematisch-Physikalische Klasse* **1918** (1918) 235–257.

[5] R. P. Feynman, "Space-Time Approach to Quantum Electrodynamics", *Phys. Rev.* **76** (Sep, 1949) 769–789, `doi:10.1103/PhysRev.76.769`.

[6] M. E. Peskin and D. V. Schroeder, "An Introduction to quantum field theory". Addison-Wesley, Reading, USA, 1995. ISBN 978-0-201-50397-5.

[7] S. L. Glashow, "The renormalizability of vector meson interactions", *Nuclear Physics* **10** (1959) 107–117, `doi:https://doi.org/10.1016/0029-5582(59)90196-8`.

[8] A. Salam and J. C. Ward, "Weak and electromagnetic interactions", *Nuovo Cim.* **11** (1959) 568–577, `doi:10.1007/BF02726525`.

[9] S. Weinberg, "A Model of Leptons", *Phys. Rev. Lett.* **19** (Nov, 1967) 1264–1266, `doi:10.1103/PhysRevLett.19.1264`.

[10] S. L. Glashow, "Partial-symmetries of weak interactions", *Nuclear Physics* **22** (1961), no. 4, 579–588, `doi:https://doi.org/10.1016/0029-5582(61)90469-2`.

[11] N. Cabibbo, "Unitary Symmetry and Leptonic Decays", *Phys. Rev. Lett.* **10** (1963) 531, `doi:10.1103/PhysRevLett.10.531`.

[12] M. Kobayashi and T. Maskawa, "CP Violation in the Renormalizable Theory of Weak Interaction", *Prog. Theor. Phys.* **49** (1973) 652, `doi:10.1143/PTP.49.652`.

[13] **Particle Data** Group, "Review of Particle Physics", *PTEP* **2022** (2022) 083C01, `doi:10.1093/ptep/ptac097`.

[14] F. Englert and R. Brout, "Broken Symmetry and the Mass of Gauge Vector Mesons", *Phys. Rev. Lett.* **13** (1964) 321, `doi:10.1103/PhysRevLett.13.321`.

[15] P. W. Higgs, "Broken Symmetries and the Masses of Gauge Bosons", *Phys. Rev. Lett.* **13** (1964) 508, `doi:10.1103/PhysRevLett.13.508`.

[16] G. S. Guralnik, C. R. Hagen, and T. W. B. Kibble, "Global Conservation Laws and Massless Particles", *Phys. Rev. Lett.* **13** (Nov, 1964) 585–587, `doi:10.1103/PhysRevLett.13.585`.

[17] **CMS** Collaboration, "Observation of a new boson at a mass of 125 GeV with the CMS experiment at the LHC", *Phys. Lett. B* **716** (2012) 30, doi:10.1016/j.physletb.2012.08.021, arXiv:1207.7235.

[18] **ATLAS** Collaboration, "Observation of a new particle in the search for the Standard Model Higgs boson with the ATLAS detector at the LHC", *Phys. Lett. B* **716** (2012) 1, doi:10.1016/j.physletb.2012.08.020, arXiv:1207.7214.

[19] **CMS** Collaboration, "Observation of a new boson with mass near 125 GeV in pp collisions at $\sqrt{s} = 7$ and 8 TeV", *JHEP* **06** (2013) 081, doi:10.1007/JHEP06(2013)081, arXiv:1303.4571.

[20] **CMS** Collaboration, "Combined Higgs boson production and decay measurements with up to 137 fb^{-1} of proton-proton collision data at $\sqrt{s} = 13$ TeV",.

[21] **CMS** Collaboration, "A portrait of the Higgs boson by the CMS experiment ten years after the discovery", *Nature* **607** (2022), no. 7917, 60, doi:10.1038/s41586-022-04892-x, arXiv:2207.00043.

[22] **ATLAS** Collaboration, "A detailed map of Higgs boson interactions by the ATLAS experiment ten years after the discovery", *Nature* **607** (2022), no. 7917, 52, doi:10.1038/s41586-022-04893-w, arXiv:2207.00092. [Erratum: Nature 612, E24 (2022)].

[23] T. Aoyama et al., "The anomalous magnetic moment of the muon in the Standard Model", *Physics Reports* **887** (2020) 1–166, doi:https://doi.org/10.1016/j.physrep.2020.07.006. The anomalous magnetic moment of the muon in the Standard Model.

[24] S. Eidelman and M. Passera, "Theory of the tau lepton anomalous magnetic moment", *Mod. Phys. Lett. A* **22** (2007) 159–179, doi:10.1142/S0217732307022694, arXiv:hep-ph/0701260.

[25] M. Davier, A. Hoecker, B. Malaescu, and Z. Zhang, "Reevaluation of the hadronic vacuum polarisation contributions to the Standard Model predictions of the muon $g-2$ and $\{\backslash alpha(m\_Z^2)\}$ using newest hadronic cross-section data", *The European Physical Journal C* **77** (Dec, 2017) 827, doi:10.1140/epjc/s10052-017-5161-6.

[26] A. Keshavarzi, D. Nomura, and T. Teubner, "Muon $g-2$ and $\alpha(M_Z^2)$: A new data-based analysis", *Phys. Rev. D* **97** (Jun, 2018) 114025, doi:10.1103/PhysRevD.97.114025.

[27] G. Colangelo, M. Hoferichter, and P. Stoffer, "Two-pion contribution to hadronic vacuum polarization", *Journal of High Energy Physics* **2019** (Feb, 2019) 6, doi:10.1007/JHEP02(2019)006.

[28] M. Hoferichter, B.-L. Hoid, and B. Kubis, "Three-pion contribution to hadronic vacuum polarization", *Journal of High Energy Physics* **2019** (Aug, 2019) 137, doi:10.1007/JHEP08(2019)137.

[29] M. Davier, A. Hoecker, B. Malaescu, and Z. Zhang, "A new evaluation of the hadronic vacuum polarisation contributions to the muon anomalous magnetic moment and to $\backslash varvec\{\backslash alpha\}(\{\{\backslash varvec\{m\}\}\}\_\{\{\backslash varvec\{Z\}\}\}^2)$", *The European Physical Journal C* **80** (Mar, 2020) 241, doi:10.1140/epjc/s10052-020-7792-2.

[30] A. Keshavarzi, D. Nomura, and T. Teubner, "$g - 2$ of charged leptons, $\alpha(M_Z^2)$, and the hyperfine splitting of muonium", *Phys. Rev. D* **101** (Jan, 2020) 014029, `doi:10.1103/PhysRevD.101.014029`.

[31] A. Kurz, T. Liu, P. Marquard, and M. Steinhauser, "Hadronic contribution to the muon anomalous magnetic moment to next-to-next-to-leading order", *Physics Letters B* **734** (2014) 144–147, `doi:https://doi.org/10.1016/j.physletb.2014.05.043`.

[32] K. Melnikov and A. Vainshtein, "Hadronic light-by-light scattering contribution to the muon anomalous magnetic moment reexamined", *Phys. Rev. D* **70** (Dec, 2004) 113006, `doi:10.1103/PhysRevD.70.113006`.

[33] P. Masjuan and P. Sanchez-Puertas, "Pseudoscalar-pole contribution to the $(g_\mu - 2)$: A rational approach", *Phys. Rev. D* **95** (Mar, 2017) 054026, `doi:10.1103/PhysRevD.95.054026`.

[34] G. Colangelo, M. Hoferichter, M. Procura, and P. Stoffer, "Dispersion relation for hadronic light-by-light scattering: two-pion contributions", *Journal of High Energy Physics* **2017** (Apr, 2017) 161, `doi:10.1007/JHEP04(2017)161`.

[35] M. Hoferichter et al., "Dispersion relation for hadronic light-by-light scattering: pion pole", *Journal of High Energy Physics* **2018** (Oct, 2018) 141, `doi:10.1007/JHEP10(2018)141`.

[36] A. Gérardin, H. B. Meyer, and A. Nyffeler, "Lattice calculation of the pion transition form factor with $N_f = 2 + 1$ Wilson quarks", *Phys. Rev. D* **100** (Aug, 2019) 034520, `doi:10.1103/PhysRevD.100.034520`.

[37] J. Bijnens, N. Hermansson-Truedsson, and A. Rodríguez-Sánchez, "Short-distance constraints for the HLbL contribution to the muon anomalous magnetic moment", *Physics Letters B* **798** (2019) 134994, `doi:https://doi.org/10.1016/j.physletb.2019.134994`.

[38] G. Colangelo et al., "Longitudinal short-distance constraints for the hadronic light-by-light contribution to $(g - 2)_\mu$ with large-N_c Regge models", *Journal of High Energy Physics* **2020** (Mar, 2020) 101, `doi:10.1007/JHEP03(2020)101`.

[39] G. Colangelo et al., "Remarks on higher-order hadronic corrections to the muon $g - 2$", *Physics Letters B* **735** (2014) 90–91, `doi:https://doi.org/10.1016/j.physletb.2014.06.012`.

[40] T. Blum et al., "Hadronic Light-by-Light Scattering Contribution to the Muon Anomalous Magnetic Moment from Lattice QCD", *Phys. Rev. Lett.* **124** (Apr, 2020) 132002, `doi:10.1103/PhysRevLett.124.132002`.

[41] T. Aoyama, M. Hayakawa, T. Kinoshita, and M. Nio, "Complete Tenth-Order QED Contribution to the Muon $g-2$", *Phys. Rev. Lett.* **109** (Sep, 2012) 111808, `doi:10.1103/PhysRevLett.109.111808`.

[42] T. Aoyama, T. Kinoshita, and M. Nio, "Theory of the Anomalous Magnetic Moment of the Electron", *Atoms* **7** (2019), no. 1, `doi:10.3390/atoms7010028`.

[43] A. Czarnecki, W. J. Marciano, and A. Vainshtein, "Refinements in electroweak contributions to the muon anomalous magnetic moment", *Phys. Rev. D* **67** (Apr, 2003)

073006, `doi:10.1103/PhysRevD.67.073006`.

[44] C. Gnendiger, D. Stöckinger, and H. Stöckinger-Kim, "The electroweak contributions to $(g-2)_\mu$ after the Higgs-boson mass measurement", *Phys. Rev. D* **88** (Sep, 2013) 053005, `doi:10.1103/PhysRevD.88.053005`.

[45] T. Aoyama, T. Kinoshita, and M. Nio, "Theory of the Anomalous Magnetic Moment of the Electron", *Atoms* **7** (2019), no. 1, 28, `doi:10.3390/atoms7010028`.

[46] D. J. Silverman and G. L. Shaw, "Limits on the composite structure of the τ lepton and quarks from anomalous-magnetic-moment measurements in e^+e^- annihilation", *Phys. Rev. D* **27** (Mar, 1983) 1196–1199, `doi:10.1103/PhysRevD.27.1196`.

[47] S. P. Martin and J. D. Wells, "Muon anomalous magnetic dipole moment in supersymmetric theories", *Phys. Rev. D* **64** (Jun, 2001) 035003, `doi:10.1103/PhysRevD.64.035003`.

[48] **DELPHI** Collaboration, "Study of tau-pair production in photon-photon collisions at LEP and limits on the anomalous electromagnetic moments of the tau lepton", *Eur. Phys. J. C* **35** (2004) 159–170, `doi:10.1140/epjc/s2004-01852-y`, `arXiv:hep-ex/0406010`.

[49] R. Escribano and E. Massó, "New bounds on the magnetic and electric moments of the tau lepton", *Physics Letters B* **301** (1993), no. 4, 419–422, `doi:https://doi.org/10.1016/0370-2693(93)91172-J`.

[50] X. Fan, T. G. Myers, B. A. D. Sukra, and G. Gabrielse, "Measurement of the Electron Magnetic Moment", *Phys. Rev. Lett.* **130** (Feb, 2023) 071801, `doi:10.1103/PhysRevLett.130.071801`.

[51] L. Morel, Z. Yao, P. Cladé, and S. Guellati-Khelifa, "Determination of the fine-structure constant with an accuracy of 81 parts per trillion", *Nature* **588** (12, 2020) 61–65, `doi:10.1038/s41586-020-2964-7`.

[52] R. H. Parker et al., "Measurement of the fine-structure constant as a test of the Standard Model", *Science* **360** (2018) 191, `doi:10.1126/science.aap7706`, `arXiv:1812.04130`.

[53] "Muon $g-2$ experiments at CERN". `https://sis.web.cern.ch/archives/CERN_archive/guide/experimental_physics/SC/isamuon`.

[54] **Muon** Collaboration, "Final Report of the Muon E821 Anomalous Magnetic Moment Measurement at BNL", *Phys. Rev. D* **73** (2006) 072003, `doi:10.1103/PhysRevD.73.072003`, `arXiv:hep-ex/0602035`.

[55] **Muon** Collaboration, "Measurement of the Positive Muon Anomalous Magnetic Moment to 0.46 ppm", *Phys. Rev. Lett.* **126** (2021), no. 14, 141801, `doi:10.1103/PhysRevLett.126.141801`, `arXiv:2104.03281`.

[56] D. P. Aguillard et al., "Measurement of the Positive Muon Anomalous Magnetic Moment to 0.20 ppm", 2023.

[57] T. Aoyama et al., "The anomalous magnetic moment of the muon in the Standard Model", *Physics Reports* **887** (2020) 1–166, `doi:https://doi.org/10.1016/j.physrep.2020.07.006`. The anomalous magnetic moment of the muon in the Standard Model.

[58] **Budapest-Marseille-Wuppertal** Collaboration, "Hadronic vacuum polarization contribution to the anomalous magnetic moments of leptons from first principles", *Phys. Rev. Lett.* **121** (2018), no. 2, 022002, `doi:10.1103/PhysRevLett.121.022002`, `arXiv:1711.04980`.

[59] **UKQCD** Collaboration, "Calculation of the hadronic vacuum polarization contribution to the muon anomalous magnetic moment", *Phys. Rev. Lett.* **121** (2018), no. 2, 022003, `doi:10.1103/PhysRevLett.121.022003`, `arXiv:1801.07224`.

[60] H. B. Meyer and H. Wittig, "Lattice QCD and the anomalous magnetic moment of the muon", *Prog. Part. Nucl. Phys.* **104** (2019) 46, `doi:10.1016/j.ppnp.2018.09.001`, `arXiv:1807.09370`.

[61] P. A. Boyle et al., "A lattice QCD perspective on weak decays of b and c quarks Snowmass 2022 White Paper", in *2022 Snowmass Summer Study*. 5, 2022. `arXiv:2205.15373`.

[62] **OPAL** Collaboration, "An Upper limit on the anomalous magnetic moment of the tau lepton", *Phys. Lett. B* **431** (1998) 188–198, `doi:10.1016/S0370-2693(98)00520-6`, `arXiv:hep-ex/9803020`.

[63] **L3** Collaboration, "Measurement of the anomalous magnetic and electric dipole moments of the tau lepton", *Phys. Lett. B* **434** (1998) 169–179, `doi:10.1016/S0370-2693(98)00736-9`.

[64] J. Illana, "Estudio de las propiedades electromagneticas del boson W y del lepton tau en procesos de dos fotones". PhD thesis, University of Granada, 1995.

[65] V. Budnev, I. Ginzburg, G. Meledin, and V. Serbo, "The two-photon particle production mechanism. Physical problems. Applications. Equivalent photon approximation", *Physics Reports* **15** (1975), no. 4, 181–282, `doi:https://doi.org/10.1016/0370-1573(75)90009-5`.

[66] F. del Aguila, F. Cornet, and J. Illana, "The possibility of using a large heavy-ion collider for measuring the electromagnetic properties of the tau lepton", *Physics Letters B* **271** (1991), no. 1, 256–260, `doi:https://doi.org/10.1016/0370-2693(91)91309-J`.

[67] L. Beresford and J. Liu, "New physics and tau $g-2$ using LHC heavy ion collisions", *Phys. Rev. D* **102** (2020) 113008, `doi:10.1103/PhysRevD.102.113008`, `arXiv:1908.05180`.

[68] L. Beresford and J. Liu, "Erratum: New physics and tau $g-2$ using LHC heavy ion collisions [Phys. Rev. D 102, 113008 (2020)]", *Phys. Rev. D* **106** (Aug, 2022) 039902, `doi:10.1103/PhysRevD.106.039902`.

[69] F. Maltoni and T. Stelzer, "MadEvent: Automatic event generation with MadGraph", *JHEP* **02** (2003) 027, `doi:10.1088/1126-6708/2003/02/027`, `arXiv:hep-ph/0208156`.

[70] I. Brivio, Y. Jiang, and M. Trott, "The SMEFTsim package, theory and tools", *JHEP* **12** (2017) 070, `doi:10.1007/JHEP12(2017)070`, `arXiv:1709.06492`.

[71] D. Hanneke, S. Fogwell, and G. Gabrielse, "New Measurement of the Electron Magnetic Moment and the Fine Structure Constant", *Phys. Rev. Lett.* **100** (2008) 120801, `doi:10.1103/PhysRevLett.100.120801`, `arXiv:0801.1134`.

[72] L. Forthomme (Wikimedia Commons), "File:Cern-accelerator-complex.svg — Wikimedia Commons, the free media repository", `https://commons.wikimedia.org/wiki/File:Cern-accelerator-complex.svg`, 2016. (Retrieved Jul 24, 2017).

[73] **CMS** Collaboration, "Public CMS Luminosity Information". `https://twiki.cern.ch/twiki/bin/view/CMSPublic/LumiPublicResults`. (Retrieved Dec 6, 2022).

[74] W. Herr and B. Muratori, "Concept of luminosity", in *CAS - CERN Accelerator School: Intermediate Course on Accelerator Physics*, CERN. CERN, Zeuthen, Germany, 2003. `doi:10.5170/CERN-2006-002.361`.

[75] C. Loizides, J. Kamin, and D. d'Enterria, "Improved Monte Carlo Glauber predictions at present and future nuclear colliders", *Phys. Rev. C* **97** (May, 2018) 054910, `doi:10.1103/PhysRevC.97.054910`.

[76] A. J. Baltz, M. J. Rhoades-Brown, and J. Weneser, "Heavy-ion partial beam lifetimes due to Coulomb induced processes", *Phys. Rev. E* **54** (Oct, 1996) 4233–4239, `doi:10.1103/PhysRevE.54.4233`.

[77] **CMS** Collaboration, "The CMS experiment at the CERN LHC", *JINST* **3** (2008) S08004, `doi:10.1088/1748-0221/3/08/S08004`.

[78] Neutelings, Izaak, "CMS coordinate system – TikZ.net", `https://tikz.net/axis3d_cms/`, 2022. (Retrieved Dec 2, 2022).

[79] Neutelings, Izaak, "Pseudorapidity – TikZ.net", `https://tikz.net/axis2d_pseudorapidity/`, 2022. (Retrieved Dec 2, 2022).

[80] **CMS** Collaboration, "Performance of the CMS Drift Tube Chambers with Cosmic Rays", *JINST* **5** (2010) T03015, `doi:10.1088/1748-0221/5/03/T03015`, `arXiv:0911.4855`.

[81] **CMS** Collaboration, "Precise Mapping of the Magnetic Field in the CMS Barrel Yoke using Cosmic Rays", *JINST* **5** (2015) T03021, `doi:10.1088/1748-0221/5/03/T03021`, `arXiv:0910.5530`.

[82] **CMS** Collaboration, "CMS Tracker Detector Performance Results", `https://twiki.cern.ch/twiki/bin/view/CMSPublic/DPGResultsTRK`, 2022. (Retrieved Dec 2, 2022).

[83] **CMS** Collaboration, "The Phase-1 upgrade of the CMS pixel detector", *JINST* **12** (2017), no. 07, C07009, `doi:10.1088/1748-0221/12/07/C07009`.

[84] **CMS Tracker** Group, "The CMS Phase-1 Pixel Detector Upgrade", *JINST* **16** (2021), no. 02, P02027, `doi:10.1088/1748-0221/16/02/P02027`, `arXiv:2012.14304`.

[85] **CMS** Collaboration, "Description and performance of track and primary-vertex reconstruction with the CMS tracker", *JINST* **9** (2014) P10009, `doi:10.1088/1748-0221/9/10/P10009`, `arXiv:1405.6569`.

[86] **CMS** Collaboration, "CMS Tracking POG Performance Plots For 2017 with PhaseI pixel detector", `https://twiki.cern.ch/twiki/bin/view/CMSPublic/TrackingPOGPerformance2017MC#Vertex_Resolutions`, 2022. (Retrieved Dec 8, 2022).

[87] **CMS** Collaboration, "The CMS electromagnetic calorimeter project: Technical Design Report", Technical Design Report CMS. CERN, Geneva, 1997.

[88] **CMS** Collaboration, "Energy Resolution of the Barrel of the CMS Electromagnetic Calorimeter", technical report, CERN, Geneva, 2007. `doi:10.1088/1748-0221/2/04/P04004`.

[89] **CMS** Collaboration, "Performance of the CMS Hadron Calorimeter with Cosmic Ray Muons and LHC Beam Data", *JINST* **5** (2010) T03012, `doi:10.1088/1748-0221/5/03/T03012`, `arXiv:0911.4991`.

[90] E. Manca, "Validation of the muon momentum resolution in view of the W mass measurement with the CMS experiment". PhD thesis, INFN, Pisa, 2016. CMS-TS-2016-024, CERN-THESIS-2016-173.

[91] **CMS** Collaboration, "The CMS muon project : Technical Design Report", Technical Design Report CMS. CERN, Geneva, 1997.

[92] **CMS** Collaboration, "Observation of Forward Neutron Multiplicity Dependence of Dimuon Acoplanarity in Ultraperipheral Pb-Pb Collisions at $\sqrt{s_{NN}} = 5.02$ TeV", *Phys. Rev. Lett.* **127** (Sep, 2021) 122001, `doi:10.1103/PhysRevLett.127.122001`.

[93] **CMS** Collaboration, "The CMS trigger system", *JINST* **12** (2017) P01020, `doi:10.1088/1748-0221/12/01/P01020`, `arXiv:1609.02366`.

[94] L. Lee, C. Ohm, A. Soffer, and T.-T. Yu, "Collider Searches for Long-Lived Particles Beyond the Standard Model", *Prog. Part. Nucl. Phys.* **106** (2019) 210, `doi:10.1016/j.ppnp.2019.02.006`, `arXiv:1810.12602`. [Erratum: Prog.Part.Nucl.Phys. 122, 103912 (2022)].

[95] D. Barney, "CMS Slice", `https://cds.cern.ch/record/2628641/`, 2015. (Retrieved Dec 8, 2022).

[96] **CMS** Collaboration, "Commissioning of the Particle-flow Event Reconstruction with the first LHC collisions recorded in the CMS detector", CMS Physics Analysis Summary CMS-PAS-PFT-10-001, CERN, 2010.

[97] **CMS** Collaboration, "Particle-flow reconstruction and global event description with the CMS detector", *JINST* **12** (2017) P10003, `doi:10.1088/1748-0221/12/10/P10003`, `arXiv:1706.04965`.

[98] W. Adam, B. Mangano, T. Speer, and T. Todorov, "Track Reconstruction in the CMS tracker", technical report, CERN, Geneva, 2006.

[99] R. Fruhwirth, "Application of Kalman filtering to track and vertex fitting", *Nucl. Instrum. Meth. A* **262** (1987) 444, `doi:10.1016/0168-9002(87)90887-4`.

[100] **CMS** Collaboration, "Observation of τ Lepton Pair Production in Ultraperipheral Pb-Pb Collisions at $\sqrt{s_{NN}} = 5.02$ TeV", *Phys. Rev. Lett.* **131** (Oct, 2023) 151803, `doi:10.1103/PhysRevLett.131.151803`.

[101] J. Alwall et al., "The automated computation of tree-level and next-to-leading order differential cross sections, and their matching to parton shower simulations", *JHEP* **07** (2014) 079, `doi:10.1007/JHEP07(2014)079`, `arXiv:1405.0301`.

[102] T. Sjöstrand et al., "An introduction to PYTHIA 8.2", *Comput. Phys. Commun.* **191** (2015) 159, `doi:10.1016/j.cpc.2015.01.024`, `arXiv:1410.3012`.

[103] **GEANT4** Collaboration, "GEANT4—a simulation toolkit", *Nucl. Instrum. Meth. A* **506** (2003) 250, `doi:10.1016/S0168-9002(03)01368-8`.

[104] **Particle Data** Group, "Review of Particle Physics", *PTEP* **2020** (2020), no. 8, 083C01, `doi:10.1093/ptep/ptaa104`.

[105] **TOTEM** Collaboration, "Observation of proton-tagged, central (semi)exclusive production of high-mass lepton pairs in pp collisions at 13 TeV with the CMS-TOTEM precision proton spectrometer", *JHEP* **07** (2018) 153, `doi:10.1007/JHEP07(2018)153`, `arXiv:1803.04496`.

[106] **CMS** Collaboration, "Performance of the CMS muon detector and muon reconstruction with proton-proton collisions at $\sqrt{s} = 13$ TeV", *JINST* **13** (2018) P06015, `doi:10.1088/1748-0221/13/06/P06015`, `arXiv:1804.04528`.

[107] **CMS** Collaboration, "Final Tracks Selector Algorithms". `https://twiki.cern.ch/twiki/bin/view/CMSPublic/SWGuideFinalTrackSelectors`.

[108] G. Cowan, K. Cranmer, E. Gross, and O. Vitells, "Asymptotic formulae for likelihood-based tests of new physics", *Eur. Phys. J. C* **71** (2011) 1554, `doi:10.1140/epjc/s10052-011-1554-0`, `arXiv:1007.1727`. [Erratum: Eur.Phys.J.C 73, 2501 (2013)].

[109] A. Gilbert, "Documentation of the RooStats-based statistics tools for Higgs PAG". `https://twiki.cern.ch/twiki/bin/viewauth/CMS/SWGuideHiggsAnalysisCombinedLimit`, 2016.

[110] **CMS** Collaboration, "Measurement of exclusive Υ photoproduction from protons in pPb collisions at $\sqrt{s_{\mathrm{NN}}} = 5.02$ TeV", *Eur. Phys. J. C* **79** (2019) 277, `doi:10.1140/epjc/s10052-019-6774-8`, `arXiv:1809.11080`.

[111] **CMS** Collaboration, "CMS Luminosity Measurements for the 2016 Data Taking Period", CMS Physics Analysis Summary CMS-PAS-LUM-17-001, CERN, 2017.

[112] M. Dyndal, M. Klusek-Gawenda, M. Schott, and A. Szczurek, "Anomalous electromagnetic moments of τ lepton in $\gamma\gamma \to \tau^+\tau^-$ reaction in Pb+Pb collisions at the LHC", *Phys. Lett. B* **809** (2020) 135682, `doi:10.1016/j.physletb.2020.135682`, `arXiv:2002.05503`.

[113] **CMS** Collaboration, "Evidence for light-by-light scattering and searches for axion-like particles in ultraperipheral PbPb collisions at $\sqrt{s_{\mathrm{NN}}} = 5.02$ TeV", *Phys. Lett. B* **797** (2019) 134826, `doi:10.1016/j.physletb.2019.134826`, `arXiv:1810.04602`.

[114] **DELPHI** Collaboration, "Study of tau-pair production in photon-photon collisions at LEP and limits on the anomalous electromagnetic moments of the tau lepton", *Eur. Phys. J. C* **35** (2004) 159–170, `doi:10.1140/epjc/s2004-01852-y`, `arXiv:hep-ex/0406010`.

[115] L. A. Harland-Lang, V. A. Khoze, and M. G. Ryskin, "Exclusive LHC physics with heavy ions: SuperChic 3", *The European Physical Journal C* **79** (jan, 2019)

doi:10.1140/epjc/s10052-018-6530-5.

[116] N. Burmasov, E. Kryshen, P. Bühler, and R. Lavicka, "Upcgen: A Monte Carlo simulation program for dilepton pair production in ultra-peripheral collisions of heavy ions", *Computer Physics Communications* **277** (2022) 108388, doi:https://doi.org/10.1016/j.cpc.2022.108388.

[117] H.-S. Shao and D. d'Enterria, "gamma-UPC: automated generation of exclusive photon-photon processes in ultraperipheral proton and nuclear collisions with varying form factors", *JHEP* **09** (2022) 248, doi:10.1007/JHEP09(2022)248, arXiv:2207.03012.

[118] R. Bruce et al., "Performance and luminosity models for heavy-ion operation at the CERN Large Hadron Collider", *The European Physical Journal Plus* **136** (jul, 2021) doi:10.1140/epjp/s13360-021-01685-5.

[119] "LHC long term schedule". https://lhc-commissioning.web.cern.ch/schedule/LHC-long-term.htm. (Retrieved Aug 19, 2023).

[120] **CMS** Collaboration, "The Phase-2 Upgrade of the CMS Tracker", Technical Report CERN-LHCC-2017-009. CMS-TDR-014, CERN, Geneva, jun, 2017.

[121] **ATLAS** Collaboration, "Observation of the $\gamma\gamma \to \tau\tau$ process in Pb+Pb collisions and constraints on the τ-lepton anomalous magnetic moment with the ATLAS detector", 2022.

[122] E. Migliore, "The Phase-2 Upgrade of the CMS Inner Tracker, iWoRiD 2023: iWoRiD 24th international Workshop on Radiation Imaging Detectors, 25-29 Jun 2023, Oslo (Norway)". https://indico.cern.ch/event/1247911/contributions/5394667/.

[123] "Hamamatsu Photonics K.K.", https://www.hamamatsu.com, 2017.

[124] "Fondazione Bruno Kessler". https://sd.fbk.eu/en.

[125] "LFoundry GmbH". http://lfoundry.com.

[126] **RD53** Collaboration, "The RD53A Integrated Circuit", Technical Report CERN-RD53-PUB-17-001, CERN, Geneva, Oct, 2017.

[127] **RD53** Collaboration, "RD53B users guide", technical report, CERN, Geneva, 2020.

[128] M. Daas et al., "BDAQ53, a versatile pixel detector readout and test system for the ATLAS and CMS HL-LHC upgrades", *Nuclear Instruments and Methods in Physics Research Section A: Accelerators, Spectrometers, Detectors and Associated Equipment* **986** (2021) 164721, doi:https://doi.org/10.1016/j.nima.2020.164721.

[129] "CMS tracker Phase2 Acquisition and Control Framework (Ph2 ACF)". https://gitlab.cern.ch/cms_tk_ph2/Ph2_ACF.

[130] L. D. Landau, "On the energy loss of fast particles by ionization", *J. Phys.* **8** (1944) 201–205.

[131] A. Jofrehei, "Observation of τ lepton pair production in ultraperipheral nucleus-nucleus collisions with the CMS experiment and the first limits on $(g-2)_\tau$ at the LHC", 2022.

[132] A. Jofrehei et al., "Investigation of crosstalk effects in RD53A modules with 100 and 150

μm thick n-in-p planar sensors", *PoS* **EPS-HEP2019** (2020) 151,
doi:10.22323/1.364.0151.

[133] A. Jofrehei et al., "Characterization of irradiated RD53A pixel modules with passive CMOS sensors", *Journal of Instrumentation* **17** (sep, 2022) C09004,
doi:10.1088/1748-0221/17/09/C09004.